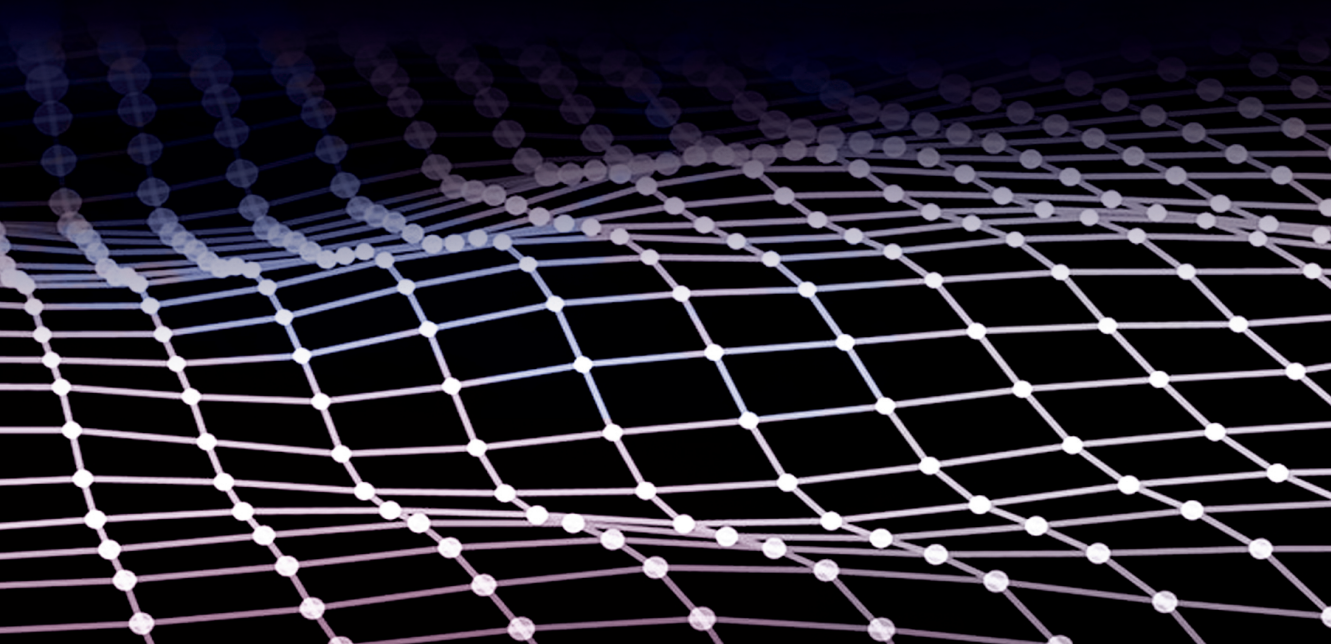


Instrumentation
and characterization techniques
for advanced gravitational-wave
observatories

Andrei Catalin Utina



“If you wish to make an apple pie from scratch,
you must first invent the universe.”

— Carl Sagan, *Cosmos*

© 2024 Andrei Utina, Maastricht, All rights reserved.

Instrumentation and characterization techniques for advanced gravitational-wave observatories

Cover designed by Dan Chirila, adapted from the Caltech post at the following address: <https://magazine.caltech.edu/post/quantum-gravity>

Nik|hef



Maastricht University



This work originates as part of the research programme of the Foundation for Fundamental Research on Matter (FOM), and falls as of April 1, 2017 under the responsibility of Netherlands Foundation of Scientific Research Institutes (NWO-I) (NWO-I), which is part of the Dutch Research Council (NWO).

Instrumentation and characterization techniques for advanced gravitational-wave observatories

Dissertation

to obtain the degree of Doctor at Maastricht University,
on the authority of the Rector Magnificus, Prof. dr. Pamela Habibović
in accordance with the decision of the Board of Deans,
to be defended in public on
Tuesday 19 November 2024, at 13:00 hours

by

Andrei Catalin Uțina

Supervisor

Prof. dr. S. Hild

Co-Supervisor

Dr. S. Steinlechner

Assessment Committee

Prof. Gerco Onderwater, Full Professor, Maastricht University (chair)

Prof. Andreas Freise, Full Professor, Vrije Universiteit Amsterdam, Nikhef

Prof. Frank Linde, Full Professor, University of Amsterdam, Nikhef

Prof. Marcel Merk, Full Professor, Maastricht University

Dr. Jessica Steinlechner, Associate Professor (UHD), Maastricht University

Contents

1	Background	1
1.1	Gravitational waves	1
1.1.1	Spacetime curvature	1
1.1.2	Propagation of metric perturbations	2
1.1.3	Gravitational-wave sources	3
	Compact binaries	4
	Spinning Neutron Stars	4
	Supernovae	5
	Cosmological sources	5
1.2	Gravitational-wave detectors	6
1.2.1	Laser interferometers	7
	The simple Michelson interferometer	7
1.2.2	Advanced detectors design	9
1.2.3	Current operating detectors	13
	LIGO	14
	Virgo	15
	GEO600	16
	KAGRA	16
1.2.4	Third generation of gravitational-wave detectors	17
	Cosmic Explorer	17
	Einstein Telescope	17
1.3	Preview of this Thesis	20
2	Radio-frequency sidebands studies during Advanced Virgo O3 run	23
2.1	Motivation	23
2.2	ISC fundamentals	24

2.2.1	The laser field	24
2.2.2	Pound-Drever-Hall Locking Technique	27
2.2.3	Longitudinal degrees of freedom	33
2.3	Sideband evolution simulation	36
2.4	Data extraction and calibration	40
2.5	Analysis	44
2.6	Results	45
2.7	Conclusions	50
3	ETpathfinder sensitivity studies	53
3.1	Introduction	53
3.2	ETpathfinder	55
3.2.1	Cleanroom	55
3.2.2	Optical Layout	55
	Interferometer arm-cavity	57
	Choice of arm-cavity finesse	57
3.2.3	ETpathfinder suspensions	59
3.3	Fundamental noise sources	61
3.3.1	Quantum fluctuations of the light field	61
3.3.2	Seismic noise	63
	Seismic campaign	63
	Suspension transfer function	64
	One degree-of-freedom example	67
	ETpathfinder suspension model	69
	Results	72
3.3.3	Thermal displacement noises	74
	Coating Brownian noise	75
	Substrate Thermal noises	77
	Substrate Brownian noise	77
	ITM thermo-refractive noise	77
	Substrate thermo-elastic noise	78
	Suspension thermal noise	79
3.3.4	Newtonian noise	82
3.3.5	Residual gas noise	83
3.4	Outlook	85
3.5	Conclusions	87
4	Analysis of vibration via cryogenic heat-links	89
4.1	Introduction	89
4.2	Prototype 0 test-setup	91
4.3	Vibration transfer simulation	93
4.3.1	Heat-link geometry	93

4.3.2	Analytical model	95
4.3.3	Results	97
4.4	Transfer measurements	98
4.4.1	Dual channel analysis fundamentals	98
4.4.2	Apparatus preparation	100
4.4.3	Measurement for six heat-links	101
4.4.4	Stiffness variability measurements	103
4.4.5	In-air and in-vacuum measurements	105
4.4.6	Conclusions from the measurements	107
4.5	Heat-link vibration projection for ETpathfinder	108
4.6	Discussion and recommendations	114
5	Automatic alignment of resonant optical cavities using Machine Learning	117
5.1	Introduction	117
5.1.1	Angular misalignment as generator of higher-order modes	118
5.1.2	Conventional methods for interferometric alignment . . .	120
5.2	Deep Learning	122
5.2.1	Convolutional neural networks	123
5.3	Test setup	126
5.4	Data set	127
5.4.1	Labeling	127
5.4.2	Pre-processing	128
5.5	The convolutional neural network algorithm	130
5.5.1	Training	132
5.5.2	Testing	132
5.6	Pre-alignment and cavity lock test	135
5.7	Conclusions	136
6	Synthesis and overall conclusions	139
	Appendix A: Error signal derivation in the presence of a higher-order transverse electromagnetic mode	141
	Appendix B: Advanced Virgo Finesse base-file	145
	Appendix C: ETpathfinder-Light noise budget	153
	Appendix D: PCB393B05 accelerometer technical details	155
	Appendix E: Calculation of cold-finger acceleration above resonance	157
	Bibliography	159
	Acknowledgements	175

Summary	177
Samenvatting	181
Impact paragraph	187
Propositions	189
Curriculum Vitae	191

1.1 Gravitational waves

1.1.1 Spacetime curvature

The theory of General Relativity (GR), developed in 1915-1916 by Albert Einstein, together with the development of Quantum Mechanics, represents the foundation of modern physics. In his theory, Einstein revolutionized the way gravity was understood at that time by showing that spacetime can be *curved* or *warped* and that gravity is a manifestation of the curvature of spacetime. John Wheeler put it best: “Matter tells spacetime how to curve; spacetime tells matter how to move”. This dependence of matter and space can be seen directly in Einstein field equations:

$$R_{\mu\nu} - \frac{1}{2}g_{\mu\nu}R = \frac{8\pi G}{c^4}T_{\mu\nu}. \quad (1.1)$$

Here, $R_{\mu\nu}$ is the Ricci tensor, obtained by contraction of the Riemann curvature tensor as $R_{\mu\nu} = R_{\mu\sigma\nu}^{\sigma} = g^{\sigma d}R_{\sigma\mu d\nu}$, R is the Ricci scalar, $g_{\mu\nu}$ is the metric tensor which describes the geometry of spacetime and $T_{\mu\nu}$ is the energy-density tensor, describing the matter distribution in spacetime.

Therefore, the absence of gravity yields a flat spacetime. A *weak* gravitational field, or *nearly flat* spacetime is defined as follow:

$$g_{\mu\nu} = \eta_{\mu\nu} + h_{\mu\nu}, \quad (1.2)$$

where $\eta_{\mu\nu}$ represents the flat, Minkowski spacetime, defined as the diagonal matrix $\text{diag}(-1, 1, 1, 1)$ and $h_{\mu\nu}$ is a small perturbation in the metric.

The objective is to expand the field equations in powers of $h_{\mu\nu}$ for a coordinate frame where the weak field condition is satisfied on a sufficiently large region of space. This formalism is called *linearized theory of gravity*. To linear order in $h_{\mu\nu}$, the Riemann tensor from Equation 1.1 becomes:

$$R_{\mu\nu\rho\sigma} = \frac{1}{2} (\partial_\nu \partial_\rho h_{\mu\sigma} + \partial_\mu \partial_\sigma h_{\nu\rho} - \partial_\mu \partial_\rho h_{\nu\sigma} - \partial_\nu \partial_\sigma h_{\mu\rho}). \quad (1.3)$$

Using this equation, the linearized form of the Einstein tensor $G_{\mu\nu} = R_{\mu\nu} - \frac{1}{2}g_{\mu\nu}R$ can be computed as follows:

$$\square \bar{h}_{\mu\nu} + \eta_{\mu\nu} \partial^\rho \partial^\sigma \bar{h}_{\rho\sigma} - \partial^\rho \partial_\nu \bar{h}_{\mu\rho} - \partial^\rho \partial_\mu \bar{h}_{\nu\rho} = -\frac{16\pi G}{c^4} T_{\mu\nu}. \quad (1.4)$$

Here, h is defined as:

$$h = \eta^{\mu\nu} h_{\mu\nu}, \quad (1.5)$$

and $\bar{h}_{\mu\nu}$ as:

$$\bar{h}_{\mu\nu} = h_{\mu\nu} - \frac{1}{2} \eta_{\mu\nu} h. \quad (1.6)$$

Choosing the *Lorentz gauge*, also called *De Donder gauge*, defined as $\partial^\nu \bar{h}_{\mu\nu} = 0$, it can be shown that the linearized Einstein tensor takes the following form:

$$\square \bar{h}_{\mu\nu} = -\frac{16\pi G}{c^4} T_{\mu\nu}. \quad (1.7)$$

Here, as well as in Equation 1.4, the operator \square is the d'Alembertian, defined as $\square = \eta_{\mu\nu} \partial^\mu \partial^\nu = \partial_\mu \partial^\mu = \frac{1}{c^2} \frac{\partial^2}{\partial t^2} - \frac{\partial^2}{\partial x^2} - \frac{\partial^2}{\partial y^2} - \frac{\partial^2}{\partial z^2}$. Expanding the d'Alembertian into the above equation and considering a flat spacetime outside the gravitational-wave source, one in which $T_{\mu\nu} = 0$, then it can be shown that:

$$\left(-\frac{\partial^2}{\partial t^2} + \nabla^2 \right) \bar{h}_{\mu\nu} = 0. \quad (1.8)$$

Therefore, linearizing the Einstein field equations yields a three-dimensional wave equation for the transverse-traceless metric $\bar{h}_{\mu\nu}$. Gravitational waves can be interpreted as traveling metric perturbations at the speed of light.

1.1.2 Propagation of metric perturbations

The elements of $\bar{h}_{\mu\nu}$ in Equation 1.8 represent the plane-wave solutions of the form $h(2\pi ft - \mathbf{k} \cdot \mathbf{x})$, for a plane wave propagating in the direction $\hat{k} \equiv \mathbf{k}/|\mathbf{k}|$ and with speed c . Therefore, for a wave propagating along the \hat{z} axis, the statement that $\bar{h}_{\mu\nu}$ is transverse and traceless yields:

$$h_{\mu\nu} = \begin{pmatrix} 0 & 0 & 0 & 0 \\ 0 & a & b & 0 \\ 0 & b & -a & 0 \\ 0 & 0 & 0 & 0 \end{pmatrix}. \quad (1.9)$$

This can be therefore written as a sum of two components:

$$h_{\mu\nu} = ah_+ + bh_\times, \quad (1.10)$$

where h_+ and h_\times , called (*h-plus* and *h-cross*) are the basis tensors which represent the two polarizations of gravitational waves propagating along the chosen axis \hat{z} . They are defined as:

$$h_+ = \begin{pmatrix} 0 & 0 & 0 & 0 \\ 0 & 1 & 0 & 0 \\ 0 & 0 & -1 & 0 \\ 0 & 0 & 0 & 0 \end{pmatrix}, \quad (1.11)$$

and

$$h_\times = \begin{pmatrix} 0 & 0 & 0 & 0 \\ 0 & 0 & 1 & 0 \\ 0 & 1 & 0 & 0 \\ 0 & 0 & 0 & 0 \end{pmatrix}. \quad (1.12)$$

The two polarization vectors can be understood intuitively by considering the effect of $h_{\mu\nu}$ on a set of points originally arranged in a circle. Figure 1.1 depicts this effect.

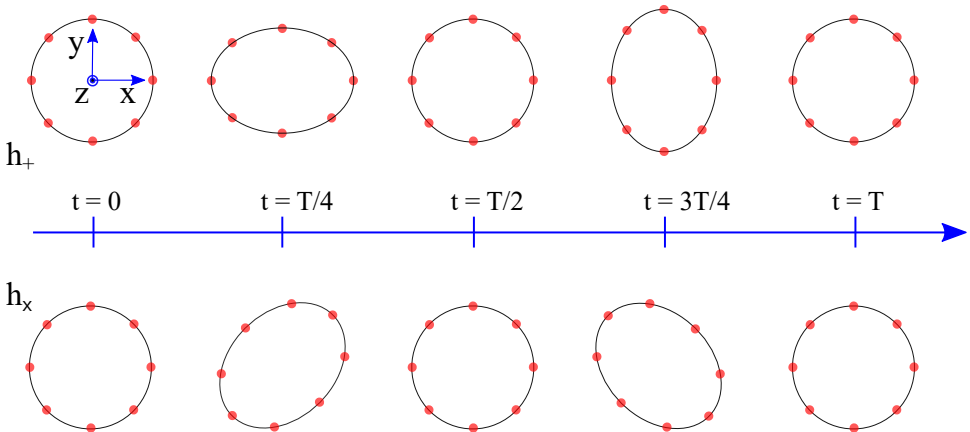


Figure 1.1: The effect of a passing gravitational wave on a ring of test particles. The two polarizations stretch and squeeze the particle ring differently by a 45° rotation at a quarter and three quarters of the oscillation period.

1.1.3 Gravitational-wave sources

There is an entire spectrum of gravitational-wave sources and the frequencies at which they can be observed depends on the mechanics that generate gravitational radiation [1].

Compact binaries

Compact binary coalescences are the only source of gravitational radiation detected so far, and they were predicted as the most probable candidates for detection in the ground-based gravitational wave observatories, such as LIGO and Virgo. They are systems of compact objects, such as black holes and neutron stars, undergoing collisions. Depending on the mass and the luminosity-distance of the components, these sources produce gravitational radiation over a wide frequency range, from the very low-frequency domain of 1×10^{-7} to 1×10^{-8} Hz to the high-frequency domain of 1 to 1×10^4 Hz. A simplified description of how gravitational waves are generated by the compact binaries can be given using the *multipole expansion* treatment, similar to the study of electromagnetic radiation.

The multipole expansion is a mathematical series describing a function dependent on angles, such as the electromagnetic or the gravitational field at distant points in terms of the sources located in a contained region. In the case of electromagnetic radiation, the dominant contribution to the radiated field is represented by the dipole moment variation. However, because the conservation of momentum requires the time derivative of a gravitational dipole moment to be constant for any isolated system, there can be no radiation associated to a gravitational dipole moment. The strongest contribution to the gravitational radiation comes from the time variation of the gravitational quadrupole moment $Q_{\mu\nu}$, defined as:

$$Q_{\mu\nu} = \int dV \left(x_\mu x_\nu - \frac{1}{3} \delta_{\mu\nu} r^2 \right) \rho(\mathbf{r}). \quad (1.13)$$

Here $\rho(\mathbf{r})$ is a mass-density distribution contained within a volume V , as a function of radial distance r , x_μ and x_ν are spatial coordinates and $\delta_{\mu\nu}$ is the Dirac Delta function. The amplitude of the gravitational-wave $h_{\mu\nu}$ can now be written in terms of the quadrupole moment as:

$$h_{\mu\nu} = \frac{2G}{rc^4} \ddot{Q}_{\mu\nu}. \quad (1.14)$$

Here c is the speed of light in vacuum, G is the Newtonian constant and r is the luminosity distance between the gravitational-wave source and the observer. It can be observed that the quantity $\frac{G}{c^4}$ is of very small value. Therefore, in order to produce measurable gravitational waves, the second order derivative of the quadruple moment should be large enough, a condition encountered in the cataclysmic astrophysical events of compact binary coalescences.

Spinning Neutron Stars

Spinning neutron stars, or pulsars, are rapidly rotating stars emitting periodic pulses of electromagnetic radiation. In its final state of formation, the star layer crystallizes

with an axisymmetric geometry that is maintained by centrifugal forces. The poloidal ellipticity of the star, ϵ_p , is proportional to the angular velocity of rotation squared.

In its fast rotation, the neutron star's principal axis might deviate slightly from the axisymmetric condition, therefore an ellipticity $\epsilon_e < \epsilon_p$ can be generated in the equatorial plane. As the neutron star rotates with this crust anisotropy, it will radiate continuous gravitational radiation with a frequency of twice the rotational frequency [2]. The amplitude of the gravitational waves are proportional to the ellipticity ϵ_e , and for typical neutron-star masses and moments of inertia, the gravitational-wave amplitude can be written as:

$$h \sim 6 \times 10^{-25} \left(\frac{f_{\text{rot}}}{500 \text{ Hz}} \right)^2 \left(\frac{1 \text{ kpc}}{r} \right) \left(\frac{\epsilon_e}{10^{-6}} \right). \quad (1.15)$$

Supernovae

When a massive star's core runs out of nuclear fuel, it collapses into a neutron star or a black hole. If the mass of the star surpasses the Chandrasekhar limit, the collapse initiates and propels a subsequent explosion of the mantle of the star, known as a supernova explosion.

There are many theoretical models of physical processes that can produce gravitational waves at high frequencies (1 to 10^4 Hz) during a core collapse supernova [3]. These include the break-up of the stellar structure when the core rotation is large enough as it reaches nuclear density, and the bounces or oscillations of the stellar core when the centrifugal forces are small enough to halt the core collapse after reaching nuclear density. However, since no core collapse source have been detected so far, there is no definite understanding about the generating mechanisms that can give rise to gravitational radiation.

Cosmological sources

Physical processes in the early universe could have created spacetime metric anisotropies which could give rise to a background of gravitational radiation that extends through the entire frequency range from 10^{-18} Hz to 10^4 Hz.

One effect producing cosmological gravitational-wave backgrounds is the early universe itself. Initial calculations have shown that the state of the graviton field immediately after being produced in the big bang could have interacted with the expanding universe, creating spacetime metric anisotropies as a form of gravitational waves [4]. Furthermore, primordial matter in the early universe allowed gravitational waves to pass through, as shown by Zel'dovic and Novikov [5].

First-order phase transitions in the early universe could also lead to the production of gravitational waves [6, 7, 8]. The first-order phase transitions are predicted to exist in the standard model of strong, weak and electromagnetic interactions. These transitions represents the evolution from a high-temperature phase of a region of the

universe as it expands to a low-temperature phase. The latter phase, even though in phase-equilibrium where there is no other transition, it still expands generating pressure waves in the matter which can give rise to backgrounds of gravitational waves.

Cosmic strings are one-dimensional topological stable objects, predicted by many theories which extend the Standard Model of particle physics [9]. If such strings were created in enormous quantities in the early universe, their vibrations could give rise to a frequency-independent gravitational-wave spectrum. The latest constraints on the cosmic strings models were obtained using the data from the science run *O3* of the network of ground-based gravitational-wave observatories [10].

The signal in the output channel of detectors produced by the gravitational-wave background is stochastic, buried in detector noise. As a consequence, the gravitational-wave background can only be detected collectively via their common interaction with multiple, largely separated detectors. However, since compact binary coalescences at large red-shifts and with low signal-to-noise ratio can also produce an astrophysical stochastic background, effective methods to disentangle the two backgrounds are currently under study [11].

1.2 Gravitational-wave detectors

The experimental efforts to detect gravitational radiation started with resonant bar detectors. The pioneer of this concept was Joseph Weber, who developed and created the first prototype detector in 1960.

A bar detector is a metal cylinder of length L of a few meters and radius of curvature R of dimensions typically 30 cm to 1 m. The resonant bar is more sensitive to vibrations in the x -direction, along the length L . If the dissipative effects are neglected during the passage of the gravitational wave, then the longitudinal oscillations for a mass element dm enclosed in a volume dV can be expressed as:

$$dm \left(\frac{\partial^2 x'}{\partial t^2} - v_s^2 \frac{\partial^2 x'}{\partial x^2} \right) = dF_x(t, x), \quad (1.16)$$

where v_s is the speed of sound in the material of the bar, x' is the small displacement from equilibrium of the mass element dm , and dF_x is the x -component of the force exerted by the gravitational wave on the mass element.

It can be seen from Equation 1.16 that the gravitational-wave induced effect should be expressed as a Newtonian force. This is possible, based on Section 1.1.1, since the length of the detector is much smaller than the typical wavelength of the travelling gravitational wave and the Newtonian force can be expressed by the equation of geodesic deviation. Therefore, Equation 1.16 can be written using the Newtonian force in the detector reference frame expressed in terms of the

gravitational wave strain component h_{ij} as:

$$dm \left(\frac{\partial^2 x'}{\partial t^2} - v_s^2 \frac{\partial^2 x'}{\partial x^2} \right) = \frac{1}{2} \ddot{h}_{ij}^{TT} x^j dm. \quad (1.17)$$

Here, $x^j = (x + x', 0, 0)$ and the gravitational wave is expressed in the TT gauge.

A passing gravitational wave excites the resonance mode of the detector at $\omega = \pi v_s / L$. Therefore, the bar detector is sensitive to frequencies at integer numbers of the fundamental mode with $\frac{L}{\lambda'} \approx \frac{\pi v_s}{c}$ with $\lambda' = \lambda / 2\pi$ being the reduced wavelength of the gravitational wave.

Numerous research groups across the world have studied and modified the initial design of resonant bar detectors, but to date, this concept has failed to discover any gravitational wave sources. The next sections, and the rest of this thesis, will describe in detail the only successful experimental enterprise in detecting gravitational radiation to date: the laser interferometer*

1.2.1 Laser interferometers

The development of laser interferometers gravitational-wave observatories marked the transition from laboratory-scale science to a global scientific effort involving thousands of scientists.

The idea of detecting gravitational waves using laser interferometers dates back to 1962, when two Russian theorists proposed a simple detection scheme with light being timed as it propagates through the arms of the apparatus. Later, Rainer Weiss developed a comprehensive version of the Michelson interferometer detector by studying the feasibility of the design with respect to the potential limiting noise sources [13]. This marked the beginning in the development of LIGO detectors.

The simple Michelson interferometer

The Michelson interferometer, developed by Michelson and Morley to demonstrate the non-existence of the ether in 1887, is a device that accurately measures the variations in the light propagation through the two perpendicular arms of the apparatus. The simplified layout of the device is depicted in Figure 1.2. The device consists of a monochromatic light source which sends the light beam into a beam-splitter which separates the beam into two light fields travelling with similar amplitudes across both arms of the interferometer. The beams are reflected back by mirrors placed at the two ends of the interferometer arms and then recombine at the beam-splitter. The interference pattern is measured by a photodetector.

*Although this was the case during the writing of this thesis, the international pulsar timing array (PTA) collaboration announced the discovery of “the first evidence for low-frequency gravitational waves permeating the cosmos” at the end of June 2023 [12].

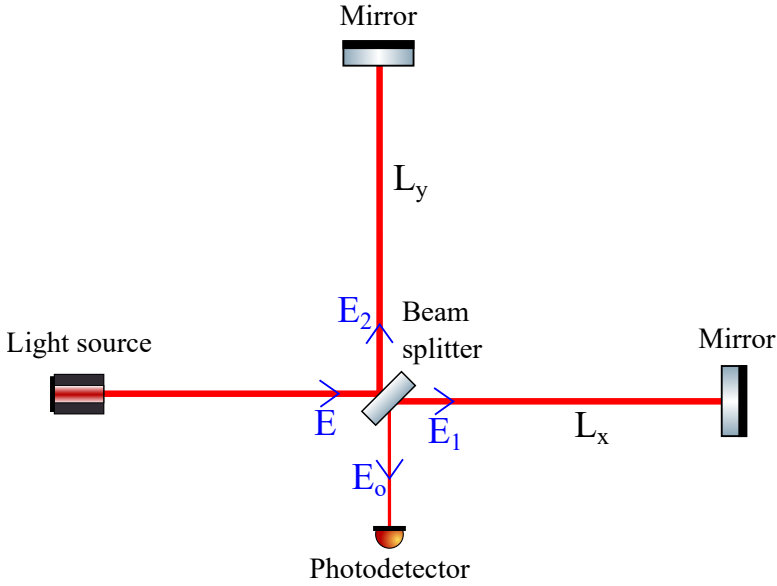


Figure 1.2: The optical layout of the simple Michelson interferometer.

The spatial x component of the electric field E can be expressed as:

$$E = E_i e^{i(k_L \cdot x - \omega_L t)}, \quad (1.18)$$

where ω_L represents the angular frequency of the laser light, $k_L = \frac{\omega_L}{c}$ is the wave number with c being the speed of light and E_i is the initial amplitude of the electromagnetic field. The time t_0 is considered when the electric field hits the beam-splitter. Therefore, a photon travelling in the x -arm of the interferometer, across L_x returns to the beam-splitter after a time $t_x = t_0 + \frac{2L_x}{c}$. Similarly, a photon travelling across the y -arm arrives at the beam-splitter after a time $t_y = t_0 + \frac{2L_y}{c}$.

It then follows that a beam which recombines at the beam-splitter is formed from the superposition of the beams that enter the beam-splitter and then propagates through each arm with the times $t_{0x} = t_x - \frac{2L_x}{c}$ for the x -arm and correspondingly $t_{0y} = t_y - \frac{2L_y}{c}$ for the y -arm. The phase of the electromagnetic field is conserved during free-space propagation along the arms. At the beam-splitter, for $x = 0$ the phase of x -beam is defined as $\exp\{-i\omega_L t_{0x}\} = \exp\{-i\omega_L t + 2ik_L L_x\}$ and the phase term of the y -beam is $\exp\{-i\omega_L t_{0y}\} = \exp\{-i\omega_L t + 2ik_L L_y\}$. The two electromagnetic fields recombining at the beam-splitter can now be expressed as:

$$E_1 = -\frac{1}{2} E_0 e^{i(2k_L L_x - \omega_L t)}, \quad (1.19)$$

and

$$E_2 = -\frac{1}{2} E_0 e^{i(2k_L L_y - \omega_L t)}. \quad (1.20)$$

The total electric field E_{out} is the sum of the recombined beams at the beam-splitter $E_1 + E_2$ and this can be shown to be:

$$E_{\text{out}} = -iE_0 e^{-i\omega_L t + ik_L(L_x + L_y)} \sin[k_L(L_y - L_x)]. \quad (1.21)$$

Squaring the total electric field in Equation 1.21 results in the power measured by the output photodiode:

$$|E_{\text{out}}|^2 = E_0^2 \sin^2[k_L(L_y - L_x)]. \quad (1.22)$$

It can now be observed that the differential displacement of the interferometer arm-lengths results in the fluctuations in power at the photodetector. Therefore, the interferometer output indicates the relative phase shift of the two orthogonal laser beams upon returning at the beam-splitter. When a gravitational-wave passes the device, it creates a phase shift Φ_{gw} between the two laser fields interfering at the beam-splitter, therefore modulating the power incident on the photodetector. For the case of a sinusoidal + polarized gravitational-wave with amplitude h , this phase shift can be expressed as:

$$\Phi_{gw} = h(t) \frac{2L}{c} 2\pi f, \quad (1.23)$$

where L is the arm-length of the interferometer, f is the laser light frequency and c is the speed of light. Therefore, a fraction h of the total phase-shift that the laser beam accumulates as it travels through the interferometer translates to the direct phase shift between the two laser beams at the beam-splitter. This implies that increasing the arm-length of the interferometer, therefore the optical path, results into a larger phase shift induced by the gravitational wave upon the two interfering laser fields. One can find that the optimal length of the arms equals to a quarter of the gravitational radiation wavelength, which for a source of frequency of about 100 Hz, this equals around 750 km. For this value and below, the phase shift induced by the gravitational wave on the light fields has the same sign all along its round-trip, and this effect accumulates. However, for larger interferometer arm-lengths, the gravitational wave flips its sign during one round-trip and this results in a partial cancellation of the phase shift that the light accumulated before recombining at the beam-splitter.

1.2.2 Advanced detectors design

Advanced laser interferometers for gravitational wave detection, such as Advanced LIGO and Advanced Virgo detectors, integrate Fabry-Perot resonant cavities in order to increase the light optical path length and therefore the detection strain sensitivity. Fabry-Perot cavities have been extensively employed in other optical applications, such as optical spectroscopy, laser amplification or as narrow band filters. They consist of a two-mirror system, m_1 and m_2 , usually called input test mass (ITM) and the end test mass (ETM), separated by a distance L . The cavity folds the optical paths

superimposed on top of each other, increasing the storage time of light inside the arm-lengths and therefore the dephasing due to gravitational waves. The Fabry-Perot cavities can be observed on the interferometer layout depicted by Figure 1.3.

For a given laser wavelength λ , the Fabry-Perot cavity length can be tuned in order to maximize the circulating power inside the cavity. This condition is called resonance. If one assumes the incident power of the electric field at the ITM to have a magnitude of one, then the circulating power inside the Fabry-Perot cavity, assuming no optical losses, can be expressed in terms of the field amplitude, a , as:

$$P_1 = |a|^2 = \frac{T_1}{1 + R_1 R_2 - 2r_1 r_2 \cos(2kL)}, \quad (1.24)$$

where $k = \frac{2\pi}{\lambda}$, r_1 and r_2 correspond to the real amplitude coefficients for reflection of ITM and ETM respectively, T_1 is the transmissivity of the ITM and R is the reflectivity with subscript 1 referring to the ITM and 2 to the ETM. The maximum power inside the cavity is reached when the cosine term in the denominator of the above equation equals one. This translates to $\cos(2kL) = n\pi \rightarrow kL = n\pi \rightarrow L = \frac{n\lambda}{2}$. Therefore, in order to have a resonant optical field inside the Fabry-Perot cavity, its round-trip length must be tuned as integer wavelengths of the laser light.

The frequency range between different resonance peaks is called *free-spectral range* (FSR) and is defined as:

$$\text{FSR} = \frac{\pi c}{L}. \quad (1.25)$$

Around each of these resonance peaks, if the denominator in Equation 1.24 is expanded to quadratic order, the *full width at half maximum* (FWHM) is obtained:

$$\text{FWHM} = 2f_p = \frac{c}{L} \frac{1 - r_1 r_2}{\sqrt{r_1 r_2}}, \quad (1.26)$$

where f_p is the cavity cut-off frequency, or the cavity *pole*.

Having the Equations 1.25 and 1.26 one can define the *finesse* \mathcal{F} of the resonant cavity as:

$$\mathcal{F} = \frac{\text{FSR}}{\text{FWHM}} = \frac{\pi \sqrt{r_1 r_2}}{1 - r_1 r_2}. \quad (1.27)$$

Another important quantity defining the performance of a resonant cavity is the photon storage time; this is the average time a photon spends inside the cavity before exiting through one of the component mirrors, defined as:

$$\tau = \mathcal{F} \frac{2L}{\pi c} = N \frac{L}{c} = \frac{\pi}{2f_p}, \quad (1.28)$$

where N is the average number of travels inside the cavity.

When the Michelson interferometer is functioning at the dark fringe, incoming laser light is reflected back into the laser port by the beam-splitter. As a result, most of the system's laser power is lost. To recycle the lost power, a *power-recycling*

mirror (PRM) is installed between the input optics system and the beam splitter. The newly installed mirror forms a resonant cavity with the Michelson interferometer, called the *power-recycling cavity* (PRC).

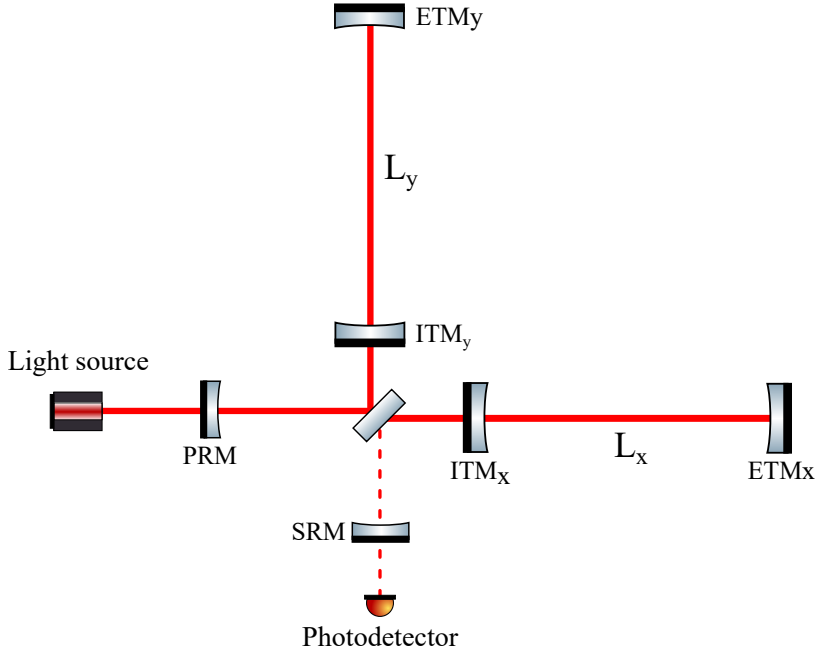


Figure 1.3: The simplified optical layout of the dual-recycled Michelson interferometer configuration.

The optical power enhancement from the PRC is given by the finesse value of the cavity, which strongly depends on the optical losses inside the Michelson interferometer, and the reflectivity of the PRM. Therefore, if the losses in the interferometer are small, the enhancement factor, or the optical gain of the PRC can be defined as:

$$G_{\text{PR}} \approx \frac{4}{T_{\text{PRM}}} \approx \frac{2\mathcal{F}}{\pi}. \quad (1.29)$$

Here T_{PRM} is the transmissivity of the PRM and \mathcal{F} is the PRC finesse. Under this condition, the PRC is over-coupled [14] with the electromagnetic field inside the Michelson interferometer. On the contrary, if the optical losses inside the main interferometer are not negligible, then one can optimize the PRM transmissibility such that it equals the interferometer losses, a condition known as impedance matching. The optical gain in this case can be expressed as:

$$G_{\text{PR}} = \frac{1}{T_{\text{PRM}}} \approx \frac{\mathcal{F}}{\pi}. \quad (1.30)$$

The advantage of integrating the power recycling mirror significantly outweighs the disadvantage of adding alignment and control complexity: it improves the interferometer's circulating power, hence enhancing the measurement's SNR. Moreover, the power recycling cavity also functions as a filter for imperfections in the distribution of the traveling laser field, such as beam jitter and laser frequency noise.

In order to optimize the power amplification in the optical cavities, it is imperative that the optical elements and platforms of the interferometer are effectively isolated from external disturbances and precisely controlled to a predetermined set point. Upon accomplishing this, the interferometer enters its operating point, the state in which the interferometer is able to detect astronomical signals. Additional details on the subject matter of instrumental sensing and control are provided in Chapters 2 and 5. The optical elements are controlled primarily through the utilization of dedicated feedback control loops. This is the process by which the system's output is fed into its input to maintain it at a predetermined set point. This is achieved for the longitudinal degrees of freedom of the interferometer, including the power recycling cavity, by opting for an error signal that provides information regarding the cavity's length in relation to its resonant point. Pound-Drever-Hall (PDH) error signals are the principal method by which interferometric control is accomplished. The core idea is based on modulating the carrier field at a selected modulation frequency to produce antiresonant control sidebands within the optical cavity; since the carrier itself resonates in the cavity, the beat note separating the carrier and sidebands provides an actuation system-applicable signal reference.

After the successful integration of the power recycling mirror in the optical topology of the laser interferometer detectors, Brian Meers considered adding an additional recycling mirror at the dark port of the interferometer [15]. This new mirror acts as *signal recycling mirror* (SRM) for the signal sidebands that are present in the anti-symmetric port. A *signal-recycling cavity* is therefore formed with the main interferometer. Generally, the signal-recycling technique increases the interferometer response or bandwidth to differential displacements. Depending on the position, or tuning, of the signal-recycling mirror, the interferometer can be in the *signal-recycling phase*, where sideband signal storage time increases in the interferometer, or the *resonant sideband extraction phase*, where the sideband storage time is decreased. A shorter sideband storage time leads to a larger detection bandwidth, and this allows the interferometer to detect a wider range of gravitational wave frequencies, making it more versatile in observing various astrophysical events. This is why the second generation of ground-based gravitational wave interferometers integrate the resonant sideband extraction method.

The combination of the two additional recycling mirrors added to the Michelson interferometers is called *dual-recycling* configuration. This was firstly demonstrated in a table-top experiment at the University of Glasgow by Ken Strain and Brian Meers [16]. This optical configuration together with employing Fabry-Perot resonators represents the baseline of advanced detectors.

Ground-based gravitational-wave interferometers with kilometer-long arms have the ability to detect differential displacements that are approximately a thousand times smaller than the size of a quark. At these minuscule scales, numerous kinds of noises can impact the measurement and mask the gravitational wave signal. There are two categories of noise sources: fundamental, which are inherent to the facility's design, and technical noise sources, which originate from the devices responsible for controlling the interferometer and conducting the measurements. The fundamental noise sources include the Brownian motion of atoms in the mirrors' coatings or the quantized nature of light, while technical noise sources include the noise caused by the control of the test masses' angular or longitudinal position. The examination of these sources of noise is expanded upon in Chapter 3 and Chapter 4.

The noise sources consist of random, ergodic processes, often characterized by a time series denoted as $n(t)$. Generally, it is useful to distinguish and analyze the individual contribution of various frequencies f on the signal power. Hence, the noise can be characterized by the *power spectral density* (PSD), which is defined as:

$$S_x(f) = \lim_{T \rightarrow \infty} \frac{2}{T} \left| \int_{-T}^{+T} n(t) e^{-2i\pi f t} dt \right|^2. \quad (1.31)$$

Often, the *amplitude spectral density* (ASD) is the most encountered quantity defining the performance figures of gravitational-wave detectors. This is defined as:

$$h(f) = \sqrt{S_x(f)}. \quad (1.32)$$

1.2.3 Current operating detectors

The network of long-baseline ground-based gravitational-wave interferometers is the first gravitational-wave observatory network. These detectors, whose positions are indicated in Figure 1.4, formed the foundational architecture of the observational network and enhanced their sensitivities with each science run. The second generation of these detectors, also called *advanced*, improved the strain sensitivity to the level where the detection of astrophysical gravitational radiation was possible. While these detectors further extend their operating sensitivities closer to the facility limits, the revolutionary third generation (3G) of gravitational-wave detectors are being studied and planned for construction in the next decade.

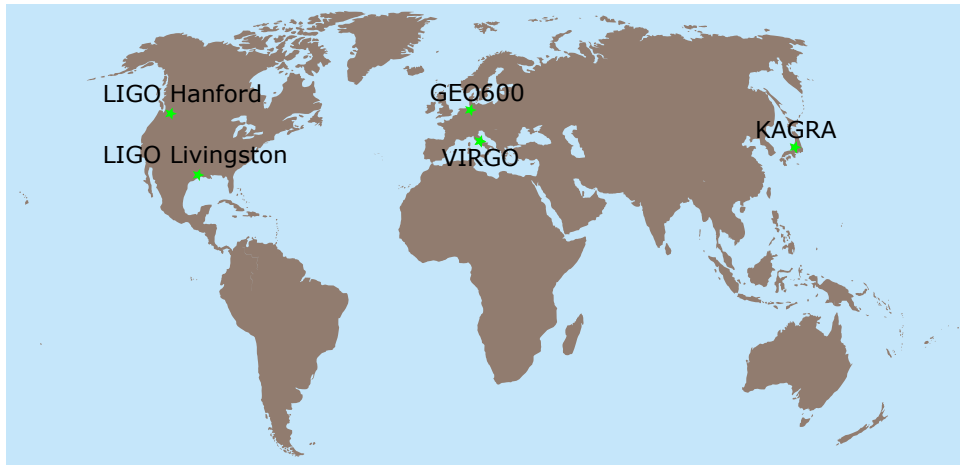


Figure 1.4: Geographical distribution of the current network of gravitational-wave detectors.

LIGO

The Advanced LIGO detectors are the culmination of decades of study and development by numerous scientific institutions across the globe. The detectors are positioned at two sites in the United States, one in Hanford, Washington, and the other in Livingston, Louisiana. These detectors have undergone a series of improvements, and the successful integration of these upgrades has enabled the Advanced LIGO detectors to become the most sensitive observatories and to detect the first gravitational wave signal on September 14th 2015 [17].

Advanced LIGO detectors are dual recycled Fabry-Perot Michelson interferometers with a baseline arm-length of 4 km. Important upgrades from the initial detector include the dual-recycled configuration, the seismic isolation system including the novel active isolation platform [18, 19] and the quadrupole pendulum suspension for heavier test masses [20], increasing the input laser power [21, 22], and the implementation of an updated sensing and control strategy [23, 24].

The last upgrade of the Advanced LIGO detectors, also called *A+*, mainly covers the broadband reduction in quantum noise by the use of squeezed light states, and the reduction in the coating thermal noise. The goal of the upgrade is to increase the sensitivity of the Advanced LIGO configuration by about 50%. There has been a proposal that between the end of this configuration and the next generation of gravitational-wave detectors, LIGO observatories can be further upgraded to cryogenic instruments with greatly enhanced sensitivities and a factor 4-5 in detector range improvement. This significant upgrade is called *LIGO Voyager* [25].

LIGO Voyager test masses will be made out of silicon, instead of fused-silica used by the current detectors, and will operate at a temperature of 123 K where

the thermo-elastic coefficient of silicon vanishes. Furthermore, the LIGO Voyager upgrade will operate with higher optical powers stored in the arms since silicon test masses with high thermal conductivity are not prone to thermally induced wavefront distortion effects. The combination of the test masses and temperature, together with higher optical power in the arms improves the broadband thermal and quantum noises. Therefore, the new sensitivity of LIGO Voyager can increase the detection rate of binary neutron star mergers to about 10 per day and the binary black hole mergers to about 30 per day [25].

Virgo

Advanced Virgo is an upgrade of the initial Virgo detector configuration [26], decommissioned at the end of 2011. The major upgrade goal was to turn the Virgo detector into a second-class generation instrument which operates with sensitivities comparable to the two LIGO detectors. This improves the initial Virgo sensitivity broadband by an order of magnitude, and this corresponds to an increase of three orders of magnitude in the detection rate. In the initial step of the upgrade, which excludes the integration of the signal-recycling mirror (SRM) and operates with a 25 W input power, the Advanced Virgo is designed to reach an inspiral range for binary neutron-star mergers of at least 100 Mpc and an inspiral range for binary black-hole mergers of about 900 Mpc [27]. In order to achieve this sensitivity, the detector had to undergo a series of enhancements in most subsystems. A summary of these is presented below. A more detailed and rigorous description of the upgrades for each subsystem is presented in the Technical Design Report [28].

In the advanced phase, the optical design of the interferometer will be modified. Firstly, the Advanced Virgo will be a dual-recycled Michelson interferometer with the SRM being integrated into the system at the anti-symmetric port. The SRM will create a signal recycling cavity that can resonantly enhance the signal sidebands generated within the interferometer. However, during O3, the SRM was not installed, but replaced with a simple lens. Secondly, the beam sizes at the test mirrors will be larger, with a beam waist placed closer to the center of the 3 km long armlength. The larger spot sizes will reduce the impact of the thermal noise to the sensitivity in middle-band frequency ranges. Lastly, the arm cavity finesse will be increased to 443.

In order to gain an appreciable improvement in the shot noise at high frequencies, the sensitivity of the Advanced Virgo assumes a laser power of at least 125 W entering the interferometer after the Input Model Cleaner (IMC). This upgrade requires a series of subsystems to be compliant, such as the input optics, which provide a stable Gaussian beam to the detector entry, or the thermal compensation system (TCS), designed to manage the thermally-induced aberrations at the test mass surfaces. Furthermore, the mass of the optics has been increased to 42 kg in order to reduce the radiation pressure noise at lower-frequencies. This also triggered the

design and implementation of a new payload system.

Since the light scattering turned out to be a challenging source of noise after the first two science runs, its understanding and control is crucial for the future performance of the interferometer. Advanced Virgo features stray light control strategies that limit the impact of the scattered light on detector sensitivity. New diaphragm baffles have been installed either inside the vacuum pipes or suspended around the main optical elements.

GEO600

The GEO600 detector is a 600 m long interferometer located in Hannover, Germany [29]. The construction of the instrument started in 1995 as a German/British collaboration based on the experience the researchers have acquired at two prototypes: the 10 m prototype at the University of Glasgow and the 30 m interferometer at Max-Planck-Institut für Quantenoptik in Garching.

Due to the inability to expand the baseline arm-lengths beyond 600 m, GEO600 is unable to attain strain sensitivities comparable with those of km-scale interferometers. However, incorporating modern technologies into its design, such as the dual-recycled optical topology and innovative seismic isolation suspensions, has enabled GEO600 to achieve sensitivities near the initial performance of km-scale detectors. Therefore, for a significant amount of time, GEO600 maintained an observational strategy known as *astro-watch*, which entails running in science mode while the LIGO and Virgo detectors are offline in order to potentially detect a gravitational-wave event with a very high SNR.

Based on the new techniques that were firstly implemented in GEO600, the detector is known as a technology demonstrator. Examples include the first integration of double-recycling cavities [30], the experimental demonstration of the fused-silica suspension technologies [31], the first implementation of squeeze light to reduce the impact of quantum noise [32] and the demonstration of the long term squeezed light injection [33].

KAGRA

The Japanese KAGRA detector was founded in 2010, and is the first cryogenic and underground interferometric gravitational-wave observatory [34, 35]. The instrument has been successfully constructed inside the Kamioka mine in Japan and operated during the last science run (O2) together with the LIGO and Virgo detectors.

The optical layout of the detector contains a dual-recycled Michelson interferometer with Fabry-Perot optical cavities of 3 km in length. The test masses in the optical resonators are maintained at cryogenic temperature and made of sapphire, while the other optical components maintained at room temperatures are made of fused silica. Therefore, KAGRA operates with the standard 1064 nm laser light.

At design sensitivities, KAGRA has the potential to observe neutron star binaries at a distance of about 150 Mpc from Earth, but the commissioning difficulties during the last science run only allowed KAGRA to achieve a peak binary-neutron-star inspiral range of 0.6 Mpc. Built underground and operating at cryogenic temperatures, KAGRA offers a km-scale test facility for the next generation detectors in the study against the seismic and thermal noises.

1.2.4 Third generation of gravitational-wave detectors

Current gravitational-wave detectors have demonstrated a sensitivity threshold for detecting gravitational waves of up to one event per week. The third generation (3G) of ground-based gravitational-wave observatories, such as the European Einstein Telescope (ET) and the U.S.-based Cosmic Explorer (CE), aim to increase the observational bandwidth to a few Hz and the strain sensitivity by at least a factor 10 over a broad frequency range. The detectors aim to achieve this performance by integrating the advanced features of the current interferometers into larger scales, and by employing new promising technologies.

Cosmic Explorer

Cosmic Explorer will integrate longer baseline Fabry-Perot cavities, and aims for a strain sensitivity improvement of at least an order of magnitude compared to Advanced LIGO+ generation. Initially, Cosmic Explorer was designed to run in two stages, similar to the Advanced LIGO detectors:

1. Cosmic Explorer 1 (CE1), which is based on the mature technologies of Advanced LIGO+. This will operate with laser light at 1064 nm and a temperature of 290 K.
2. Cosmic Explorer 2 (CE2), which is the upgrade of the previous generation and relies on the technologies demonstrated by LIGO Voyager. This will operate with laser light at 1550 nm and at cryogenic temperatures of around 123 K.

Both CE1 and CE2 were designed with a 40 km arm-length baseline [36, 37] with a dual-recycled Fabry-Perot optical topology. However, in the Horizon study for CE, the authors proposed the possibility of building two CE detectors largely separated, one with a 40 km baseline, and the second one with a 20 km baseline [38]. The strain sensitivities for both CE detectors is depicted in Figure 1.5, while Figure 1.6 shows the corresponding response distance.

Einstein Telescope

The design of the Einstein Telescope is derived from an original objective that it developed, which later became employed by the Cosmic Explorer: achieving

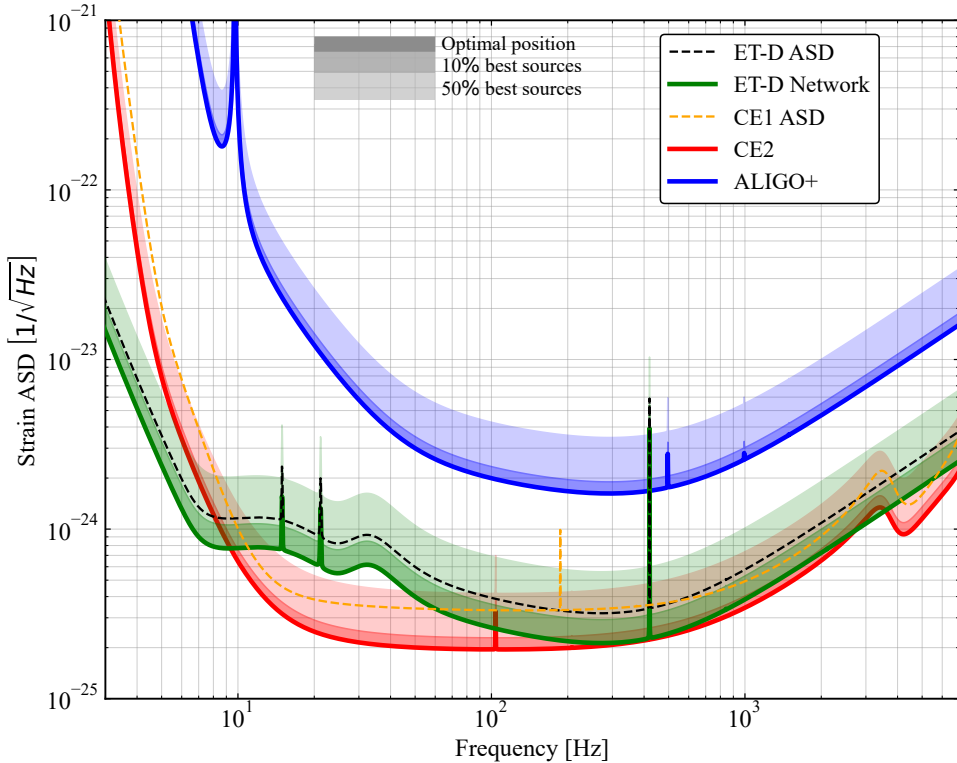


Figure 1.5: Strain amplitude spectral densities of typical third generation of gravitational wave detectors compared to the Advanced LIGO + sensitivity. The strain is scaled by 10% and 50% best sources selected from the antenna pattern function for each detector. The sources are monochromatic, distributed isotropically in sky position, inclination and polarization. The orange solid curve shows the simple detector amplitude spectral density (ASD) of the CE2 configuration, while the dark dashed curve shows the ASD of ET-D detector. The solid lines denote the effective strain for an optimally oriented source with respect to the detector antenna pattern. A similar plot initially appeared in [39], however the curves presented above were simulated independently.

a hundredfold greater broad-band sensitivity than the initial LIGO and Virgo observatories. In addition, ET aims to extend the high-sensitivity band to frequencies as low as a few Hz. Therefore, reducing the fundamental noise sources impacting the broadband and low-frequency sensitivities, such as the quantum, thermal and seismic gravity-gradient noise is the major drive of the ET design.

In order to reduce the impact of the gravity-gradient noise at low frequencies below 10 Hz, the entire ET detector will be placed underground, where the Rayleigh waves from natural and anthropogenic sources diminish [40]. Moreover, advanced noise cancellation techniques will be implemented to reduce the underground body-waves Newtonian noise produced by shear and compression waves impinging on the cavity walls hosting the interferometer components [41]. There are currently

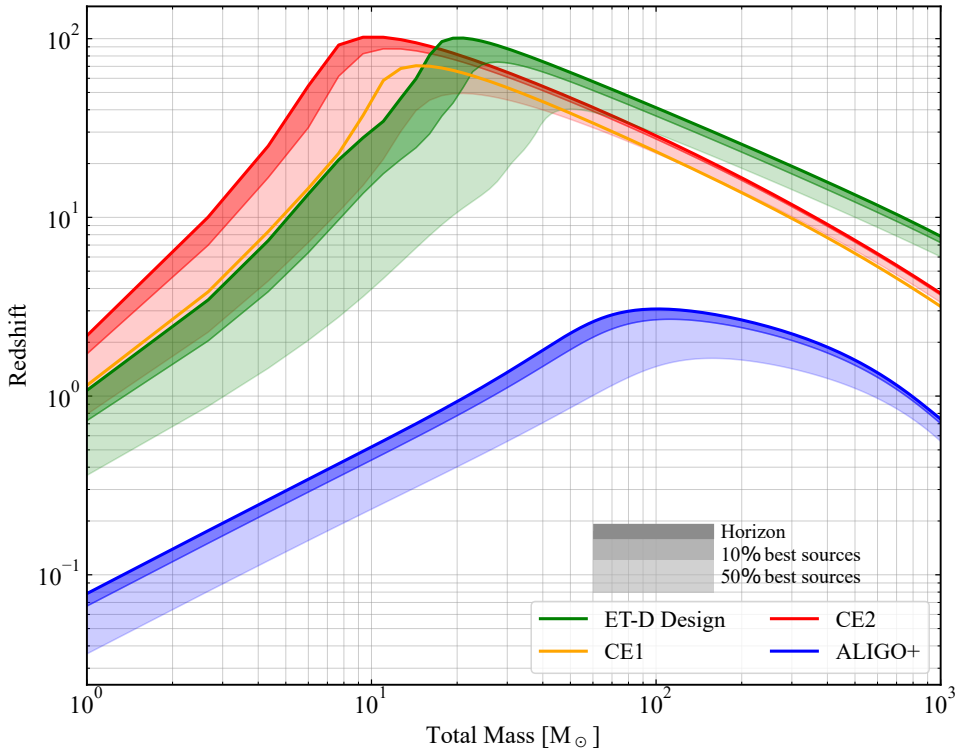


Figure 1.6: The luminosity distance of the third generation gravitational-wave detectors compared to Advanced LIGO + response, as a function of total merger mass. The strain is scaled by 10% and 50% best sources selected from the antenna pattern function for each detector. The sources are sampled isotropically in sky position, inclination angle and polarization. The solid lines represent the horizon distance or the redshift after which the detectors can not detect the particular source. A similar plot initially appeared in [39], however the curves presented above were simulated independently.

two candidate sites for the underground construction of ET infrastructure, with ongoing studies for the subsurface geology and the seismic mapping: the Euregio Meuse–Rhine nearby the Belgium, Dutch and German border, and Sos Enattos site in Sardinia, Italy [42, 43].

The optical topology of ET is different than that of a second generation gravitational-wave observatory. In order to achieve the large bandwidth with high sensitivity, ET will be composed of two different interferometers: a low power cryogenic interferometer optimized for low-frequencies and a high-power room temperature interferometer tuned for high frequencies, in a configuration called the *xylophone* detector. The optical topology of both interferometers features a dual-recycled Fabry-Perot Michelson interferometer.

In order to reduce the impact of radiation pressure noise, the ET low-frequency interferometer makes use of lower power stored in the Fabry-Perot arms, in the order

of kW. The quantum noise is further suppressed in both high and low-frequency interferometer by injecting squeezed light states with a frequency dependent squeezing angle at the output port of the interferometer. The low-frequency detector is designed to operate at cryogenic temperatures of the order of 10 K to reduce the impact of the thermal noises. Therefore the test-mass substrates have to be made of materials with low mechanical dissipation at cryogenic temperatures and sapphire and silicon have been proposed as candidates with silicon being recently integrated into multiple R&D project, such as ETpathfinder described in Chapter 3. Since silicon is highly absorptive for the laser wavelength used in the second generation of gravitational-wave detectors, 1550 nm laser light is proposed as the design wavelength for the low-frequency interferometer.

Using fused silica as the substrate material for the test masses, the high-frequency interferometer will work at room temperature. To reduce shot noise, the detector's arms will include a high laser light power of the order of megawatts. The thermal noise is expected to be a limiting factor for the sensitivity of the ET high-frequency detector, and this can be significantly reduced by either increasing the beam size at the test masses or by using higher-order Laguerre-Gauss laser-field modes.

Based on initial work by Rüdiger, Winkler and collaborators about the advantages of triangular co-located interferometers with a redundant receiving station, developed further in [44, 45], the ET design features three co-located detectors arranged in an equilateral triangle. Therefore, six interferometers will form the full optical topology of ET. There are many advantages that this geometry brings compared to two largely separated, or co-located, L-shaped Michelson interferometers. Besides the practical advantage brought by the redundant receiving station, the triangular configuration allows the construction of the so-called *null-stream* channel, which can be a very powerful instrumental noise discriminator, and can fully reconstruct both polarization amplitudes of gravitational waves. Detecting both source polarization amplitudes allows the reconstruction of the source geometry and testing general relativity.

1.3 Preview of this Thesis

On a broader scientific basis, the research conducted in this thesis is about modeling and developing novel characterization techniques for gravitational-wave interferometers. These techniques can help with improving commissioning procedures and guiding design decisions that can enhance the sensitivity of both current and future gravitational-wave observatories.

The chapters of this thesis focus on two main issues, addressing the broad scientific theme described above: 1) enhancing the control of longitudinal and angular displacements of the interferometric degrees of freedom in both current and future observatories (Chapter 2 and Chapter 5), and 2) ensuring that the integration of new technologies in future gravitational-wave observatories does not compromise

their design sensitivities, which are primarily determined by fundamental physics limitations (Chapter 3 and Chapter 4).

The thesis chapters can be regarded as discrete sections, each consisting of its own introduction to the topic being discussed and independent conclusions drawn from the study's findings. However, connections between chapters are established when relevant concepts are introduced in advance. The primary rationale for dividing the chapters was to ensure that each one yielded a substantial amount of material suitable for publication. For instance, a paper has been published in [46] that is based on the research conducted in Chapter 3.

Ultimately, the thesis concludes with two overarching sections: Chapter 6 and Summary. The loop to this preview of the thesis is closed in Chapter 6, and an explanation of how each chapter conclusion satisfied the problem statement is provided. The impact statement presents a comparable discourse in layman's terms. The summary section illustrates all of the primary discoveries of this thesis including key numerical findings.

Radio-frequency sidebands studies during Advanced Virgo O3 run

2.1 Motivation

The Advanced Virgo detector [27] utilizes three modulation frequencies transmitted by the Input Mode Cleaner. These frequencies are subsequently employed to construct error signals, which are essential for the longitudinal and angular controls of the interferometer. The photodiodes utilized for constructing the error signals possess broadband characteristics, rendering them sensitive to not just the primary sidebands of interest but also all other contributions. During the last science run, O3, as well as prior commissioning phases, the saturation of the readout electronics caused by the presence of sidebands of sidebands has posed challenges, necessitating the instrumental team to significantly reduce the intensity of one of the primary sidebands. These issues were most evident during the lock acquisition phases. It is therefore imperative to consider these factors during the commissioning process of the interferometer as well as the design of the new electronics.

This chapter examines the evolution of radio-frequency control sidebands in the Advanced Virgo interferometer during the most recent science run. The goal is to compare actual data from photodiodes to simulations of an ideal detector, therefore determining how well it can be characterized without introducing optical defects for the interferometer test masses. The following parts explain the Advanced Virgo detector optical configuration and the instrumental science and control needed to introduce the research sections. The investigation begins with the sideband propagation simulation. The next two portions show how to retrieve detector data and compare simulation results. The final chapter briefly summarizes the findings.

2.2 ISC fundamentals

As previously introduced in the Chapter 1, the *null* operational nature of gravitational-wave interferometers is achieved by controlling the interferometer using a combination of procedures known as *feedback control*. This permits the primary optical component to be maintained at predetermined set points that define the operating mode of the interferometer. The residual seismic motion at lower frequencies will couple to the test masses via the suspension systems, displacing their positions and therefore altering their working point. Active control is required to continuously update the mirrors positions in this situation.

Multiple resonant cavities constitute the optical structure of the Advanced Virgo interferometer, and these cavities must be tuned into resonance through precise control. The optical cavities that must be controlled in order to allow the interferometer to be sensitive to the passage of gravitational waves are called interferometer *degrees of freedom*. The Instrumental Sensing and Control (ISC) group conducts research into the selection of appropriate error signals for each degree of freedom and the use of the optimal control strategy that minimizes the impact of control on the instrument sensitivity. This chapter focuses exclusively on the control of the longitudinal degrees of freedom.

2.2.1 The laser field

In order to introduce the derivation of a longitudinal control signal in the presence of a higher order Hermite-Gaussian mode in Section 2.2.2, a brief introduction to Gaussian optics is provided.

The laser generates an electromagnetic field with a profile that resembles a Gaussian distribution. This is more of an approximation than an exact solution to the electromagnetic field equations under certain conditions. A simpler theoretical treatment is introduced here. As a reference, an exhaustive analysis of laser fields and their application can be found in *Lasers* [47].

The spatial part of the electromagnetic wave, expressed in the x, y and z coordinates, is given in terms of the complex function $u(x, y, z)$, which described the beam profile during propagation in the z direction, as:

$$\Psi = u(x, y, z)e^{-ikz}. \quad (2.1)$$

Here $k = 2\pi/\lambda$ is the angular wavenumber with λ being the wavelength of light. These electromagnetic fields in free space are generally described by the scalar Helmholtz equation:

$$[\nabla^2 + k^2]\Psi = 0. \quad (2.2)$$

Substituting Equation 2.1 into Equation 2.2 yields the reduced equation:

$$\frac{\partial^2 u}{\partial x^2} + \frac{\partial^2 u}{\partial y^2} + \frac{\partial^2 u}{\partial z^2} - 2ik \frac{\partial u}{\partial z} = 0. \quad (2.3)$$

In general, for well-collimated laser beams that travel along the z axis, the two-dimensional field characteristics in x and y axes vary faster compared to the variation along the z axis, from diffraction or propagation effects. This allows us to drop the second derivative of the function $u(x, y, z)$ with respect to the z axis. This results in the *paraxial wave equation*:

$$\frac{\partial^2 u}{\partial x^2} + \frac{\partial^2 u}{\partial y^2} - 2ik \frac{\partial u}{\partial z} = 0. \quad (2.4)$$

The solutions for the function u in the above equation represent descriptions of the orthogonal properties of the paraxial light beam. One of fundamental importance for our case is the Gaussian function and this is expressed as:

$$u(x, y, z) = \sqrt{\frac{2}{\pi}} \times \frac{1}{w(z)} \times \exp(i\psi(z)) \times \exp\left(-ik \frac{x^2 + y^2}{2R(z)} - \frac{x^2 + y^2}{w^2(z)}\right). \quad (2.5)$$

Here, $w(z)$ is the beam size, transversal to the direction of propagation z . This is the radial distance where the field amplitude is reduced to $1/e$. It is defined as:

$$w(z) = w_0 \times \sqrt{1 + \left(\frac{z - z_0}{z_R}\right)^2}. \quad (2.6)$$

If the coordinate $z = z_0$, the beam size $w(z)$ reaches its minimum, called the *waist* and denoted by w_0 . The term z_R is called the *Rayleigh range* and is defined as:

$$z_R = \frac{\pi w_0^2}{\lambda}. \quad (2.7)$$

The extra phase shift along z , $\psi(z)$, is called *Gouy phase*. The term $R(z)$ defines the radius of curvature of the wavefront at each point z . This is expressed mathematically as:

$$R(z) = z \times \left[1 + \left(\frac{z_R}{z}\right)^2\right]. \quad (2.8)$$

It can be observed that the two-dimensional lateral distribution of light intensity resembles a Gaussian function, thus the *Gaussian beam*. Therefore, the entire spatial distribution of the Gaussian beam at any given point can be determined if one knows w_0 , its position z_0 and the wavelength. A drawing of the Gaussian beam profile is shown in Figure 2.1.

The Gaussian beam can be divided into two regions along the propagation axis. These are defined with respect to the Rayleigh range. The *near field* is the region in the proximity of the beam waist, where $z_R > z$. The *far field*, where the opposite holds true, $z_R < z$, is the region further away from the waist position where the beam size increases more linearly with the distance from the waist.

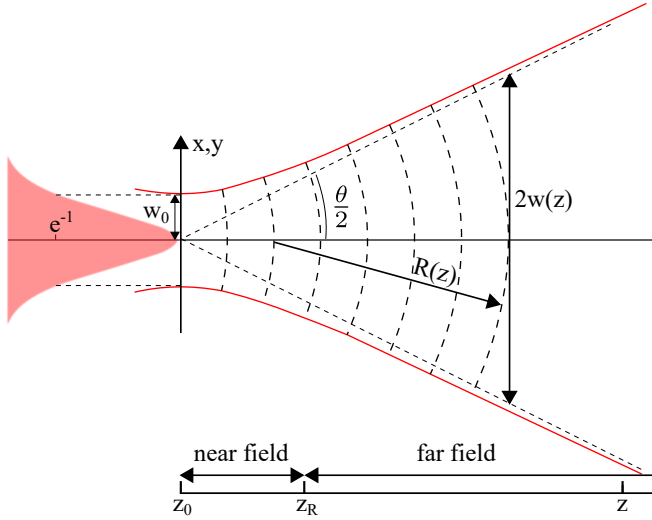


Figure 2.1: The figure depicts the geometrical features of the Gaussian TEM_{00} mode propagating along the z axis. The two-dimensional intensity of the laser beam is symmetric around the propagation axis and decreases orthogonally with the distance from the center. The beam converges to the waist and then it propagates with the divergence angle θ .

The Gaussian beam expression is only the lowest-order solution to the free space paraxial wave equation. One class of solutions in the infinite set of higher order functions is given by the Hermite-Gaussian modes. They are also called *transverse electromagnetic* modes $TEM_{(m,n)}$, where (m,n) corresponds to the mode order in x and y directions. This class of solutions is solved in rectangular coordinates with the final field variation $u_{nm}(x, y, z)$ separating into a product of identical solutions in both orthogonal directions x and y :

$$\begin{aligned}
 u_{nm}(x, y, z) &= u_n(x, z) \times u_m(y, z) \\
 &= \left(2^{n+m-1} n! m! \pi\right)^{-1/2} \times \frac{1}{w(z)} \times \exp(i(n+m+1)\Psi(z)) \\
 &\quad \times H_n\left(\sqrt{2}\frac{x}{w}\right) \times H_m\left(\sqrt{2}\frac{y}{w}\right) \times \exp\left(-ik\frac{x^2+y^2}{2R(z)} - \frac{x^2+y^2}{w^2(z)}\right).
 \end{aligned} \tag{2.9}$$

Here, $H_n(x)$ and $H_m(x)$ are the characteristic Hermite polynomials. For example, $H_0 = 1$ and $H_1 = 2x$. Using this, the full Hermite series can be computed by following the recursion equation:

$$H_{n+1}(x) = 2xH_n(x) - 2nH_{n-1}(x). \tag{2.10}$$

A plot of different intensity profiles of Hermite-Gaussian modes is shown in Figure 2.2. Because of the Gouy phase shift, different higher order modes will resonate at different frequencies inside optical cavities. The mode-splitting frequency

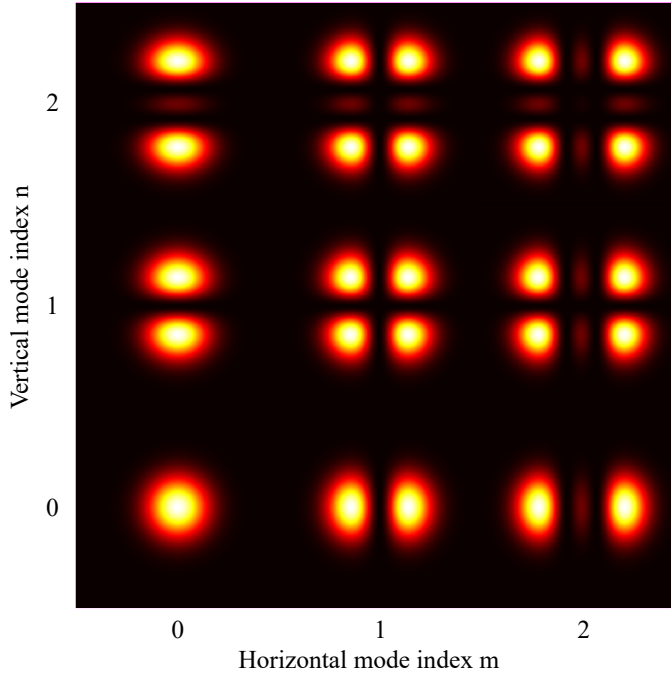


Figure 2.2: The figure depicts intensity patterns for different higher order Hermite-Gaussian modes up to the mode number 4.

ν_{nm} is given as:

$$\nu_{nm} = \text{FSR} \left\{ q + (n + m + 1) \frac{1}{\pi} [\Phi(z_1) - \Phi(z_2)] \right\}. \quad (2.11)$$

Here, $\text{FSR} = \frac{c}{2L}$, with L being the cavity length, is the *free spectral range*. The term q is an integer representing the axial mode. The term $[\Phi(z_1) - \Phi(z_2)]$ represents the Gouy phase shift from one end of the optical cavity to the other and it can be expressed in terms of cavity length and mirror radii of curvature R_1 and R_2 :

$$[\Phi(z_1) - \Phi(z_2)] = \cos^{-1} \sqrt{\left(1 - \frac{L}{R_1}\right) \times \left(1 - \frac{L}{R_2}\right)}. \quad (2.12)$$

2.2.2 Pound-Drever-Hall Locking Technique

The Pound-Drever-Hall (PDH) laser frequency stabilization method was invented to stabilize the frequency of light emitted by a laser by means of locking to a stable cavity [48]. Although this was its main purpose, this technique became essential for controlling the optical cavities in gravitational-wave detectors. This is accomplished

by generating an error signal that encodes information about minute changes in the cavity length, and then sending this information back to a control scheme that will compensate for the offset and *locks* the cavity to the laser frequency. The technique exploits the phenomenon wherein the phase of the electromagnetic field undergoes a change around the resonance point within the cavity, while being relatively constant outside of resonance. The PDH technique involves the introduction of additional sidebands surrounding the primary field or carrier, with a frequency carefully selected to be anti-resonant within the Fabry-Perot cavity, while the carrier itself remains resonant. In this manner, they serve as a phase reference for the carrier signal that enters the cavity, conveying essential information on the length of the cavity. The error signal of interest, also called PDH error signal, is the result of the interaction between the sidebands and the carrier. A good introduction to the topic can be found in the paper of Eric Black [49].

A demonstration of how the error signal amplitude is derived in reflection of a resonant cavity is provided in order to comprehend how the technique operates. In addition, the derivation in the presence of a mode of higher-order is presented. The latter error signal form is useful in the context of marginally stable cavities, such as the Advanced Virgo power recycling cavity. In this cavity, as it is close to the edge of the stability criterion and near degenerate, higher-order spatial modes can build up when the fundamental mode is resonant.

These demonstrations can be comprehended using Figure 2.3. A laser beam with an oscillating electric field of the form $E_0 e^{i\omega t}$ is sent into an optical cavity and is picked off in reflection by an auxiliary mirror. The laser beam is phase-modulated by an electro-optic modulator, a device containing a crystal which modifies the properties of the propagating carrier light by applying an electric field. As a result of the modulation process, sidebands are created around the carrier field.

The frequency of the sidebands are chosen to be outside the line-width of the cavity. Furthermore, the modulation frequency Ω does not coincide with the FSR of the cavity. Therefore, the modulation sidebands are not resonant in the optical cavity. The modulated field has the following form:

$$\begin{aligned}
 E_{in} &= E_0 e^{i(\omega t + b \sin(\Omega t))} \\
 &\approx E_0 [J_0(b) + 2iJ_1(b) \sin(\Omega t)] \sin(\omega t) \\
 &= E_0 \left[J_0(b) e^{i\omega t} + J_1(b) e^{i(\omega + \Omega)t} - J_1(b) e^{i(\omega - \Omega)t} \right].
 \end{aligned} \tag{2.13}$$

In Equation 2.13, b is the modulation depth and Ω is the modulation frequency. It can be seen from the right part of the equation that the carrier will be modulated at plus and minus the modulation frequency. The equation expands into a series formed by specific order Bessel functions J_i . The reflected beam that impinges on the photodiode (PD) can be expressed as:

$$E_{ref} = F(w) \times E_{in}, \tag{2.14}$$

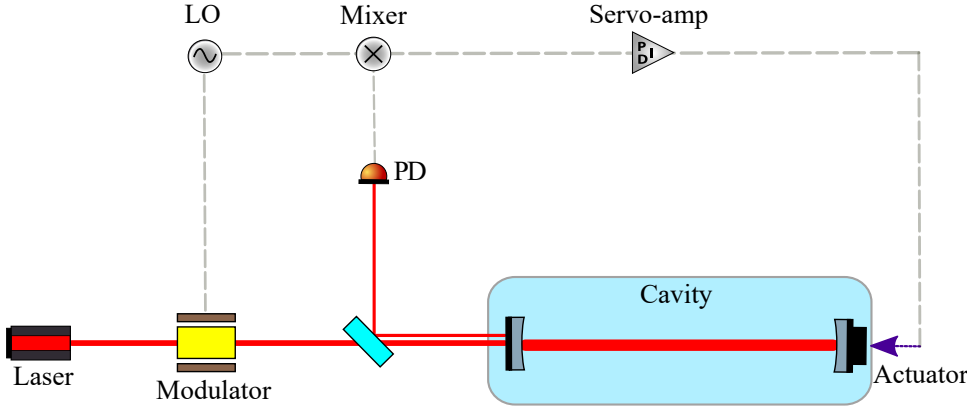


Figure 2.3: Simplified setup showing the configuration of a cavity length control employing PDH error signals. The laser carrier is modulated creating sidebands at $\omega \pm \Omega$. The optical signals are picked off in reflection of the cavity and sent to a photodiode. The beating between the carrier and the sidebands is used as error signal for the feedback control scheme.

where $F(\omega)$ is the complex field reflectivity which can be expressed in terms of the input mirror reflectivity r and transmissivity t as:

$$F(\omega) = \frac{-r_1 + r_2 (r_1^2 + t_1^2) e^{\frac{i\omega}{FSR}}}{1 - r_1 r_2 e^{\frac{i\omega}{FSR}}}. \quad (2.15)$$

The photo-diode senses the power of the electromagnetic field, expressed as $|E_{ref}|^2$. Expanding Equation 2.14, the general form of the modulated light power impinging on the photo-diode is:

$$\begin{aligned} P_{PD} = & P_0 |F(\omega)|^2 + P_1 |F(\omega + \Omega)|^2 + P_1 |F(\omega - \Omega)|^2 \\ & + \sqrt{P_0 P_1} F(\omega) \overline{F(\omega + \Omega)} e^{-i\Omega t} - \sqrt{P_0 P_1} F(\omega) \overline{F(\omega - \Omega)} e^{i\Omega t} \\ & + \sqrt{P_0 P_1} F(\omega + \Omega) \overline{F(\omega)} e^{i\Omega t} - P_1 F(\omega + \Omega) \overline{F(\omega - \Omega)} e^{2i\Omega t} \\ & - \sqrt{P_0 P_1} F(\omega - \Omega) \overline{F(\omega)} e^{-i\Omega t} - P_1 F(\omega - \Omega) \overline{F(\omega + \Omega)} e^{-2i\Omega t}. \end{aligned} \quad (2.16)$$

Here, P_0 is the carrier power, given as $E_0^2 J_0^2(b)$, and $P_1 = E_1^2 J_1^2(b)$ is the sideband power. The term $\overline{F(\omega)}$ represents the complex conjugate of $F(\omega)$. After the field reaches the photodiode, its current is mixed with the modulation signal reference from the local oscillator (LO). The frequencies similar to the modulation frequency are extracted. These beat notes between the carrier and the modulation sidebands contain a phase reference for the length of the cavity which is used as error signal. Thus, the resulting photocurrent from Equation 2.16 takes the following form:

$$\begin{aligned} P_{PD}^\Omega = & \sqrt{P_0 P_1} [F(\omega) \overline{F(\omega + \Omega)} - F(\omega - \Omega) \overline{F(\omega)}] e^{-i\Omega t} \\ & + \sqrt{P_0 P_1} [F(\omega + \Omega) \overline{F(\omega)} - F(\omega) \overline{F(\omega - \Omega)}] e^{i\Omega t}. \end{aligned} \quad (2.17)$$

Here, it can be observed that the four terms inside the brackets are complex conjugate pairs. Writing $P_{PD}^\Omega/\sqrt{P_0P_1} = T_1e^{-i\Omega t} + T_2e^{i\Omega t}$ with $T_2 = \overline{T_1}$ and expressing each T term as a complex number:

$$T_1e^{-i\Omega t} + T_2e^{i\Omega t} = 2a \cos(\Omega t) + 2b \sin(\Omega t). \quad (2.18)$$

Finally, the photocurrent formulation expressed in Equation 2.17 can be written as:

$$\begin{aligned} P_{PD}^\Omega &= 2\sqrt{P_0P_1} \Im\{[F(\omega)\overline{F(\omega + \Omega)} - \overline{F(\omega)}F(\omega - \Omega)]\} \sin(\Omega t) \\ &+ 2\sqrt{P_0P_1} \Re\{[F(\omega)\overline{F(\omega + \Omega)} - \overline{F(\omega)}F(\omega - \Omega)]\} \cos(\Omega t). \end{aligned} \quad (2.19)$$

By multiplying the above equation with either a sine or a cosine, the first out-of-phase dispersion component or the second in-phase absorption component can be determined. The dispersion term gives the shape of the error signal that is useful for controlling the cavity length. An example of the PDH error signal is illustrated in Figure 2.4.

Adding a higher order mode in the calculation presented increases the complexity of the expressions. For simplicity, the following treatment assumes the higher order mode to be TEM₁₀. Since a linear superposition is assumed, Equation 2.13 can be written as:

$$\begin{aligned} E_{ref} &= E_{00} \left[F(\omega_1) J_0(b) e^{i\omega_1 t} + F(\omega_1 + \Omega) J_1(b) e^{i(\omega_1 + \Omega)t} \right] \\ &- E_{00} \left[F(\omega_1 - \Omega) J_1(b) e^{i(\omega_1 - \Omega)t} \right] \\ &+ E_{10} \left[F(\omega_2) J_0(b) e^{i\omega_2 t} + F(\omega_2 + \Omega) J_1(b) e^{i(\omega_2 + \Omega)t} \right] \\ &- E_{10} \left[F(\omega_2 - \Omega) J_1(b) e^{i(\omega_2 - \Omega)t} \right]. \end{aligned} \quad (2.20)$$

This equation contains two angular frequency terms. The first one, ω_1 is the angular field of the carrier, as before. The second term, ω_2 is the angular frequency of the higher order mode and this is now defined in terms of the mode splitting from Equation 2.11 as $\omega_2 = \omega_1 + \nu_{10}$. The modulation frequency is Ω . The two electromagnetic fields will be multiplied by the corresponding complex reflectivities. The TEM₀₀ field will have a similar reflectivity as in Equation 2.15, while the higher order mode reflectivity contains now ω_2 in the exponential term. The further calculation presented in the Appendix A yields the final photocurrent expression for

the error signal:

$$\begin{aligned}
P_{PD}^{\Omega} = & + \sqrt{P_{c0}P_{s0}} \cdot \frac{1}{2} \Im \{ F(\omega_1) \overline{F(\omega_1 + \Omega)} - F(\omega_1) \overline{F(\omega_1 - \Omega)} \\
& + F(\omega_1 + \Omega) \overline{F(\omega_1)} + F(\omega_1 - \Omega) \overline{F(\omega_1)} \} \\
& + \sqrt{P_{cm}P_{sm}} \cdot \frac{1}{2} \cdot \Im \{ -F(\omega_1) \overline{F(\omega_2 - \Omega)} - F(\omega_1) \overline{F(\omega_2 + \Omega)} \\
& + F(\omega_1 - \Omega) \overline{F(\omega_2)} + F(\omega_1 + \Omega) \overline{F(\omega_2)} \} \\
& + \sqrt{P_{cl}P_{sl}} \cdot \frac{1}{2} \cdot \Im \{ F(\omega_2) \overline{F(\omega_1 + \Omega)} - F(\omega_2) \overline{F(\omega_1 - \Omega)} \\
& + F(\omega_2 + \Omega) \overline{F(\omega_1)} - F(\omega_2 - \Omega) \overline{F(\omega_1)} \} \\
& + \sqrt{P_{c1}P_{s1}} \cdot \frac{1}{2} \cdot \Im \{ F(\omega_2) \overline{F(\omega_2 + \Omega)} - F(\omega_2) \overline{F(\omega_2 - \Omega)} \\
& + F(\omega_2 + \Omega) \overline{F(\omega_2)} - F(\omega_2 - \Omega) \overline{F(\omega_2)} \}.
\end{aligned} \tag{2.21}$$

Here, different power values appear in the equation. The terms P_{c0} and P_{s0} are the carrier and the sideband powers respectively. P_{cm} and P_{sm} are defined as $P_{cm} = E_{00} \cdot \overline{E_{10}} \cdot J_0(b)^2$ and $P_{sm} = E_{00} \cdot \overline{E_{10}} \cdot J_1(b)^2$. The same calculation is applied to the P_{cl} and P_{sl} terms, but the Bessel functions are multiplied by $E_{10} \cdot \overline{E_{10}}$ instead. The last two powers define the TEM₁₀ mode with $P_{c1} = |E_{10}|^2 \cdot J_0(b)^2$ and $P_{s1} = |E_{10}|^2 \cdot J_1(b)^2$.

As an example, this error signal was simulated for a resonant optical cavity with arbitrary parameters defined in Table 2.1. The resultant error signal morphology is shown in Figure 2.4.

Cavity Parameter	Value
Cavity length	1.5 m
Wavelength	1064 nm
Roc HR Input mass	150 m
Roc HR End mass	150 m
Finesse	626
Gouy phase	0.2 rad
Frequency splitting	12.7 MHz
Modulation frequency	30 MHz
Sideband power, P_{s0}	4 W
Mixed powers terms	2 W
Carrier power	16 W

Table 2.1: Optical parameters defining the resonant cavity and the optical fields for the PDH error signal simulation. Most of the presented parameters are arbitrary in order to demonstrate the additional zero-crossing of the error signal from Figure 2.4.

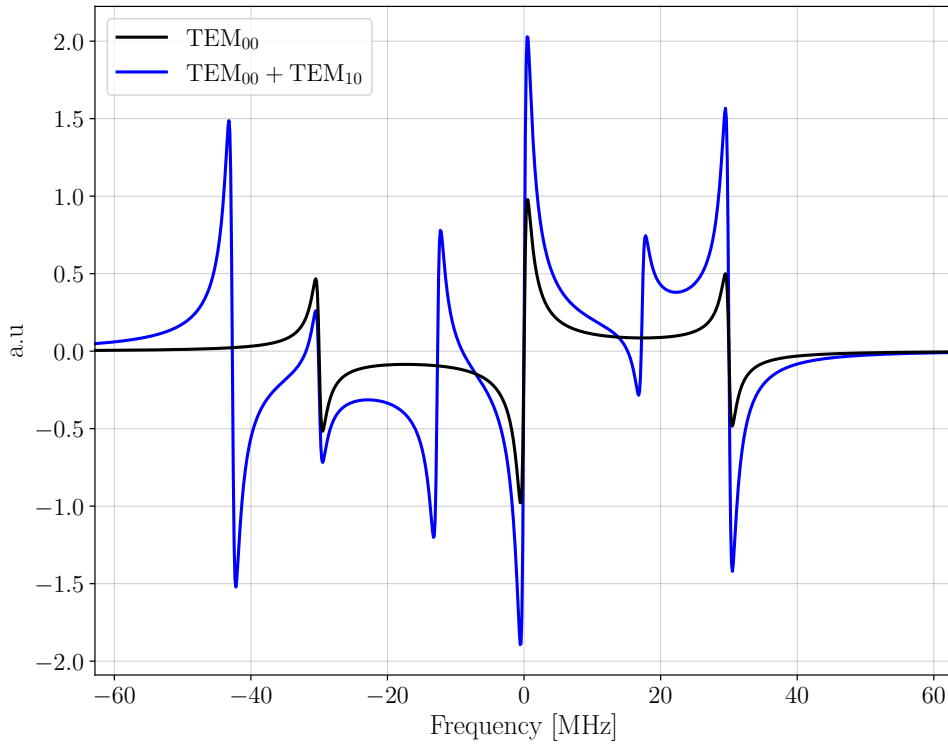


Figure 2.4: The figure depicts the shapes of the simulated error signals from Equation 2.19 and Equation 2.21. The bipolarity of both error signals is similar around zero point, when the cavity is on resonance. While the fundamental mode error signal crosses zero at \pm the modulation frequency 30 MHz, the error signal containing the higher order mode crosses zero again at a splitting frequency difference of 12.7 MHz from the first crossing of the fundamental mode.

2.2.3 Longitudinal degrees of freedom

In Advanced Virgo there are four main longitudinal degrees of freedom and 16 angular degrees of freedom. The longitudinal degrees of freedom are defined in terms of different lengths between the main optical components of the detector. These can be seen in Figure 2.5.

The common mode L_+ will affect only the carrier field, while the differential mode L_- controls the relative distance between the two arms and is the mode sensitive to the passage of the gravitational wave:

$$\begin{aligned} L_+ &= \frac{L_N + L_W}{2}, \\ L_- &= \frac{L_N - L_W}{2}. \end{aligned} \quad (2.22)$$

Here, N stands for *North* and W for *West*, a typical convention used for naming the two arm lengths of the Virgo detector.

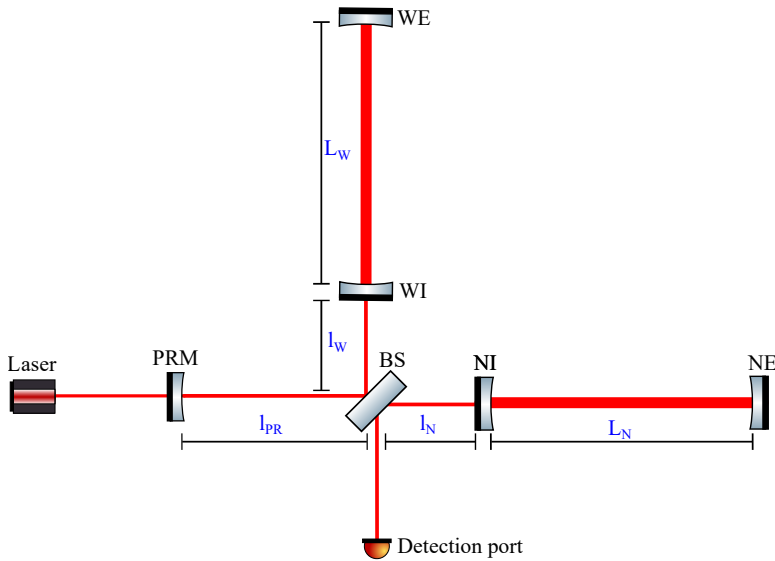


Figure 2.5: The figure depicts the Advanced Virgo simplified optical topology. Different combinations of the blue lengths shown form the longitudinal degrees of freedom of the power-recycled Fabry-Perot interferometer.

The next degree of freedom to be controlled is the Michelson interferometer or *Mich*, constructed by the distances l_W and l_N from the beam splitter to the two input mirrors as:

$$l_{\text{Mich}} = \frac{l_N - l_W}{2}. \quad (2.23)$$

The final degree of freedom in this configuration is the power recycling cavity, which is constructed by the two Michelson distances and the distance of the power

recycling cavity l_{PR} :

$$l_{PRC} = l_{PR} + \frac{l_N + l_W}{2}. \quad (2.24)$$

To get the complete detector to its functioning point, these four degrees of freedom must be controlled. Because the electromagnetic field in the system is strongly coupled, locking each cavity in a specific order is necessary. This order is called the lock acquisition sequence and is discussed in further detail below.

The control of each cavity requires a well-chosen error signal based on the radio frequency sidebands which provide a phase reference when beating with the carrier field. The following conditions apply to Advanced Virgo:

1. The carrier field is resonant inside the interferometer arms and is therefore sensitive to the path-length changes of the test mirrors.
2. The carrier field must be resonant inside the power-recycling cavity in order to increase the power in the main interferometer.
3. The radio frequency sidebands should resonate inside the power recycling cavity and not in the arms. This ensures a phase reference with the resonant carrier inside the arms.
4. One radio frequency field must not resonate inside the power recycling cavity since this has to be controlled.
5. The carrier field in the Michelson degree of freedom will leak through the dark port to allow a DC readout. This requires a small offset to be added in its control scheme.

All of these radio frequency sidebands are captured by pick-off ports (POP) at certain detection ports in Advanced Virgo. Figure 2.6 depicts these. Without including the signal recycling mirror into the design, three main modulation frequencies are present. The initial frequency, **Fmod1**, is selected to be anti-resonant in the arms for an offset of 300 Hz to prevent the sidebands of sidebands from being resonant in the arm cavities. For a FSR of the arm cavities of 49.968 Hz, the first modulation frequency is calculated as follows:

$$\mathbf{Fmod1} = 125.5 \times \text{FSR} - 300 \text{ Hz} = 6.27 \text{ MHz}. \quad (2.25)$$

For this to be resonant in the power recycling cavity, the length has to be multiple integers of the wavelength associated to **Fmod1**:

$$l_{PR} = (2n + 1) \times \frac{c}{4 \times \mathbf{Fmod1}}. \quad (2.26)$$

This results in a length of the power recycling cavity of 11.95 m. The second modulation frequency **Fmod2** is 9 times the first frequency and about 56.43 MHz.

The third modulation frequency, $F_{\text{mod}3}$, is not resonant in the interferometer, and is 8 times the free spectral range of the input mode cleaner, about 8.36 MHz.

These main modulation sidebands are created as a result of the carrier field passing through a series of three electro-optical modulators placed on the external injection bench. The external injection bench represents the subsystem between the laser and the interferometer, placed between the laser and the IMC in Figure 2.6. Besides modulating the carrier, the injection subsystem places an important role in matching the laser beam size, position and power to the interferometer, as well as controlling the technical noises of the propagating laser beam.

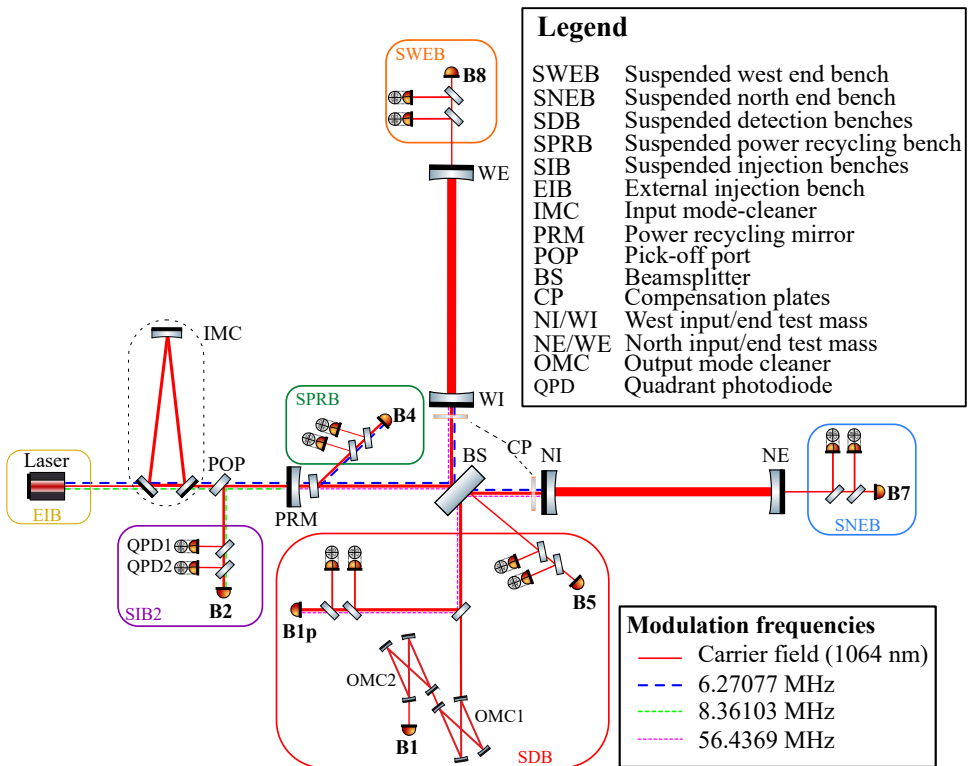


Figure 2.6: The figure shows a simplified optical layout of the Advanced Virgo detector. Since the signal recycling mirror was not integrated in the interferometer during O3, this was excluded from the layout. The main detection ports for collecting the signals required for controlling both longitudinal and angular degrees of freedom are shown. The carrier field is shown by solid lines and the modulation sidebands by dashed and dotted traces. The longitudinal and angular controls at the detection bench (SDB) is carried out using the photodiodes before the output mode cleaners, B1p. The differential sensing of the arm-lengths in response to a gravitational wave is obtained at the dark port B1.

Since the electro-optical modulators are placed in series, when the beam passes through the second or third modulators, it is already modulated in phase. As a result,

the sidebands from the initial modulation are also modulated in phase, creating therefore sidebands of sidebands. In the study presented in this chapter, only the sidebands of sidebands modulated at double and triple of the main frequencies are selected for demonstrating the methodology.

2.3 Sideband evolution simulation

Since the amplitude evolution of the control sidebands must be studied during interferometer control, the optimal interferometer state to search for this fluctuation in power is during the lock-acquisition procedure.

Bringing a gravitational-wave detector to its working point is a difficult task. The main optical cavities in the interferometer are strongly coupled. Since the optical response of the arm cavities during the lock is non-linear, this can alter the state of the other degrees of freedom. Therefore, a carefully studied locking procedure called *Variable Finesse locking* was developed for the Virgo interferometer [50, 51, 52].

This procedure is simulated using Finesse, which is a frequency-domain interferometer simulation program. The baseline structure of the Finesse file was taken from the ISC group of Virgo. This was then used in *Pykat* [53], a Python wrapper for Finesse software. The baseline Finesse file is presented in the Appendix B.

Modeling a real-time feedback controller is required for a proper simulation of cavity locking. Nonetheless, the frequency domain can characterize the steady-state behavior of the interferometer, which can offer insights on the interaction between the electromagnetic fields in multiple degrees of freedom. The simulation therefore consists of recording the electromagnetic field variation at different detection ports from Figure 2.6 during a series of arrangements of the optical cavities, which mimics the variable-finesse locking procedure.

During the variable finesse locking acquisition, the coupling of the power recycling cavity with the other longitudinal degrees of freedom is strongly controlled. At the beginning of the procedure, the power recycling mirror is fully misaligned in order to decouple its effect and freely control the arm cavities. The Michelson degree of freedom is maintained in an intermediate interference condition to reduce the finesse in the power recycle cavity while this is aligned. In this steady-state arrangement, in which all other degrees of freedom are already controlled, the Michelson offset reduction adiabatically drives the interferometer to its working point. Figure 2.7 illustrates a series of lock-acquisition steps simulated using Finesse.

Step 1 of the simulation decouples the power recycling cavity from the other degrees of freedom. This was mimicked in Finesse by altering the transmissivity of the power recycling mirror to 1. The arm cavities are now controlled independently using the PDH signals in transmission, extracted at B7 and B8 ports from Figure 2.6. This is accomplished by fine-tuning one end mirror (for instance, the end West mirror) and adjusting the other mirrors to match its location. Due to the fact that the tuning is performed on the West end mirror, the B8 DC level displays resonance

peaks. When the arm-cavity is locked, the last peak corresponds to the maximum transmitted power to the B8 photo-diode. At these resonances, the Michelson transmits and reflects half of its light, as detected by the photo-diodes B2 and B4. As anticipated, the light reflected by the beam splitter does not change.

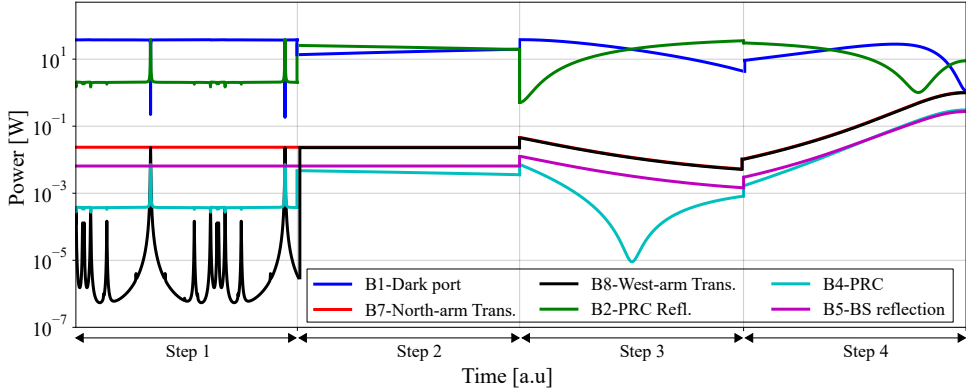


Figure 2.7: The figure depicts the variation of the DC power in different detection ports of Advanced Virgo during the positional control of the longitudinal degrees of freedom. The simulation is composed of discrete steps where different test masses are tuned to achieve the resonant state of the particular longitudinal degree of freedom.

Step 2 brings the Michelson at half-fringe. Since the PRC is decoupled, the transmitted power of the arms remains constant (red and black curves in Figure 2.7). Power levels between the B2 and B4 ports evolve in a similar manner. However, B4 has a smaller magnitude due to the reduced reflectivity of the pick-off port. Since B1 monitors the differential signal, the signals detected by B2 and B4 evolve in the opposite direction.

Step 3 simulates the power recycling cavity coupling. The power recycling mirror transmissivity is reduced to 0.5. This phase is crucial for the variable finesse lock acquisition. The central interferometer's power gradually increases. Power fluctuations at different ports are also to be expected, requiring the error signals to be normalized by the varying power.

Step 4 is the one of interest for the data collection presented in this research. At this step, the Mich degree of freedom is reduced slowly until the interferometer is brought to its working point. During this step, PRC power sensed by B4, as well as the power transmitted through the arms, increase until reaching a maximum. The PRC evolves from an under-coupled cavity to critically coupled, giving the valley in the green trace from Figure 2.7, and finally to an over-coupled cavity.

The sideband amplitude evolution during the last phase is extracted for the 6.2 MHz, 8.3 MHz, and 56.4 MHz and for the double and triple frequencies of the main sidebands. The evolution plots are presented in the Figures 2.8 to 2.11.

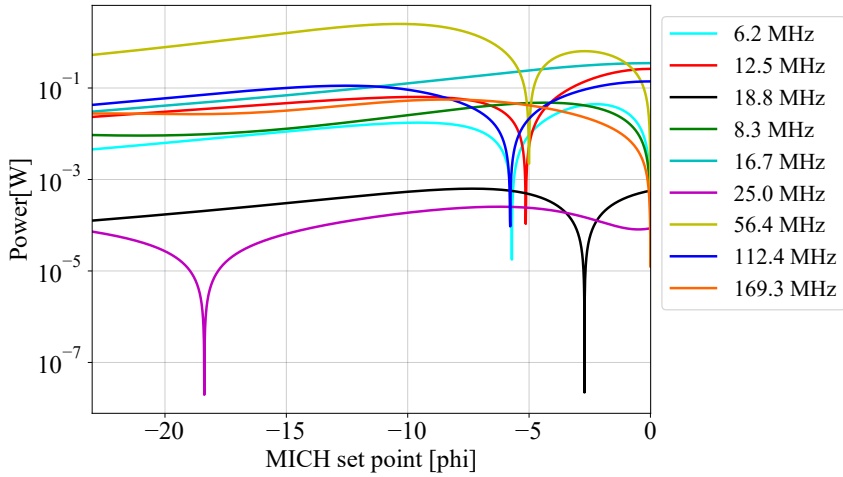


Figure 2.8: Sidebands evolution in B2 port during the last phase of the variable finesse lock acquisition.

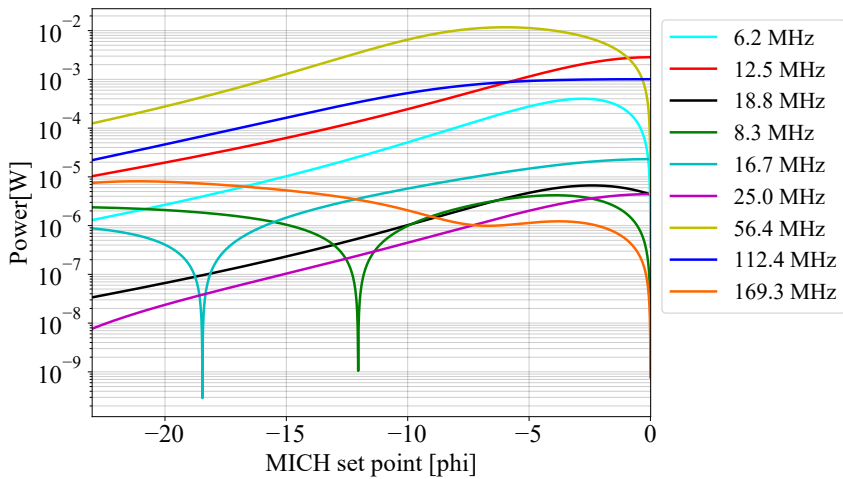


Figure 2.9: Sidebands evolution in B4 port during the last phase of the variable finesse lock acquisition.

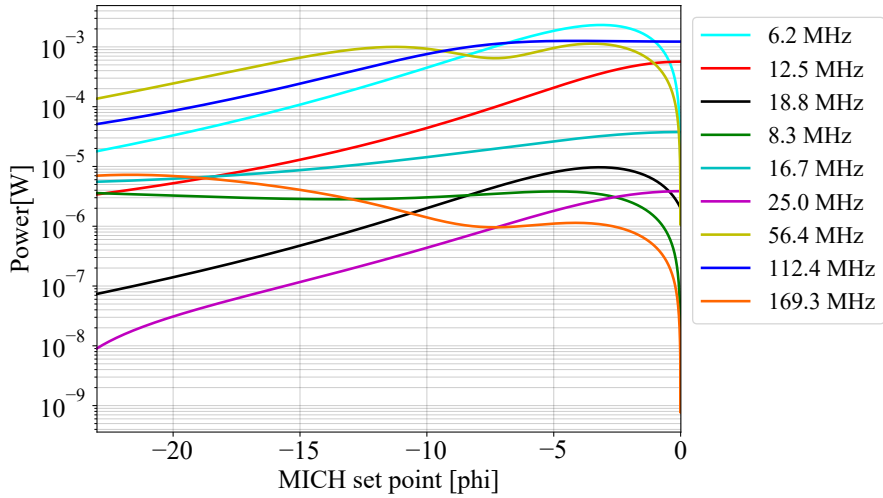


Figure 2.10: Sidebands evolution in B5 port during the last phase of the variable finesse lock acquisition.

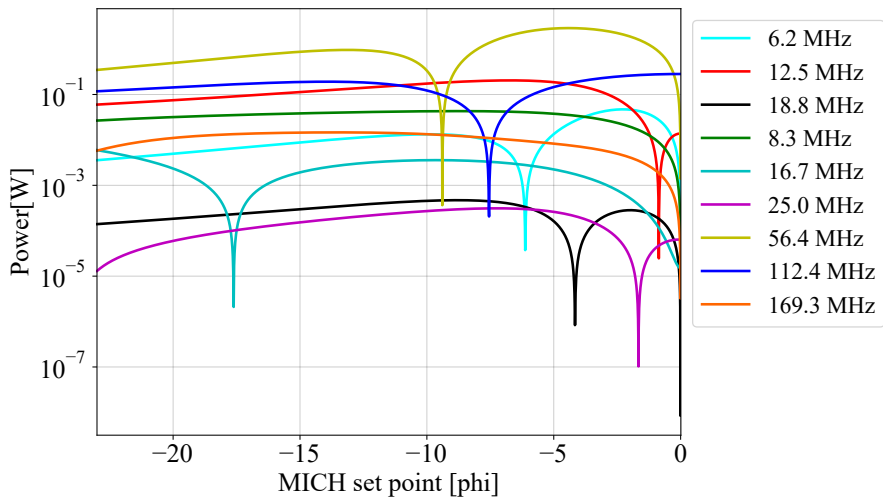


Figure 2.11: Sidebands evolution in B1 port during the last phase of the variable finesse lock acquisition.

2.4 Data extraction and calibration

The experimental data was collected from the photodiodes present in the detection ports **B1p**, **B2**, **B4** and **B5** depicted in Figure 2.6. In this investigation, the data from the photodiodes placed in the transmission of both arm lengths were omitted for simplicity and since the arms may be locked individually with relative ease. The raw data is extracted from the following channels from the Virgo detector data-channel system: *SDB2_B1p_PD1_sample*, *SIB2_B2_PD1_sample*, *SPRB_B4_PD1_sample*, *DB2_B5_PD1_sample*. The time series present in these channels are sampled at 400 MHz. Therefore, at every recorded second, for each collected sample of 32768 data points, the duration of continuous observation is around 80 μ s.

Each time series sample was turned into an amplitude spectral density using Welch method [54]. This method computes an estimate of the power spectral density by dividing the data sample into segments and averaging periodograms computed on each segment. The length of the Fast Fourier Transform (FFT) is chosen equal to the number of data points 32768. The window used was *Hanning* and the scaling was set to *density*, which outputs power spectral density units. One example of a time series together with its corresponding amplitude spectral density is shown in Figure 2.12.

Once the amplitude spectral density has been computed, a search is conducted for the nine sideband frequencies and the corresponding amplitude values are recorded. These extraction points are also illustrated on Figure 2.12.

The data collection procedure needs to be carried out at certain points which are compatible to the simulation. In the case here, the domain for data extraction is the Michelson reduction from half-fringe to the operation point. In Virgo, the status of the interferometer can be obtained by looking at *Metatron* operation. *Metatron*, similar to *Guardian* in LIGO, is a top level framework for detection automation which defines hierarchical relationships between finite state machines. This outputs a flag which describes the state of the detector at that certain GPS time. Once the flag defines the Michelson mid-fringe state, the GPS time is recorded. Starting with this, data is collected for each second iteration until the *Metatron* reaches a MICH offset of 0. During this operation, the Michelson offset is also recorded from the channel *LSC_MICH_SET*. An example of the interferometer state and the MICH set point variation is seen in Figure 2.13.

Twenty locks of data were gathered during the MICH set reduction to 0 for all sidebands in each detection port. This establishes the statistical significance of the analysis and eliminates any biases linked to the initial alignment of the interferometer. All of the locks were successful, bringing the interferometer to within 55 Mpc for a binary neutron star search. The times at which the locks were extracted are presented in Table 2.2.

The data between individual locks in some detection ports show a large variance in their power. This can be attributed to the change in the initial conditions at the

Event	Date	Starting time (UTC)
Lock 1	February 05 2020	14:00:45
Lock 2	February 10 2020	19:46:13
Lock 3	February 13 2020	12:03:45
Lock 4	February 14 2020	01:25:06
Lock 5	February 14 2020	02:00:35
Lock 6	February 17 2020	09:02:23
Lock 7	February 17 2020	11:33:00
Lock 8	February 17 2020	12:21:40
Lock 9	February 20 2020	07:12:00
Lock 10	February 22 2020	00:30:15
Lock 11	February 23 2020	00:36:52
Lock 12	February 23 2020	01:39:00
Lock 13	February 23 2020	03:23:58
Lock 14	February 23 2020	16:45:37
Lock 15	February 24 2020	00:01:20
Lock 16	February 24 2020	03:06:40
Lock 17	February 24 2020	08:04:18
Lock 18	February 25 2020	12:08:38
Lock 19	February 26 2020	17:17:00
Lock 20	February 27 2020	10:40:52

Table 2.2: Temporal coordinates for the population of locks studied. After the interferometer maintain locks, a binary neutron-star merger range of at least 55 Mpc is achieved. Since the locks were selected across the entire month of February, the systematic biases associated with the interferometer initial conditions during lock acquisition are reduced.

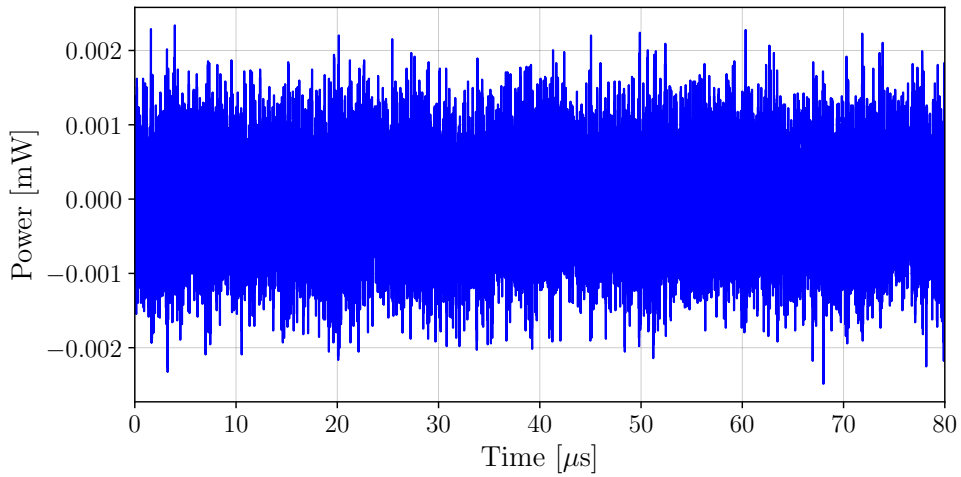
start of the lock-acquisition sequence and is the main motivation for averaging the data from the population of locks.

During the lock acquisition, the modulation depth for the 6 MHz and the 56 MHz photodiodes were reduced to control the excess power causing sensing issues. These variations were verified using *INJ_LNFS_AMPL* channel. An example of the modulation index variation with Michelson offset reduction can be seen in Figure 2.14.

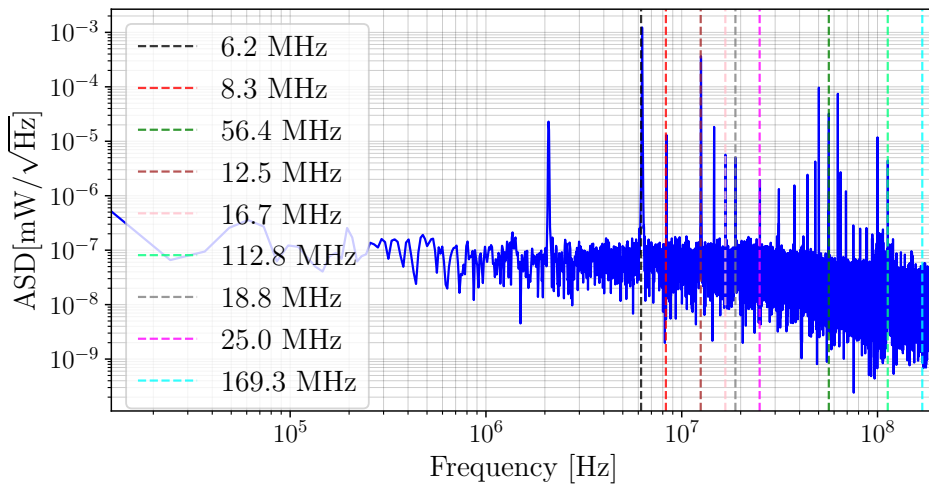
The change in modulation depth expressed in dbm was converted to mW using the following equation:

$$P_{\text{dBm}} = 10 \times \log \left(\frac{P_{\text{mW}}}{1\text{mW}} \right). \quad (2.27)$$

Therefore, for 6 MHz sideband, having the modulation depth changing from 15 dBm to about 9 dBm, a scaling factor of 1.66 was calculated and for 56 MHz sideband a scaling factor of 1.46 was obtained.



(a)



(b)

Figure 2.12: An example of a continuous data sample of $80 \mu\text{s}$, extracted from the **B4** photodiode. (a) A raw time series is shown. (b) The corresponding amplitude spectral density by a Welch method is illustrated. The vertical lines show the sideband frequencies for which amplitude values were extracted.

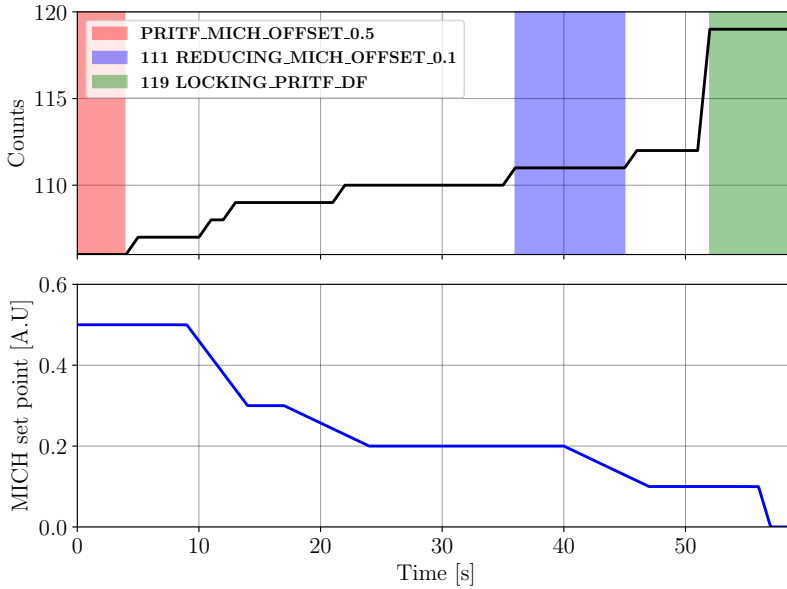


Figure 2.13: The figure depicts examples of Metatron states (upper plot) and the variation in Michelson set point (lower plot) during one lock acquisition. During this period, data for six sideband frequencies are extracted at four photodiodes used for longitudinal control. The analysis investigates a series of twenty locks.

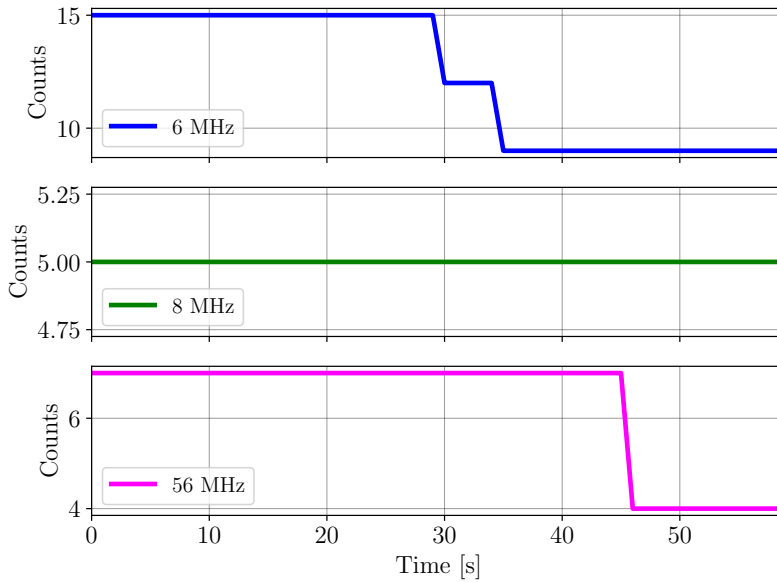


Figure 2.14: The variation in modulation depths for the three main modulation frequencies during a lock acquisition.

2.5 Analysis

The initial data point for both the simulation and experimental data was selected as the 0.5 Mich set point. Starting with the 0.5 Mich set point, the amplitude of each sideband is retrieved at discrete phases during the interferometer locking acquisition process. This allows for the observation of amplitude variations when the detector is adjusted to its operating point. This is chosen since the Finesse simulation can not predict the demodulation effects at the photodiode level, and an absolute amplitude comparison can not be produced accurately.

The hardware transfer function is inherently included in the retrieved signals for each sideband, as they are obtained at the output of the readout chain. Nevertheless, the signal observed at the photodiode input has a spectrum characterized by shot noise that is constant across frequencies. Hence, it is necessary to apply compensation to the transfer function of the photodiode pre-amplifier in order to ensure that the amplitude of each sideband frequency closely mimics the electromagnetic field present at the input of the photodiode. Failure to execute this procedure results in an underestimation of the magnitudes of the sideband amplitudes beyond the corner frequency of the transfer function. However, the impact of the hardware transfer function on the results is not affected by the analysis method, which involves examining the amplitude trend for each frequency in several detection ports. The compensating of the transfer function for sideband frequencies with underestimated heights involves shifting the entire trend of points along the y-axis, while preserving the shape of the trend.

The Mich offset in the Finesse simulation corresponding to the x-axis data needs to be mapped into a suitable domain to be compared to the Metatron time at which the data is extracted. The new Mich offset for the simulation is therefore constructed from a balance between the B1 and B4 photodiode DC powers.

The DC signal at the B4 photodiode represents the power reflected from the symmetric port, whereas the DC signal at the B1 photodiode represents the power arriving at the antisymmetric port. The power distribution between these two photodiodes provides information regarding the MICH interference condition; hence, the sum of both provides the overall interference power at the BS and is a suitable normalization factor for B1-DC signal to construct the error signal. Therefore, the simulation x-axis is constructed as follows:

$$x_{\text{simulation}} = \frac{B1_{\text{DC}}}{B1_{\text{DC}} + 5431 \times B4_{\text{DC}}}, \quad (2.28)$$

where 5431 is a numerical factor which turns the first value to 0.5 half-fringe.

To produce a quantitative metric for the comparison, a Pearson linear coefficient r between the two sets of data is used:

$$r = \frac{\text{cov}(x, y)}{\sigma_x \sigma_y}. \quad (2.29)$$

Here, $\text{cov}(x, y)$ is the covariance between the two variables x and y . The quantities in the denominator $\sigma_{x,y}$ represents the standard deviation for each variable data.

The x-axis variance of the data is assumed to be negligible. However, the y-axis variance is estimated assuming a normal distribution spread. Therefore, the simulation data is compared to the mean value of the twenty locks data for the particular Mich set point. The mean uncertainty Δ_N is then:

$$\Delta_N = \frac{\sigma}{\sqrt{N}}, \quad (2.30)$$

where σ is the standard deviation in the data set for each Michelson iteration and N is the number of events.

2.6 Results

The data-simulation comparison results are illustrated below. Three types of examples are presented in Figures 2.15 to 2.17, randomly selected at different detection ports. The first figure shows an example of a good fit of the simulation to the data. The second example shows a statistically significant result of the fit, but with higher divergence between the two data sets. The third examples illustrate a no-significance match of the simulation to the data. All figures illustrate the full data variation from the lock population and the resulted average variation which is compared to the simulation.

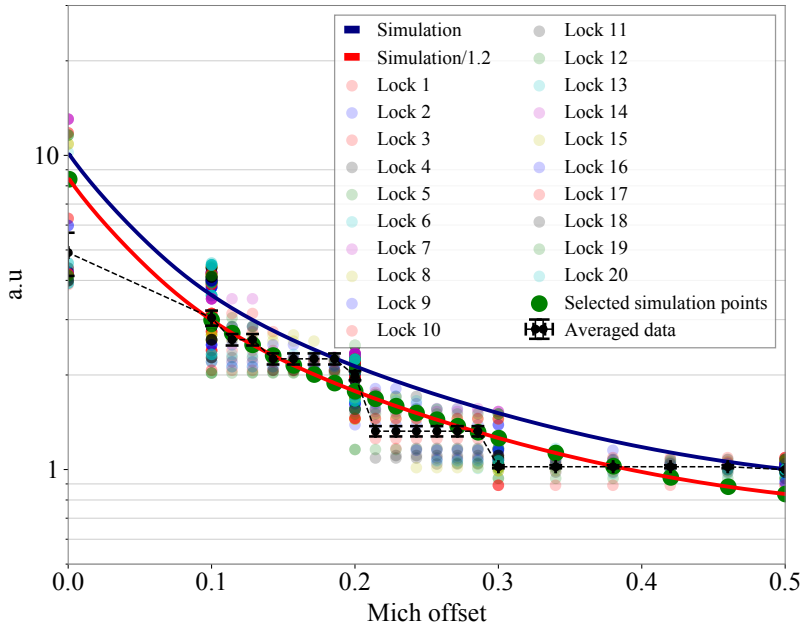
The simulation points are selected at each Michelson offset iteration and compared to the corresponding lock averaged data. The main plots are accompanied by linear regression plots depicting the statistical significance of the linear match of the varying amplitudes.

It can be seen in Figure 2.17 b) that the calibrated data are also shown in by the red data points. These are obtained with the calibration coefficient expressed in Equation 2.27.

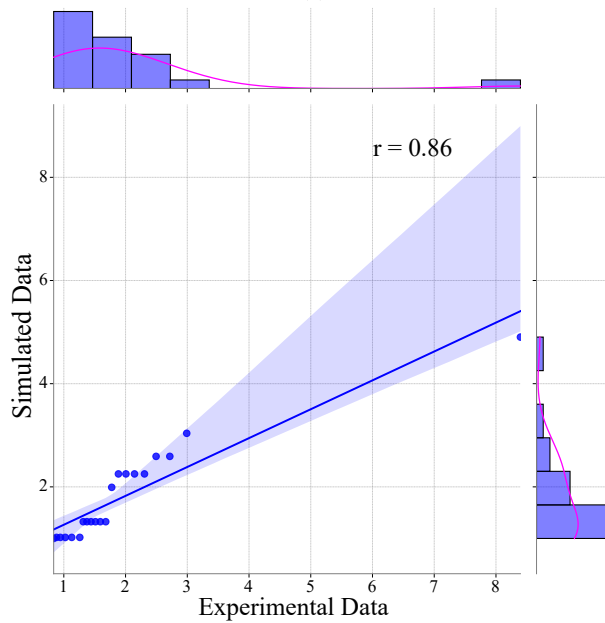
Two notable observations can be made looking at the data and the linear regression results. The first one is regarding the distribution of the data for each MICH set point. Since Metatron generates an interferometer state for many seconds, the data extraction algorithm outputs multiple sideband amplitudes for each set point. This has an effect on the regression slope although not as strong as the following point. The second aspect is represented by the comparison space between the two data sets. It can be seen that some point are *outliers*, as in Figure 2.15, with respect to the general distribution of the rest points. This produces a bias in estimating the values of the linear coefficients.

The full set of results for the linear correlation coefficients from matching the simulation with the photodiode data is presented in Table 2.3. The significance threshold is defined as follows:

$$N_l < 0.15 < N_m < 0.6 \leq N_h. \quad (2.31)$$



(a)



(b)

Figure 2.15: a) Comparison between the lock population data and the Finesse simulation and b) the result of Pearson correlation coefficient between the two data sets, illustrating a strong level correlation. These data corresponds to 16.7 MHz sidebands detected at B5 port.

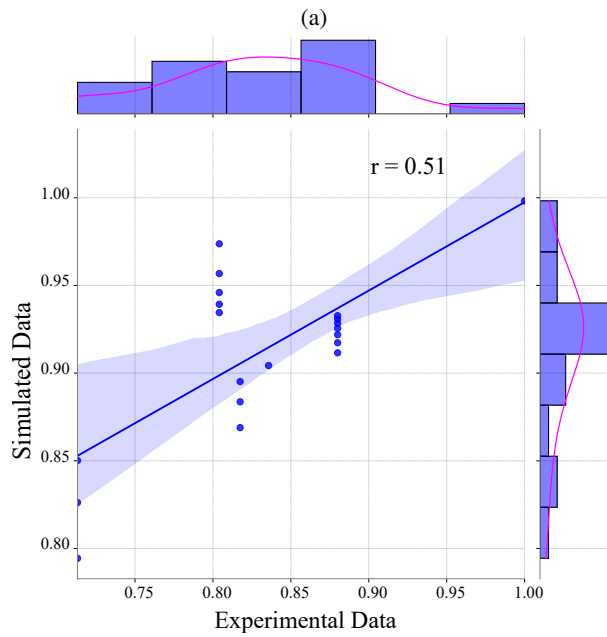
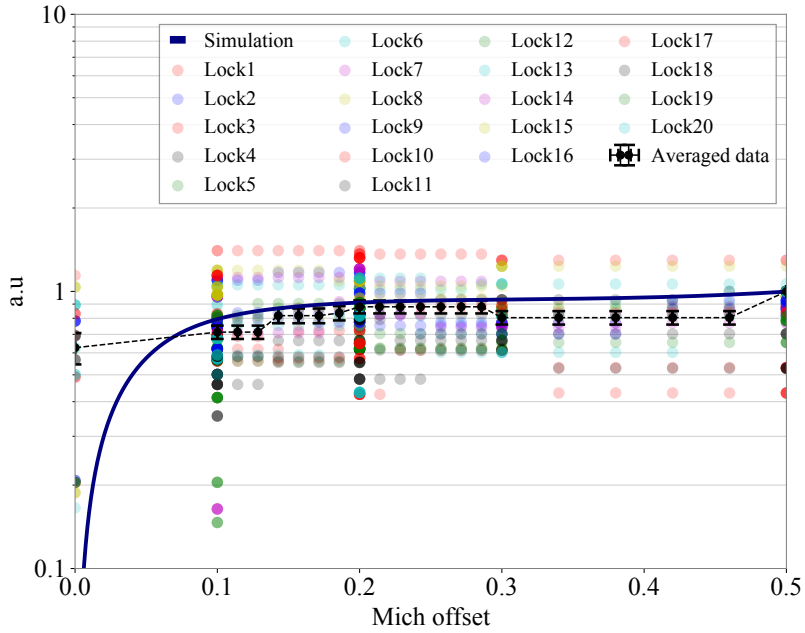
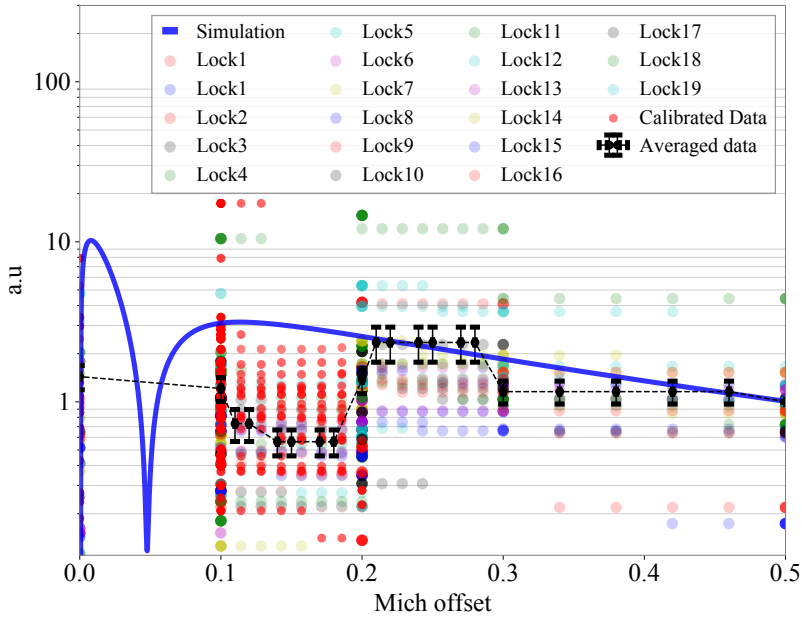
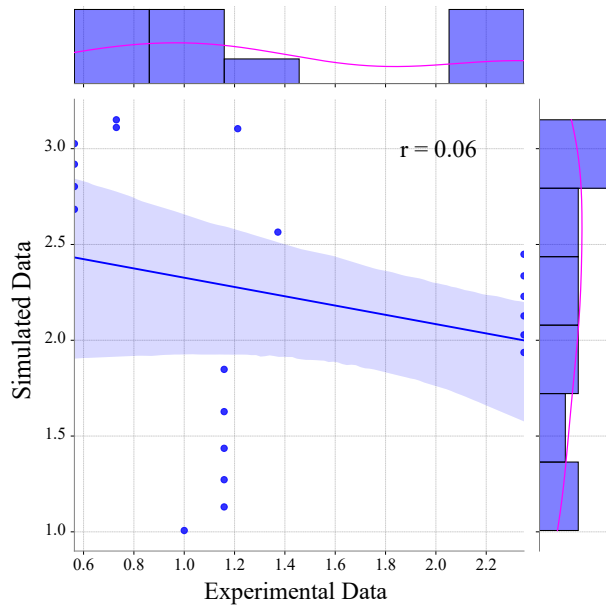


Figure 2.16: a) Comparison between the lock population data and the Finesse simulation and b) the result of Pearson correlation coefficient between the two data sets, illustrating a small level of correlation. These data corresponds to 16.7 MHz sidebands detected at B1p port.



(a)



(b)

Figure 2.17: a) Comparison between the lock population data and the Finesse simulation and b) the result of Pearson correlation coefficient between the two data sets, illustrating an insignificant level of correlation. These data corresponds to 6.2 MHz sidebands detected at B1p port.

Here, N_l are the results which fit poorly the data with low Pearson correlation coefficient. The terms N_m are the results which show good linear correlations for a subset of the evolution, but not for the full simulation. The terms N_h represent results which indicate good simulation-data fit. These definitions are not based on any rules or references in statistics. Instead, they are used to make it easier to show the results for the whole data set.

Sideband Frequencies [MHz]	B1p	B2	B4	B5
6.2	0.06	0.46	0.91	0.88
12.5	0.64	0.62	0.90	0.87
18.8	0.60	0.73	0.86	0.85
8.3	0.72	0.09	0.75	0.19
16.7	0.51	0.83	0.93	0.86
25.0	0.01	0.34	0.01	0.26
56.4	0.3	0.24	0.3	0.86
112.8	0.75	0.001	0.83	0.83
169.3	0.13	0.71	0.71	0.56

Table 2.3: Pearson linear correlation coefficients were obtained as a result of comparing the Finesse simulation with the raw photodiode data. The blue numbers represent significant results with good fit to the data. The black numbers reflect outcomes with some statistical significance, whereas the red colors represent sidebands with poor data fit. The orange values correspond to noisy data with meaningless outcomes.

The results presented in the table above indicate that at least three quarters of the full data set show either some or a strong statistical significance for a linear correlation between the Finesse simulation and the experimental data of the sideband evolution as the interferometer is brought to its operating point. The low-significance results are present in detection benches with B4 and B5 showing the strongest matches to the data. This indicates that there is no evident bias towards saturating a particular photodiode during the lock-acquisition procedure.

The results show no strong discrepancy between the correlation coefficients for the sidebands at the main modulation frequencies (6.2, 8.3 and 56 MHz) and the double and triple frequency sidebands. However, it can be clearly observed that the sidebands at 12.5 MHz and 18.8 MHz fit very well the simulation in all detection ports. This, together with three significant results of the main sideband frequency may indicate that the 6.2 MHz and its triple and double modulated frequencies are less affected by the coupling with the imperfections in the interferometer optical masses. The 8.3 MHz together with its double and triple modulation frequencies are lowest in confidence with the 25 MHz results showing only one weak significance match to the simulation. This weak matching can indicate the strong coupling of these sidebands to the optics imperfections in the interferometer. Finally, the 56 MHz and its double and triple sidebands show a good match to the simulation

with significant results in all detection ports.

2.7 Conclusions

This chapter explored the radio frequency sideband behavior for the Advanced Virgo interferometer during O3. The two study sections centered on the derivation of a Pound-Drever-Hall error signal in the presence of a higher-order laser mode and the comparison between the Finesse simulation of the sideband amplitudes during lock acquisition with the experimental data from the four longitudinal control photodiodes.

The Pound-Drever-Hall error signal was analytically calculated for a Fabry-Perot resonant cavity and picked off in reflection of the input mirror. The shape of the resulted error signal is bipolar and additionally crosses the zero point at the mode-splitting frequency. This can be used to build an analytical understanding of the error signals in cavities prone to containing resonant higher order modes, such as the Advanced Virgo power recycling cavity.

A Finesse simulation scanning various degrees of freedom during their positional variations, which mimics the variable finesse lock acquisition procedure, was performed. Sidebands at main frequencies and multiple of these were tracked during the last phase of the lock acquisition: the Michelson offset reduction from half-fringe to operating point. The tracking was performed at the four main detection ports of the interferometer: B1p, B2, B4 and B5. The experimental data sets were produced by extracting raw time-series photodiode data during the same lock acquisition phases indicated by Metatron and turning them into amplitude spectral densities by the Welch method. These data for twenty locks during O3 to a prior binary neutron-star range of at least 55 Mpc for all four detection ports, together with the simulated data, constitute the full data matching sets.

The simulation-data comparison was produced via linearly correlating the data of the sidebands evolution during Michelson offset reduction. The results show a Pearson linear coefficient of high significance for three quarters of the tests. The rest of the coefficients indicate either low significance or are associated with noisy data, which can be disregarded. Therefore, the results signify correlation between the simulation and real world. Moreover, the results are homogeneous, i.e low and high significance results being equally distributed by frequency and detection ports. These can indicate that the low-significance correlation coefficients in red from Table 2.3 are due to photodiode saturation and underline the importance of maintaining vigilance over the multiple-frequency sidebands throughout detector commissioning.

The data-simulation results suggest that a Finesse simulation without imperfections can be regarded as a relevant representation of the states of the interferometer during various conditions. However, the study has its clear limitations and a strong conclusion can not be presented. Firstly, integrating mirror maps into the simulation

and performing a similar analysis can shed lights into the effect of imperfections and the coupling with the resonant sidebands. Secondly, the photodiodes data was raw sample data, with no conditioning and filtering applied. If the non-concluding correlating coefficients can be removed, the confidence of the results in the analysis can increase. Finally, the interferometer state during which the comparison is performed adds a bias to the analysis. Prior longitudinal control phases to the Michelson reduction from half-fringe condition can be analysed, as well as the later stages during the lock acquisition with a Metatron flag greater than 119. These can shed light on the consistency and limitations of the results.

3.1 Introduction

The third generation of gravitational-wave detectors such as the European ET, or the US-based CE, aim to increase their sensitivity by at least a factor of ten over a broad frequency range compared to the design sensitivity of the current advanced detectors. This will significantly improve the observable range of detected sources. An observatory such as ET operating at design sensitivity will be able to produce a detection rate of at least hundreds of neutron-star mergers and thousands of black-hole mergers per week of observation [55, 56].

Reducing the impact of thermal noise on the interferometer's broadband sensitivity is one of the primary milestones for achieving the ET design sensitivity. This will be realized by operating at cryogenic temperatures, according to the equipartition theorem: at lower temperatures, broadband thermal noise is concentrated into well-defined resonances of the test mass, and this effect is enhanced for materials with a higher mechanical Q-factor [57].

Currently, fused-silica is employed for the test masses of gravitational-wave interferometers. This material's mechanical Q-factor diminishes with decreasing temperature [58], making it unsuitable for use in 3G detectors at cryogenic temperatures. Therefore, a new material such as silicon, which improves in mechanical Q-factor with decreasing temperatures [59], has been proposed.

Silicon heavily absorbs the currently used laser light at 1064 nm, necessitating a modification to a longer laser wavelength. The proposed choices are based on the telecommunication wavelengths at 1550 nm and a choice of thulium- and holmium-based laser sources in the 1800 nm to 2100 nm range. As a result of the widespread application of 1550 nm, it is simple and inexpensive to acquire

components. Moreover, imaging and diagnostic instruments at 1550 nm are substantially cheaper and superior than at longer wavelengths. This makes 1550 nm laser wavelength a baseline choice for the cryogenic Einstein Telescope [60] and together with silicon test masses are known as the building blocks of the next-generation of gravitational-wave detectors [61]. At this wavelength, the substrate absorption was measured to be as low as a few ppm/cm [62]. Furthermore, squeezed states of light, which are now extensively used in gravitational-wave detectors to reduce the effect of quantum noise, have been produced at 1550 nm with a suppression factor greater than 12 dB [63].

Nonetheless, increasing the laser wavelength to 2090 nm can result in a significant improvement in coating thermal noise due to the decreased absorption in highly reflecting mirror coatings [64], and a decrease in wide-angle scattering power. Future advanced detectors, including LIGO Voyager [25] and CE, are considering to operate at this laser wavelength.

During the technical design of large-scale 3G facilities, the readiness of the core technologies and necessary subsystems must be investigated. In addition, new technologies and techniques can be created to optimize the primary conceptual design. This is performed in dedicated test facilities. For ET, four specialised facilities have evolved across Europe [65], and ETpathfinder is one of them.

ETpathfinder is a cryogenic research and development laboratory that expects to test and integrate the key 3G technologies using a 10 m arm-length, low-noise interferometer in an environment comparable to that of ET. ETpathfinder's cryogenic technology closely resembles that of the Japanese gravitational wave detector KAGRA [66, 67] and the proposed cryogenic upgrade LIGO Voyager. Similar to ETpathfinder, KAGRA operations are designed for cryogenic temperatures as low as 20 K, integrating conduction cooling via low-stiffness heat-links. However, KAGRA operates with the standard 1064 nm laser wavelength with sapphire test masses and suspension fibres. The LIGO Voyager is designed to operate at approximately 2000 nm laser light, with silicon test masses maintained at 123 K, a similar configuration to one in ETpathfinder (ETpathfinder-B).

The compatibility of the subsystems tested in ETpathfinder with the technical design of ET is intrinsically linked to the obstacles that must be overcome in order to achieve sensitive interferometric operations at cryogenic temperatures. As an illustration, there is a significant discrepancy between isolating the test mass from the environment as much as possible and connecting it to the conduction cooling system in order to achieve the required low temperatures. The potential seismic shortcut of the cooling system must be resolved, with conduction cooling performed during operation in a controlled manner by minimizing its impact on the fundamental noise-limited sensitivity of the interferometer.

The development and understanding of the noise budget is the first step in this endeavour. Therefore, this chapter studies the underpinning noise contributions and combines them into full noise budgets for two targeted configurations of

ETpathfinder: 1) operating with 1550 nm laser light and at a temperature of 18 K, called ETpathfinder-A and 2) operating at 2090 nm wavelength and at a temperature of 123 K, called ETpathfinder-B.

3.2 ETpathfinder

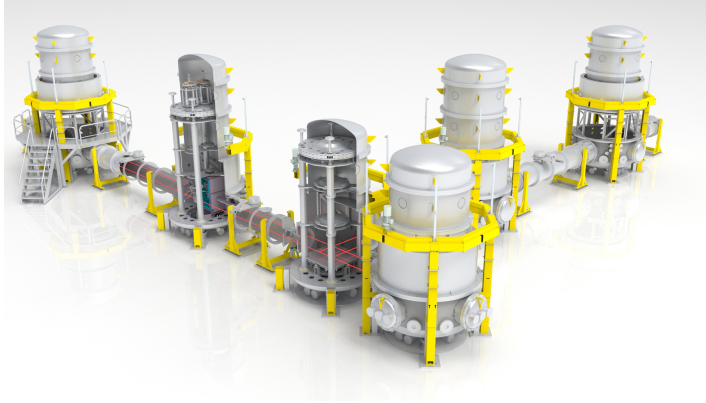
3.2.1 Cleanroom

ETpathfinder is being constructed in a former warehouse in Maastricht Randwyck neighborhood. The building's floor has been replaced with a 45-centimeter-thick concrete slab supported by 170 pillars that extend approximately 5 meters into the ground. The building floor is decoupled from the building walls in order to reduce the coupling of wind forces on the building into tilt movements of the foundation. The purpose-built ISO 7 and 8 cleanroom with specific air handling and climate control lies above this concrete slab. The cleanroom's footprint measures 34.7 m by 22.7 m. A 64 m² space is set aside for the preparation, cleaning, and baking of components that will enter the main cleanroom and vacuum system. Large items, such as the vacuum system itself, enter the cleanroom through a goods reception area that is accessible from the exterior and is also within the reach of a 2 × 2 tonne crane that has been installed in the facility. Large components can be moved into the cleanroom without exposing it to the outside or losing overpressure due to the multiple lock system. In an effort to minimize vibrational coupling, noisy equipments, such as vacuum pumps, are placed in a separate room whose floor is decoupled from the experimental area.

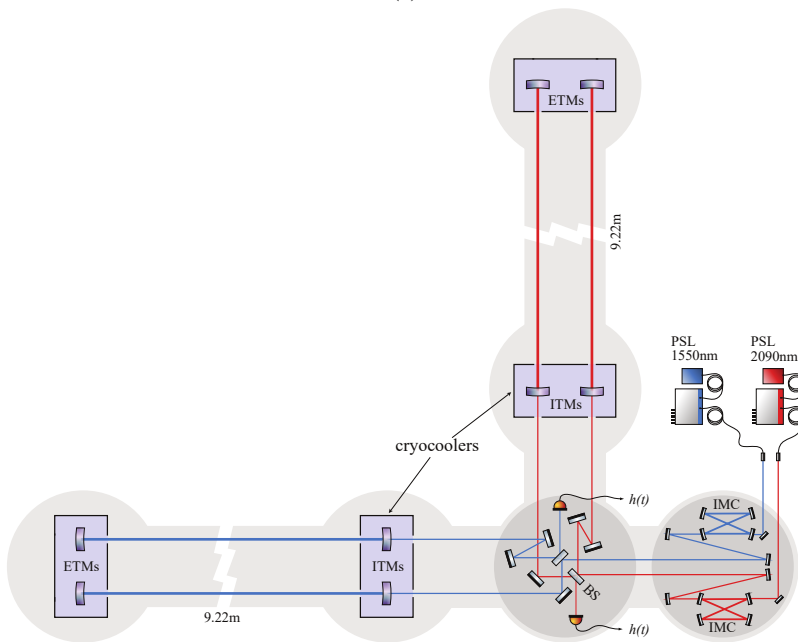
3.2.2 Optical Layout

ETpathfinder is comprised initially of two Michelson interferometers with Fabry-Perot resonators in their arms. One interferometer will operate at 1550 nm (here labelled ETpathfinder-A) and the second one at 2090 nm laser wavelength (ETpathfinder-B). Both interferometers are co-located in the same vacuum envelope. This is schematically presented in Figure 3.1. There are six vacuum towers in total, of which two, the input-optics tower and the beam-splitter tower, contain suspended optical benches, while the other four towers contain the individually suspended input and end test mass mirrors (ITMs and ETMs, respectively). The test masses are placed within numerous double-layered thermal shield-equipped cryostats. The interferometer arms are folded to run in parallel, this way the two interferometers can be operated at different temperatures with both ITMs and ETMs inside the same cryostat. Additionally, in the longer term future one may choose to operate with a single Fabry-Perot Michelson interferometer with heavier test masses, each per cryostat.

The interferometers' light sources are pre-stabilized lasers (PSLs) placed on



(a)



(b)

Figure 3.1: a) A 3D rendering of the actual setup and b) a simplified optical layout of ETpathfinder. Each of the two interferometers, here distinguished by the blue (1550 nm) beams and red (2090 nm) beams, occupies one of the two arms of the L-shaped vacuum system, with shared beam-splitter bench and input-optics bench. The input test-masses (ITMs) and end test-masses (ETMs) are separated by a distance of 9.22 m and placed into cryostats (light blue boxes). Light is provided by two pre-stabilized laser sources (PSLs), outputting around 1 W each. Inside the vacuum system, the laser beams are further stabilized and cleaned by input mode-cleaners (IMCs), before mode-matching telescopes guide the beams towards the beam-splitter and arm resonators. The interferometer outputs are kept close to a dark fringe and are detected by photodiodes. Their signal is proportional to the difference in arm-length (DARM), providing the main science signal $h(t)$.

an optical table outside the vacuum system. This optical table is mounted on conventional vibration-isolating self-leveling supports that are effective for both horizontal and vertical degrees of freedom. The lasers provide around 1 W of continuous-wave input light in the TEM₀₀ fundamental mode. Control loops lower the free-running laser noise by multiple orders of magnitude for both frequency and amplitude noises in the frequency region of interest, which is between 10 Hz and 10 kHz. A more detailed description of the 1550 nm laser system is provided in [68].

Inside the vacuum system, the laser beams are initially directed to input mode-cleaners, which are four-mirror ring resonators that offer a steady beam reference, decreasing beampointing noise and functioning as a quiet frequency reference for further laser noise stabilization. Mode-matching telescopes modify the geometry of the beam to match the eigenmode of the arm cavities, and then transmit the beam to the beam-splitter bench. The central interferometer optics, including the beam-splitters, are mounted on triple suspensions closely built after Advanced LIGO's HRTS design [69].

The ETM and ITM mirrors are made of silicon and placed 9.22 m apart. The units have a diameter of 150 mm and a thickness of 80 mm. For a density of crystalline silicon of 2329 kg/m³, the mirror mass of each test mass equals 3.29 kg.

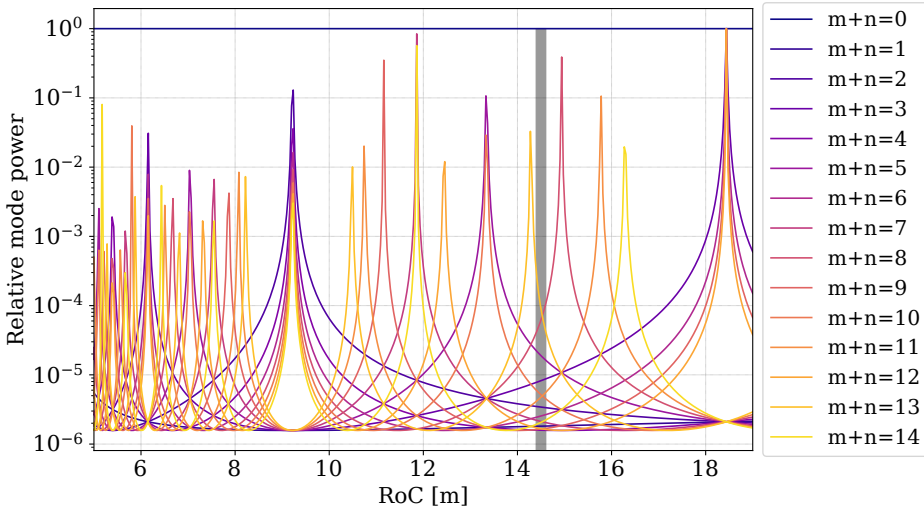
Interferometer arm-cavity

The highly reflective (HR) surfaces of the test masses have a radius of curvature (RoC) of 14.5 m, which results in a symmetric cavity with a beam waist size of 1.8 mm for the 1550 nm interferometer. This gives a beam radius of 2.2 mm on the mirror surfaces. These numbers were the result of the calculations shown in Figure 3.2. The two plots in the figure depict the higher order transverse-electromagnetic mode splitting as a function of RoC and matches a selected value of RoC with the appropriate beam radius at the HR surface of the test masses.

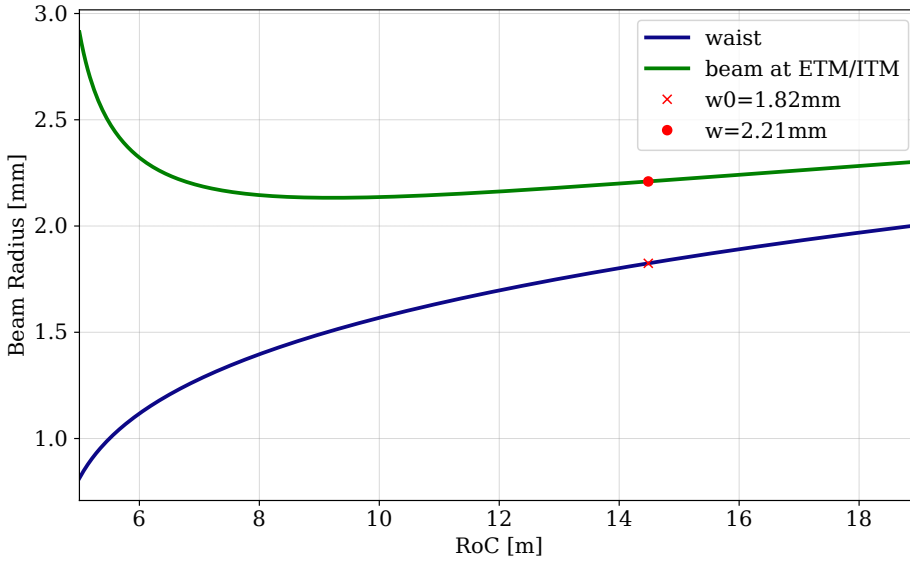
For the 2090 nm interferometer the beam dimensions will scale with $\sqrt{\frac{2090}{1550}}$ since this has the same RoC for both test masses and the same Rayleigh range as the 1550 nm interferometer. Practical benefits arise from having the same RoC on all test masses, as this permits the running of a second interferometer operating at a different wavelength using the arms of the first interferometer. Finally, to combat the divergence of the beam caused by the high refractive index of 3.5 of the test masses in both arms, the anti-reflective coated rear surfaces have a radius of 9.0 m, resulting in a collimated beam leaving the arm cavities.

Choice of arm-cavity finesse

The arm-cavity finesse of ETpathfinder was chosen by balancing the ease of cavity locking with the potential science targets given by noise sources that are enhanced by the finesse value. Since ETpathfinder does not incorporate a suspension point



(a)



(b)

Figure 3.2: Plot a) shows the normalized power built-up of higher order transverse-electromagnetic modes relative to the TEM_{00} mode as a function of test mass radius of curvature. Due to the simulation's coarseness level, the amplitudes of the higher order modes have varying heights, but in reality they should all equal one. However, the determination of a suitable radius of curvature is based solely on the position of the peaks, rather than their amplitude. A radius of curvature of 14.5 m was selected, which is located between the resonances of the modes $TEM_{m+n=7}$ and $TEM_{m+n=13}$. The selected RoC value is contained within a 0.1 m error shown by the grey vertical box. For this radius of curvature, a beam radius of 2.21 mm at the end mirrors HR surface results, and this is shown in plot b).

interferometer to facilitate the lock acquisition procedure, the locking flexibility remains a priority for the first test phases of the project.

From the noise budgets explained later, it can be seen that the ITM thermo-refractive noise is strongly linked to the arm cavity finesse, since this noise source is produced in transmission of the ITM. It was concluded that an arm cavity finesse of about 2050 will reduce enough the ITM thermo-refractive noise such that the coating Brownian noise will dominate the sensitivity of ETpathfinder over a wider frequency range. The coating Brownian noise is favored as a dominant noise source since this can offer a testbed for a noise source that limits the design of 3G detectors.

Due to numerous physical constraints, it is not possible to lock a cavity using a linear controller when the mirror is traversing a resonance at an arbitrary high velocity. The largest threshold velocity estimate v_{\max} comes from the response time of the feedback loop which is inversely proportional to the control bandwidth B and can be shown to be [70]:

$$v_{\max} = \frac{\pi\lambda B}{\mathcal{F}}, \quad (3.1)$$

where λ is the laser wavelength and \mathcal{F} is the arm-cavity finesse. For a feedback loop bandwidth of 250 Hz, similar to Advanced Virgo, and a wavelength of 1550 nm, the estimate is within a safety margin of three compared to the ETpathfinder expected rms velocity derived from the seismic measurement explained in Section 3.3.2. This allows some flexibility in the lock-acquisition precision and makes the finesse value of 2050 a viable option.

The arm cavity finesse of ≈ 2050 was therefore selected as the starting choice for ETpathfinder and all the noise budgets presented later will assume this value. For the baseline coating choice of silica and tantala quarter-wavelength pairs, the end test masses contain 17 pairs of layers to achieve high reflectivity, while the input test masses, lower in reflectivity, contain 9 pairs of layers. The layers have an optical thickness, which is the actual thickness d multiplied with the refractive index n , of a quarter of the interferometer wavelength, except for the outermost layer pair of the input mirrors, which was tuned for slightly lower reflectivity to result in an arm cavity finesse of ≈ 2050 .

3.2.3 ETpathfinder suspensions

In order to shield the test mirrors from the seismic background and to obtain a sensitivity performance of 10^{-18} m/ $\sqrt{\text{Hz}}$ at 10 Hz, the main interferometer optics will be suspended via multi-stage vibration isolation systems or suspensions. The suspensions need to isolate at least nine orders of magnitude in the direction parallel to the laser beam, or the horizontal direction. Typically, such a suspension translates around 0.1% of the vertical motion into the horizontal degree of freedom, therefore the vertical motion needs to be attenuated by at least six orders of magnitude.

The ETpathfinder isolation system resembles the mature technology of the Virgo

superattenuators [71] and is presented in more details in [72]. A diagram showing the main components of the isolation chain is shown in Figure 3.3.

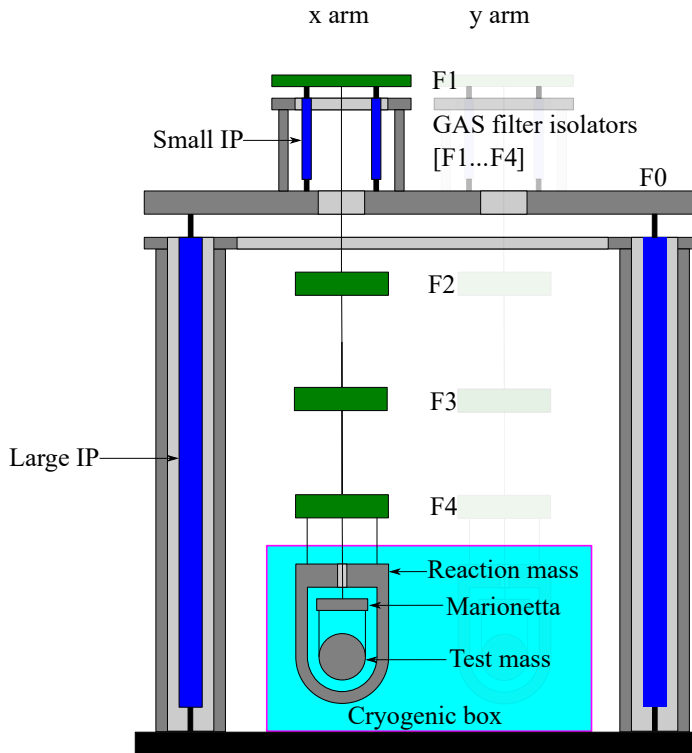


Figure 3.3: Simplified representation of the ETpathfinder suspension system. The blue rectangles show the two stages of inverted pendulums (four large IP stages for the entire suspension structure and three small IP stages per each suspension chain) which together with five cascaded bodies provide an attenuation that falls with $1/f^{14}$ after the pendulum mode of the test mass. The green rectangles provide vertical attenuation via geometric anti-spring systems. The cryogenic payload comprises of the reaction mass, the marionetta and the test mass.

The vibration isolators of ETpathfinder are based on a hybrid approach. The seismic attenuation below 5 Hz is provided by a system of four degree-of-freedom preisolators (two horizontal, yaw and vertical) designed for enhanced performance through active attenuation. Furthermore, the isolation above 5 Hz is provided passively by means of a cascade of low natural frequency mechanical oscillators or filters. Horizontal pendulums and a set of vertical cantilever springs are used to construct filters. The system uses feedback control to dampen the low frequency rigid body eigenmodes and to preserve the position and orientation of the suspended body, which may be a mirror or an optical bench, over the long term. High-frequency natural modes are attenuated by passive resonant dampers. Each attenuator suspends a payload consisting of a mirror (or optical bench), suspension, and control

mechanisms.

3.3 Fundamental noise sources

3.3.1 Quantum fluctuations of the light field

Quantum noise derives from fundamental fluctuations of the electromagnetic vacuum, which is the manifestation of the Heisenberg uncertainty principle [73]. The presence of quantum noise affects the interferometer via two mechanisms: *quantum shot noise* and *quantum radiation pressure noise*.

Quantum shot noise is a sensing noise caused by the phase variations detected at the dark port of the interferometer as a result of the statistical nature of the light entering the photodetector. These phase fluctuations increase directly proportional with the square root of the laser power. Additionally, the output signal of the gravitational-wave interferometers is directly proportional with the laser power. Therefore, the signal-to-shot-noise ratio improves with the square root of the laser power. This can be seen in the mathematical formulation of the shot noise amplitude spectral density:

$$S_{\text{sn}}(f) = \frac{1}{L} \sqrt{\frac{\hbar c \lambda}{2\pi P}}, \quad (3.2)$$

where f is the laser frequency, L is the arm-length of the interferometer, P is the optical power in each interferometer arm, c is the speed of light and λ the laser wavelength. Shot noise phase variations are independent of frequency, therefore they have the greatest impact on the interferometer's sensitivity at high frequencies, where signal response wanes due to the final bandwidth of the meter.

The non-zero variance of the background electromagnetic field produces vacuum background fluctuations which can enter the interferometer at any open port, i.e., through any optical component which loses light. When beating with the carrier light in the interferometer's arms, the vacuum fluctuations drive the radiation pressure forces impinging on the suspended test mirrors, therefore causing stochastic displacements of the mirrors and of the arm-lengths that may mask or even mimic a gravitational-wave signal. The amplitude spectral density of the quantum radiation pressure noise in a Michelson interferometer is given by:

$$S_{\text{rpn}}(f) = \frac{1}{m f^2 L} \sqrt{\frac{\hbar P}{2\pi^3 c \lambda}}. \quad (3.3)$$

Here m is the mirror mass, L is the arm-length of the interferometer, P is the optical power in the arms, c is the speed of light and λ the laser wavelength. The radiation pressure noise is dominant at lower frequencies where the test mass displacement is larger for a given force.

The total quantum noise is therefore the uncorrelated sum of the photon shot noise and the radiation pressure noise $S_{\text{QN}}(f) = \sqrt{S_{\text{sn}}(f)^2 + S_{\text{rpn}}(f)^2}$. The two

quantum noise components have an inverse dependence with the laser power in the detector arms, as observed in Equations 3.2 and 3.3. Therefore, enhancing the displacement sensitivity of an interferometer at higher frequencies by increasing the laser power results in a degradation of the radiation pressure noise at lower frequencies.

The inverse dependence on power of the two quantum noise components and the fact that the underlying fluctuations in phase and amplitude are uncorrelated, gives rise to the *Standard Quantum Limit* (SQL). For any given frequency, there is a minimum amplitude spectral density and this occurs for an optimum power where $S_{\text{sn}}(f) = S_{\text{rpn}}(f)$. The mathematical expression for the SQL reads:

$$S_{\text{SQL}}(f) = \frac{1}{\pi f L} \sqrt{\frac{\hbar}{m}}, \quad (3.4)$$

with m being the mirror mass and L is the arm-length of the interferometer. The total quantum noise and its components, together with the SQL curve is depicted in Figure 3.4. This figure also shows how increasing the laser power by one order of magnitude enhances the shot noise-limited sensitivity at the expense of the radiation pressure degradation.

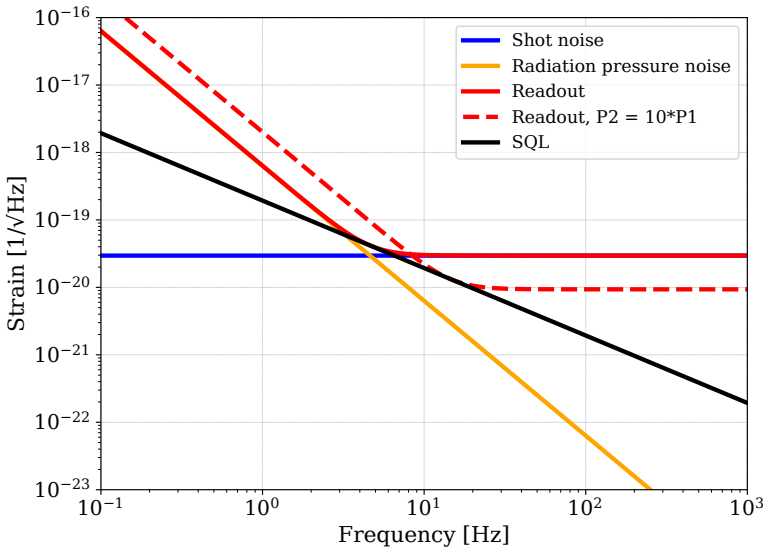


Figure 3.4: Quantum noise amplitude spectral density for two optical power levels. The two components of the quantum noise are summed in quadrature to give the total readout noise. The standard quantum limit is also shown for reference by the black curve. The calculation assumes ETpathfinder mirror masses of 3.2 kg with and arm-length of 9.2 m and a laser wavelength of 1550 nm. The power level in the arms is assumed to be 10^5 W.

For ETpathfinder, the calculation of the baseline quantum noise curve assumes an input power at the beam-splitter of 1 W, an arm-cavity finesse of 2050 and

50 ppm average loss per mirror. The radiation pressure noise limits the sensitivity of ETpathfinder-A between 4 to 10 Hz. The shot noise sensitivity drops outside of the arm-cavity pole at about 3.9 kHz.

3.3.2 Seismic noise

A combination of the seismic and Newtonian noise dominates the fundamental noise sensitivity of the Einstein Telescope at very low frequencies, as well as the current ground-based laser interferometers. Seismic noise is the principal driver for the advanced engineering of the mechanical isolation systems employed in gravitational-wave interferometers and the need for such advanced suspension systems was recognized since the beginning of the field [13]. In this study, the noise spectral density is computed using seismic measurements of the ground motion transmitted via the mechanical transfer function of the proposed suspension system.

Seismic campaign

The first component of the seismic noise is comprised of the measured seismic activity of the laboratory ground. This was measured for the ETpathfinder hall during three week-ends, between 30th of October 2020 and 21st of November 2020. At that time, the ETpathfinder laboratory concrete slab had been finalised.

The data was collected using a seismic station installed on the concrete slab on which the ETpathfinder interferometers will be located. The seismic station comprises of a Trillium T240 sensor and a stand-alone data acquisition system. The Trillium T240 is a broadband seismometer with a flat response function between 4 mHz to 35 Hz and an instrumental noise below the low-noise seismic model of Peterson [74]. The seismometer is placed directly in contact with the concrete slab with a polyurethane thermal and acoustic shield covering its body. The read-out system contains an internal computer with a National Instrument data acquisition card (NI6289), a low-noise pre-amplifier and an uninterruptible power supply (UPS).

The seismometer generates precise measurements of ground velocity in three directions (North, East, and Vertical) as well as diagnostic signals. The magnitude of the velocity signals from the seismometer is measured in millivolts. In order to increase the measurement resolution, these signals are amplified by a factor of around 100 to maximize the analogue-to-digital converter (ADC) input range (± 10 V). This amplifier contains a low-pass anti-aliasing filter with a -30 dB point at 30 Hz. The data-acquisition process was operated via a custom-made LabView program run on the internal PC. For each measurement, a sampling rate of $f_s = 128$ Hz was selected and the data was recorded for every 128 s into an ASCII file inside the hard-drive of the internal PC.

The output velocity signal of the Trillium T240 is integrated in a post-processing script and the mean density per frequency bin computes the tri-axial ground displacement set: $S_V(f)$ for the displacement spectral density of the vertical axis

signal, $S_E(f)$ and $S_N(f)$ for the displacements corresponding to the eastern and northern axis respectively. A total horizontal displacement spectrum $S_H(f)$ used in this study is given by $S_H = \sqrt{S_E(f)^2 + S_N(f)^2}$. The mean displacement of the ground for each measurement axis with data recorded during six hours of night time is shown in Figure 3.5.

The seismic variability during a 24 hours measurement duration can be seen in the spectrogram from Figure 3.6 as well as the variation in the ground displacement measured at different times during the day. Being in an inner-city location, a large amplitude contribution from anthropogenic noise is clearly visible between 1 to 20 Hz, with slight reduction during night-time.

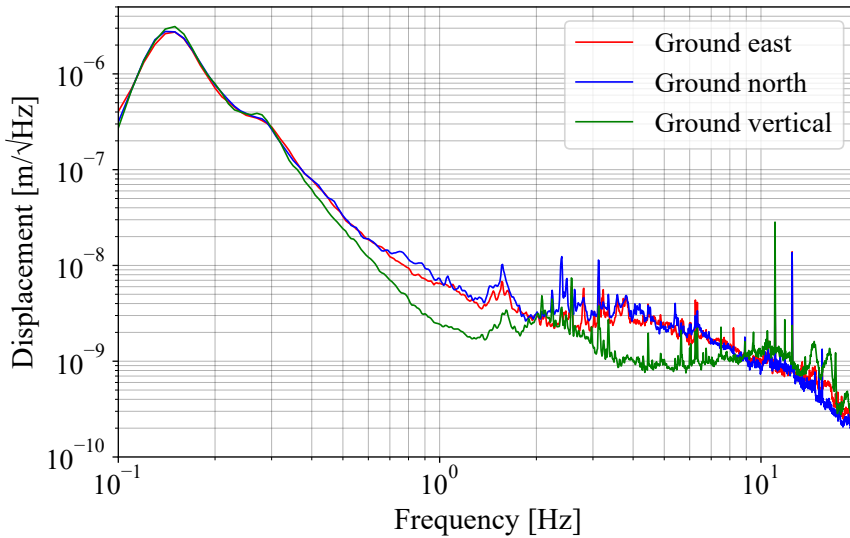
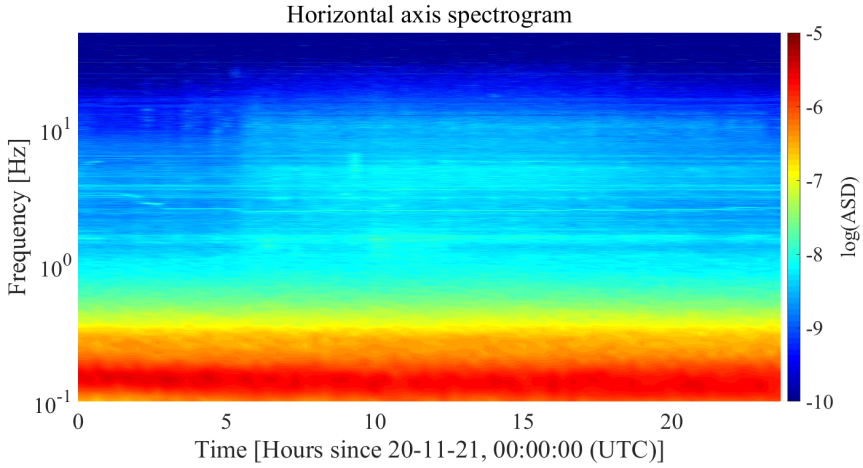


Figure 3.5: Triaxial measurement of ground displacement during the first six hours of night time from Figure 3.6.

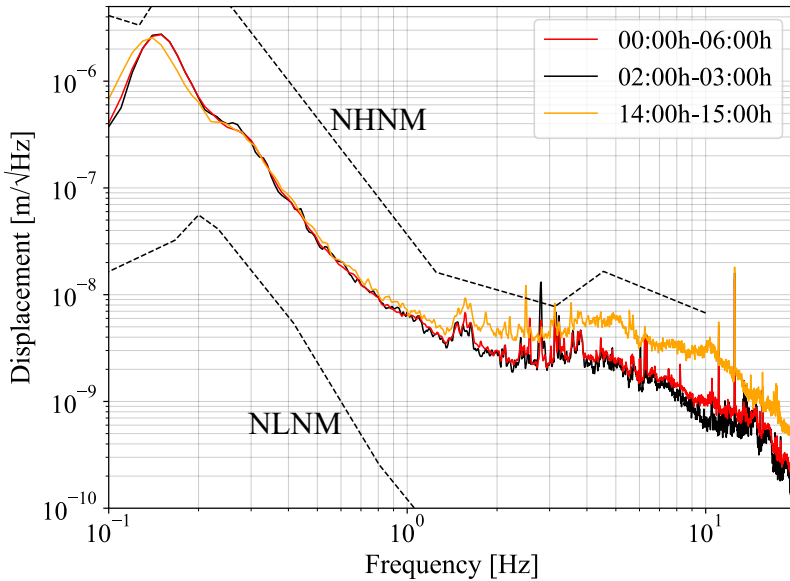
Suspension transfer function

In order to understand how vibrations from the ground propagates to the interferometer mirrors, the concept of *transfer function* should be introduced. As its name indicates, a transfer function is a mapping of a system's inputs to its output via the system's mechanics. In our studies, the transfer function describes the *transmissibility* of the input motion x_{in} , such as ground vibration, to the output motion x_{out} , such as the motion of the test mass, in any chosen degree-of-freedom. If the system is treated to be linear, then the linear operator $T(\omega)$ representing the transfer function in the frequency domain can be expressed as:

$$x_{in}(\omega) = T(\omega)x_{out}(\omega). \quad (3.5)$$



(a)



(b)

Figure 3.6: The variability of the laboratory ambient field displacement during a 24 hours period. The spectrogram in Figure a) shows the continuous variation in the magnitude of the ground displacement for one horizontal axis with the colorbar units according to the exponents of the amplitude spectral density. Plot b) shows the displacement amplitude S_H of the ground during three intervals of the day. The red curve corresponds to the data used for the estimation of seismic noise component. The curves are compared to the new low noise model (NLNM) and new high noise model (NHHM) from Peterson [74]. The corresponding spectrogram of the vertical ground displacement shows a variability similar to the horizontal one.

In general, a complete representation of a system, such as a mechanical suspension system employed in gravitational-wave detectors, includes a model for the non-linear effects in the system. When the system is assumed to be linear, the transfer function is therefore only an approximation of the system's dynamics. The suspension systems of gravitational-wave detectors are exposed to small displacements and forces around their equilibrium positions. In this regime, suspension systems exhibit a linear behavior, making linear models a suitable approximation for the system's dynamics.

The mechanical transfer functions of the isolation systems in gravitational-wave detectors have been extensively studied. The LIGO quadrupole suspension systems have been described by both the numerical, Newtonian model [75, 20], as well as the Lagrangian formalism [76]. Furthermore, the VIRGO superattenuators have been successfully modelled via the impedance matrix approach developed under the name of Octopus [77].

There are two main parts in calculating a transfer function. The first part comprises of deriving the equations of motions of the system, thus understanding its dynamics. The second part is based on estimating the frequency domain response function, usually illustrated graphically by Bode plots. In this thesis, the transfer function is estimated by a Lagrangian derivation of the equations of motions in two degrees-of-freedom and the frequency response calculation performed in the state-space domain.

Modern control theory overcomes numerous limitations of the classical control theory, especially by integrating a more robust description of the plant dynamics. The *state-space* description describes the plant dynamics as a set of coupled first-order differential equations in a set of internal variables, called *state variables*, together with a group of linear equations which combine the state variables into the physical output variables. The state-space equations can be written as:

$$\dot{\mathbf{x}} = \mathbf{Ax} + \mathbf{Bu}, \quad (3.6)$$

where \mathbf{x} is the state vector, containing the set of n state variables and \mathbf{u} is the input vector, containing a set of input vectors. The output set can be written as:

$$\mathbf{y} = \mathbf{Cx} + \mathbf{Du}. \quad (3.7)$$

Here \mathbf{y} represents the column vector of the output variables. The matrices \mathbf{A} , \mathbf{B} , \mathbf{C} , \mathbf{D} are the state-space matrices. The matrices \mathbf{A} and \mathbf{B} contains the properties of the system encoded by the structure and dynamics of the system. The matrices \mathbf{C} and \mathbf{D} correspond to the output equations and are determined by the particular choice of output variables.

Therefore, calculating the elements in the state space matrices allows one to perform the frequency response analysis and to obtain an estimate of the transfer function for the particular system. Generally, for a harmonic oscillator, such as a pendulum, its dynamics is described by the second order differential equation of the

following type:

$$\mathbf{M} \frac{d^2 x(t)}{dt^2} = -\mathbf{K}x(t) - \mathbf{c} \frac{dx(t)}{dt} + \mathbf{F}, \quad (3.8)$$

where \mathbf{M} , \mathbf{K} and \mathbf{c} represents the mass, stiffness and damping matrices associated with the system, x represents any of the six degrees-of-freedom and \mathbf{F} is the matrix with the components representing externally applied forces and torques. Therefore, the state-space matrices for this harmonic oscillator can be written as:

$$A = \begin{pmatrix} 0 & 1 \\ -\mathbf{M}^{-1}\mathbf{K} & -\mathbf{M}^{-1}\mathbf{D} \end{pmatrix}, \quad B = \begin{pmatrix} 0 \\ \mathbf{M}^{-1} \end{pmatrix}, \quad C = (1 \ 0), \quad D = (\mathbf{c}). \quad (3.9)$$

As it can be seen in the state space matrices, obtaining the mass, stiffness and the damping matrices is enough for calculating the mechanical transfer function of that system.

One degree-of-freedom example

A simple pendulum is a suitable example of a one-dimensional harmonic oscillator which can be used to understand the principles behind the transfer function and its computation using state space matrices. The pendulum is equivalent to the mass on a spring example depicted in Figure 3.7. In this example, a viscous damping force F_v is also introduced, defined as $F_v = -c \frac{dx(t)}{dt}$ with c being the viscous damping coefficient and $x(t)$ the displacement from equilibrium with time of the suspended mass. The introduction of this force can be understood, for example, as the motion of this oscillator in air.

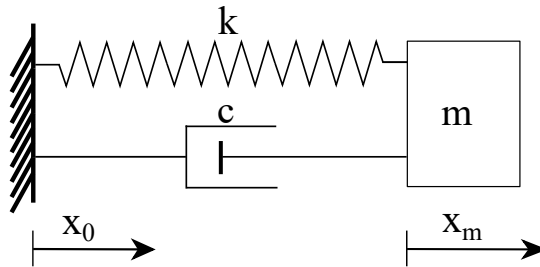


Figure 3.7: A free body diagram showing a mass on a spring as an example of an one-dimensional simple harmonic oscillator.

The time domain equation of motion for such a system can be expressed as:

$$m \frac{d^2 x_m(t)}{dt^2} = -k (x_m(t) - x_0(t)) - c \frac{d(x_m(t) - x_0(t))}{dt}. \quad (3.10)$$

Here k is the stiffness of the spring, m is the mass of the body, x_0 is the point of suspension coordinate and x_m is the distance moved by the mass as it is displaced from equilibrium.

Turning Equation 3.10 in the frequency domain using Laplace transform: $\dot{x} \rightarrow sx$ and $\ddot{x} \rightarrow s^2x$, where s is a complex variable defined in terms of the angular frequency ω as $s = i\omega$, and defining the resonant frequency of the system as $\omega_0^2 = k/m$:

$$-\omega^2 x_m + \omega_0^2 x_m - \omega_0^2 x_0 + \frac{c}{m} i\omega x_m - \frac{c}{m} i\omega x_0 = 0, \quad (3.11)$$

and therefore the transfer function can now be calculated as:

$$TF(\omega) = \frac{x_m}{x_0} = \frac{\omega_0^2 + \frac{c}{m} i\omega}{\omega^2 - \frac{c}{m} i\omega - \omega_0^2}. \quad (3.12)$$

For a pendulum of length 25 cm and a mass of 1 kg, with a damping factor of 0.2 Ns/m, the transfer function is simulated in Figure 3.8.

There are some interesting facts about the transfer function of the single pendulum presented above and seen in Equation 3.12 and Figure 3.8. Some of them can be understood by introducing the mechanical Q-factor, defined as $Q = \frac{m\omega_0}{c}$, equivalent with the ratio of the stored energy in the system to the dissipated energy per cycle. For this example, the mechanical Q-factor is about 31.

At low frequency, the magnitude of the mechanical transfer function is 1. This unitary response is equivalent with the suspension point, or the attachment point of the spring, moving in-phase with the pendulum mass, therefore making the pendulum mass following the motion of the attachment point. After the resonance frequency of about 1 Hz, in the limit of $\omega \gg \omega_0$, the magnitude of the transfer function falls with $\frac{1}{\omega^2}$. Therefore, a pendulum of 25 cm length with a resonance frequency of 1 Hz in the longitudinal direction, provides an attenuation factor of 10^4 at around 100 Hz. The power and elegance of the suspension isolation system employed in gravitational-wave observatories can now be understood. When n number of pendulums are stacked in series, the isolation falls off with $\frac{1}{\omega^2}$ above the last resonant frequency for a high mechanical Q-factor system.

If a damping force is introduced, the transmissibility falls as $\frac{1}{\omega^2}$ until the frequency reaches an inflexion point given by $\approx Q\omega_0$, after which it falls as $\frac{1}{\omega}$. This can be observed by the red curve in Figure 3.8. The frequency at which the inflexion happens in the example above is ≈ 31 Hz.

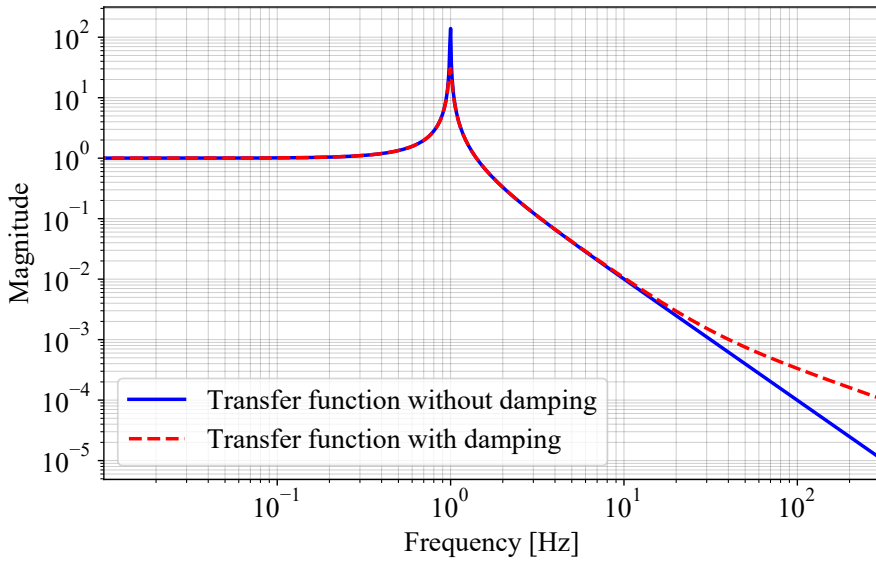


Figure 3.8: Transfer function of a single degree-of-freedom pendulum.

The transfer function for the pendulum dynamics can be constructed also by writing the A, B, C, D matrices for the equation of motion in 3.10. These read:

$$A = \begin{pmatrix} 0 & 1 \\ -\frac{k}{m} & -\frac{c}{m} \end{pmatrix}, \quad B = \begin{pmatrix} 0 \\ \frac{1}{m} \end{pmatrix}, \quad C = (1 \ 0), \quad D = (c). \quad (3.13)$$

ETpathfinder suspension model

The system components, such as stiffness and masses, can be expressed to generate state space matrices and determine the transfer function. Figure 3.9 depicts a free-body diagram that can be used to comprehend the ETpathfinder's complete seismic isolation model.

The model in the Figure 3.9 is valid for both the horizontal and vertical degrees of freedom, but for vertical, the derivation of the equations of motion start from mass m_2 , which is the first attenuation filter in the vertical direction. Therefore, expressing the stiffness and mass components for each degree-of-freedom allows the construction of component matrices for the state space representation.

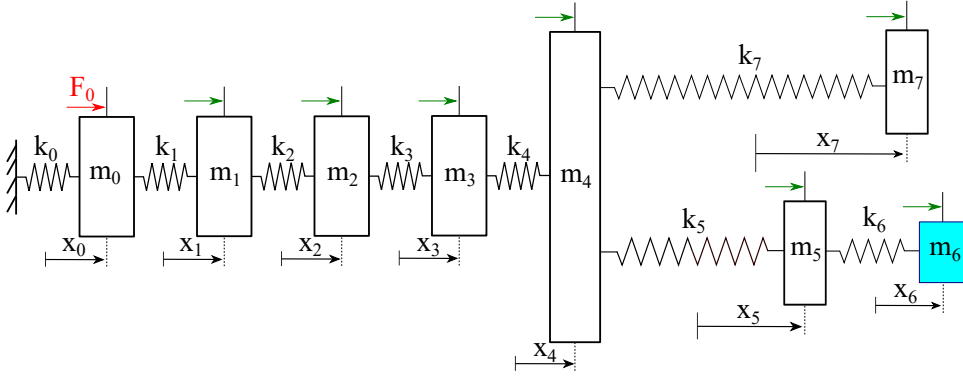


Figure 3.9: A free body diagram of the ETpathfinder suspension system. The vibrations propagate from the ground, shown as force F_0 to the test mass m_6 . The green arrows represent the direction of the forces that are pushing the bodies out of equilibrium. The reaction mass m_7 interacts with the marionette m_5 and the test mass via actuators, but this coupling is not modeled in the proposed method for the sake of simplicity.

The first two components, m_0 and m_1 represent the large and short inverted pendulum (IP) stages. These two components contain both the mass of the platform stages which are the payloads of the pendulums, denoted by m_0 and m_1 and the two IP masses, denoted by u_0 and u_1 . Therefore, the two stiffness components k_0 and k_1 represent the overall IP stiffness of the two stages and are a function of the overall flexure stiffness of each IP stage, k_{00} and k_{11} [78]:

$$k_0 = k_{00} - \sum_{i=0}^7 m_i \times \frac{g}{l_0} = \left(\sum_{i=0}^7 m_i + \frac{u_0}{2} + u_1 \right) \times \left(\frac{g}{l_0} + \omega_0^2 \right) - \sum_{i=0}^7 m_i \times \frac{g}{l_0}, \quad (3.14)$$

$$k_1 = k_{11} - \sum_{i=0}^7 m_i \times \frac{g}{l_1} = \left(\sum_{i=0}^7 m_i + \frac{u_1}{2} \right) \times \left(\frac{g}{l_1} + \omega_1^2 \right) - \sum_{i=0}^7 m_i \times \frac{g}{l_1}, \quad (3.15)$$

where g is the gravitational acceleration constant, ω_0 and ω_1 correspond to the two resonant frequencies of the IP stages, tuned to 0.07 Hz and 0.1 Hz respectively, and l_0 and l_1 are the lengths of the IP legs.

The horizontal stiffness of the filters with masses m_2 , m_3 and m_4 are expressed as:

$$k_n = \sum_{i=n}^7 m_i \times \frac{g}{l_n}. \quad (3.16)$$

The last three stiffness values, k_5 , k_7 and k_6 corresponding to the marionette, the reaction mass and the test mirror are expressed in terms of each elastic bending

stiffness k_e of the suspension fibres as in [78]:

$$k_n = \frac{m_n g}{l_n} + \frac{k_e}{l_n^2} = \frac{m_n g}{l_n} + \frac{\sqrt{\frac{N \pi Y m_n d_n^4}{64}}}{l_n^2}, \quad (3.17)$$

where n is the index which iterates through all three stages, N corresponds to the number of suspension wires per stage, Y is the young modulus, l_n the length of suspension fibres and d_n the diameter of each fibre. The mass for k_5 will be defined as $m_5 = m_5 + m_6$, since the test mass is suspended from the marionetta.

The mass and stiffness matrices for the horizontal motion of the full suspension system are represented by:

$$\mathbf{K} = \begin{pmatrix} k_0 + k_1 & -k_1 & 0 & 0 & 0 & 0 & 0 & 0 & 0 \\ -k_1 & k_1 + k_2 & -k_2 & 0 & 0 & 0 & 0 & 0 & 0 \\ 0 & -k_2 & k_2 + k_3 & -k_3 & 0 & 0 & 0 & 0 & 0 \\ 0 & 0 & -k_3 & k_3 + k_4 & -k_4 & 0 & 0 & 0 & 0 \\ 0 & 0 & 0 & -k_4 & k_4 + k_5 + k_7 & -k_5 & 0 & -k_7 & 0 \\ 0 & 0 & 0 & 0 & -k_5 & k_5 + k_6 & -k_6 & 0 & 0 \\ 0 & 0 & 0 & 0 & 0 & -k_6 & k_6 & 0 & 0 \\ 0 & 0 & 0 & 0 & -k_7 & 0 & 0 & 0 & k_7 \end{pmatrix},$$

$$\mathbf{M} = \begin{pmatrix} m_0 + (u_0 + u_1) / 3 & u_1 / 6 & 0 & 0 & 0 & 0 & 0 & 0 & 0 \\ u_1 / 6 & (m_1 + u_1) / 3 & 0 & 0 & 0 & 0 & 0 & 0 & 0 \\ 0 & 0 & m_2 & 0 & 0 & 0 & 0 & 0 & 0 \\ 0 & 0 & 0 & m_3 & 0 & 0 & 0 & 0 & 0 \\ 0 & 0 & 0 & 0 & 0 & m_4 & 0 & 0 & 0 \\ 0 & 0 & 0 & 0 & 0 & 0 & m_5 & 0 & 0 \\ 0 & 0 & 0 & 0 & 0 & 0 & 0 & m_6 & 0 \\ 0 & 0 & 0 & 0 & 0 & 0 & 0 & 0 & m_7 \end{pmatrix}.$$

The vertical stiffness components are split in two categories: the stiffness of the filters containing geometric anti-spring (GAS) filters, m_1 and m_4 , tuned to the resonance frequency of the GAS filters $\omega_0 = 1.5$ rad/s, and the bouncing mode stiffness of the reaction mass and the mirror, k_6 and k_7 . The stiffness of the gas filters is defined as:

$$k_n = \sum_{i=0}^6 m_i \times \omega_0^2, \quad (3.18)$$

and the bouncing mode stiffness is defined as:

$$k_n = \frac{0.25 \pi d_n^2}{l_n}, \quad (3.19)$$

where d_n is the diameter of the suspension fibres and l_n their length. Therefore, the mass and stiffness matrices for the full suspension system in vertical degree of freedom can be assembled as:

$$\mathbf{K} = \begin{pmatrix} k_2 + k_3 & -k_3 & 0 & 0 & 0 & 0 \\ -k_3 & k_3 + k_4 & -k_4 & 0 & 0 & 0 \\ 0 & -k_4 & k_4 + k_5 + k_7 & -k_5 & 0 & -k_7 \\ 0 & 0 & -k_5 & k_5 + k_6 & -k_6 & 0 \\ 0 & 0 & 0 & -k_6 & k_6 & 0 \\ 0 & 0 & -k_7 & 0 & 0 & k_7 \end{pmatrix},$$

$$\mathbf{M} = \begin{pmatrix} m_0 + (u_2 + u_3) / 3 & u_3 / 6 & 0 & 0 & 0 & 0 \\ u_3 / 6 & m_3 + (u_3 + u_4) / 3 & u_4 / 6 & 0 & 0 & 0 \\ 0 & u_4 / 6 & m_4 + (u_4 + u_5) / 3 & u_5 / 6 & 0 & 0 \\ 0 & 0 & u_5 / 6 & m_5 + u_5 / 3 & 0 & 0 \\ 0 & 0 & 0 & 0 & m_6 & 0 \\ 0 & 0 & 0 & 0 & 0 & m_7 \end{pmatrix}.$$

In the equation above, the terms μ_x with x between 2 and 5 are the masses of the cantilever blades for each vertical filter stage, ranging from μ_2 the mass of the top filter blade to μ_5 the mass of the bottom filter blade. The blade masses are defined as:

$$u_x = \sum_{i=x}^7 m_i \times \frac{1}{40}, \quad (3.20)$$

where m_i corresponds to each rigid body mass suspended under the load of the cantilever blades in each filter stage, starting with the mass body having the same index as the filter blade and summing up to seven total rigid bodies. There is one exception to Equation 3.20 and that is for the bottom filter $\mu_5 = \frac{m_5 + m_6}{40}$ since three wires clamped on the side of the filter body suspend the payload reaction chain and this is not under the load of the cantilever blades. The term 40 defines the mass ratio between the blades and the loads and represents a design choice.

In both degrees of freedom, the damping matrix is set to zero, while the \mathbf{C} matrix equals the unity matrix. The full set of parameters which enters the calculation of the transfer function are shown in Table 3.1. The resulting transfer function $TF(f)$ are shown in Figure 3.10.

Results

The displacement amplitude spectral density of the seismic noise $S_s(f)$ can be calculated using the seismic spectral data $S(f)$ for the cumulative horizontal direction and the vertical one, and the transfer function previously calculated $TF(f)$ as:

$$S_s(f) = S(f) \times TF(f) \times 2, \quad (3.21)$$

where the factor 2 accounts for the uncorrelated effect of four test masses in the power spectral density. The result of the seismic noise can be seen in Figure 3.11. The 0.1% coupling of vertical degree-of-freedom to horizontal is assumed as before.

Masses	Number of fibres N	Lengths	Fibre diameter
$\mu_0 = 48$ kg	NA	4 m	NA
$\mu_1 = 0.8$ kg	NA	0.5 m	NA
$m_0 = 600$ kg	NA	NA	NA
$m_1 = 30$ kg	NA	NA	NA
$m_2 = 20$ kg	NA	1.2 m	NA
$m_3 = 20$ kg	NA	0.8 m	NA
$m_4 = 20$ kg	NA	0.9 m	NA
$m_5 = 10$ kg	1	0.6 m	8×10^{-4} m
$m_6 = 3.2$ kg	4	0.4 m	150×10^{-6} m
$m_7 = 9.5$ kg	3	0.6 m	600×10^{-6} m

Table 3.1: Parameters defining the suspension chain of ETpathfinder and used in the calculation of the suspension transfer function. In the real setup, the filter bodies (masses m_1 to m_4) are suspended via a single suspension fibre at their centre, but since their vertical modes are only modelled based on the preset value of the GAS filter resonance, the wires are disregarded from the current simulation.

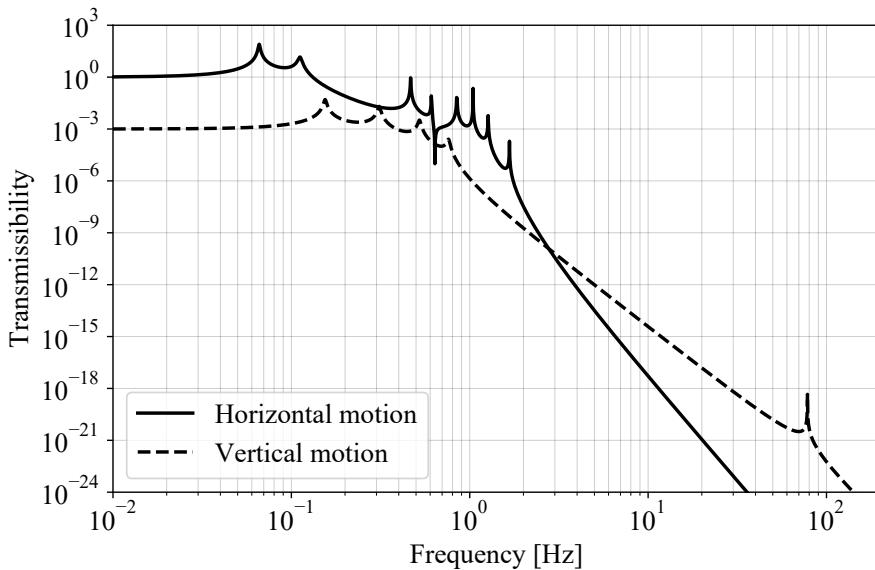


Figure 3.10: Mechanical transfer function for the ETpathfinder suspension system in two degrees-of-freedom. The magnitude of the transfer function has a roll-off proportional to $1/f^{14}$ after the last horizontal resonance frequency, while the vertical transfer function has a roll-off proportional to $1/f^{10}$ after the vertical mode of the test mass at 79 Hz.

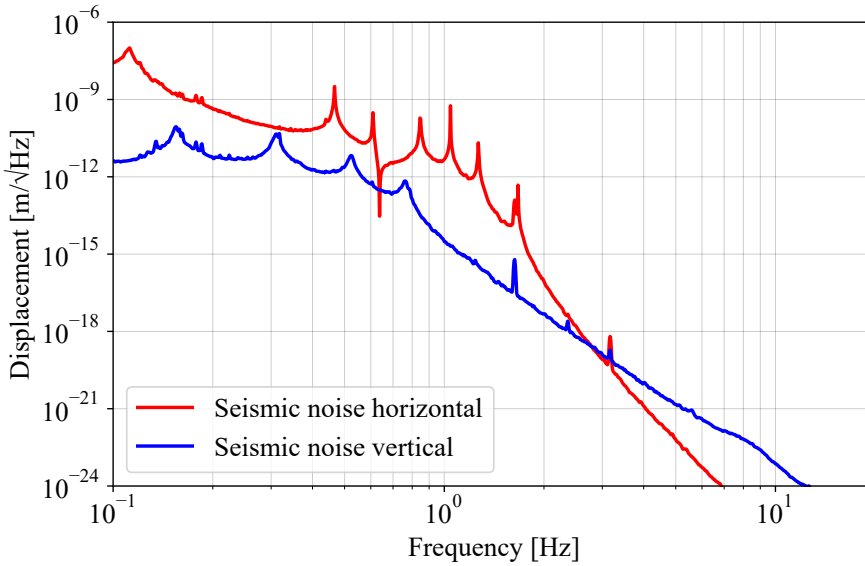


Figure 3.11: Displacement spectral density of seismic noise for two degrees-of-freedom in ETpathfinder.

It can be seen that the seismic noise is strongly suppressed by the vibration attenuation system with the displacement falling below $1 \times 10^{-22} \text{ m}/\sqrt{\text{Hz}}$ at 10 Hz. This will allow ETpathfinder to test fundamental noise sources at low frequencies, such as quantum noise, but also technical noises associated to novel cryogenic and control techniques which will be developed.

3.3.3 Thermal displacement noises

Thermal effects in the substrates and coatings of the optical test masses, as well as thermal effects in the isolation suspension systems, cause displacement fluctuations. All these displacement noises can be expressed using the fluctuation-dissipation theorem, which relates the amount of fluctuation at the test mass surface to the dissipation in the system [57]. It can be expressed mathematically as:

$$S(f) = \frac{k_B T}{\pi^2 f^2} \text{Re}[Z(f)^{-1}], \quad (3.22)$$

where $S(f)$ is the power spectral density of the fluctuations in any degree of freedom for each frequency f , k_B is the Boltzmann constant, T is the temperature of the mass and $Z(f)$ is the complex impedance of the system, or the inverse of the mechanical admittance.

Coating Brownian noise

The coating Brownian noise is caused by the thermal motions of individual atoms in the coating of the test mirrors. A simplified mathematical expression of the spectral density fluctuation, $S_x(f)$, is given by [79]:

$$S_x(f) = \frac{2k_B T}{\pi^2 f} \frac{d}{w^2} \phi \left(\frac{Y_{\text{coat}}}{Y_{\text{sub}}^2} + \frac{1}{Y_{\text{coat}}} \right). \quad (3.23)$$

Here, T is the coating temperature, w is the beam radius at the coating, ϕ is the mechanical loss angle of the coating, d is the coating thickness and Y_{coat} , Y_{sub} being the Young's modulus of the coating material and substrate respectively.

The baseline thermal noise model for ETpathfinder, shown as the red curve in Figure 3.12 for ETpathfinder-A configuration, uses coating materials with excellent optical properties: silica, SiO_2 , as a low-refractive index material and tantala, Ta_2O_5 , as a high-refractive index material. For these materials, the coatings produced by LMA* via ion beam sputtering obtained optical absorptions as low as a quarter of a ppm [80].

Both SiO_2 and Ta_2O_5 have been characterized extensively for their use in gravitational-wave observatories. At room temperatures, tantala shows a low mechanical loss of 2.3×10^{-4} [81], while silica measures a mechanical loss as low as 0.46×10^{-4} [82]. Both materials show an increase in mechanical loss angles at low temperatures. The mechanical losses entering the baseline calculation of the coating Brownian noise are shown in Appendix C, Table 1. Using these low-temperature mechanical losses, the displacement sensitivity to coating thermal noise from Figure 3.12 results. The coating thermal noise is dominant over a wide frequency band between 40 Hz and 2 kHz.

While the standard approach of using well-studied coating materials in the sensitivity model shows ETpathfinder as an interesting experimental setup for this noise source, it is also valuable to test other materials or concepts explored within the gravitational-wave community but not yet implemented in any detector. Such options are presented in Figure 3.12 with respect to the baseline noise model.

One such option is given by amorphous silicon (aSi). This is a material with low mechanical loss [83, 84, 64] and high refractive index of $n > 3.5$. Therefore, the coating composition of aSi, as a high-reflectivity material together with SiO_2 , requires fewer and thinner coating layers to achieve high reflectivity. As a consequence, the coating thermal noise is reduced and results in the pink line from Figure 3.12. This noise level is dominated by the coating thermal noise of the SiO_2 layers. The optical absorption hinders the application of aSi in gravitational-wave detectors. The lowest absorption measured to date corresponds to 7.6 ppm for an SiO_2/aSi coating with a high reflectivity at 1550 nm [84]. This is certainly still too high for the Einstein

*Laboratoire des Matériaux Avancés, Lyon

Telescope to utilize aSi. Although it may be a reasonable amount of absorption for ETpathfinder, such a low degree of absorption has only been achieved in R&D and is not yet reproducible. Even though commercially available aSi may still exhibit too high absorption for ETpathfinder [64, 85], investigating this coating material with ETpathfinder would be a significant step forward for coating research in the gravitational-wave community.

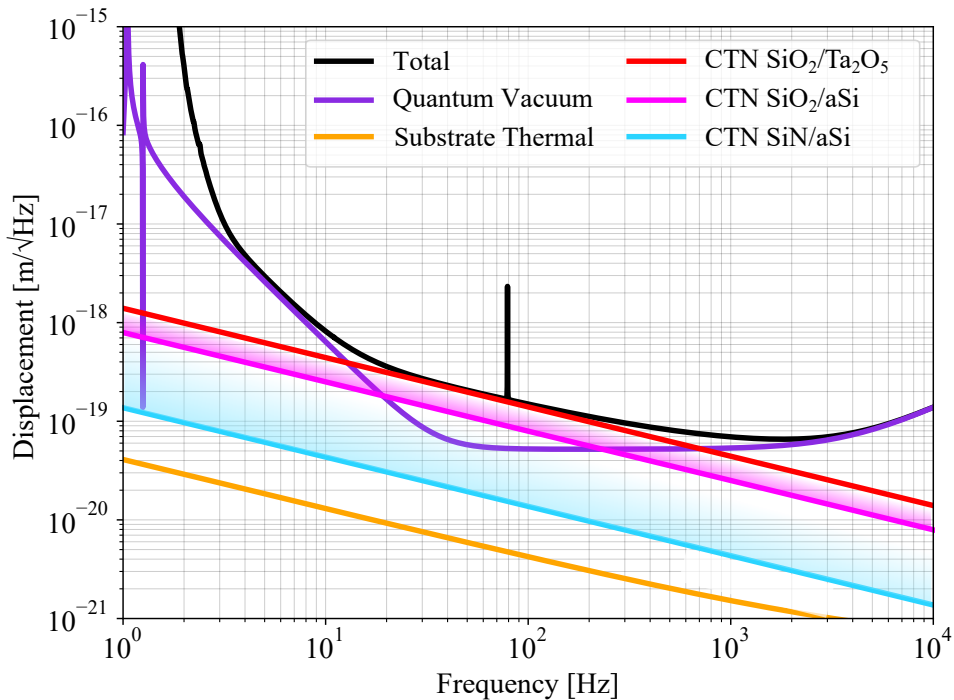


Figure 3.12: The displacement spectral density of coating Brownian noise. Shown are the coating thermal noise (CTN), and the total noise and quantum noise for comparison. Substrate thermal noise is also shown as another mirror-based noise source. While the red line shows CTN for conventional $\text{SiO}_2/\text{Ta}_2\text{O}_5$ coatings, the pink line shows CTN for coatings with the same reflectivity, but using aSi instead of Ta_2O_5 . The blue line shows CTN for coatings made of aSi and SiN_x . The shaded areas indicate the range of CTN when using multi-material designs for absorption reduction.

Another interesting coating material to be investigated in ETpathfinder is silicon nitride (SiN_x), which demonstrates a low mechanical loss, but also comes with similar absorption limitations as aSi [86, 87, 88]. The refractive index of SiN_x is similar to that of Ta_2O_5 , but this depends on the deposition method used and exact stoichiometry. Therefore, silicon nitride can serve as a low-refractive index material in stacks with aSi, or as a high-refractive index material together with SiO_2 . The first option produces a very low coating thermal noise as the one given by the solid blue curve in Figure 3.12.

Multimaterial coatings can be investigated for ETpathfinder in order to prevent excessive absorption levels and to test an innovative concept that may prove useful for future gravitational-wave detectors. These coatings contain a few layer pairs of low-absorption materials that reflect most of the laser light, such as $\text{SiO}_2/\text{Ta}_2\text{O}_5$, before materials with higher absorption and low mechanical losses, such as SiN_x or aSi, are exposed to the radiation [89, 90, 91]. Such options can result in a thermal noise indicated by the pink and blue shades of Figure 3.12.

Substrate Thermal noises

The substrate thermal noises arise as a result of different thermal effects in the bulk of the test mass material. In this study, since the temperature-dependent parameters for silicon are generally well studied in the literature, three different types of substrate thermal noise sources are modelled: *substrate Brownian noise*, *the substrate thermo-elastic noise* and *the ITM thermo-refractive noise*.

Substrate Brownian noise

The substrate Brownian noise is associated with the Brownian fluctuations of molecules in the substrate material. The spectral density of the noise $S_x(f)$ is calculated using Levin's direct approach, developed by Bondu et al. as:

$$S_x(f) = \frac{2k_B T}{\sqrt{\pi^3} f} \frac{1 - \sigma^2}{Y_w} \phi_{\text{substrate}}(f, T). \quad (3.24)$$

Here σ is the Poisson ratio of the material, Y is the Young modulus and $\phi_{\text{substrate}}$ is the substrate loss angle. Finite test mass corrections to the thermo-elastic and Brownian noises were derived by Liu and Thorne [92] and are applied to the current calculations inside pygwinc [93].

ITM thermo-refractive noise

Thermo-refractive noise is the change in optical path length caused by fluctuations in the refractive index of the test mass as a result of random fluctuations in the temperature of the refracting substance. This phase noise is transmitted through the ITMs into the arm cavities, degrading the sensitivity of the differential measurement. The power spectral density of ITM thermo-refractive noise $S^{\delta z}(f)$ is estimated from the exact series expansion as [94]:

$$S^{\delta z}(f) = \frac{a\beta^2 k_B T^2}{2\pi\kappa} \times (e^{it} E_1(it) + e^{-it} E_1(-it)). \quad (3.25)$$

Here $\beta = \partial n / \partial T$, with n being the material refractive index, is the thermo-optic coefficient, k_B is the Boltzmann constant, T is the substrate temperature, a is the

test mass thickness and κ is the thermal conductivity of the substrate material. The term t here is defined as $t = \frac{2\pi f w^2 \rho C}{2\kappa}$. Inside this term, w is the laser beam size on the substrate surface, ρ is the density of the material and C is the specific heat. The functions $E_1(x)$ are exponential integrals which equal $E_1(x) = \int_x^\infty e^{-xy} y^{-1} dy$. For the effect on both ITMs, the noise is then projected to the differential arm-length signal as $S_{\text{DARM}}^{\delta z}(f) = S^{\delta z}(f) \times \frac{\pi}{F}$, with F being the arm cavity finesse value.

Substrate thermo-elastic noise

The time-averaged power dissipated by the laser beam into the material surface generates a temperature gradient that causes the substrate to deform due to the thermal expansion coefficient. This noise source was initially investigated by Braginsky *et al* [95] and is known as the BGV formulation. In the BGV treatment, the substrate volume involved in the fluctuations is approximated as being of the order of the thermal diffusion length, a function of material thermal conductivity κ , its density ρ and specific heat C for the characteristic time $1/f$: $\sqrt{\frac{\kappa}{\rho C f}}$.

The BGV treatment is a good approximation for room temperature and large beam spot sizes at the mirror, but corrections must be implemented in the opposite regime, when the adiabatic approximation is not satisfied. For low temperatures and small beam sizes hitting the silicon mirrors of the ETpahfinder, a clear departure from the BGV approximation is observed. At 18 K temperature, the thermal diffusion length at 10 Hz is about two orders of magnitude higher than the beam dimension at the test mass. Moreover, at the same measurement frequency and 123 K temperature, the diffusion length is about a factor of two higher. Therefore, the full series solution from [96] is implemented here with the spectral density of the displacement noise can be estimated as :

$$S_{\text{TE}}(f) = \frac{8}{\sqrt{2\pi}} \alpha^2 (1 + \sigma)^2 \frac{k_B T^2 w}{\rho C a^2} J[\Omega], \quad (3.26)$$

with $J[\Omega]$ being defined as:

$$J[\Omega] = \sqrt{\frac{2}{\pi}} \int_0^\infty du \int_{-\infty}^\infty dv \frac{u^3 e^{-u^2/2}}{(u^2 + v^2) \left((u^2 + v^2)^2 + \Omega^2 \right)}, \quad (3.27)$$

where C is the specific heat of the material, α is the coefficient of linear expansion, ρ is the density of the substrate, w is the beam radius at the test mass and $a = \sqrt{w^2 \cdot \omega_c}$ with ω_c being the angular frequency of the adiabatic limit given by $\omega_c = \frac{\kappa}{\rho C w^2}$.

The simulation of the substrate thermal noises is performed with the parameters shown in Table 3.2. The results are shown in Figure 3.13. The thermo-refractive noise dominates the other substrate noises at 123 K. This is due to the combination of a small beam radius at the substrate and the large value of the thermo-refractive coefficient $\beta = \partial n / \partial T$ of $1 \times 10^{-4} \text{ K}^{-1}$ at 123 K [97]. However, at lower temperatures,

because of vanishingly small linear expansion coefficient and a thermo-refractive coefficient of the order of 10^{-6} , the substrate thermal effects have negligible noise contributions to the total sensitivity curve.

Parameter	ETpathfinder-A	ETpathfinder-B
Temperature [K]	18	123
Beam waist [m]	1.8×10^{-3}	2.1×10^{-3}
Beam radius at test mass [m]	2.2×10^{-3}	2.5×10^{-3}
Substrate Young modulus [Pa]	162.0×10^9	155.8×10^9
Substrate thermal conductivity [W/(m·K)]	3000	700
Thermal expansion coefficient [1/K]	1×10^{-9}	1×10^{-9}
Substrate specific heat [J/(kg·K)]	3.5	333.0
Thermo-optic coefficient [1/K]	1×10^{-6}	1×10^{-4}
Substrate loss angle	1.25×10^{-9}	1.25×10^{-9}

Table 3.2: Summary of the most important parameters for both ETpathfinder interferometers at two different temperatures when estimating the substrate thermal noises.

Suspension thermal noise

As a result of mechanical dissipation, viscous damping, or inelastic behavior, the pendulums of the cascaded suspension structures fluctuate thermally. Thermal noise in suspension systems is expressed using the fluctuation-dissipation theorem. To perform the calculation, two variables must be defined. The first variable is the mass admittance and the second one is the introduction of the inelastic oscillatory regime [98].

The admittance $Y(f)$ can be defined in the fluctuation-dissipation theorem as follows:

$$Y(f) = Z(f)^{-1} = \frac{v(f)}{F_{\text{thermal}}} = \frac{2\pi i f x(f)}{F_{\text{thermal}}}. \quad (3.28)$$

Here $Z(f)$ is the mechanical impedance of the system, F_{thermal} corresponds to the thermal driving force and $v(f)$ is the resulting velocity, derivative of the readout variable $x(f)$.

For a suspended pendulum, the driving force producing the harmonic oscillation can be understood as a Langevin stochastic force on the body. Therefore, the force response $\frac{x(f)}{F_{\text{thermal}}}$ is estimated by the transfer function formalism presented in the Section 3.3.2. The present calculation takes into account not only the horizontal force response, but also the vertical response, which creates a dominant factor in the noise. This is allowed, since the impedance formulation from the fluctuation-dissipation theorem characterises a system for a superposition of eigenstates [57]. A complete description of this noise, similar to the seismic noise, can be given if the suspension

transfer function is modelled in six degrees-of-freedom, similar to work done in LIGO [99] and VIRGO [77].

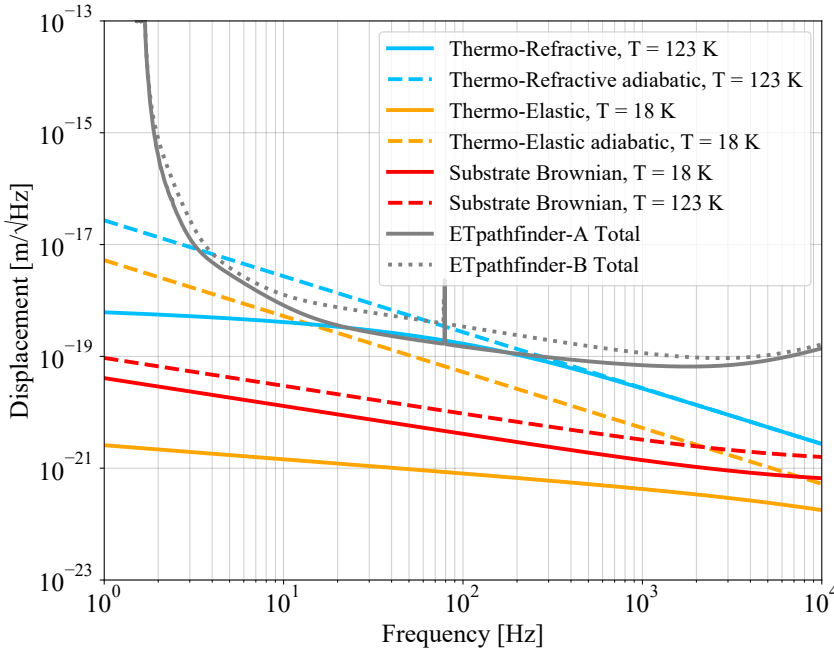


Figure 3.13: Substrate thermal noises for two different temperatures. Displacement noises due to the ITM thermo-refractive effect and the substrate thermo-elastic noise when deviate from the adiabatic approximation are also shown. A substantial noise reduction is observed at frequencies below the adiabatic limit ω_c . For silicon, ω_c increases with decreasing temperature as the thermal conductivity maintains high values while the specific heat of the material sharply decreases.

Anelasticity is the system attribute responsible for energy loss. This is incorporated in a trivial manner by describing the suspension wire's stiffness as a complex element in the frequency domain:

$$k \rightarrow k_{\text{spring}}(1 + i\phi). \quad (3.29)$$

Here ϕ expresses the phase angle in radians for which the response $x(f)$ lags behind the driving force F_{thermal} . It is the structural loss angle encountered in the definition of thermal noises described earlier and known to be constant with frequency [98, 100].

In the initial phase of the ETpathfinder, the silicon test masses will be suspended by Copper Beryllium (CuBe) fibres which are suitable for their low surface thermoelastic dissipation at 123 K. Their diameter is designed for a tensile strength about a third of the yield strength of the material which is about 1.2 GPa. Additionally, in the later stages of the project, ETpathfinder will integrate silicon suspension fibres or

ribbons. Their design is driven by the material strength and the thermal conductive power required. We consider 80 MPa to be the minimum yield strength of silicon suspension fibres [101]. In Figure 3.14, the baseline thermal noise curve is shown, together with silicon suspension estimates at two different temperatures. The relevant parameters are shown in Table 3.3.

Parameter	Material	Loss angle	Length [m]	Fibre diameter [m]
Marionetta wire	Ti grade 5	10^{-5}	0.6	8×10^{-4}
Test mass wire 1	CuBe	10^{-5}	0.4	150×10^{-6}
Test mass wire 2	Si	10^{-9}	0.4	7×10^{-4}

Table 3.3: Suspension fibres characteristic parameters. All the values correspond to 123 K temperature. For the silicon fibres at 123 K, the values are assumed the same as for the 18 K ones, designed for conductive cooling capability.

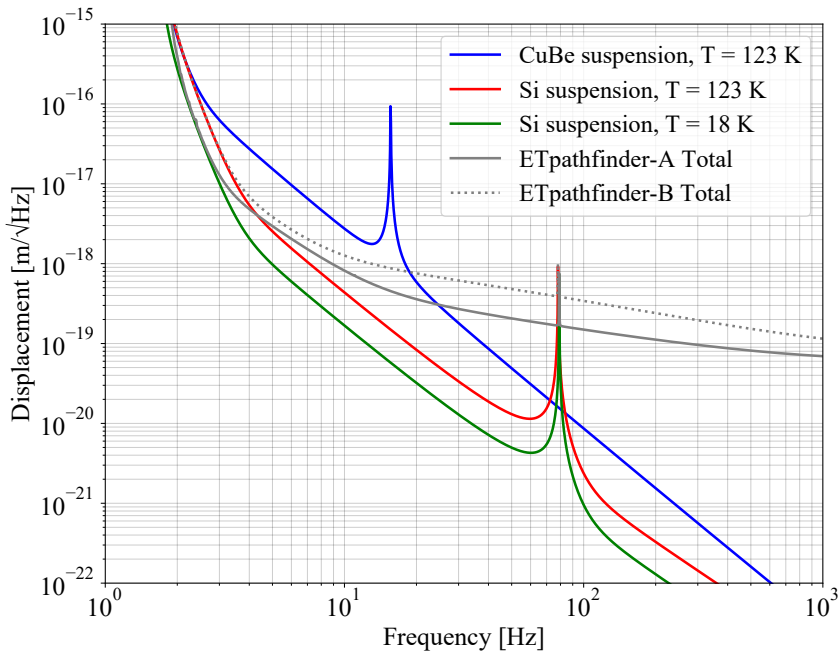


Figure 3.14: Amplitude spectral density of the suspension thermal noise for different last stage suspension wires and temperatures. The two resonances at 17 Hz and 79 Hz correspond to the vertical bounce mode of the mirror for each suspension fibre diameter. With lower mechanical dissipation, silicon suspensions provide a five-fold broadband improvement in the suspension thermal noise. Reducing the temperature from 123 K to 18 K, there is a decrease in the noise by a factor $\sqrt{\frac{123}{18}}$.

3.3.4 Newtonian noise

The test mass is subject to gravitational forces from either stationary or moving mass-density oscillations. This noise source is referred to as Newtonian noise, which is also known as gravity-gradient noise or terrestrial gravity noise. It was recognized since the beginning of the field, with some important work being developed early on [102, 13]. In this thesis, the Newtonian noise is estimated using the formalism shown in [103], which was developed based on previous work showing that the dominant contribution to Newtonian noise is generated by the seismic surface Rayleigh waves [104, 105]. The displacement spectral density is therefore estimated using the ambient seismic measurement in the vertical axis, $S_v(f)$, described in Section 3.3.2. ETpathfinder is distinguished by its short arm lengths and folded interferometer topology, which locates similar test masses in close proximity to one another. In this instance, the seismic wavelength exceeds the separation between adjacent test masses. As a result, the test masses move in phase in response to passing Rayleigh waves, which greatly suppresses the gravity-gradient impact of the interferometer's differential measurement.

The power spectral density of differential acceleration, $S_{nn}(f)$, propagating along the arm-length L , defined by the x axis, is estimated as:

$$S_{nn}(f) = (2\pi G\rho_0 e^{-hk_\rho} \gamma(v))^2 \times \frac{1}{2} \times S_v(f) \times \begin{bmatrix} 1 - 2J_0(k_\rho L) + 2J_1(k_\rho L)/(\rho L) \\ 1 - 2J_1(k_\rho L)/(\rho L) \\ 2 - 2J_0(k_\rho L) \end{bmatrix}. \quad (3.30)$$

Here G is the gravitational constant, ρ_0 is the density of the ground which is assumed to be 1800 kg/m^3 . The height above ground h is 1.2 m. The term $k_\rho = \frac{2\pi f}{c}$ requires knowledge about the Rayleigh wave speed c . A generally good approximation of c is 200 m/s, similar to the measurements performed at the LIGO Livingston site [106]. The term $\gamma(v)$ is related to the dispersive properties of the site's ground and it is set to 0.8 here. The equations in the bracket correspond to three directional averaged response terms where $J_n(x)$ is a Bessel function of order n .

Under the assumption that the seismic field is isotropic, each acceleration component of Equation 3.30 becomes independent at a point measurement. It is therefore possible to assume that two orthogonal correlations can be introduced by multiplying the two acceleration components, in the x and y directions, with a simple estimate of the Newtonian noise assuming no correlations. Thus, the x term in Equation 3.30 assumes an effective length L of 9.2 m and the y term assumes an effective length of 0.45 m, which is the distance between the two center of masses of adjacent input or end mirrors.

The estimate of the displacement spectral density across the full interferometer with a double correlated effect is then calculated as:

$$S_{nn}^{i,fo}(f) = \frac{\sqrt{S_{nn}(f) \times 2}}{(2\pi f)^2}. \quad (3.31)$$

The results are shown in Figure 3.15. Compared to the estimate of the Newtonian noise for singular test masses, the calculation using orthogonal correlations strongly suppresses the displacement level. However, depending on the measurement duration, the variation in seismic activity and possible anisotropies in the propagating field, the resulting Newtonian noise will most probably lie between the two estimates shown. This will not affect the target displacement sensitivity at lower frequencies.

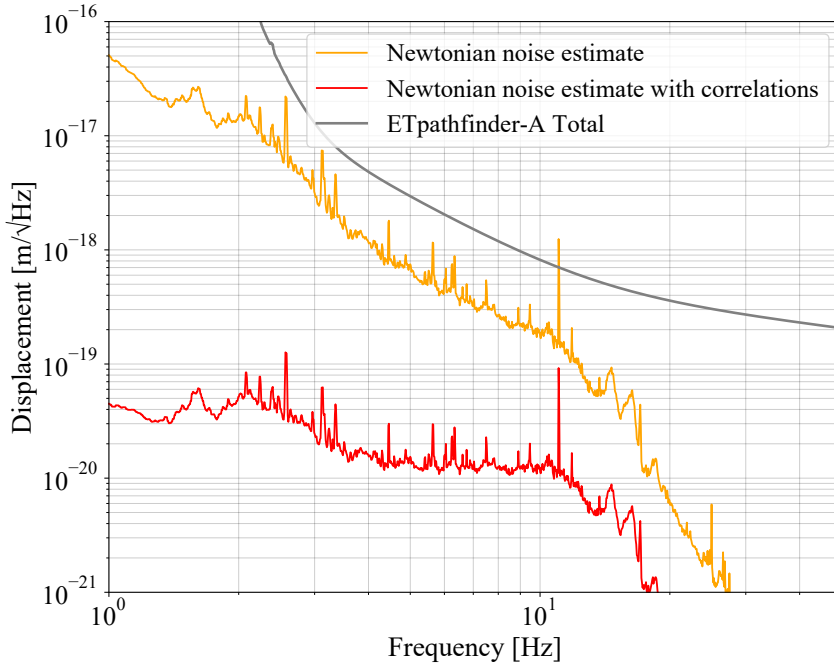


Figure 3.15: The amplitude spectral density of the Newtonian noise. By adding the simple seismic correlations, both across the arm-length and orthogonal to the adjacent test masses, a substantial suppression of noise is obtained.

3.3.5 Residual gas noise

The residual gas noise source is determined by a combination of the arm-length gas scattering noise and the test mass gas damping noise. Statistical fluctuations in the gas column density across the interferometer beam tube result in molecule interaction with the laser field, leading to optical path fluctuations that might obscure the required readout signal [107]. The power spectral density of the gas scattering noise takes the form as in [108]:

$$S_L(f) = \frac{4\rho(2\pi\alpha)^2}{v_0} \int_0^L \frac{\exp[-2\pi f w(z)/v_0]}{w(z)} dz. \quad (3.32)$$

Here, ρ is the gas number density for each molecular species, α is the polarizability, $v_0 = \sqrt{\frac{2k_bT}{m}}$ is the molecule's most probable velocity, L is the arm-length and $w(z)$ is the Gaussian beam radius.

The residual damping noise takes effect in the proximity of the test masses. At the end of the arms, the free test masses exchange momentum with the residual particles resulting in a transitional damping coefficient β_{tr} , proportional to the gas column pressure p [109]. The FD theorem then relates the damping coefficient with the corresponding power spectrum of the Brownian noise:

$$S_{dn}(f) = 4k_bT\beta_{tr}. \quad (3.33)$$

The proximity-enhanced gas damping takes into account the nearby surfaces to the test mass which can amplify the particle flux hitting its surface [110]. This is not considered in the present calculation, since the current design of ETpathfinder payload system assumes no additional hardware parallel to the test mass surface.

Figure 3.16 shows the two residual gas effects for different molecular species. The associated pressures for each molecule are taken from the acceptance tests of one of the vacuum tube sections and the first delivered vacuum tower. These are presented in Table 3.4.

Molecule	Bench tower pressure [Pa]	Beam tube pressure [Pa]
H ₂	1.2×10^{-6}	3.8×10^{-7}
N ₂	4.0×10^{-7}	1.2×10^{-7}
H ₂ O	1.1×10^{-6}	3.3×10^{-7}
O ₂	5.8×10^{-8}	7.0×10^{-9}

Table 3.4: Molecular species characteristic pressures extracted from the the residual gas analyser acceptance tests of the first delivered vacuum tower and the first beam tube section.

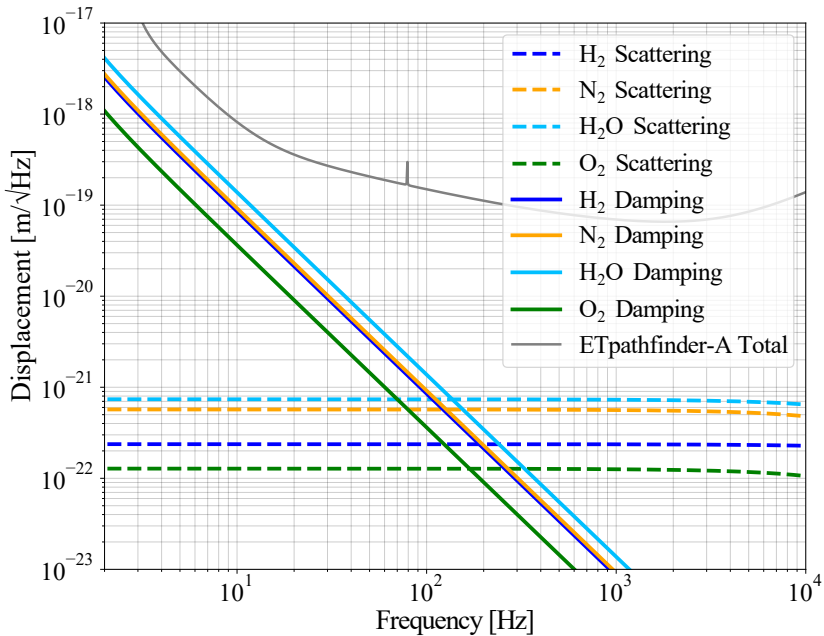


Figure 3.16: Displacement spectral densities of the gas damping noise and the gas scattering noise for different molecular species. The combination of high polarizability and partial vacuum pressures makes H₂O excess gas noises spectrum dominate. Even though the small beam radius is strongly affected by residual scattering, the noise effect is integrated over a very short arm-length and does not constitute a limiting factor.

3.4 Outlook

ETpathfinder aims to reduce all fundamental noise sources to a level below $1 \times 10^{-18} \text{ m}/\sqrt{\text{Hz}}$ at 10 Hz for the interferometer operating at 1550 nm and at 18 K. With the noise sources simulated so far, the ETpathfinder fundamental noise budgets are assembled and depicted in Figure 3.17. It can be observed from the noise budget that the 2090 nm interferometer during operation using cryogenic silicon suspensions will be close to reaching the target. However, the 18 K interferometer at 1550 nm will be able to reach the low-noise sensitivity broadband.

As reaching this performance in a single step is very challenging, we first aim for an initial running phase with simplified mirror suspensions and a higher operating temperature of 123 K that allows for radiative instead of conductive cooling. This configuration, called ETpathfinder-Light, is presented in the Appendix C.

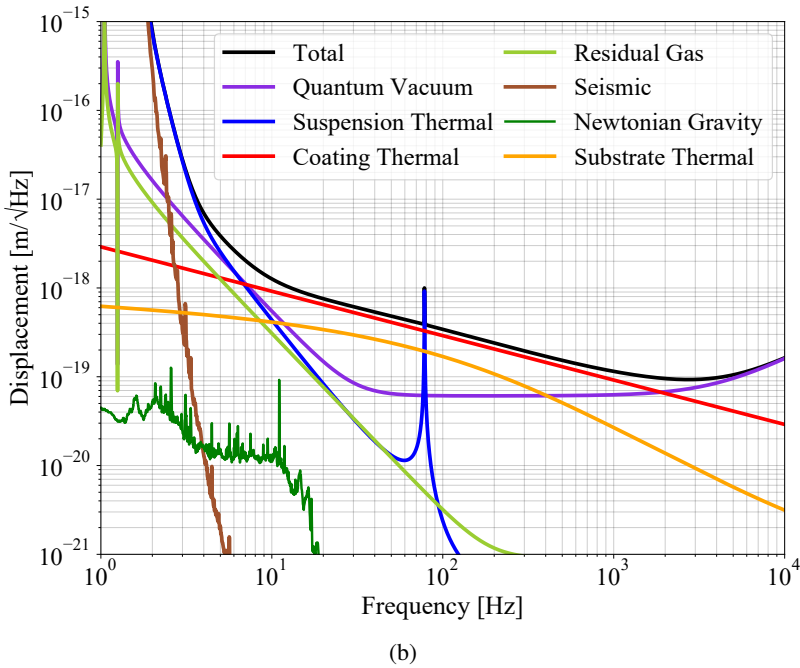
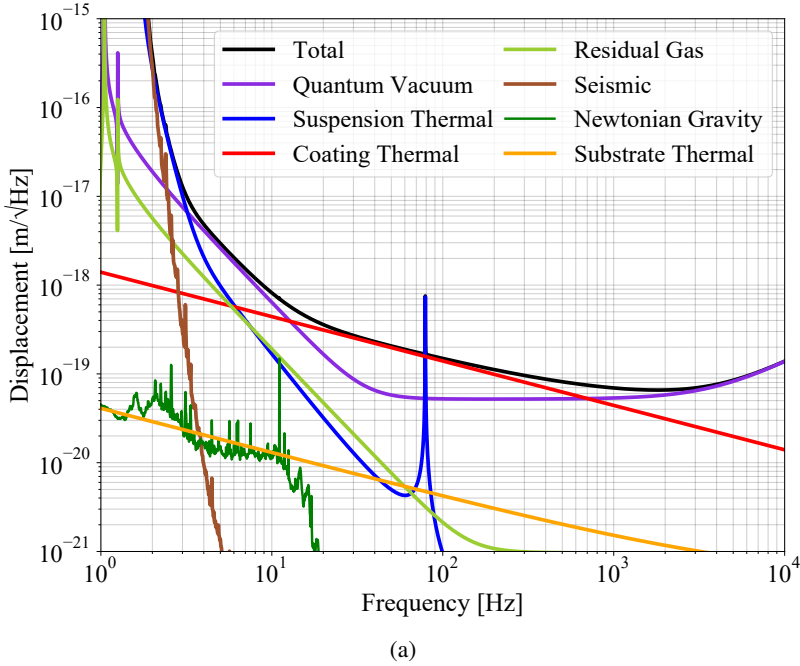


Figure 3.17: Projection of displacement sensitivity for the ETpathfinder operating at 1550 nm laser light and 18 K (a) and at 2090 nm and radiatively cooled down at 123 K (b).

3.5 Conclusions

ETpathfinder is a prototype interferometer that provides a one-of-a-kind testing environment for the technology necessary for future gravitational-wave detectors such as the Einstein Telescope and Cosmic Explorer. This chapter investigates the fundamental noise sources of the ETpathfinder facility for two targeted configurations, the first one having a laser wavelength of 1550 nm and an operating test mass temperature of 18 K and the second configuration with a 2090 nm laser and operating at 123 K temperature.

In the first running phase at 123 K, the displacement sensitivity of the interferometer will be limited by suspension thermal noise at low frequencies, coating thermal noise in middle band and shot noise at very high frequencies. At this temperature, the thermo-optic coefficient for crystalline silicon is high, and in combination with the very small beam diameters on the optics makes the ITM thermo-refractive noise dominate the middle sensitivity band. Therefore, this noise is reduced by increasing the arm-cavity finesse to 2050. This reduction allows the middle sensitivity band to be limited by the coating Brownian noise providing a testing ground directly linked to the limiting noise of the 3G detectors even at a transitory temperature of operation.

The integration of silicon suspension fibres helps reducing the suspension thermal noise broadband. This substantial improvement in sensitivity allows the ETpathfinder interferometer operating with 1550 nm laser light and below 20 K temperature to reach the target sensitivity of 1×10^{-18} m/ $\sqrt{\text{Hz}}$ at 10 Hz. Due to the thermo-elastic coefficient's infinitesimally small value, low substrate thermal noise at 18 K can also be attained. For precise projection of this noise source at extremely low temperatures and for smaller beam diameters on the test masses, the full series solution of the power spectrum estimation is utilized. The reduction leaves a significant gap with the coating Brownian noise.

The coating Brownian noise-limited sensitivity allows for the evaluation of various coating methods. Combining amorphous silicon and amorphous silicon nitride as a material with a low refractive index is an intriguing example of this. The coating's ensuing Brownian noise will be significantly decreased. Consequently, the overall displacement sensitivity would be essentially constrained only by the well-understood quantum-noise over a broad frequency band, allowing for the investigation and resolution of a variety of technical noise sources associated with the operation at cryogenic temperatures. The degree to which these noise sources are mitigated and the approaches adopted to do so have a direct impact on the technical design of 3G detector.

At a later stage of operation and depending on the outcome of the initial running phases, ETpathfinder will operate at a single temperature and laser wavelength. The test masses of this experimental phase will resemble the ET scale and will be integrated into single cryostats.

Analysis of vibration via cryogenic heat-links

4.1 Introduction

Current detectors of gravitational waves operating at room temperature use fused silica for their test masses. Thermal noise limits the displacement sensitivity of these detectors, both at low frequencies, where the next generation of detectors aims to enhance, and in their most sensitive band. Reducing the disturbances caused by thermal fluctuations is of utmost importance and will considerably boost the sensitivity of the interferometers and, therefore, their detection rate. The equipartition theorem states that lowering the temperature will decrease the overall thermal noise associated with the test mass and its coating structure. Consequently, the third generation (3G) of gravitational-wave detectors are intended to work at cryogenic temperatures.

Two target temperatures for the next generation detectors and operational temperatures for ETpathfinder are around 120 K and in between 10 K - 20 K. At 123 K and below 20 K the thermal expansion coefficient of silicon tends to zero, which reduces significantly the thermo-optic noise associated with the material expansion. The 120 K temperature will be reached via radiative cooling, which is efficient for cooling the test mass at higher temperatures. However, conduction cooling needs to be employed to reach below 20 K in a reasonable time and to maintain the system in thermal equilibrium.

The transfer of heat to a cold bath starts at the test mass via the suspension fibres. Silicon suspensions are ideal due to their steep increase in thermal conductivity between 1 K and 25 K [111]. The heat is then extracted from the intermediate suspension mass and the recoil mass via soft conductive heat-links which connect to auxiliary systems with low isolation. A schematic representation of the process

is illustrated in Figure 4.1. The links are designed as low-stiffness rods, usually of the highest purity aluminium to increase the thermal conductivity [112]. Since the heat-links are connected to the cryocoolers, large residual vibration noise can couple to the test mass displacement and degrade the interferometer sensitivity. As a result, the dynamical analysis and vibration transfer via the links must be scrutinized, which is what this chapter investigates.

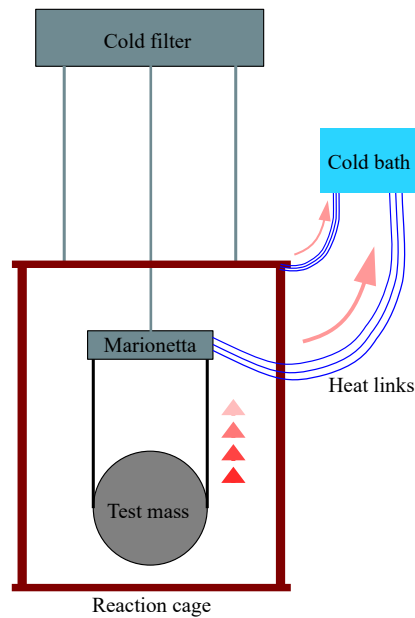


Figure 4.1: Simplified drawing showing the heat-extraction path from the suspended test mass in ETpathfinder. Conduction heat-links are attached to the reaction mass and the penultimate stage. The arrows in red indicate the heat flow from the test mass to the cold bath, which is a composite system connecting to the cryocoolers.

The ETpathfinder, as a facility that aims to demonstrate core technologies for future gravitational-wave detectors, is an ideal place to test different cryogenic technologies. A miniature suspension prototype, called Prototype 0 throughout this manuscript, was developed at Nikhef with manufacturing help from multiple ETpathfinder partners. The suspension prototype houses a payload system, similar to the first design iteration for the facility.

This chapter illustrates the experimental efforts to test the heat-links vibrational transmissibility and the validation of the analytical model describing the transfer function. The model is used to project residual seismic noise into the displacement sensitivity of the ETpathfinder operating at 18 K. The required amount of heat to be extracted from different stages of the cryogenic payload is driven by different interferometric configurations and the practical limitations of the cryogenic payload, which can potentially necessitate design modifications. Hence, this study presents

the foundational methodologies for conducting the aforementioned research which can be applied to mitigate the risk associated with the final design of ETpathfinder. Finally, the last part of the chapter presents conclusions and recommendations for the seismic isolation of the cryogenic link.

4.2 Prototype 0 test-setup

The prototype test suspension is designed to qualify the readiness of the payload system, to perform the vibration analysis on the cryogenic heat-links and to test the manoeuvrability of the entire assembly. The prototype can be also used to test and develop suspension control schemes since three levels of actuation are installed in the system. The assembly of the full prototype and the lead design was carried out by Rogier Elsinga at Nikhef. A realistic representation of the actual suspension is shown in Figure 4.2.

The test-setup for the experiment is represented by the two auxiliary suspended masses, the heat-link ring and the cold-finger ring. Each ring is suspended as a trifilar pendulum by Titanium wires. The experimental demonstration is carried out for the short heat-link connection between these two rings. A voice-coil actuator is suspended at the base of the cold-finger by an actuation pendulum, two accelerometers are mounted on the two pendulums and one accelerometer is mounted on the suspension rigid structure. A central signal analyzer unit performing the computational load is used for the measurements. The full experimental setup is shown in Figure 4.3.

The accelerometers are glued directly to the rings and they probe the acceleration of each body. Two accelerometers were used for the end-to-end transfer estimation. These are of the type *PCB 393B05* which enclose integrated micro-electronics. The micro-electronics convert a high-impedance charge signal generated by the inertial mass interacting with the piezoelectric crystal into a low-impedance voltage signal that can be sensed by the readout apparatus. The sensitivity of the *PCB 393B05* accelerometer and further technical details are illustrated in Appendix D.

A voice coil actuator excites the cold-finger which imprints momentum to the heat-link ring via the soft heat-links. The coil is double wound by 112 copper wire turns in opposite directions with a measured resistance of 6.8 Ohm. A closer examination of the magnetic field distribution and additional parameters are illustrated in Appendix E.

The data is being recorded via the *Keysight 35670A Dynamic Signal Analyzer* which is a superior apparatus for high-performance FFT-based calculations.

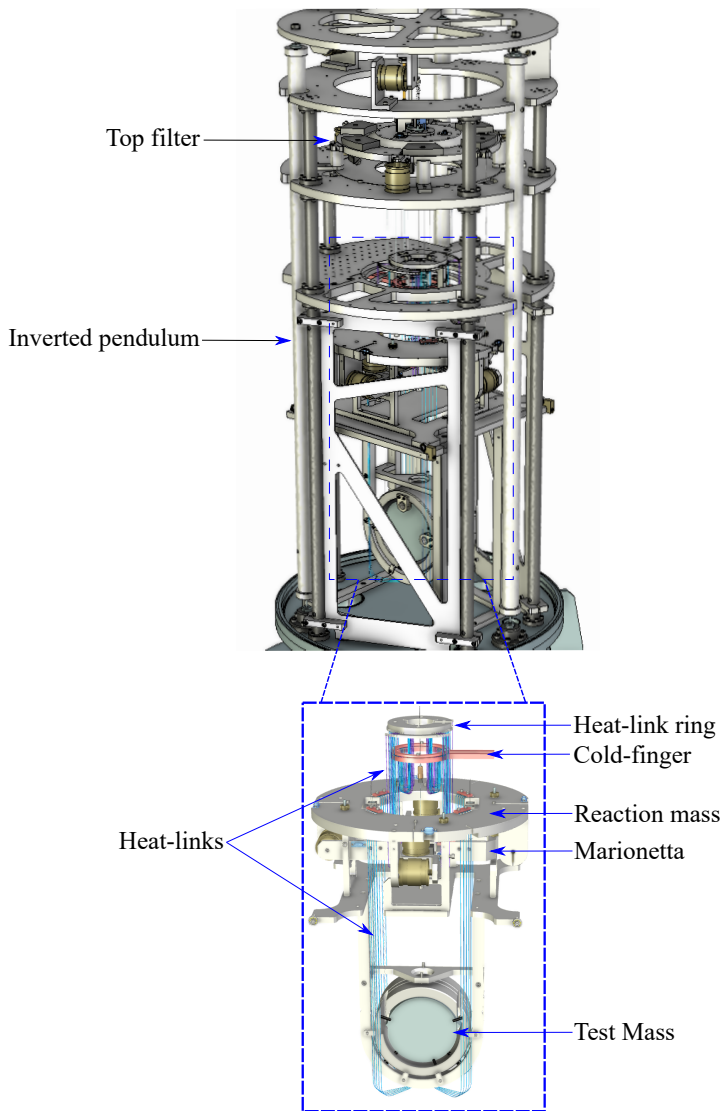


Figure 4.2: Three-dimensional CAD rendering of the Prototype 0 suspension and a focused representation of the initial payload system. The prototype suspension consists of an isolated stage by a set of three inverted pendulums, and a top-filter performing vertical isolation via geometric anti-springs and holding the payload stage. The payload is formed by the intermediate mass, called marionetta, and the test mass, together with two reaction masses used for actuation. The heat-link ring is suspended via the top filter while the cold-finger is suspended from the suspension rigid structure. Multiple heat-link connections are integrated in the system for the first conceptual design.

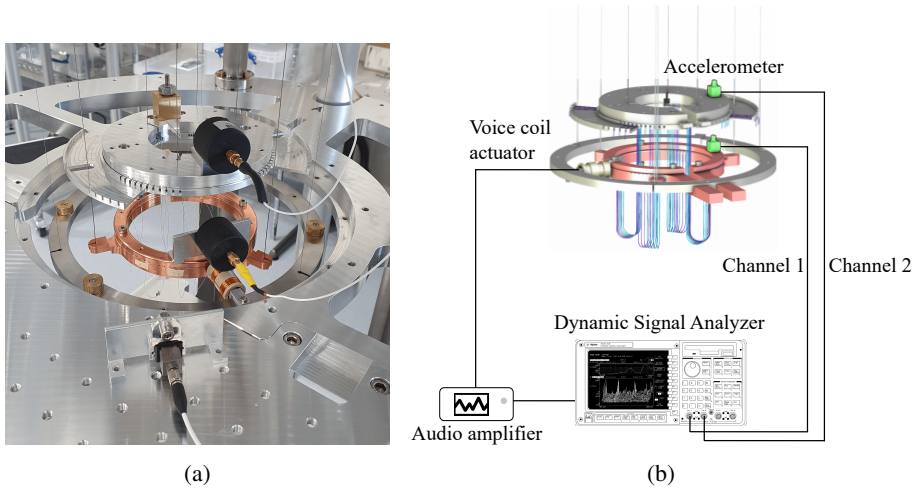


Figure 4.3: The measurement apparatus. Figure (a) shows a photograph of the actual setup during testing, while Figure (b) graphically illustrates the connections between all the components in the setup. An auxiliary accelerometer of the type *B&K DeltraTron 4508B 002* is mounted on the suspension cage to investigate coherent disturbances from exterior that can affect the transfer function.

4.3 Vibration transfer simulation

4.3.1 Heat-link geometry

To realistically capture the dynamics of the soft wires, a finite-element (FEM) analysis of the end-to-end transfer function was carried out by Eric Hennes at Nikhef. Furthermore, using the calculated stiffness from the FEM analysis, an analytical model was developed. The analytical model has a practical advantage: it can be integrated as a linear extension inside the rigid-body mechanical model for the entire suspension system of ETpathfinder.

While performing the FEM analysis, the geometrical model of the heat-link is constructed. This resembles closely the measured dimension of the short heat-links used in the tests. The geometrical representation can be seen in the illustration from Figure 4.4. There are two geometrical variants illustrated: the *Straight* model follows closely the initial CAD drawings while the *Curved* model shows a heat-link with a larger wire-loop to account for possible deformations during installation. Both models assume the same wire length of 0.28 m.

The FEM analysis model constructs a heat-link element by connecting parallel beams with circular sections. The beams are defined by a connecting angle and a radius of curvature. The elastic element is then placed between two suspended rings which resembles closely the test setup from Figure 4.3. To evaluate the spring constant of the elastic heat-link, the end connection point is fixed in all degrees of freedom, while the excitation end, where longitudinal and transverse to plane forces

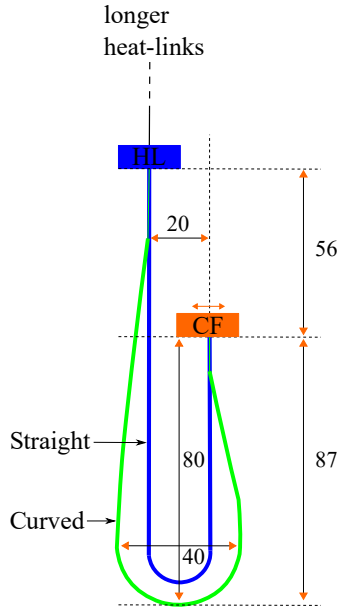


Figure 4.4: A geometrical illustration of the heat-link variants. The blue, straight, geometry corresponds to the initial CAD design while the green, curved, geometry accounts for possible deformations of the wire during installation. The curved wire has the same total length as the blue one in the simulation. The shown dimensions have units of mm.

are applied, is only fixed in the rotational degrees of freedom. This will produce displacement density profiles and resonant modes of the spring with an example shown in Figure 4.5.

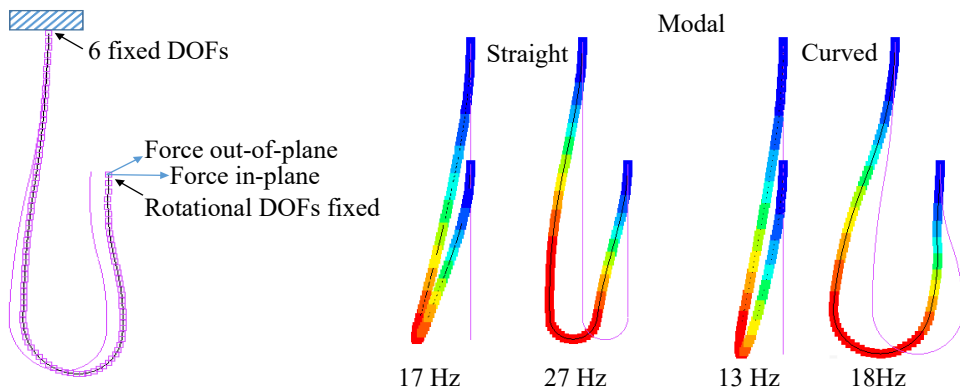


Figure 4.5: An illustration of different resonant modes and the variation in displacement density across the geometry of the heat-link from [113]. The left figure shows the constraints applied at the two ends of the wires in the FEM model. The red color indicates regions of higher mechanical transfer in the fiber.

Because the excitation from the actuator causes heat-link deflection in both longitudinal (along the excitation axis) and transverse (perpendicular to the excitation axis) directions, an effective heat-link stiffness is calculated as follows:

$$k_{\text{effective}} = N \cdot (k_{\text{in-plane}} + k_{\text{out-of-plane}}). \quad (4.1)$$

Here N gives the total number of heat-link connections, $k_{\text{in-plane}}$ is the resistance to deformation to forced applied in the plane of the wire and $k_{\text{out-of-plane}}$ is the resistance to deformation to forces applied orthogonal to the plane of the wire. The resultant longitudinal and vertical stiffness of the short heat-link are shown in Table 4.1.

Bending	In-plane [N/m]	Out-of-plane [N/m]	Vertical [N/m]
Straight	0.0475	0.0369	0.773
Curved	0.0366	0.0264	0.268

Table 4.1: Summary of the stiffness parameters from the FEM analysis for both longitudinal degrees of freedom and the vertical one.

The stiffness and transfer analysis of the short heat-link sheds light on the non-linear dynamic of the conduction rod. Since the payload contains heat-links with different geometrical shapes between multiple pendulum stages, as illustrated in Figure 4.2, an inference about the longer heat-link dynamics is made, based on the results obtained for the short connection. As the wire-loops are highly non-linear in their deformation response with length and of same approximated geometry for all the heat-links, they are excluded from the estimation of the longer heat-link stiffness. The remaining straight and long connection can scale the stiffness using the following formula from [114]:

$$k = K \frac{EI}{L^3} = K \frac{E}{L^3} \frac{\pi r^4}{4}. \quad (4.2)$$

Here K is the shape factor determined by the geometry of the conduction element, E is the Young modulus of the heat-link material, I is the moment of inertia and L is the length of the heat-link. The final design of the ETpathfinder 18 K interferometer payload system is not finalized, but the baseline CAD model for ETpathfinder 123 K interferometer assumes heat-link connections between the heat-link ring and both marionetta and the reaction cage of similar lengths. The straight connection, excluding the wire-loop section is about 28 cm. This will be assumed for the projection of noise to the test mass in the later section.

4.3.2 Analytical model

The setup of the two rings can be simplified as a two rigid-body harmonic resonator with the soft heat-links being modelled as springs between the two bodies. Figure 4.6

shows the simplified setup. The cold-finger acts as a reaction body to the dynamics of the heat-link ring. Since the ground or the actuation comes from the cold-finger, its stiffness does not enter the calculation. As small momentum is transferred via the heat-links, the heat-link ring undergoes simple harmonic oscillations around the equilibrium point. The equation of motion of the heat-link ring for small vibrations around the equilibrium point reads:

$$m_{HL} \cdot \frac{d^2 x_{HL}}{dt^2} = k_j \cdot (x_{CF} - x_{HL}) - k_{HL} \cdot x_{HL}. \quad (4.3)$$

Here, m_{HL} is the mass of the heat-link ring, x_{HL} and x_{CF} are the displacements from equilibrium of the heat-link ring and the cold-finger respectively and the k_{HL} and k_{CF} are the two associated stiffnesses for the particular degree of freedom. The assumption here is that $x_{CF} > x_{HL}$. This is analogous to applying the oscillation from the cold-finger and test the resulting momentum imprint at the second mass.

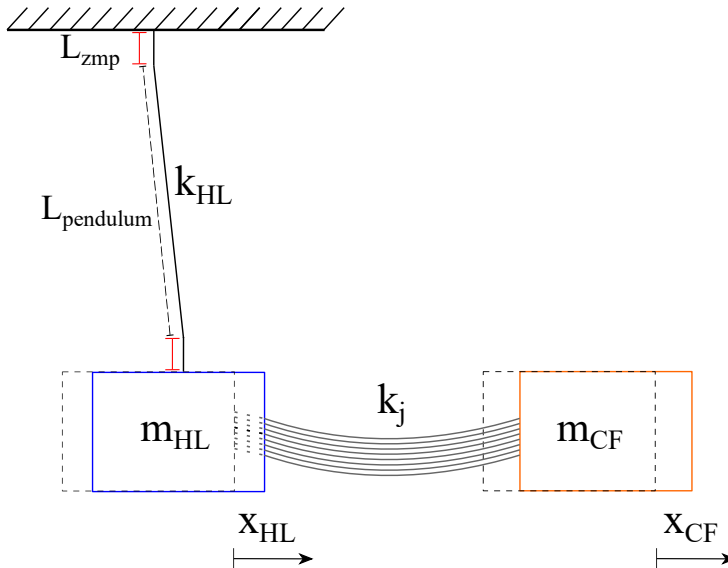


Figure 4.6: Simplified schematics of the two pendulum rings connected via conductive heat-links. The heat-links are modelled as springs with a cumulative stiffness k_j .

The stiffness of the jellyfish wires k_j is the key parameter extracted from the FEM analysis. Turning Equation 4.3 in the frequency domain using Laplace transform: $\ddot{x} \rightarrow s^2x$ where s is a complex variable defined in terms of the angular frequency ω as $s = i\omega$:

$$\begin{aligned} -m_{HL} \cdot \omega^2 x_{HL} &= k_j \cdot x_{CF} - x_{HL}(k_{HL} + k_j) \\ &= -\omega^2 x_{HL} = \frac{k_j \cdot x_{CF}}{m_{HL}} - x_{HL}\omega_0^2 \\ &= TF(f) = \left| \frac{x_{HL}}{x_{CF}} \right| = \frac{k_j}{m_{HL}} \cdot \frac{1}{\omega_0^2 - \omega^2}. \end{aligned} \quad (4.4)$$

Here, ω_0 is the common mode of the oscillation between the two rings and is defined as $\omega_0 = \frac{k_{HL}+k_j}{m_{HL}}$. The stiffness of the pendulum, k_{HL} is defined as $\frac{m_{HL} \cdot g}{L_{pendulum}}$ with $L_{pendulum}$ being the effective pendulum length, as illustrated in Figure 4.6. This is expressed as: $L_{wire} - 2L_{ZMP}$ with L_{wire} being the full, undeformed pendulum wire length and L_{ZMP} , the *zero-moment point* to the driving point length. The horizontal force produced from the interaction with the cold finger deforms the suspension wire [115] producing this bending length. When the pendulum wires are relatively short and of larger diameter, a precise formulation of L_{ZMP} can be used as [116]:

$$L_{ZMP} = \sqrt{\frac{E \cdot I}{T}} \cdot \tanh\left(\frac{L_{wire}}{2 \cdot \sqrt{\frac{E \cdot I}{T}}}\right). \quad (4.5)$$

Here, E is the young modulus of the wire material, $I = \frac{\pi \cdot d^4}{64}$ is the moment of section of the wires of diameter d , and $T = \frac{m_{HL} \cdot g}{3}$ is the tension in the wires for the trifilar pendulum.

The stiffness can now be calculated and consequently the magnitude of the transmissibility given Equation 4.4 can be obtained. The Table 4.2 shows the relevant numerical factors that contribute to the transfer function estimations.

The vertical transfer can be estimated using the same treatment. As the heat-links transport vibrations to the heatlink-ring from the cold-finger, vertical harmonic motions around the center of mass are induced. The vertical stiffness $k_{vertical}$ of the heat-link ring pendulum with three suspension wires now takes the form:

$$k_{vertical} = \frac{3E\pi d^2}{4L_{wire}}. \quad (4.6)$$

4.3.3 Results

The transfer function is now simulated for both vertical and horizontal motions. The magnitude of the vibration transmissibility is shown in Figure 4.7. Two noticeable

Description	Symbol	Value
Young modulus of titania	E_{HL}	1.14×10^{11} Pa
HL ring length	L_{HL}	0.28 m
HL ring mass	m_{HL}	0.58 kg
CF ring mass	m_{CF}	0.56 kg
HL pendulum wires thickness	d_{HL}	5×10^{-4} m
Tension in HL pendulum wires	T	1.89 N
HL pendulum measured wire length	L_{wire}	0.28 m
Bending length	L_{ZMP}	0.013 m
Effective pendulum length	$L_{pendulum}$	0.26 m
HL pendulum mode frequency	$f_{horizontal}$	0.97 Hz
HL vertical mode frequency	$f_{vertical}$	100 Hz

Table 4.2: Heat-link ring and cold-finger parameters relevant for the transfer function estimation.

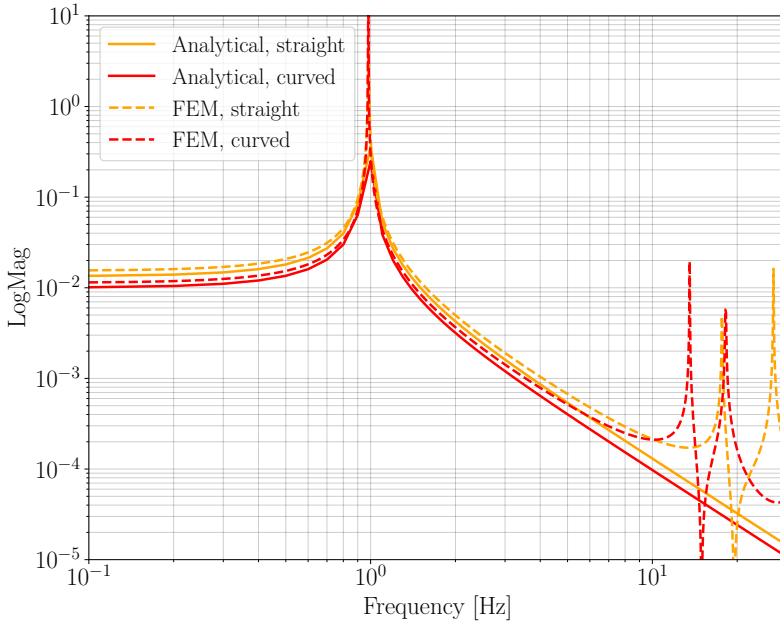
results are drawn from the simulations. Firstly, the analytical representation matches well the FEM simulation at DC and at the common resonant modes, such as the pendulum mode about 1 Hz for the longitudinal motion and the bounce mode about 100 Hz for the vertical motion. The analytical model generally fits the roll-off after the resonance; however, it deviates due to the internal resonances of the heat-links represented by the FEM, an effect that is significantly enhanced for the vertical motion due to the presence of a close anti-resonance. Secondly, it is clear that the shape wire-loop influences the stiffness and dynamics of the heat-link. A straighter, more tense, heat-link will have its internal resonances starting at higher frequencies than a deformed one.

4.4 Transfer measurements

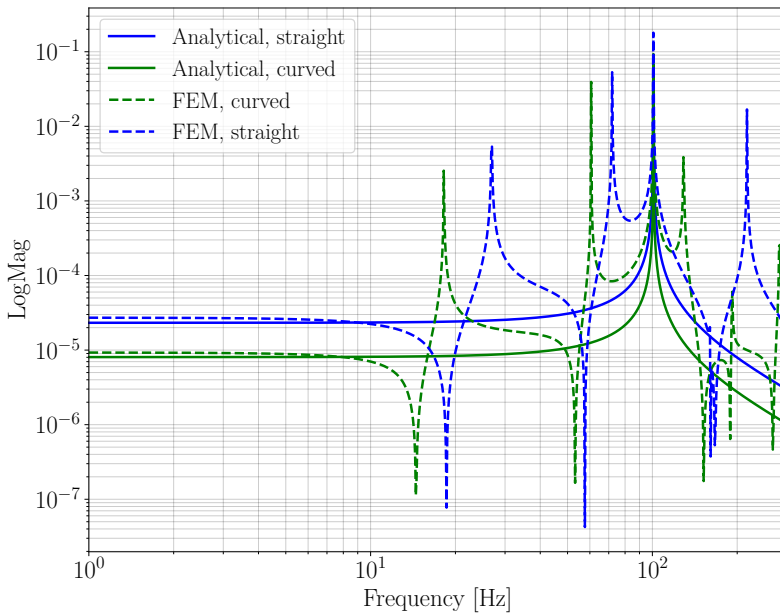
4.4.1 Dual channel analysis fundamentals

The sketch of the setup in Figure 4.3 b) shows all the important components. The dynamics signal analyzer feeds an actuator with an amplified signal via the audio amplifier. The magnetic interaction will produce a force that accelerates the cold finger, which at the same time transfers momentum to the heat-link ring via the jellyfish wires. The acceleration of the rings is sensed using two accelerometers which feed back the signal to the spectrum analyzer.

To measure the acoustic transfer between the two masses, two quantities specific to the dual-channel measurements are recorded via the signal analyzer: *the frequency response function* and *the coherence function* [117]. The frequency response function is a result of the ratio between the Fourier transform of the response and the Fourier transform of the excitation signal. If the Equation of motion 4.3 is solved for an



(a)



(b)

Figure 4.7: Transfer function simulation for both horizontal (a) and vertical (b) motions of the two pendulums. The heat-links are modelled as springs with the stiffness simulated using a FEM model of the wire. The transfer function is simulated for 8 heat-links of 0.25 mm diameter each.

arbitrary Fourier component $F_0 e^{2\pi i f t}$, then this can be expressed as:

$$m_{HL} \cdot \frac{d^2 x_{HL}}{dt^2} = k_j \cdot (x_{CF} - x_{HL}) - k_{HL} \cdot x_{HL} = F_0 e^{2\pi i f t}. \quad (4.7)$$

The complex response function $H(f)$ gives information about the absolute value of the response or magnitude, but also the phase lag between the response and the excitation. It defines the general solution of the above equation as:

$$X(f) = H(f) F_0 e^{2\pi i f t}. \quad (4.8)$$

To get precise conditions for measuring the transfer function, the signal in the first channel must arise from the signal in the second channel. Using the coherence function, this relationship can be constrained.

The coherence function gives a measure of the amount of linear dependence between multi-channel signals as a function of frequency. It is defined in terms of channel auto-spectrum, $S_1(f)$, and the dual channel cross-spectrum $S_{12}(f)$. The channel auto-spectrum, alternatively known as the power spectrum, is calculated from averaged instantaneous measurements of squared amplitudes of the signal. The dual channel cross spectrum, from 1 to 2, is defined as: $S_{12}(f) = S_1^*(f) S_2(f)$ with S_1^* being the complex conjugate of the auto-spectrum of channel 1. This leads to the Coherence formulation as:

$$\gamma^2 = \frac{|S_{12}(f)|^2}{S_1(f) \cdot S_2(f)}. \quad (4.9)$$

It can be seen that the Coherence term can be interpreted as a linear correlation coefficient between two variables, in this case two signals at an instant of frequency with the power spectrum of each channel being interpreted as the variance in the signal, while the cross spectrum can be seen as the covariance. A coherence that tends towards 1 means that the signals are linearly dependent. As a consequence, the signal sensed in Channel 2, or the upper heat-link ring, is a most probable result of the excitation sensed in Channel 1 or the cold-finger stage.

4.4.2 Apparatus preparation

The dynamical signal analyzer is the central component and allows the main calibration settings for the measurements. The analyzer feeds conditioned signal to the sensors, provides a filtered source to the coil and performs the data acquisition with the suitable scaling for the measurements.

There were two types of excitation signals for the transfer measurements: short-bandwidth random noise and frequency injection lines. For the particular setup, both approaches have advantages and disadvantages. While the line frequency transfer has better coherence between the two channels, the disadvantage of automatic data acquisition becomes noticeable after repeated measurements and the tendency for

lower resolution data is amplified. Furthermore, it is important that the line injections produce a measurable effect in both channels, which can be verified above the sensor noise.

An example of the power spectrum at different line injections is illustrated in the plots of Figure 4.8. From this plot, it is clear that below 32 Hz, both channels measure signals with a high enough signal-to-noise ratio such that the resonant lines can be distinguished from other structures in the proximity of the signal. These other structures can originate from the environment or other parts of the device. Above 32 Hz, there is a measurement band of strong resonances which are not attributed to the transfer and represent the limit of the measurements.

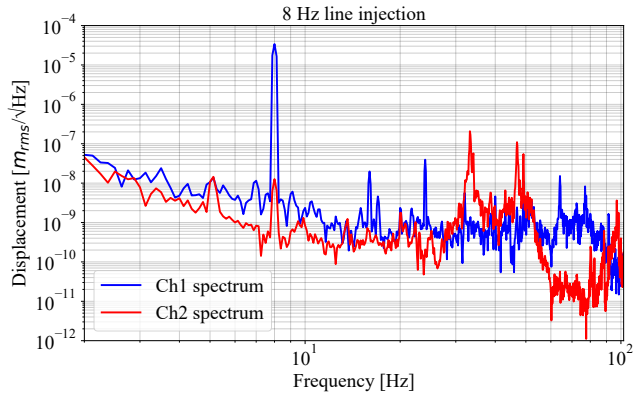
Both measurement types will be limited by the clipping voltage of the coil. This was measured and is approximately $550 \text{ mV}_{\text{rms}}$ with the root-mean-square (rms) voltage being defined as $V_{\text{rms}} = V_0/\sqrt{2}$. The following set of procedures were applied to the data acquisition analyzer:

1. The Integrated Circuit-Piezoelectric (ICP) signal is *on* for both accelerometer channels.
2. The accelerometer channels range are set to automatic.
3. The accelerometers units are activated and calibrated to their design values. For the PCB 393B05 transducers, a sensitivity of 10 V/g is used.
4. The fast Fourier Transform (FFT) is averaged 32 times for one measurement with an overlap percentage of 0.5.
5. The FFT calculations which correspond to signals overloading the transducer channels are rejected from the average.
6. The frequency resolution is set to 400 lines.
7. The frequency range varies by measurement.
8. The window type was *Hanning*.

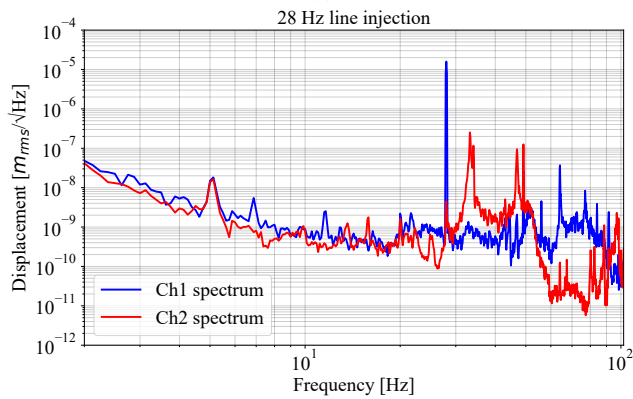
4.4.3 Measurement for six heat-links

A transfer measurement with six soft heat-links installed was performed. This is shown in Figure 4.9 where the magnitude of the transfer is taken with both methods. The injected lines transfer function has magnitude errors which correspond to one standard deviation away from the mean after a repeated measurement twenty four times. Variability in each frequency decade is assumed to be constant.

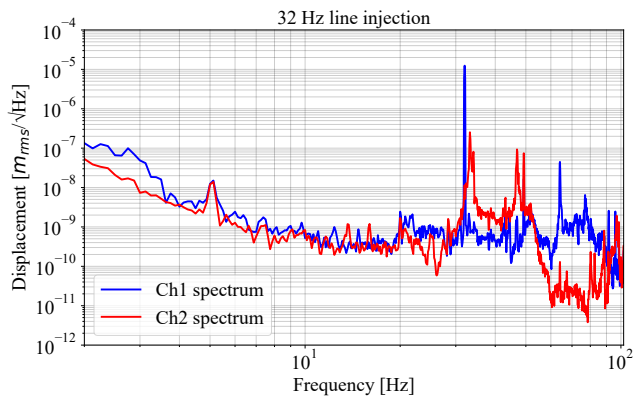
The general features of the measurements which will be encountered in the following examples can be drawn from this plot. It can be seen that at lower



(a)



(b)



(c)

Figure 4.8: The figures show how the power spectrum of the signal injection at different frequencies for both channels compares to the broad-band environmental structures in the signal.

frequencies, the coherence and the sensitivity of the measurement are high. Close to approximately 20 Hz, the standard errors of the injection measurement are low and they fit well the broadband measurement. After this, the coherence function decreases, and this implies a measurement without significance. Thus, the limit to the clear transfer via the heat-links is taken up to the maximum 32 Hz.

The plot also compares the simulations with the measurements for 6 heat-links. It can be seen that the straighter-shaped model of the heat-link is favorable as this gives higher stiffness and fits better the data. Even though the frequency of the longitudinal mode for the trifilar heat-link ring is fit well by the models, the roll-off for 8 ideal heat-links is more representative for the measured transfer function.

4.4.4 Stiffness variability measurements

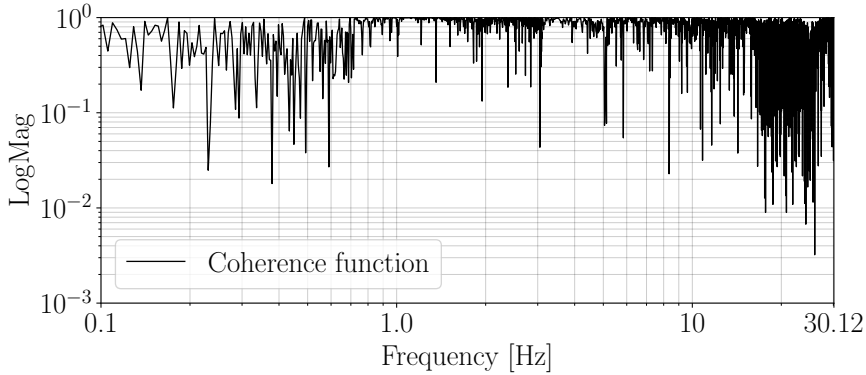
Together with the simple measurements, an experiment to test the variability in the magnitude of the transfer function as the stiffness decreases was performed. Two heat-links were removed at each iteration, starting from eight, and ending with measuring the null transfer.

In order to qualify the null measurement, a theoretical estimation of the sensor noise floor was produced. Since the transfer function assumes that the displacement of the excitation mass is much larger than the displacement of the effect mass, the noise of the transfer function is mostly caused by the accelerometer noise on the heat-link ring. Generally, the noise associated with the injection transfer function measurement at each frequency, $TF_n(f)$, can be written as:

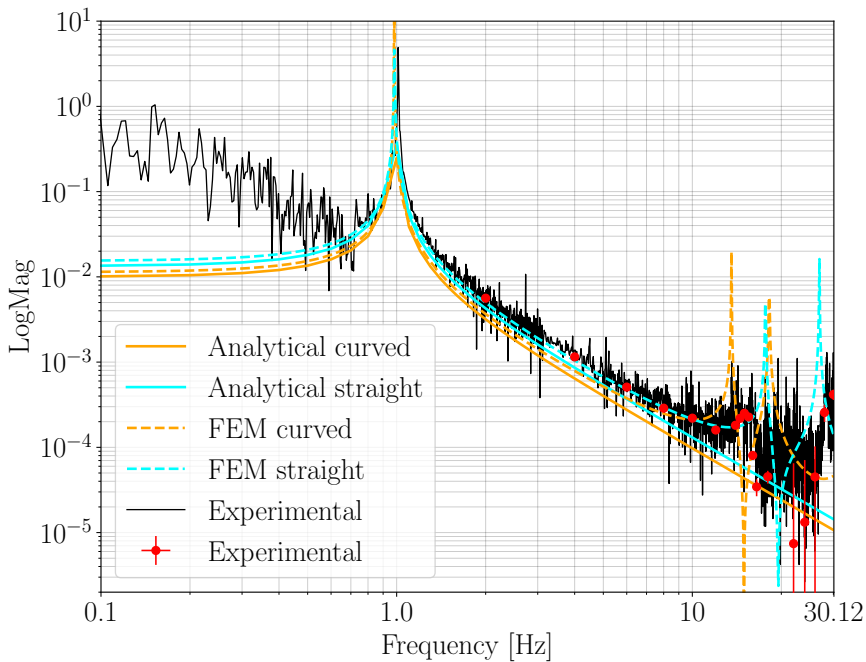
$$TF_n(f) = \frac{1}{a_{CF}^{rms}} \cdot \sqrt{(|N_{env}(f)|^2 + |N_{acc}(f)|^2) \cdot B_w(f)}. \quad (4.10)$$

Here a_{CF}^{rms} is RMS acceleration of the cold-finger mass, $N_{acc}(f)$ is the acceleration noise spectral density of the heat-link ring, $N_{env}(f)$ is the acceleration spectral density of the environmental sources and $B_w(f)$ is the bin-width of the FFT (inverse of the measurement time). The environmental effects on the transfer function are neglected for now, since these are difficult to estimate for the measurement timescale. The accelerometer noise spectral density is taken from the specification, stated in the Appendix D. The final part required for the estimation, a_{CF}^{rms} , can be calculated analytically.

Assuming the measurement is taken above the pendulum frequency, a_{CF}^{rms} can be expressed as $\frac{F_{CF}(f)}{m_{CF}}$, where $F_{CF}(f)$ is the force spectral density provided by the actuator above resonance and m_{CF} is the mass of the cold-finger. Using the coil modelling from the Appendix E, a maximum actuating force above resonance is estimated to be around 0.125 N which gives the maximum acceleration of the cold-finger above resonance of $a_{CF}^{rms} = 2.6 \cdot 10^{-2}g$. For a measurement time of 8 seconds, the sensor floor estimation is plotted together with the transfer measurement variation in Figure 4.10.



(a)



(b)

Figure 4.9: Transfer function measurement for 6 Al heat-links using signal input via small bandwidth random noise (black curve) and via frequency injections (red data). The plot a) shows that the Coherence function approaching unity signifies a meaningful measurement. The experimental data is compared to the analytical simulations for 6 heat-links (solid cyan and orange curves) and FEM analysis results for 8 heat-links (dashed curves). Both simulations are performed considering a straight or ideal heat-link geometry and a curved geometry.

It can be observed that the magnitude of the mechanical transfer decreases almost by a constant factor with the stiffness reduction. The second and third iteration show

a similar reduction factor for a high coherence and low-frequency measurement. Since the installation position of each heat-link on the two rings was not perfectly symmetric, the reduction factor implies that after the first iteration, heat-links positioned more radially with respect to the excitation axis were removed. The null measurement gives some background residual transfer across the scanned frequency band, well above the accelerometer noise floor for each frequency measurement. It also signifies that below 20 Hz the measurement is generally significant and the common structure at 30 Hz and above originate from exterior and it is sensed in both sensors.

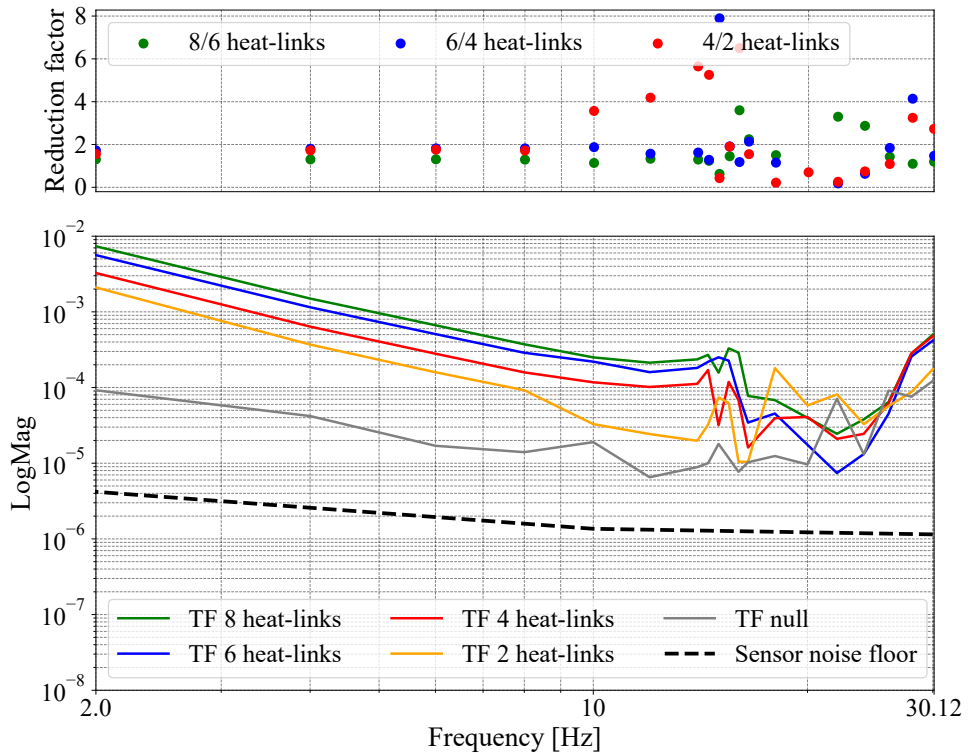


Figure 4.10: The magnitude of the mechanical transmissibility as the heat-link connection reduces in stiffness, together with the magnitude reduction factors for each iteration. The noise associated with the transfer function for each frequency line is shown by the dashed curve.

4.4.5 In-air and in-vacuum measurements

In order to probe the higher frequency domain of the transfer measurement and to determine whether the magnitude is dominated by the environmental noise of the lab, such as the vacuum pumps vibration or the clean-room air conditioning fans and other acoustic noises, the experiment was performed in vacuum conditions. The prototype

was fully enclosed within the vacuum mantle with the test setup operating in the same calibration as before. Together with Rogier Elsinga, the prototype tower was pumped down to about 0.01 mbar. The heat-links were installed in full symmetrical arrangements on the two rings. An additional resonance at lower frequencies was present in the transfer measurement. This was an angular resonance of the ring above and was solved by clamping the mass to the structure. The comparison for the transmissibility data is illustrated in Figure 4.11. Furthermore, a free spectrum comparison of the two sensor channels is also presented in Figure 4.12.

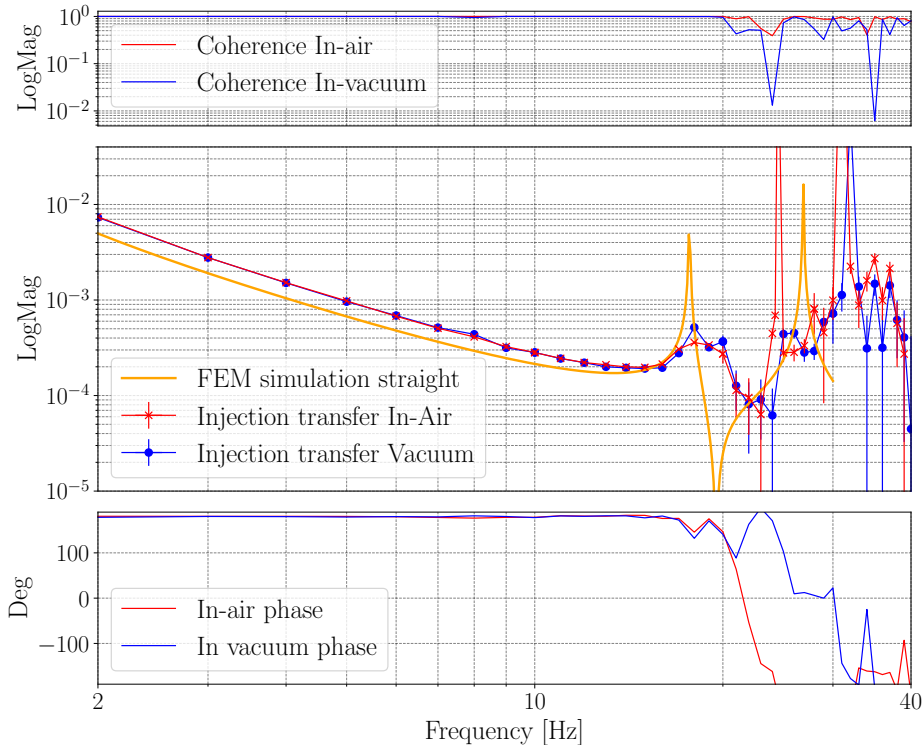


Figure 4.11: The comparison of the mechanical transmissibility showing the variation of the frequency response magnitude and phase and the coherence function in two different environmental conditions.

It can be seen from Figure 4.11 that the transmissibility via heat-links at lower frequencies is independent on the environmental conditions, with a good similarity in magnitude. Furthermore, there is some consistency between the FEM simulation of the transfer for the straight heat-link and the measured internal resonances of the wires. However, a higher resolution for the injection measurements is required to determine the degree of consistency. The resonances can be seen around 17 Hz and at 24 Hz.

These results are not surprising if Figure 4.12 is examined. There, it can be

seen that the RMS displacement spectral density of each mass, without actuation, is generally similar between vacuum and in-air measurements, although some clear resonances differ. Moreover, there is a clear increase in magnitude envelope above 20 Hz between the two channels, which implies that the internal sensor noise can dominate the measured signal above this frequency.

These all suggest that the abundance of resonances above 30 Hz do not come from the acoustic noise in the lab, as the vacuum environment is expected to shield this. The resonances can be attributed to spectral or electronic noise of the particular sensor, but strangely two different accelerometers mounted for Channel 2 showed similar transfer function behaviours above 30 Hz. Moreover, the accelerometers were also swapped between the two channels with the same behaviour being observed.

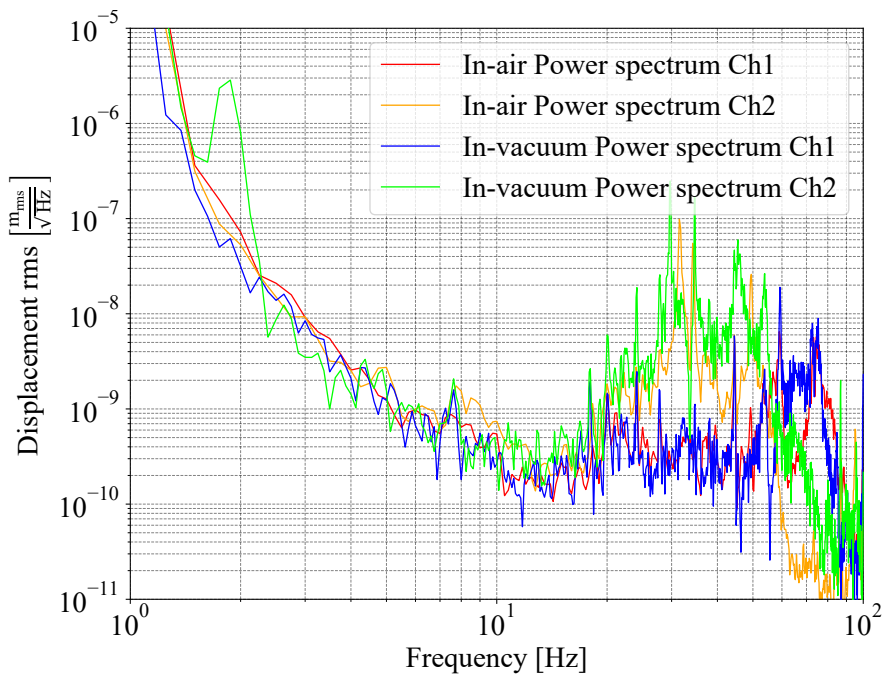


Figure 4.12: Displacement spectral density of the two accelerometers when unperturbed in two environmental conditions.

4.4.6 Conclusions from the measurements

The experiment and the simulations of transmissibility are in good agreement, favoring the heat-link model with a more linear shape. At low frequency, the simulation accurately represents the longitudinal mode of the upper ring. Although the roll-off of the frequency response function matches the data precisely with a $1/f^2$ propagation, its magnitude is projected to be smaller. This signifies a 25 percent increase in the total stiffness of the heat-link connection. This disparity

in rigidity might stem from numerous reasons. With the heat-link loops bending less than anticipated, the real setup during operation will likely resemble straighter wire configurations more. In addition, it is likely that the FEM analysis does not accurately capture the weight effect of the heat-link, which can result in a higher stiffness value.

The measurements produced transfer functions with good coherence. The transfer function becomes less indicative of the heat-links transmission of mechanical vibrations as frequency increases. The upper limit of the measuring band was set to around 30 Hz, with the vacuum transfer spectrum and the free displacement spectrum displaying a similar level of noise above this limit. There is no indication that these resonances are caused by the prototype mechanics. Whether they were caused by equipment noise is not certain and can still be investigated.

The magnitude of the transfer function consistently decreased as the stiffness of the heat-link connection decreased. Theoretically, the sensors were capable of measuring well below the lowest stiffness reduction increment. The measurement of variability also revealed that the installation position of heat-links on the masses influences the transmissibility.

4.5 Heat-link vibration projection for ETpathfinder

In a previous section, the transmissibility model of the ETpathfinder suspension system was introduced. Using the same formalism, one can also integrate the heat-links and their support structures as rigid bodies connected via springs. The diagram in Figure 4.13 illustrates the heat-links integration. Under this formalism, the equation of motion can be written in matrix form and the state-space model transfer function can be obtained.

In Figure 4.13, the direction of the ground injection via the cold-finger is adjacent to the ground, with the aim to show that there is an additional coupling from the ground to the test mass. However, in the equations of motion, the restoring force from the spring under deformation can be taken in the direction of the green vectors. Under this approach, the displacement from the equilibrium of the cold-finger, or the ground, is assumed to be larger than the others. This is similar to the case shown in Section 4.3. The problem is that of n coupled oscillators, and for the sake of simplicity, damping is not considered. The equation of motion can be written in matrix form as:

$$\mathbf{M} \frac{d^2 \mathbf{x}}{dt^2} = -\mathbf{K} \mathbf{x} + \mathbf{F}_{\text{total}}. \quad (4.11)$$

In Equation 4.11, \mathbf{M} is the matrix containing the masses of bodies, \mathbf{K} is the stiffness matrix and \mathbf{F} is the vector containing the applied forces and torques on the bodies. As an example, the matrices for the horizontal degree-of-freedom are expressed as follow:

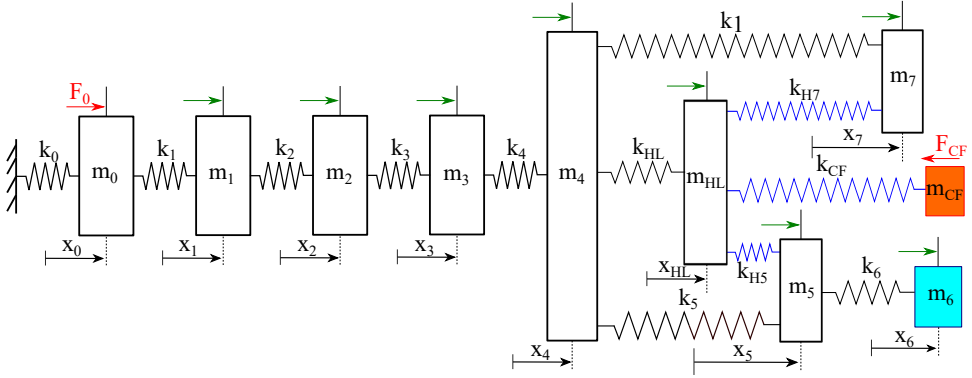


Figure 4.13: A schematic representation of the rigid-body model for the ETpathfinder suspension system. There are two ground inputs that reach the test mass (m_6), one coming from the large inverted pendulum base (m_0) and another one coming from the cold-finger mass (m_{CF}). The green arrows indicate the direction of the force pushing the bodies away from their equilibrium position. The springs shown in blue color represent the heat-link connections. The reaction mass m_7 interacts via the actuators to both the marionette (m_5) and the test mass, but for simplicity this coupling is not modelled in the proposed treatment.

$$\mathbf{K} = \begin{bmatrix} k_0 + k_1 & -k_1 & 0 & 0 & 0 & 0 & 0 & 0 & 0 & 0 & 0 \\ -k_1 & k_1 + k_2 & -k_2 & 0 & 0 & 0 & 0 & 0 & 0 & 0 & 0 \\ 0 & -k_2 & k_2 + k_3 & -k_3 & 0 & 0 & 0 & 0 & 0 & 0 & 0 \\ 0 & 0 & -k_3 & k_3 + k_4 & -k_4 & 0 & 0 & 0 & 0 & 0 & 0 \\ 0 & 0 & 0 & -k_4 & k_4 + k_5 + k_7 + k_{HL} & -k_5 & 0 & -k_7 & -k_{HL} & 0 & 0 \\ 0 & 0 & 0 & 0 & -k_5 & k_5 + k_6 & -k_6 & 0 & -k_{H5} & 0 & 0 \\ 0 & 0 & 0 & 0 & 0 & -k_6 & k_6 & 0 & 0 & 0 & 0 \\ 0 & 0 & 0 & 0 & -k_7 & 0 & 0 & k_7 & 0 & -k_{H7} & 0 \\ 0 & 0 & 0 & 0 & -k_{HL} & -k_{H5} & 0 & -k_{H7} & k_4 + k_{HL} + k_{H5} + k_{H7} & -k_{CF} & 0 \\ 0 & 0 & 0 & 0 & 0 & 0 & 0 & 0 & -k_{CF} & k_{CF} & 0 \end{bmatrix},$$

$$\mathbf{M} = \begin{bmatrix} m_0 + (u_0 + u_1) / 3 & u_1 / 6 & 0 & 0 & 0 & 0 & 0 & 0 & 0 & 0 & 0 \\ (u_1) / 6 & (m_1 + u_1) / 3 & 0 & 0 & 0 & 0 & 0 & 0 & 0 & 0 & 0 \\ 0 & 0 & m_2 & 0 & 0 & 0 & 0 & 0 & 0 & 0 & 0 \\ 0 & 0 & 0 & m_3 & 0 & 0 & 0 & 0 & 0 & 0 & 0 \\ 0 & 0 & 0 & 0 & m_4 & 0 & 0 & 0 & 0 & 0 & 0 \\ 0 & 0 & 0 & 0 & 0 & m_5 & 0 & 0 & 0 & 0 & 0 \\ 0 & 0 & 0 & 0 & 0 & 0 & m_6 & 0 & 0 & 0 & 0 \\ 0 & 0 & 0 & 0 & 0 & 0 & 0 & m_7 & 0 & 0 & 0 \\ 0 & 0 & 0 & 0 & 0 & 0 & 0 & 0 & m_{HL} & 0 & 0 \\ 0 & 0 & 0 & 0 & 0 & 0 & 0 & 0 & 0 & 0 & m_{CF} \end{bmatrix}.$$

Here, the components of the stiffness and mass matrices are similar to the ones expressed in Chapter 3. The force vector is defined as the *Identity* matrix and the \mathbf{x} corresponds to a one-dimensional column vector containing all the displacements from equilibrium of the bodies in the chain. By adding the effect of the heat-link ring and the cold-finger, two more entries (two rows and columns) appear in the matrices of Equation 4.11 with their stiffness distribution of pendulum wires and conduction heat-links represented by the off-diagonal entries of the stiffness matrix.

In order to estimate the total transfer function of the system with two inputs connected to the ground and the output at the test mass, one has to combine the two single-input single-output systems into a multiple-input single-output representation of the transfer function in the state-space domain. In that way, the two input-to-test mass systems can be taken as parallel transfer functions, one that represents the transmissibility from the ground to the test mass, TF_{0-TM} (the suspension transfer function without a seismic shortcut) and one from the cold-finger to the test mass, TF_{CF-TM} (the seismic shortcut). A schematic representation of this abstraction is shown in Figure 4.14. The total transfer function is thus a sum of the two parallel ones:

$$TF_{\text{total}} = TF_{0-TM} + TF_{CF-TM}. \quad (4.12)$$

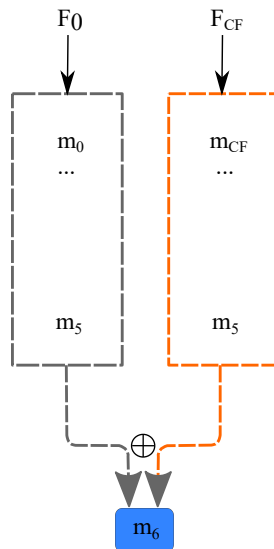


Figure 4.14: The figure depicts an abstraction of Equation 4.12. The transfer function from the ground to the interferometer test mass (TF_{0-TM}) adds up the transfer function from the cold-finger to the test mass (TF_{CF-TM}) into a net parallel transfer function with two inputs and a single output.

Using the stiffness variation factor with length from above and calibrating by 25% increase the total horizontal stiffness to correctly match the experiment, transfer functions are drawn and shown in Figures 4.15 and 4.16.

Including the seismic noise spectral in horizontal and vertical degrees of freedom for six hours of measurement time at night, corresponding to the data taken as reference in the construction of the noise budget, the seismic noise projections for the total mechanical transfer function is presented in Figure 4.17 and Figure 4.18. The projection assumes 20 heat-links, five connected between the cold-finger and the heat-link ring and the marionetta and ten connected to the reaction mass.

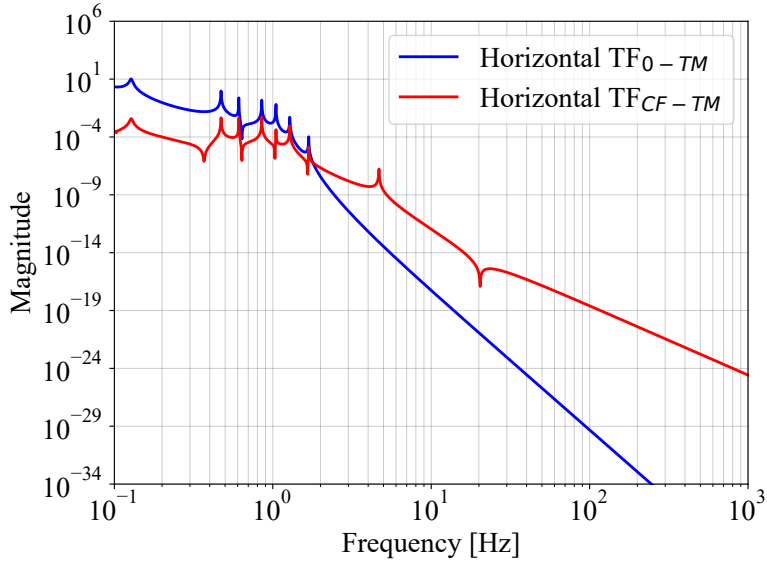


Figure 4.15: Mechanical transfer functions of the two single-input single-output systems in the horizontal degree-of-freedom. The transmissibility from the cold-finger to the test mass takes into account 20 heat-links, ten connected to the reaction mass and five for both the heat-link stage and the marionetta.

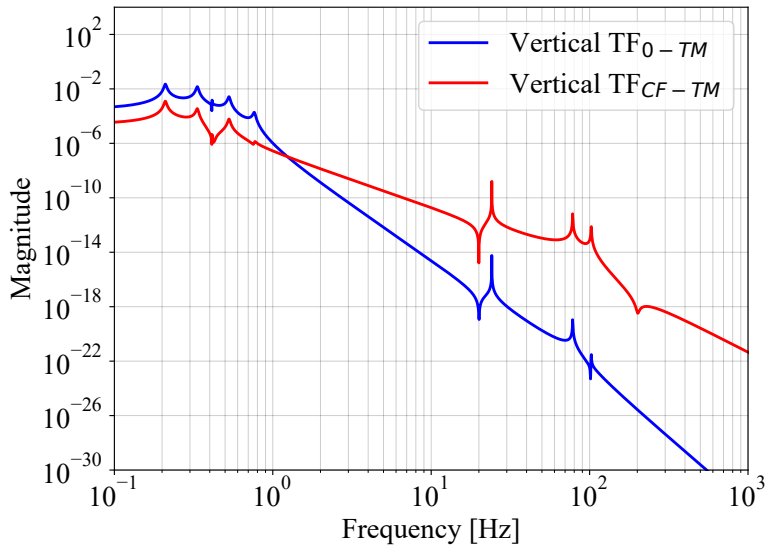


Figure 4.16: Mechanical transfer functions of the two single-input single-output systems in the vertical degree-of-freedom. The transmissibility from the cold-finger to the test mass takes into account 20 heat-links, ten connected to the reaction mass and five for both the heat-link stage and the marionetta.

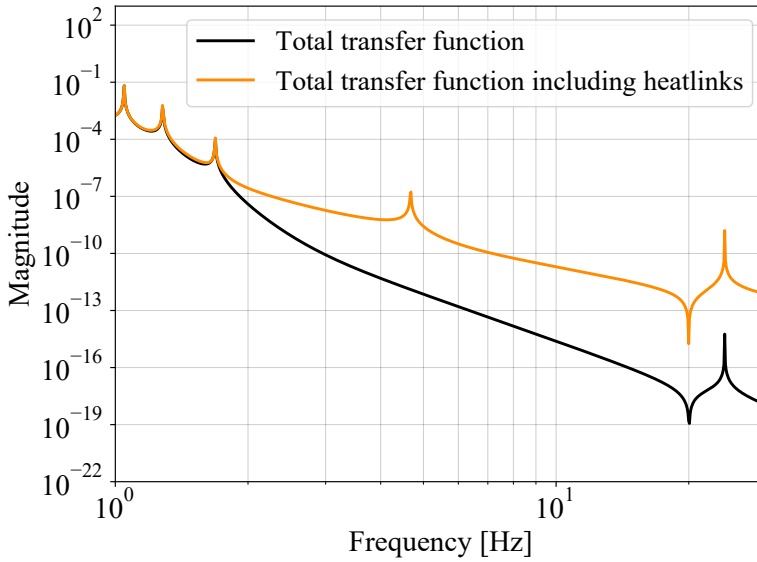


Figure 4.17: The figure depicts the change in the mechanical transfer function when heat-links are integrated in the suspension.

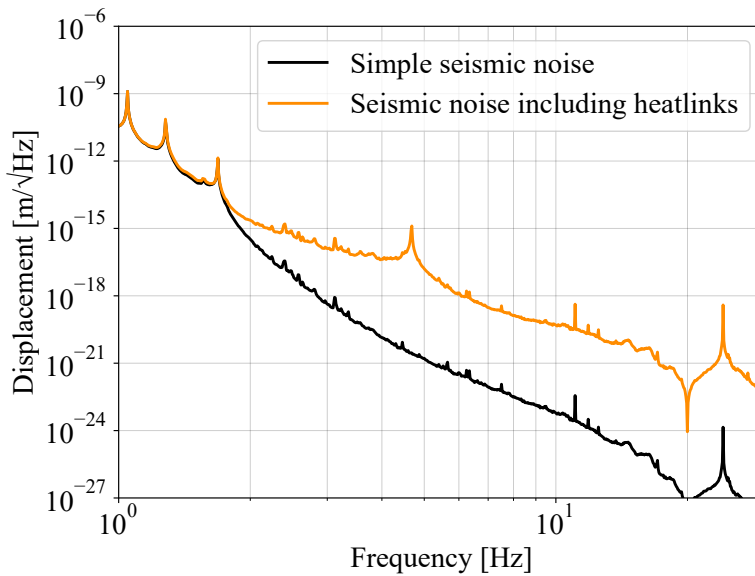


Figure 4.18: Total amplitude spectral density of the seismic noise assuming that the cold-finger moves as the ground. A total of 20 heat-links between the stages is assumed.

To properly assess the potential degradation of displacement sensitivity during the cryogenic operation, one has to consider the optimal number of heat-links at different stages to reach the target temperature and to maintain the system in thermal

equilibrium.

The amount of heat that must be transported from the test masses in order to keep the system in thermal equilibrium and the temperatures at which the interferometer operates determine the number of heat-links that must be integrated into the system. This can be expressed using the Fourier's law:

$$\frac{dQ}{dt} = \frac{kA\Delta T}{L}. \quad (4.13)$$

Here k is the thermal conductivity of the material, $A = 0.25 \cdot \pi \cdot d^2$ is the cross-section area of the heat-link wire for a diameter d , and L is the heat-link length. The difference in temperature at the ends of the wire is given by ΔT .

KAGRA heatlink dimensions can be used to explore the cooling requirements for ETpathfinder. As an example, for a minimum 20 mW/K for a 3-K difference between the cold-finger and the marionetta, or reaction mass, with a KAGRA average thermal conductivity of the conduction heat-link of 13 kW/mK and a wire length of around 600 mm, the total cross sectional area of about 1 mm² results. Therefore, for a KAGRA-type heat-link of 0.15 mm diameter, a total number of at least 50 heat-links are required to maintain the system in thermal equilibrium.

ETpathfinder payload design has three stages of heat-link connections: first stage between the cold-finger and the heat-link ring with a straight heat-link section of length 11 cm, the second stage between the heat-link ring and the marionetta, similar in length to the last stage between the heat-link ring and the reaction mass, and of length 28 cm. Therefore, assuming the minimum conduction power flux value of 20 mW/K, a similar total cross sectional area of about 1 mm² for the conduction heat-link results. For a 0.25 mm diameter of the tested heat-link in the experiments presented above, a number of at least 20 heat-links are required to maintain the system in thermal equilibrium.

The large reaction mass in the ETpathfinder payload requires more heat-links for cool-down as a result of size and exposure to more incoming radiation. Therefore, for 20 heat-links, ten of them can be placed between the heat-link ring and the reaction mass and an equal number of five between the other two heat-link stages. Using this approach, other combinations can be found depending on the optimization criteria.

In order to achieve the desired operating temperature more rapidly, it is necessary to integrate a greater number of conductive heat links at each stage. This will result in an increase in the effective overall stiffness of the cryocooler suspension path leading to the test mass. This will ultimately result in a greater conversion of seismic noise into displacement of the test mass, hence diminishing the instrument's sensitivity.

In order to test the impact of multiple heat-links being integrated into the system, a plot of seismic noise against the ETpathfinder total projected sensitivity is shown in Figure 4.19. The variation in stiffness corresponds to adding five more heat-links per each iteration, three between the heat-link ring and the reaction mass and one for the other two heat-link stages.

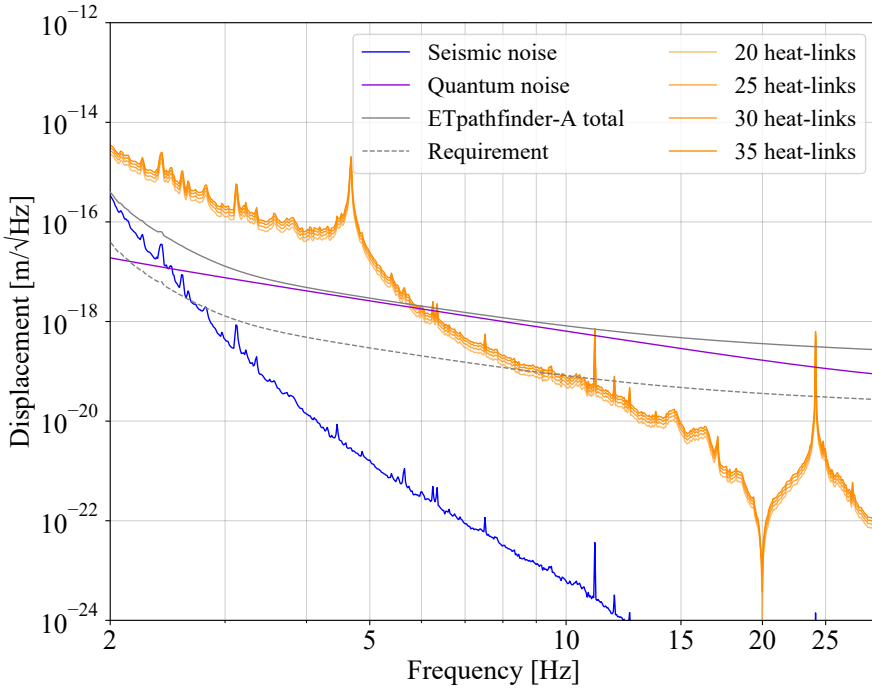


Figure 4.19: Displacement of the seismic noise from the variation in the number of heat-link connections. The blue curve shows the seismic noise from the ETpathfinder noise budget, constituent of the total sensitivity given by the solid grey line curve. The requirement is defined as one order of magnitude below the total noise budget curve broadband.

The requirement is defined as one order of magnitude below the the broadband sensitivity of the ETpathfinder. It can be seen that this is satisfied above 10 Hz even if we increase the conduction cooling capability.

4.6 Discussion and recommendations

The measurements presented in this chapter correspond to coherent momentum transfer between the two rings, which is the result of vibration transport via the cryogenic heat-links. The magnitude of the frequency response function is compatible with the simulated transfer function. The FEM method allows the probing of the heat-link connection loop from the initial design and its stiffness to various degrees of freedom.

A good agreement on the transfer function magnitude between the two models, FEM and analytical, is observed. The experimental results are in favor of a straight geometrical heat-link with the internal resonances being captured in the FEM model transfer. However, a small discrepancy between the data and the model in the broadband magnitude of the transfer function roll-off is observed. This corresponds

to about 25% increase in the total effective heat-link stiffness. This mismatch can be associated with the improper heat-link arrangement on the disks or a resultant straighter heat-link during testing. Furthermore, clear evidence of the non-linear displacement profile of the wire loop is observed, and this can result in a multitude of internal resonances of the heat-link at different frequencies. In conclusion, straighter heat-link connections are recommended. This will make both the practical installation and the analytical understanding of their stiffness variation easier.

The analytical model of the transfer function is inversely proportional to the weight of the heat-link ring. In fact, every transfer function model with a suspended response body will scale down with its mass. Firstly, the heat-link ring mass can be increased to reduce the magnitude of the transfer function. On the other hand, advantage can be taken of the fact that the suspended singular reaction cage is heavy, about three times the mass of the test mirror. The heat-link path can then be adjusted to come from the heat-link ring, to the reaction mass, and then to the marionetta, increasing the attenuation chain of the heat-link to the mirror. A small price has to be paid in the small length of the reaction mass-marionetta heat-links, which have an increased stiffness compared to the rest.

The heat-link path is integrated into the rigid-body mechanical transfer function of the full ETpathfinder suspension system. The mechanical complete transfer function, including heat-links, is then realized by assuming the two single-input single-output systems to act in parallel. It can then be observed that the integration of heat-links, even in low numbers, degrades the seismic noise of the instrument above 2 Hz when assuming that the cold-finger moves with the same displacement spectrum as the ground.

To provide a target on the stability of the cold-finger, one needs to define a requirement and a minimum condition for which this should be satisfied. The requirement can be represented by one order of magnitude lower displacement amplitude spectral density from the projected ETpathfinder sensitivity running at 18 K. For a 20 mW/K, minimum power through the heat-links between the cold finger and the test mass in order to maintain the test mass in thermal equilibrium at the target temperature, an effective total stiffness is obtained and can be split into 20 heat-links of 0.25 mm each. Increasing the total heat-link stiffness by a quarter from the starting value each iteration minimally decreases the instrument sensitivity. However, above 35 heat-links, the resultant seismic noise level reaches above the stability requirement at 10 Hz.

Automatic alignment of resonant optical cavities using Machine Learning

5.1 Introduction

When discussing the resonance conditions of various interferometric optical cavities, only the longitudinal degrees of freedom have been examined up to this point in this thesis. As suspended rigid bodies interacting with the residual seismic field of the ground, the test mirrors are susceptible to five additional degrees of freedom. A simplified figure showing the degrees of freedom is shown in Figure 5.1. Two degrees of freedom are translations along the axes that are perpendicular to the longitudinal axis, whereas the remaining three are rotations about all axes. The rotations which are more relevant for the test masses in gravitational-wave detectors are represented by the rotation around the vertical axis, also called *yaw*, and the rotation around the remaining orthogonal axis to the laser beam direction, also called *pitch*. Roll is not important, since the test masses are spherically symmetric around the center.

The interference condition at the beam splitter necessitates that the two Fabry-Perot resonant cavities in the arms have both mirrors aligned with respect to each cavity eigenmode and both cavity axes orthogonal to each other. In addition, the precise alignment of the input beam to the cavity's eigenmode ensures maximum power coupling and suppression of beam jitter noise. However, once a test mass tilts or yaws as a result of a disturbance, it shifts the optical axis with respect to the perfect resonant condition where the bouncing laser beam is assumed to be perpendicular to the incoming beam. A geometrical example is shown in Figure 5.2. Therefore, sensing and controlling the angular degrees-of-freedom of the mirrors is important

and essential for the functionality of the gravitational-wave detectors [118].

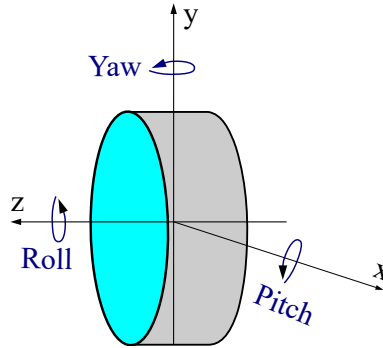


Figure 5.1: A diagram of a test mass being susceptible to six degrees of freedom with three rotations around the translation axes.

Sensing mirror angular misalignment can be performed in multiple ways. For example, the tilt of a suspended test mass can be sensed with respect to a chosen target level, usually the foundation of the vacuum system, via optical levers. The disadvantage of this method is that the position sensor is directly attached to the ground, making it susceptible to seismic motion. In case of a quiet local reference frame, drifts in the position of the optics in the interferometer due to, for example, Earth tides, still require an additional control intrinsic to the interferometer reference frames, such as the technique of global control in gravitational-wave detectors. Therefore, the goal of an optimal sensing method is to calculate the effect of the angular misalignment directly on the laser fields interacting with the suspended optics.

The work in this chapter investigates modern computer vision techniques as pattern recognition tools for the higher-order Hermite-Gaussian beams produced as a result of optical misalignments. The morphological information is then transformed into an error signal which is used to pre-align a resonant optical cavity and lock it on resonance by integrating the method into a classical control scheme.

5.1.1 Angular misalignment as generator of higher-order modes

In order to quantitatively describe the production of the higher-order electromagnetic modes when the optical field is misaligned, one can start with the paraxial approximation solution of the wave beam equation in one dimension. Following a similar treatment as, for instance, described in [47] or [119], this can be written as:

$$\begin{aligned}
 U_m(x, z) = & \left(\frac{2}{\pi}\right)^{1/4} \left(\frac{1}{2^m m! w(z)}\right)^{1/2} H_m\left(\frac{\sqrt{2}x}{w(z)}\right) \times \\
 & \times \exp\left(-x^2\left(\frac{1}{w(z)^2} + \frac{ik}{2R(z)}\right)\right) \exp\left(i\left(m + \frac{1}{2}\right)\eta(z)\right) e^{-ikz}.
 \end{aligned} \tag{5.1}$$

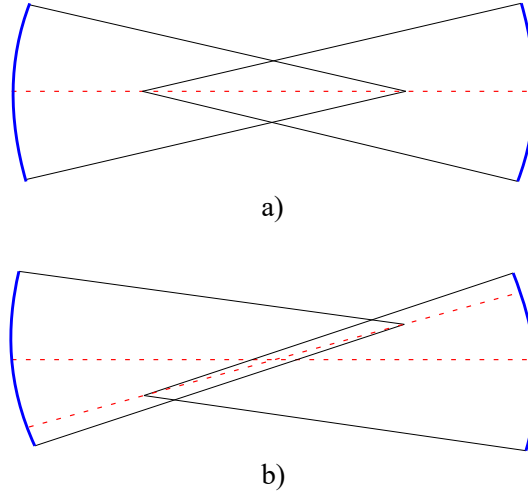


Figure 5.2: The geometry of an angular misalignment in an optical resonator formed by two curved mirrors. The dashed red lines represent the optical axes. Figure b illustrates how the optical axes shift when both mirrors are tilted counterclockwise by the same angle.

This equation resembles the one presented in Chapter 2, but one transverse dimension was dropped from the formulation. As before, m is the mode number, $w(z)$ the beam radius, $R(z)$ the radius of curvature of the wavefront and $\eta(z)$ the Gouy phase. The functions $H_m(x)$ are Hermite functions of order m .

The higher order solutions of the laser mode can now be calculated. A standard approach to simplify the expressions is to consider the mode at the beam waist. Here, $w(z) = w_0$ and the radius of curvature of the wavefront asymptotically approaches infinite, thus reducing the $\frac{ik}{2R(z)}$ expression to zero. The spatial distribution of the fundamental mode $U_0(x)$ and the first higher-order mode $U_1(x)$ reads:

$$U_0(x) = \exp\left(-x^2/\omega_0^2\right), \quad (5.2)$$

and

$$U_1(x) = (2\pi)^{1/2} \frac{x}{\omega_0} \exp\left(-x^2/\omega_0^2\right). \quad (5.3)$$

Any electric field at the position $z = 0$ can therefore be expressed as an amplitude H_m multiplied by the corresponding higher order mode spatial distribution function U_n , for each mode number n :

$$E_m = H_m \cdot U_n. \quad (5.4)$$

If we consider a Gaussian beam initially described as $E_1 = H_1 U_0$, but then displaced in the positive x direction by an offset x_0 , it can be expressed as:

$$E_1 = H_1 \exp\left(-(x - x_0)^2/\omega_0^2\right), \quad (5.5)$$

which, when expanded to first order \ddagger around x_0 :

$$\begin{aligned} E_1 &= H_1 \exp\left(-x^2/\omega_0^2\right) \left(1 + \frac{2xx_0}{\omega_0^2}\right) \\ &= U_0 + \sqrt{\frac{2}{\pi}} \left(\frac{x_0}{\omega_0}\right) U_1. \end{aligned} \quad (5.6)$$

Similarly, if the beam is pitched by a small angle θ in the direction of the x axis, then this can be written as:

$$E_1 = H_1 \exp\left(-x^2/\omega_0^2\right) \exp(ik\theta x), \quad (5.7)$$

which expanded to the first order around the small angle θ is given by:

$$\begin{aligned} E_1 &= H_1 \exp\left(-x^2/\omega_0^2\right) (1 + ik\theta x) \\ &= U_0 + i \frac{k\omega_0}{\sqrt{2\pi}} \theta U_1. \end{aligned} \quad (5.8)$$

It can be seen from both Equations 5.6 and 5.8 that the amplitude of the TEM₁₀ mode is proportional to the normalized shift or pitch. Tilting a laser beam in the fundamental mode produces a coupling to the first higher-order mode 90° out-of-phase. When the beam axis is displaced by an offset, this is equivalent to adding a higher order mode in-phase. These results are in agreement with the ones presented in [120, 121].

5.1.2 Conventional methods for interferometric alignment

Different alignment techniques have been employed in gravitational wave research. They all utilize the higher-order mode generation of the laser field as a result of misalignment, but sensing the mode content is performed in different ways.

One technique takes advantage of the fact that the test masses are spherically symmetric around their center. It consists of adding angular oscillations at different frequencies in both pitch and yaw to the test mirrors in a Fabry-Perot cavity [122]. If no misalignment is present, the angular vibrations do not induce any detectable signal useful for sensing. However, when an optical misalignment is present between the resonator mirrors, the transmitted signal power spectral density records the oscillations lines. Therefore, error signals can be obtained by demodulating the oscillation lines at the injection frequencies. This method is easily implemented, however it adds additional lines to the signal spectrum and has only limited sensitivity. Therefore, the technique has been employed as a pre-alignment method in Advanced

\ddagger Taylor series expansion around x_0 , defined as: $\sum_{n=0}^1 \frac{f^n(0)x_0^n}{n!}$

Virgo detector, offering thus only a good initial working point for the optical cavities [51].

The frontal modulation techniques rely on wavefront sensing, measuring the spatial distortions in the laser beam wavefront due to misalignment in optical cavities. The first approach was undertaken by Anderson in 1984 [123], also called the *Anderson technique*. Only the fundamental mode is resonant in a locked cavity, while the sidebands and higher-order modes are anti-resonant and are strongly suppressed in transmission of the cavity. However, it is possible to add a phase modulation of the entering carrier at the frequency difference between the carrier and the first higher-order TEM mode inside the cavity. Consequently, one of the two first-order sideband modes, TEM₀₁, will resonate and be forcefully transmitted through the cavity. A quadrant photodiode can be used to determine the transmission error signal.

The second technique, also known as the *Ward technique* uses the modulation sidebands of the carrier already present in the longitudinal control scheme [121]. A photodiode positioned in reflection of the cavity will sense the carrier and its sidebands and also the higher-order modes and their sidebands, produced as a result of optical misalignments. The beat note between all these optical fields is the signal detected and the demodulated photocurrent at the modulation frequency gives the required error signal. However, since all the angular information is contained within a singular projection of the error signal, the pitch and shift information are mixed together. This is resolved by using quadrant photodiodes placed at two different locations of the field propagation. Even though it requires more quadrant photodetectors, this technique has the advantage of introducing no additional optical fields inside the interferometer. As a consequence, it was widely used in different schemes for the global alignment of the gravitational-wave detectors.

Machine learning (ML) based applications for Hermite-Gaussian (HG) mode analysis can also be found in the literature. In [124] the authors trained a convolutional neural network to classify HG-based images to high accuracies and in [125] the authors trained a convolutional neural network to perform HG modal decomposition. However a sign ambiguity is present when the modal decomposition is performed due to the lack of phase information in intensity images. This aspect was addressed in [126] where authors used a pre-trained neural network to perform modal decomposition on simulated heterodyne images and allow the complete modal phases to be predicted.

The method provided in this chapter is comparable to other machine learning approaches in HG modal decomposition. However, the practical approach of training the algorithm on real setup data and testing it within a real control scheme distinguishes it from the other methods and to the best of our knowledge, it is the first time this method has been tested.

5.2 Deep Learning

Artificial Intelligence (AI) is one of the most important areas of study in computer science. Machine learning is a subfield of artificial intelligence whose primary objective is to enable computers to learn from data without being specifically programmed to do so. Therefore, the performance of an algorithm on a certain learning task depends on the representation of the data it receives as input.

In recent years, the natural sciences, and gravitational-wave research in particular, have seen a proliferation of machine learning applications [127, 128]. These emphasize data-intensive disciplines, such as data analysis and detector characterization, but also areas of detector noise reduction. Two particular examples are: the demonstration that machine learning can achieve comparable performance with matched filtering for gravitational-wave searches [129] and gravitational-wave data denoising via subtracting the non-linear and non-stationary noises that couple to the interferometer output signal [130, 131].

Artificial neural networks (ANN) are a category of ML algorithms that execute computations using an architecture inspired by the human brain [132]. The *perceptron* is a key computational architecture in ANN [133]. This generates an output z by computing a weighted sum of its inputs x_i ($z = \omega_1 x_1 + \omega_2 x_2 + \mathbf{x}^T \mathbf{w}$) and then applying a Heaviside step function. A simple perceptron can be employed as a binary classifier; i.e., a linear combination of the input values is computed, and if the result exceeds a specified threshold, an output that belongs to one of the two classes is generated, and vice versa for a negative threshold (similar to a Logistic Regression).

The real power of the perceptrons comes when multiple of them are stacked together and they gain the ability of non-linear function approximation. Multi-layer perceptrons perform a series of intermediate operations between the input and the output layers at the level of the *hidden* layers. When all the neurons in one layer are connected to all the neurons in the previous layers, the layer is called *fully connected* or *dense layer*. A simple diagram showing the artificial neural unit and a dense layer is presented in Figure 5.3. A deep neural network is such a computational architecture containing multiple hidden layers.

Historically, training the multi-layer perceptrons was difficult. A groundbreaking paper by Rumelhart, Hinton and Williams solved this problem by introducing the idea of backpropagation [134]. This method depends on the gradient-descent algorithm, but with an efficient mechanism to automatically compute the gradients of the parameters. As the backpropagation algorithm traverses the network once in both directions, it is possible to calculate the gradient of the network error with respect to each basic model parameter, so revealing how the weights and biases of the layers should be adjusted to lower a defined loss function for the particular task. Every iteration of this method is known as an *epoch*.

The backpropagation algorithm replaces the step activation function with the logistic *sigmoid* function σ ($\sigma = \frac{1}{1+e^{-z}}$) in order to allow the calculation of gradients,

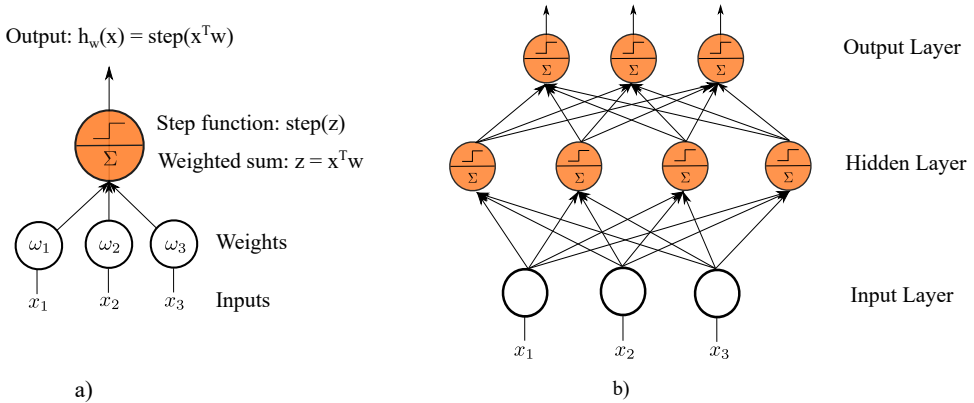


Figure 5.3: A diagram illustrating the building blocks of artificial neural networks. The perceptron takes a vectorized input and calculates a weighted sum of its constituents with its output conditioned by the step function.

which are used to update the weights of the neural network during backpropagation. The step activation function outputs a binary value (e.g., 0 or 1) based on whether the input is above or below a certain threshold, with its derivative being given by the Dirac delta function. On the other hand, the sigmoid function is a smooth and differentiable function that maps the input to a value between 0 and 1.

For the study presented in this chapter, *softmax* activation function is used. This is a generalization of the sigmoid function used in the multi-class ML tasks. It is defined as follows:

$$\text{softmax}(\mathbf{z})_i = \frac{\exp z_i}{\sum_j \exp z_j}, \quad (5.9)$$

where i and j correspond to the indexes of the input and output vectors respectively.

Machine learning applications require different degrees of human supervision. In this work, the algorithm is *supervised*. The training data set that is fed to the algorithm contain the required solutions called *labels*. This type of training can be performed for many applications, such as regression or binary classifications. Here, the algorithm performs multiclass classification. Given a set of beam profile images, the algorithm recognizes the mode number associated with each image.

5.2.1 Convolutional neural networks

Convolutional neural networks (CNNs) are a specialized type of neural networks on the analysis of grid-like structured data input. They were made popular in the late 1980s to the end of 1990s with a notable work from Yann LeCun developing *LeNet* [135], and showing that it performs better than other machine learning algorithms in pattern recognition tasks. In recent years, with the increase of computational capabilities world-wide, CNNs became popular again as a result of their success in the image recognition-type tasks [136, 137].

The main characteristic of the CNNs is given by the convolutional filters or *kernels*. These are analogous to the computational nodes in an artificial neural network, but with the operation performed being convolution. In ML-based computer vision applications, the input is usually a multidimensional array containing the pixels of the image data set, and the filter is a multidimensional array containing the parameters that are adapted by the learning algorithm. The convoluted output $S_{i,j}$ over a two-dimensional image I of size $(i \times j)$ can be written as:

$$S(i, j) = (I * K)(i, j) = \sum_m \sum_n I(m, n)K(i - m, j - n). \quad (5.10)$$

Here, K is the two-dimensional filter applied to the input image. This operation is presented graphically in Figure 5.4. It can be seen that the filter slides only by one element as it is applied. This variation is called *stride*, and it is at the power of the programmer to define it.

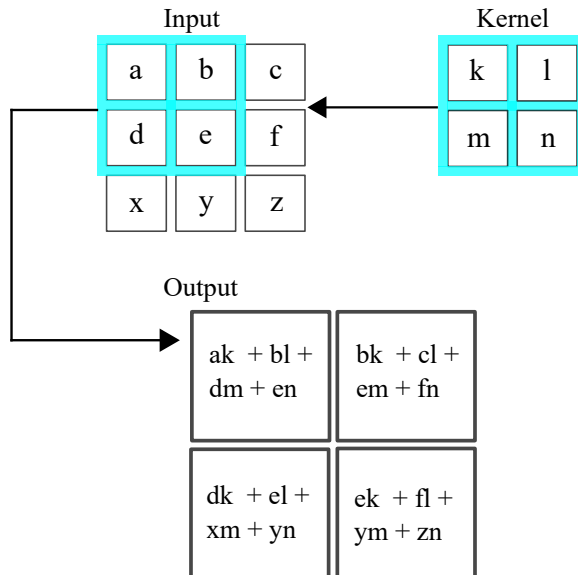


Figure 5.4: The convolution operation performed by the kernel at the level of the convolutional layer in a CNN. The kernel is a 2×2 matrix with randomly chosen weights for each element in the matrix. Each kernel element multiplies the corresponding input vector element that it is covering. The multiplications are summed together and result in the kernel output. The output is calculated only for the positions where the kernel lies fully on the image.

Usually, a deep CNN contains multiple layers of operations with both similar and different functionalities. Additional to the affine transformation at the convolutional stage presented earlier, the convolutional layer contains a non-linear detection stage and a *pooling* stage. A diagram depicting a typical CNN algorithm is shown in Figure 5.5.

The detection stage takes the set of linear activations produced by the convolutional stage and runs it through non-linear activation functions. The most popular and the one used in this work is the *Rectified-linear* (ReLU) function. The stage is named *Rectified-linear Unit* (ReLU). The rectified linear activation function is a basic calculation that returns the input value x or 0 if the input is less or equal to 0:

$$f(x)_{ReLU} = \max(0, x). \quad (5.11)$$

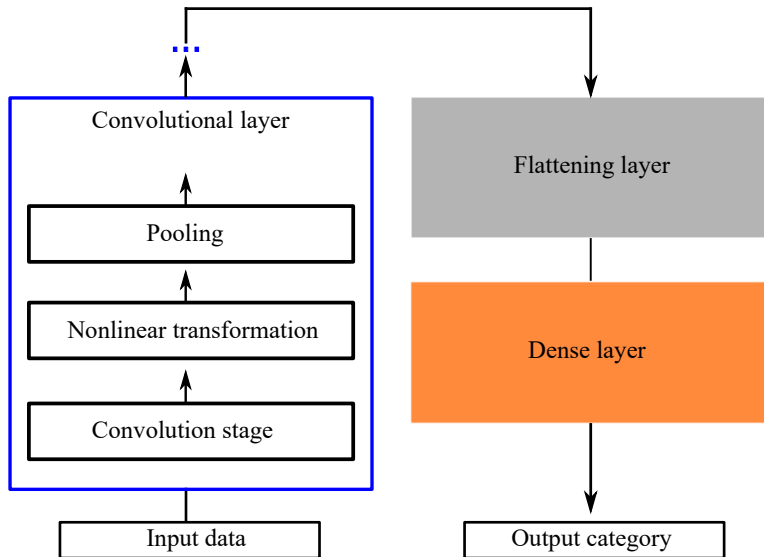


Figure 5.5: The figure shows a schematic diagram depicting a typical layer structure of a CNN algorithm. The convolutional layer contains multiple operations that are repeatable. In a deep CNN, the entire convolutional block connects in series with other similar blocks. Additionally, the dense layer can also repeat multiple times.

In the pooling stage, the output of the convolutional filter is further processed after going through the non-linear activation function. This substitutes the output with a rectangular grid containing a summary statistic of nearby outputs. The pooling function can execute a variety of different actions. The *max pooling* algorithm, for instance, computes the maximum output in a rectangular region. Pooling is a standard approach to constructing CNNs. This stage has the advantage of making representations or learned features nearly invariant to input translations. If the image is slightly skewed or the pixels are adjusted, the majority of the outputs from the convolutional layer remain unchanged.

The *flattening* layer takes this multidimensional data after the pooling stage and transforms it into a vector. This flattened representation of the data is finally inserted into the artificial neural network constructed by the *dense layer*.

5.3 Test setup

The test setup includes a Fabry-Perot suspended optical cavity by means of simple pendulums which can be actuated in two degrees of freedom. The full setup, together with the classical control pipeline was built by Rob Walet at Nikhef. This is explained in more detailed in his PhD thesis [138]. A simplified diagram of the optical components of the setup is shown in Figure 5.6.

The laser beam passes through a polarizing beam splitter (BS21) which reduces the light power in half to about 70 mW. The light then passes through the quarter wave-plate and creates a circularly polarized light for the linear cavity. The beam then enters the suspended cavity formed by the input test mass (ITM) and the end test mass (ETM). The light reflected from the cavity is also reflected by the polarizing beam splitter (BS21) towards the detectors.

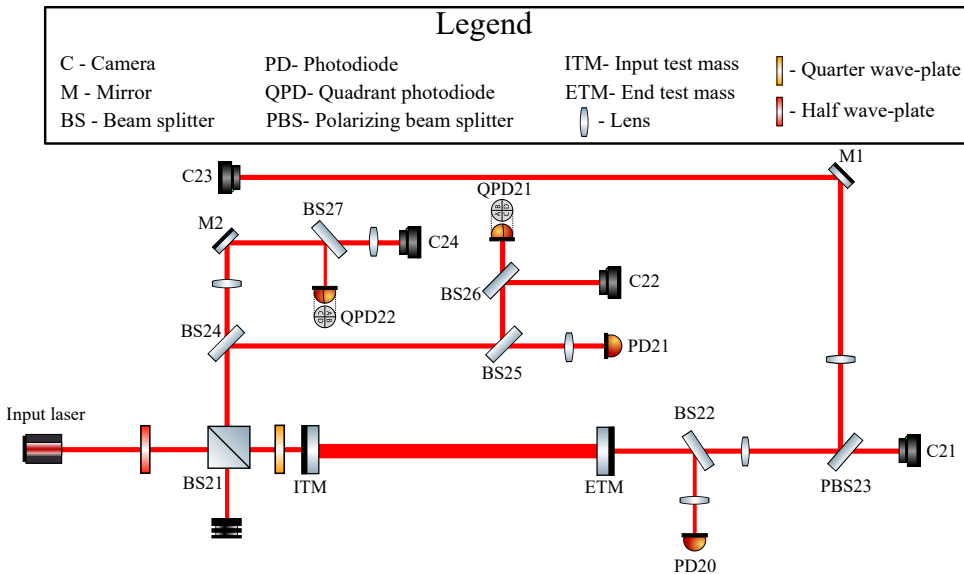


Figure 5.6: The figure depicts the simplified optical setup of the resonant cavity used for the alignment demonstration. All the optical components are housed inside a windshield with aluminium pillars and 2 mm thick plates.

Conventional error signals are produced using the signal from the transmission photodiode (PD20) and the reflection photodiode (PD21). Different phase cameras investigate the mode content of the beam. These are placed in transmission and reflection, in both near and far-field. The near-field camera (C23) images are the ones extracted as input data in this work. The convex lens placed before this camera has a long focal distance that maintains the quality of the light-field wavefront.

The real-time control is performed using MicroLabBox, a commercial, ready-to-use system from dSPACE which incorporates real-time programmable software and hardware systems. The MicroLabBox unit is based on a 2 GHz dual-core processor and contains a field-programmable gate array (FPGA). The unit performs at 10 kHz with one sample measured delay.

The data-acquisition system contains 24 analog-to-digital (ADC) channels of 16 bits, and eight digital-to-analog (DAC) channels. The channel's input/output signals range at ± 10 V. The control scripts and the model-based hardware is created in Matlab Simulink by Rob Walet.

The data set images are acquired by four monochrome light cameras of type *DMK 37BUX287* from Imaging Source Europe GmbH. The devices feature an external hardware trigger which allows to condition in real-time the image capturing via the error signals from the digital outputs of the dSPACE MicroLabBox. Being equipped with a USB 3.1, the cameras enable a throughput of 612 images per second at a resolution of 640×480 pixels. The photons are captured by the *Sony IMX287LLR* sensor with a pixel size of $6.9 \times 6.9 \mu\text{m}$. In order to control the saturation, the exposure time and the electronic gain of the sensor can be calibrated. For the photos used in this work, taken at the resolution of 640×480 pixels, the gain was set to 0 dB and the exposure time to $1/3414$ seconds. Based on the constraints from the writing speed to disk, the images from this work were acquired at 170 frames per second.

5.4 Data set

The data set comprises of 30103 near field camera images which are unprocessed. Examples of different higher-order TEM modes captured in the images are shown in Figure 5.7. The images are then pre-processed in two stages. At the beginning, the raw images are labelled, by scanning their content using a conventional pattern recognition algorithm. In the second stage, the images are cropped and the data set is transformed into vector space as input to the CNN pipeline.

5.4.1 Labeling

The labeling is performed by finding the dominant features in the images and counting them. In the case of the higher-order transverse electromagnetic modes, as shown in Figure 5.7, the number of resolvable circular patterns N is counted and the mode number is calculated as $N - 1$. Since the demonstration considered a mirror actuated in only one degree-of-freedom, non-zero vertical modes, such as TEM₂₂, is not acquired in the data.

To maximize the power of the algorithm, the images are turned into binary sets (formed by only white and dark pixels). The procedure of morphological closing is performed on the binary set. This removes small anomalies or *holes* in the representation, if present. The computation is performed using the *binary_closing*

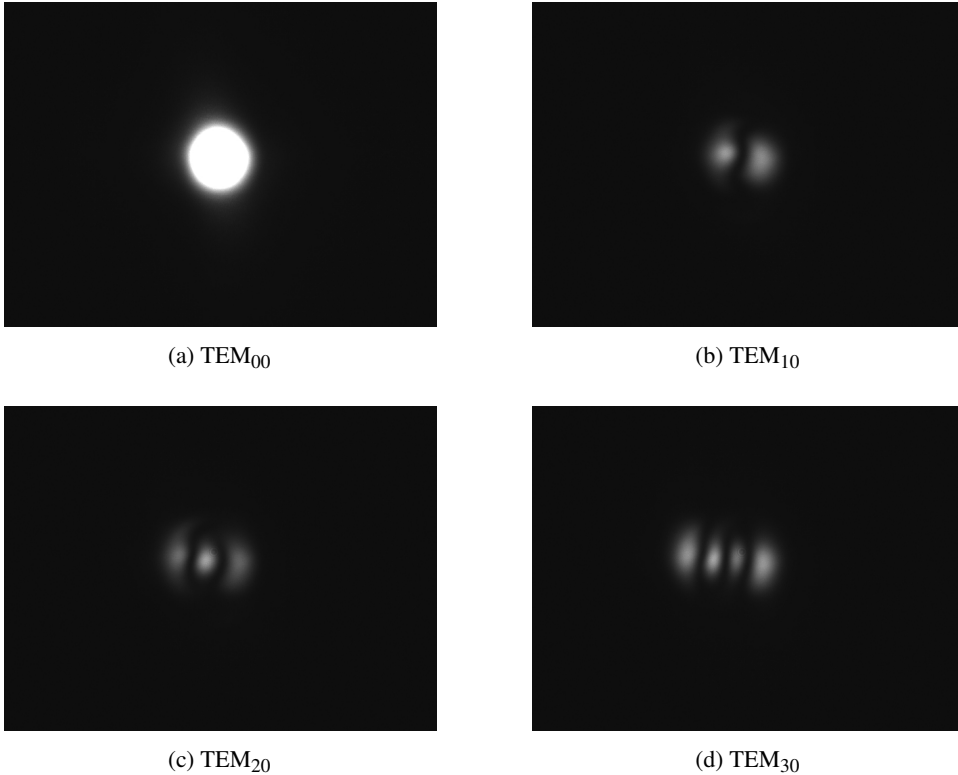


Figure 5.7: Examples of raw images from the data set used for training the machine learning algorithm. The images depict different higher-order transverse electromagnetic modes selected randomly from the full set of images during the free swing of the cavity test masses.

module from *scikit-image* python package [139]. Then, the application of the *label* module from *ndimage* in *SciPy* [140] calculates the number of features. The full process is shown in Figure 5.8.

Before processing the images, the labelling content was investigated. Some very large mode number labels were present in the data. These can be attributed to either statistical errors of the morphological detection algorithm or the cavity passing different phases of very large misalignment which can create images with large mode numbers. For simplicity of the demonstration, every image with a label above mode number 5 was removed from the data. The resulting data set and the mode content is shown in the Figure 5.9.

5.4.2 Pre-processing

The pre-processing of data is the stage where the images are prepared to appropriate shapes and representations as input to the machine learning pipeline. It consists on cropping the images and transforming the representation into the vector space.

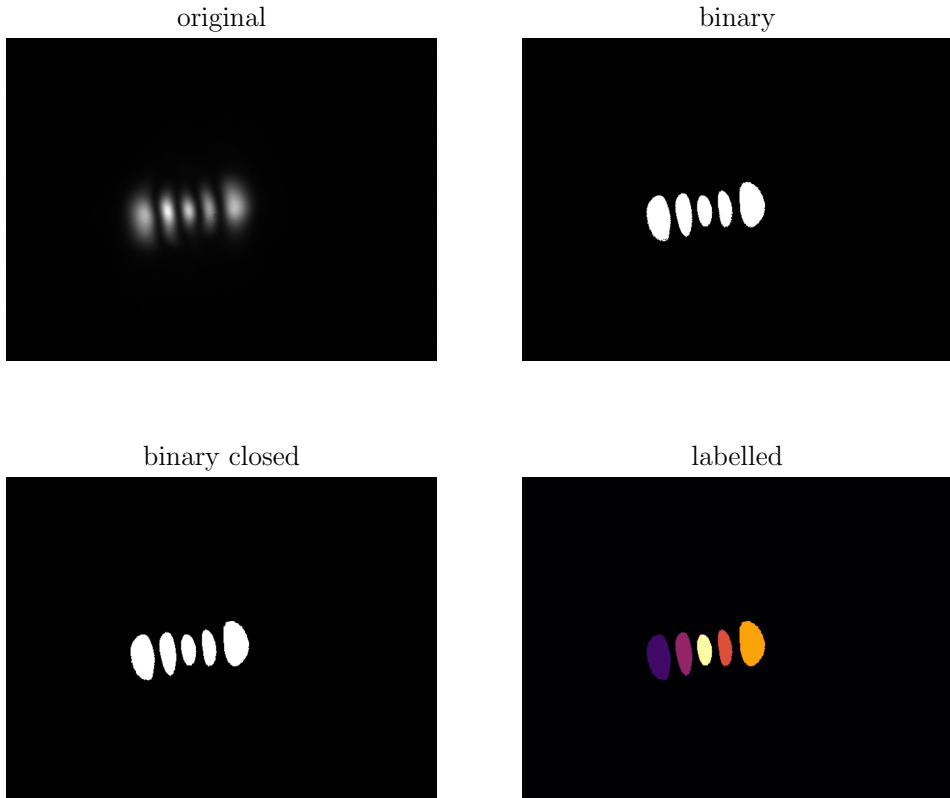


Figure 5.8: The process of the feature extraction algorithm and labeling for one image example from the training data set. The algorithm detects 5 morphological features on the image, which corresponds to a TEM mode number of 4.

Cropping ensures that the size of the sample is reduced, which improves the training time and the performance of the classification algorithm. Cropping is performed manually, by finding an appropriate rectangle that encloses the representation in multiple higher-order mode images. This is performed using Python Imaging Library (PIL) [141].

Turning the images into the vector space is required for the common computational basis with the convolutional network layers. This is performed using the *img_to_array* module from the *Keras* [142] library. The size of the arrays are reduced to 64×64 pixels. This is an empirical number based on network performance versus the computational time from multiple training runs. The images are then split into training and testing data sets, as shown in Figure 5.9. The training set is 80% of the full data set.

Scaling the pixel values is the final step before feeding the data to the CNN algorithm. Without normalizing, the range of possible pixel values is between 0 and 255. During forward propagation, the dot product is calculated between

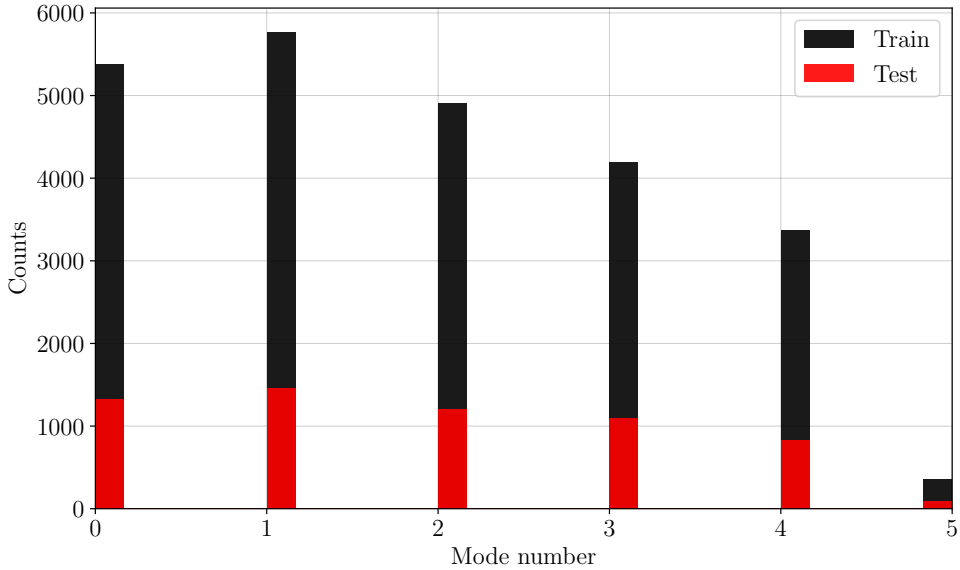


Figure 5.9: The histogram shows the population of images by mode content. There are 23,974 images forming the full training set and 5,994 images forming the testing or validation data set. Patterns corresponding to TEM₅₀ are less than 1.5% compared to the other morphologies. This affects the accuracy with which TEM₅₀ modes are recognized.

big matrices containing these pixel values and their respective weight matrices. Without normalization, the computing procedure can be cumbersome, and the lack of adaptability can compromise the precision of the results. Therefore the numerical distribution of pixel values is scaled between 0 and 1 after dividing the entire array by 255. An example of a vectorized and cropped mode pattern after pre-processing is given in Figure 5.10.

5.5 The convolutional neural network algorithm

The model is constructed using the *Keras* application programming interface of Google *Tensorflow* [143]. It is a novel algorithm, constructed based on trial and error iterations searching for the best accuracy results with changing the network parameters, such as the kernel number, their size, and the number of hidden layers. The final architecture that was used in the locking tests is shown in Figure 5.11.

The convolutional neural network comprises of three hidden layers formed by convolutional and MaxPooling stages. The first two stages are similar in size, with 64 filters each of size 3×3. The last hidden layer contains 32 filters being applied on the 3×3 grid. The convolutional stages contain the ReLU activation function. The MaxPooling operation is performed within a 2×2 grid and similar for all three layers.

The features extracted after the convolutional stage is flattened into a column

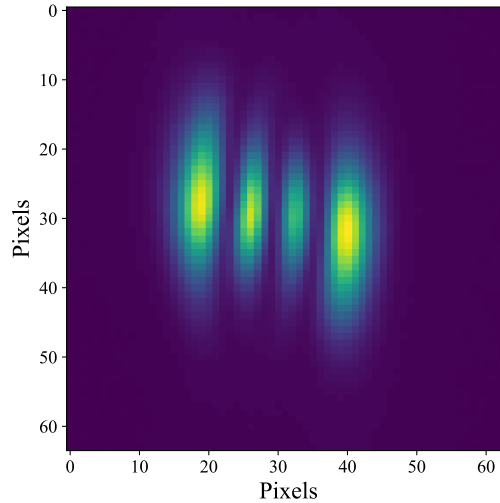


Figure 5.10: The figure illustrates a processed camera image depicting a higher order TEM mode. The image has been cropped and turned into vector space yielding a 64 by 64 pixels representation of the actual pattern recorded by the camera in the experiment.

vector of size $(1, 1568)$ by the Flattening layer. Therefore, the Flattening layer produces a 1D feature vector with 1568 elements for a batch of input data. This Flattening layer output size is determined by the size of the feature maps produced by the convolutional and pooling layers. The results are then input to the fully connected stage. The first layer contains 100 artificial neurons. This value is chosen based on trial and error iterations with monitoring the accuracy of the classification. The second layer contains six artificial neurons which correspond to the number of higher-order modes which should be classified by the system. A softmax activation function is used in the output of the layer to assign probabilities, between 0 and 1, for each image representing a particular mode number.

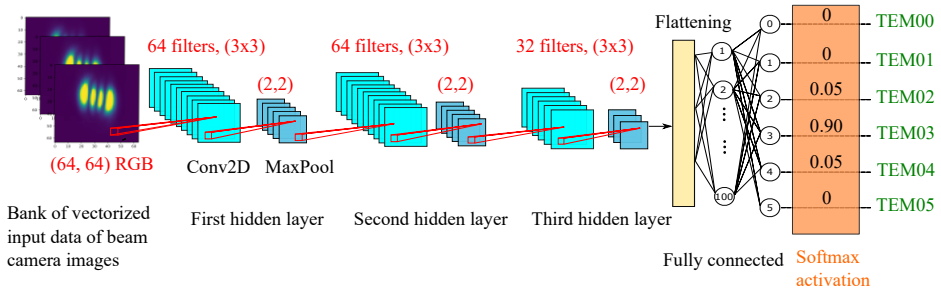


Figure 5.11: The architecture of the CNN algorithm used in the demonstration. The example depicts an image with a mode number three being correctly classified by the network.

The neural network contains 213,538 total trainable parameters which are optimized with each training epoch. These include the weights and biases of each layer in the network.

5.5.1 Training

During the training, the entire data set is passed in batches of 64 images to the machine learning algorithm, and with each epoch, its constituent parameters are updated in order to minimize the loss function. The training performance can be assessed with respect to the training and validation accuracy and the training and validation loss.

The variation of both metrics is illustrated in Figure 5.12. If the performance on the training data set is superior to the performance on the validation data set, the algorithm has learned to characterize noise, also known as *overfitting*. If the behaviour of these two metrics are reversed, the model *underfits* and can still be improved.

From both figures, it can be observed that the model converges very fast to a good performance. This fast convergence could suggest that the model is able to quickly learn the patterns and features in the training data and generalize well to the test data. This may indicate that the model architecture and hyperparameters are well-suited to the problem at hand. However, while this model performs well for the given data-set, it is important to be re-trained and re-tune to accommodate new data-sets for other tests, such as recognizing patterns when multiple cavity degrees of freedom are being sensed.

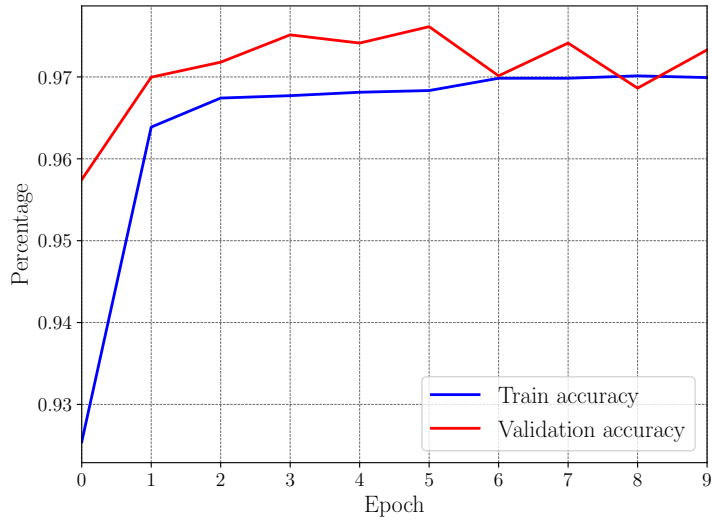
After about five epochs, the model starts to overfit the data, with the validation accuracy decreasing and the validation loss increasing. During the lock test, the model was trained for about five epochs.

5.5.2 Testing

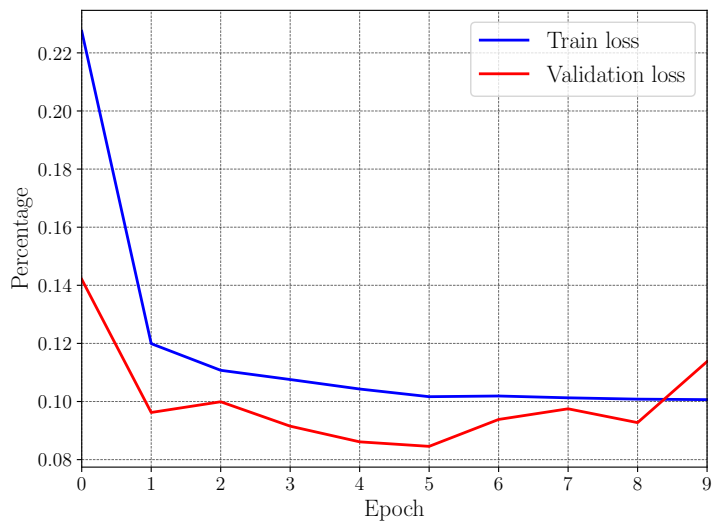
Testing is performed on 20% of the data set. When the mode content of the test images are predicted correctly, this is regarded as a True-Positive (P_{TP}). On the contrary, when an undesired class is determined correctly, the probability is assigned as a True-Negative (P_{TN}). In case of false predictions, the probabilities are either False-Negatives (P_{FN}) or False-Positives (P_{FP}). An ideal classifier returns no false predictions. The overall performance of a machine learning classifier can be understood through the balance of two metrics: the *precision* and the *recall*. The precision is the accuracy of the positive predictions, with its probability defined as:

$$P_P = \frac{P_{TP}}{P_{TP} + P_{FP}}. \quad (5.12)$$

The recall, also known as *sensitivity* represents the fraction of relevant patterns



(a) Training and validation accuracy.



(b) Training and validation loss.

Figure 5.12: The two figures show the evolution of performance metrics with each epoch during training. The training accuracy and loss show that the model converges very fast at the middle point. The testing metrics help with early-stopping the model and avoid incorrect fitting of the data.

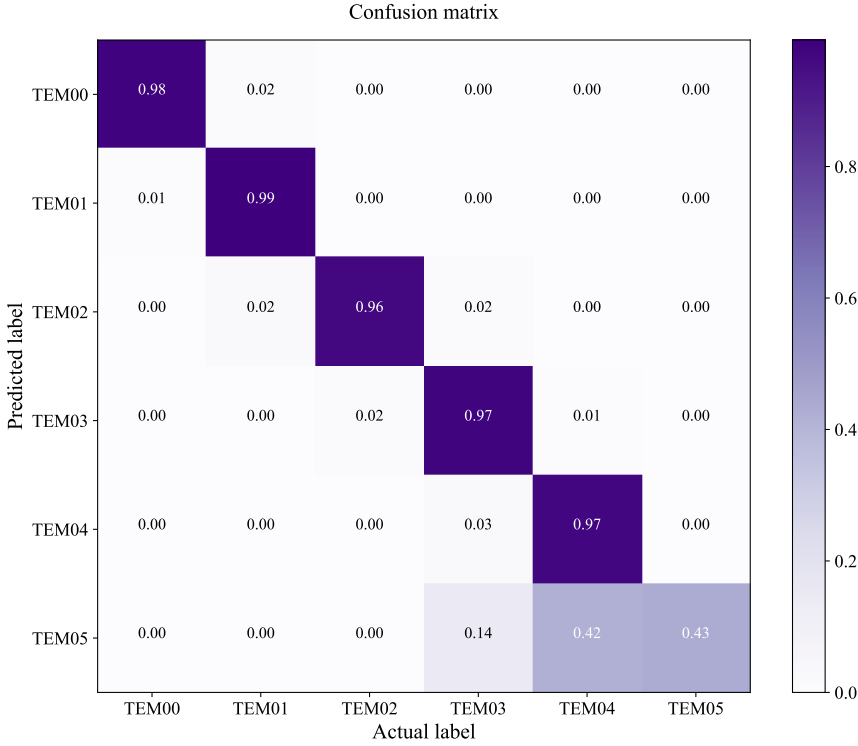


Figure 5.13: The normalized confusion matrix. Each row in the matrix corresponds to a predicted mode number by the algorithm. Each column represents an actual class. The highlighted values on the diagonal represent probabilities of correct mode detection. The off-diagonal elements are errors and add noise to the control algorithm.

that are successfully retrieved, and is defined as:

$$P_R = \frac{P_{TP}}{P_{TP} + P_{FN}}. \quad (5.13)$$

The metrics are also illustrated by the confusion matrix plotted in Figure 5.13. This shows the classification performance of the algorithm defined by the accuracy of labelling various mode numbers. The model was trained for ten epochs, corresponding to the performance depicted in Figure 5.12. The figure shows that the True Positives are almost entirely representative of the classification. The data corresponding to mode number five was poorly classified, with a True Positive rate of 0.43, almost equal to the False negative rate of 0.42. Therefore, this number of errors in both directions signify an imbalance performance that is due to the lower availability of training data for TEM₅₀, as it can be seen in Figure 5.9.

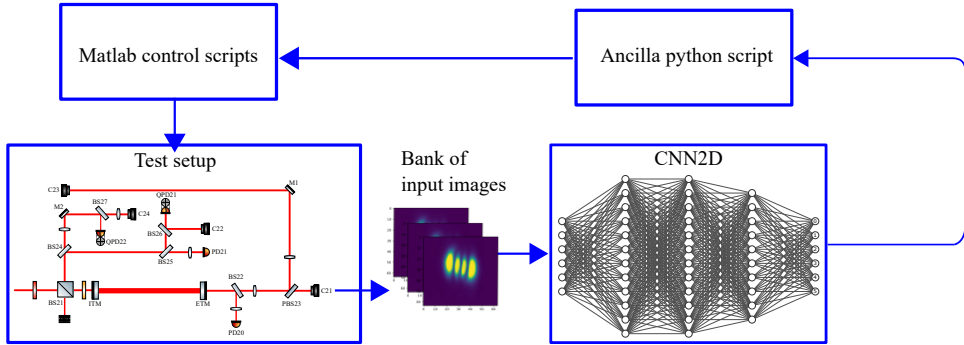


Figure 5.14: A schematic diagram showing the interaction between different procedures forming the pre-alignment and locking scheme of the resonant cavity.

5.6 Pre-alignment and cavity lock test

The ML pattern recognition algorithm was integrated into the full control scheme of the cavity. The following steps presented in the diagram of Figure 5.14 are taken inside the live classical control algorithm run in MATLAB [138]:

- The test setup is initialized, with the dSPACE Microlab box being checked.
- Interface the Microlab dSPACE control variables and perform the camera image trigger sequence.
- Execute an ancillary script which load the pre-trained weight matrices of the neural network and outputs the mode content for new images.
- The mode contents are used as error signals with a gain assigned to each class. The algorithm updates the angular setpoints based in the gains and pushed the mirror to the linear control regime.
- Once the linear regime is reached, PDH error signals are generated to lock the cavity on resonance.

A prealignment result is shown in Figure 5.15.

The network speed in recognizing the mode content is around 4.4 ms per image, which gives a theoretical frame rate of at least 225 Hz. This compares well with the simple binary closed algorithm which computes the labelling content at around 80 Hz frame rate. At the time of the conducted experiment, the latency of image storage on disk limited the frame rate to about 170 Hz. Therefore, the machine learning algorithm achieves the calculation of the mode numbers without adding additional latency to the computational framework of the control unit, condition not met by the labelling algorithm alone.

Regarding the conducted test, there are two crucial factors to consider. When the algorithm recognizes the mode pattern from the photos and activates the feedback

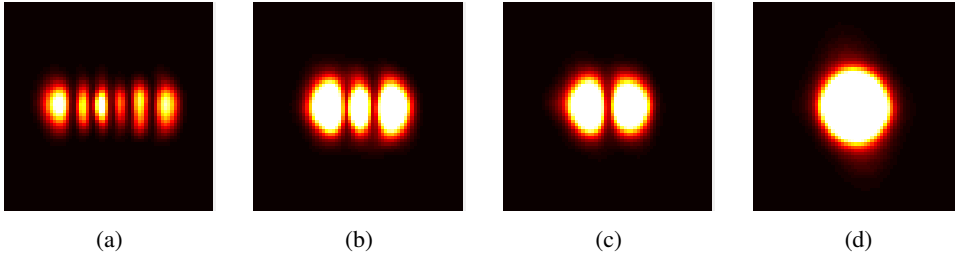


Figure 5.15: The figure depicts a sequence of images obtained during the machine learning-based auto alignment test. As higher mode patterns are recognized by the pre-trained CNN, the angular offset of the test mass is reduced producing lower mode patterns and reaching the linear control regime where the longitudinal mode is engaged.

controller, the right sign for the controller to turn the mirror is the opposite of the sign used by the controller to misalign the test mass. Therefore, for one degree-of-freedom cavity misalignment during a test mass free swing, the algorithm must address the degeneracy caused by the creation of comparable patterns at two opposite angles. In this situation, a memory function that provides feedback to the controller must be implemented. The memory function should determine if the mode number of the image at a specific instance is less than or equal to the mode number of the image at a later instance. If the condition is true, the sign of the controller's correction remains unchanged; otherwise, the sign changes. Secondly, operating an optical cavity with two freely-moving test mirrors depends heavily on the number of degrees of freedom that imprint unique patterns on the camera images and the ability to recognize them. In the absence of such a test, one can only hypothesize that if the memory function technique is successful in managing a freely swinging test mass, then it can also be used to more than two degrees-of-freedom.

5.7 Conclusions

Detecting the misalignment of optical cavities in a gravitational-wave interferometer and having the ability to quickly and non-invasively correct it is a crucial step for the functionality and duty cycle of the detectors.

There are various ways in which commissioners use the information about the misalignment of test masses to convert it into error signals for the automatic feedback correction loops.

This work proposed a fast and automatic coarse alignment of optical cavities using pattern recognition by deep neural networks. The field pattern of the transverse electromagnetic mode is used as a morphological error signal for the pre-alignment sequence.

Using a test setup built at Nikhef, raw monochrome images are obtained in the near field of a resonant cavity during free swings of the end test mass in one angular

degree of freedom. The images are then labelled in six classes based on their mode number and transferred into vector space.

A two-dimensional convolutional neural network was created to classify the images based on their mode number. This was trained on the 80% of the data-set, with 20% allocated for validation. The algorithm generalizes very fast in a few epochs, after which it starts to overfit the data. The performance is almost perfect for the first five transverse modes, with only a 43% detection accuracy for the last mode due to its low presence in the training data set. The algorithm detects the mode pattern at a frame rate of at least 225 Hz, depending on the quality of the laser beam alignment and mode-matching. A further frame rate increase for a potential application in real gravitational-wave detectors can be achieved by employing a variety of optimization strategies. These include CNN model optimization, hardware acceleration by running the tests on graphic processing units and run-time optimization techniques which remove unnecessary operations or fuse operations together for improved efficiency.

The algorithm was successfully integrated into a sequence of control scripts to lock the resonant cavity. The recognized mode numbers each had a gain number assigned inside the control and actuation script which steadily rotates the mirror to its correct position and triggers the linear Pound-Drever-Hall error signal control.

The advantage of the algorithm relies in its modularity. Despite the fact that the experiment demonstrated the alignment of a singular degree of freedom which is non-degenerate, the algorithm can be trained to recognize patterns of multiple degrees of freedom and be transformed in a multi-modal learning using the time domain information to enhance the representation of the error signals. In this way, the technique can be extended to global interferometric control and mode matching. However, challenges are to be overcome when dealing with non-degenerate degrees of freedom. The patterns produced by the misalignment of mirrors can be difficult to recover and in the case of pure patterns, the gain application should change to a technique that incorporates a record of previous corrections.

Synthesis and overall conclusions

The full realization of the gravitational-wave science will be achieved when a network of gravitational-wave instruments probe the full observational spectrum of gravitational radiation, from extremely low frequency regimes ($f \sim 10^{-15}$ to 10^{-18} Hz) to very high frequencies ($f \sim 1$ to 10^4 Hz). Einstein Telescope aims to be the next leap forward in ground-based gravitational-wave interferometry, building upon the success of the current second-generation detectors like Advanced LIGO and Virgo.

While sharing the core instrumental principles of laser interferometry for gravitational-wave detection, the Einstein Telescope aims to achieve a tenfold improvement in sensitivity through advancements in several key areas. These include a significant increase in arm length of at least 10 km, a different optical topology based on three detectors arranged in a triangular configuration each comprising of two interferometers optimized for different observational bandwidths, as well as the underground placement of the full detector.

Proven technologies from the current observatories will be employed by Einstein Telescope. One example of such technology is given by the strategy for controlling the multitude of optical degrees of freedom at predefined operating points to achieve maximum sensitivity and enable active null operations. These degrees of freedom are formed by both longitudinal and angular displacements of the suspended mirrors forming the resonant optical cavities of the interferometer. Chapter 2 of this thesis provides a detailed examination of the Advanced Virgo Interferometer's radio-frequency control signals during a period when the detector is in an active operational state, in February 2020. By comparing the simulated amplitudes of these signals with the experimental values, the analysis emphasizes the significance of monitoring the full spectrum of control signals when bringing the

detector towards its final operational state. This helps prevent saturation of control electronics and ensures proper control of the interferometer to its set point when gravitational waves are detected. Furthermore, Chapter 5 proposes a novel method of automatically controlling the angular degrees of freedom of suspended optics. This method can align a suspended mirror based on an error signal formed by pattern recognition via machine learning of transverse electromagnetic modes generated when a mirror is misaligned. By demonstrating it experimentally on a suspended optical cavity, it is concluded that the method can help the commissioning of current and future gravitational wave instruments, potentially increasing the duty cycle of the observatories.

Typically, large physical observatories need to undergo technological validation and operational de-risking in smaller test setups. ETpathfinder is a cryogenic research and development laboratory focused on testing essential technologies for the Einstein Telescope and other third-generation advanced gravitational-wave detectors. This facility comprises two folded interferometers with arm lengths of 10 meters each which operate at different temperatures and laser wavelengths. Chapter 3 of this thesis explores the fundamental noise sources that are projected to define the performance of the ETpathfinder testbed. By modeling the displacement sensitivity of each interferometer, this chapter helped with understanding how different physical effects couple to the ETpathfinder test masses. Ultimately, this leads to optical design optimization such that the sensitivity of ETpathfinder interferometers is limited to noise sources relevant for next-generation detectors, such as coating Brownian noise in the middle detection band or radiation pressure noise at lower frequencies. As a result, ETpathfinder will act as a testbed for directly testing interferometric operations with new methods that can limit these relevant noise sources. In Chapter 4, the simulated noise budget from Chapter 3 is used as a reference to project the technical noise that originates from vibrations during the cooling of test masses via conduction at cryogenic temperatures. The chapter details the experimental efforts conducted in a dedicated test setup to measure the acoustic vibrations transported by soft links acting as cooling connections between the interferometer's test masses and the cryocoolers. The measured transfer function is used to calibrate the analytical models, enabling a thorough simulation of the passive vibration isolation chain in the ETpathfinder and low-frequency Einstein Telescope. Therefore, the complete transfer function model and the ETpathfinder noise budget baseline can be used to optimize the design of a cryogenic system such that the mirror cooling does not introduce residual noises that limit the fundamental noise sources relevant for the next generation interferometers.

Appendix A: Error signal derivation in the presence of a higher-order transverse electromagnetic mode

Starting from the reflected electromagnetic field containing the carrier and the scattered higher order mode component:

$$\begin{aligned}
 E_{ref} = & E_{00} \left[F(\omega_1) J_0(b) e^{i\omega_1 t} + F(\omega_1 + \Omega) J_1(b) e^{i(\omega_1 + \Omega)t} \right] \\
 & - E_{00} \left[F(\omega_1 - \Omega) J_1(b) e^{i(\omega_1 - \Omega)t} \right] \\
 & + E_{10} \left[F(\omega_2) J_0(b) e^{i\omega_2 t} + F(\omega_2 + \Omega) J_1(b) e^{i(\omega_2 + \Omega)t} \right] \\
 & - E_{10} \left[F(\omega_2 - \Omega) J_1(b) e^{i(\omega_2 - \Omega)t} \right],
 \end{aligned} \tag{1}$$

as the field reflects off the cavity, one has to multiply it with the complex reflectivities corresponding to each amplitudes. The TEM_{00} amplitudes are multiplied by $F(\omega_1)$:

$$F(\omega_1) = \frac{-r_1 + r_2 (r_1^2 + t_1^2) e^{\frac{i\omega_1}{FSR}}}{1 - r_1 r_2 e^{\frac{i\omega_1}{FSR}}}, \tag{2}$$

while the TEM_{10} components are multiplied by $F(\omega_2)$:

$$F(\omega_2) = \frac{-r_1 + r_2 (r_1^2 + t_1^2) e^{\frac{i\omega_1}{FSR} + \frac{iv_{nm}}{FSR}}}{1 - r_1 r_2 e^{\frac{i\omega_1}{FSR} + \frac{iv_{nm}}{FSR}}}. \tag{3}$$

The resultant photocurrent impinging on the photodiode, $P_{PD} = E_{ref} \cdot \overline{E_{ref}}$ is

expanded as follows:

$$\begin{aligned}
P_{PD} = & \left[P_{c0}F(\omega_1)\overline{F(\omega_1)} + P_{s0}F(\omega_1 + \Omega)\overline{F(\omega_1 + \Omega)} \right. \\
& \left. + P_{s0}F(\omega_1 - \Omega)\overline{F(\omega_1 - \Omega)} \right] \\
& + \left[P_{c1}F(\omega_2)\overline{F(\omega_2)} + P_{s1}F(\omega_2 + \Omega)\overline{F(\omega_2 + \Omega)} \right. \\
& \left. + P_{s1}F(\omega_2 - \Omega)\overline{F(\omega_2 - \Omega)} \right] \\
& + \left[\sqrt{P_{c0}P_{s0}}F(\omega_1)\overline{F(\omega_1 + \Omega)}e^{-i\Omega t} - \sqrt{P_{c0}P_{s0}}F(\omega_1)\overline{F(\omega_1 - \Omega)}e^{i\Omega t} \right] \\
& + \left[\sqrt{P_{c0}P_{s0}}F(\omega_1 + \Omega)\overline{F(\omega_1)}e^{i\Omega t} - P_{s0}F(\omega_1 + \Omega)\overline{F(\omega_1 - \Omega)}e^{2i\Omega t} \right] \\
& - \left[\sqrt{P_{c0}P_{s0}}F(\omega_1 - \Omega)\overline{F(\omega_1)}e^{-i\Omega t} - P_{s0}F(\omega_1 - \Omega)\overline{F(\omega_1 + \Omega)}e^{-2i\Omega t} \right] \\
& + \left[P_{cm}F(\omega_1)\overline{F(\omega_2)}e^{i(\omega_1 - \omega_2)t} + \sqrt{P_{cm}P_{sm}}F(\omega_1)\overline{F(\omega_2 + \Omega)}e^{i(\omega_1 - \omega_2 - \Omega)t} \right. \\
& \left. - \sqrt{P_{cm}P_{sm}}F(\omega_1)\overline{F(\omega_2 - \Omega)}e^{i(\omega_1 - \omega_2 + \Omega)t} \right] \\
& + \left[\sqrt{P_{sm}P_{cm}}F(\omega_1 + \Omega)\overline{F(\omega_2)}e^{i(\omega_1 - \omega_2 + \Omega)t} \right. \\
& \left. + P_{sm}F(\omega_1 + \Omega)\overline{F(\omega_2 + \Omega)}e^{i(\omega_1 - \omega_2)t} \right. \\
& \left. - P_{sm}F(\omega_1 + \Omega)\overline{F(\omega_2 - \Omega)}e^{i(\omega_1 - \omega_2 + 2\Omega)t} \right] \\
& - \left[\sqrt{P_{sm}P_{cm}}F(\omega_1 - \Omega)\overline{F(\omega_2)}e^{i(\omega_1 - \omega_2 - \Omega)t} \right. \\
& \left. - P_{sm}F(\omega_1 - \Omega)\overline{F(\omega_2 + \Omega)}e^{i(\omega_1 - \omega_2 - 2\Omega)t} \right. \\
& \left. + P_{sm}F(\omega_1 - \Omega)\overline{F(\omega_2 - \Omega)}e^{i(\omega_1 - \omega_2)t} \right] \\
& + \left[P_{cl}F(\omega_2)\overline{F(\omega_1)}e^{i(\omega_2 - \omega_1)t} - \sqrt{P_{cl}P_{sl}}F(\omega_2)\overline{F(\omega_1 + \Omega)}e^{i(\omega_2 - \omega_1 - \Omega)t} \right. \\
& \left. - \sqrt{P_{cl}P_{sl}}F(\omega_2)\overline{F(\omega_1 - \Omega)}e^{i(\omega_2 - \omega_1 + \Omega)t} \right] \\
& + \left[\sqrt{P_{sl}P_{cl}}F(\omega_2 + \Omega)\overline{F(\omega_1)}e^{i(\omega_2 - \omega_1 + \Omega)t} + P_{sl}F(\omega_2 + \Omega)\overline{F(\omega_1 + \Omega)}e^{i(\omega_2 - \omega_1)t} \right. \\
& \left. - P_{sl}F(\omega_2 + \Omega)\overline{F(\omega_1 - \Omega)}e^{i(\omega_2 - \omega_1 + 2\Omega)t} \right] \\
& + \left[\sqrt{P_{sl}P_{cl}}F(\omega_2 - \Omega)\overline{F(\omega_1)}e^{i(\omega_2 - \omega_1 - \Omega)t} - P_{sl}F(\omega_2 - \Omega)\overline{F(\omega_1 + \Omega)}e^{i(\omega_2 - \omega_1)t} \right. \\
& \left. + P_{sl}F(\omega_2 - \Omega)\overline{F(\omega_1 - \Omega)}e^{i(\omega_2 - \omega_1)t} \right] \\
& + \left[\sqrt{P_{c1}P_{s1}}F(\omega_2)\overline{F(\omega_2 + \Omega)}e^{i(-\Omega)t} - \sqrt{P_{c1}P_{s1}}F(\omega_2)\overline{F(\omega_2 - \Omega)}e^{i(\Omega)t} \right] \\
& + \left[\sqrt{P_{s1}P_{c1}}F(\omega_2 + \Omega)\overline{F(\omega_2)}e^{i(\Omega)t} - P_{s1}F(\omega_2 + \Omega)\overline{F(\omega_2 - \Omega)}e^{i(2\Omega)t} \right] \\
& + \left[\sqrt{P_{c1}P_{s1}}F(\omega_2 - \Omega)\overline{F(\omega_2)}e^{-i(\Omega)t} - P_{s1}F(\omega_2 - \Omega)\overline{F(\omega_2 + \Omega)}e^{i(-2\Omega)t} \right]
\end{aligned} \tag{4}$$

The output of the mixer is the multiplication of the local oscillator signal $\sin(\Omega't)$ with the photocurrent field P_{PD} . If the above equation has the exponential terms expanded into sines and cosines terms, then the following multiplication occurs for each term:

$$\sin(\Omega t) \sin(\Omega' t) = \frac{1}{2} \{ \cos[(\Omega - \Omega')t] - \cos[(\Omega + \Omega')t] \} \tag{5}$$

The sinusoidal nature of the local oscillator results only in the imaginary terms to be selected for filtering. If the local oscillator frequency is close to the modulation frequency, then the first term in the above equation is the DC component of interest and the second term vanishes after low-pass filtering. The same can be observed when multiplying components such as: $\sin(\omega_1 - \omega_2 - \Omega) \cdot \sin(\Omega)$. Keeping only the low-pass components in the error-signal, the final photocurrent equation results, as presented in the main text:

$$\begin{aligned}
P_{PD}^{\Omega} = & + \sqrt{P_{c0}P_{s0}} \cdot \frac{1}{2} \Im \{ F(\omega_1) \overline{F(\omega_1 + \Omega)} - F(\omega_1) \overline{F(\omega_1 - \Omega)} \\
& + F(\omega_1 + \Omega) \overline{F(\omega_1)} + F(\omega_1 - \Omega) \overline{F(\omega_1)} \} \\
& + \sqrt{P_{cm}P_{sm}} \cdot \frac{1}{2} \cdot \Im \{ -F(\omega_1) \overline{F(\omega_2 - \Omega)} - F(\omega_1) \overline{F(\omega_2 + \Omega)} \\
& + F(\omega_1 - \Omega) \overline{F(\omega_2)} + F(\omega_1 + \Omega) \overline{F(\omega_2)} \} \\
& + \sqrt{P_{cl}P_{sl}} \cdot \frac{1}{2} \cdot \Im \{ F(\omega_2) \overline{F(\omega_1 + \Omega)} - F(\omega_2) \overline{F(\omega_1 - \Omega)} \\
& + F(\omega_2 + \Omega) \overline{F(\omega_1)} - F(\omega_2 - \Omega) \overline{F(\omega_1)} \} \\
& + \sqrt{P_{c1}P_{s1}} \cdot \frac{1}{2} \cdot \Im \{ F(\omega_2) \overline{F(\omega_2 + \Omega)} - F(\omega_2) \overline{F(\omega_2 - \Omega)} \\
& + F(\omega_2 + \Omega) \overline{F(\omega_2)} - F(\omega_2 - \Omega) \overline{F(\omega_2)} \}
\end{aligned} \tag{6}$$

Appendix B: Advanced Virgo Finesse base-file

```
l laser 40 0 0 nmod1
s sEOM1 1 1 nmod1 nEOM1
mod EOM1 $f1 $f1_mid 3 pm 0 nEOM1 nsEOM2
s sEOM2 0.1 1 nsEOM2 nEOM2
mod EOM2 $f2 $f2_mid 3 pm 0 nEOM2 nsEOM3
s sEOM3 0.1 1 nsEOM3 nEOM3
mod EOM3 $f3 $f3_mid 3 pm 0 nEOM3 nsEOM4

s sp_INJ_PR 0.2 1 nsEOM4 nPR1

#####PRM
m2 PRAR $R_PRAR $L_PRAR $phi_PRAR nPR1 nPRi1
s PR_sub $PR_thick $nsilica nPRi1 nPRi2
m1 PR $T_PR $L_PR $phi_PR nPRi2 nPR2

s sp_PR_POP $l_PR_POP nPR2 nPOP1

#####Pick-Off-Plate
bs2 POP2 $R_POP2 $L_POP2 $phi_POP2 $alpha_POP2 nPOP1 dump nPOPi1 dump
s POP_sub $POP_thick $nsilica nPOPi1 nPOPi2
bs2 POP1 $R_POP1 $L_POP1 $phi_POP1 $alpha_POP1 nPOPi2 dump nPOP4 nB4

#####PRCL
s sp_POP_BS $l_POP_BS 1 nPOP4 nBSs

#####BS
bs1 BS $T_BS $L_BS $phi_BS $alpha_BS nBSs nBSw nBSi1 nBSi3
s BS1_sub $BS_thick $nsilica nBSi1 nBSi2
bs2 BSAR1 $R_BSAR $L_BSAR $phi_BSAR $alpha_BSAR nBSi2 dump nBSn nB5
s BS2_sub $BS_thick $nsilica nBSi3 nBSi4
bs2 BSAR2 $R_BSAR $L_BSAR $phi_BSAR $alpha_BSAR nBSi4 dump nBSe dump

#####Interferometer West Arm

## from BS to CPW
s sp_BS_CP_W $l_BS_CP_W 1 nBSw nWin

## CP
m2 CPW1 0 $L_CPW1 0 nWin nCPWi1
```

```

s CPW_sub $CPW_thick $nsilica nCPWi1 nCPWi2
m2 CPW2 0 $L_CPW2 0 nCPWi2 nCPWi3

## Thermal Lens (at null space from CP)
s sp_CP_TL_W 0 nCPWi3 nCPWi4
lens CPW_TL $f_CPW_TL nCPWi4 nCPMW
s sp_TL_WI 0.2 nCPMW nWi1

## WI mirror
m2 WIAR $R_WIAR $L_WIAR $phi_WIAR nWi1 nWi1
s WI_sub $WI_thick $nsilica nWi1 nWi2
m1 WI $T_WI $L_WI $phi_WI nWi2 nWi2

## West cavity lenght
s sWARM $l_WARM nWi2 nWE1

## WE mirror
m1 WE $T_WE $L_WE $phi_WE nWE1 nWE1
s WE_sub $WE_thick $nsilica nWE1 nWE2
m2 WEAR $R_WEAR $L_WEAR $phi_WEAR nWE2 nWE2

#####Interferometer North Arm

## from BS to CPN
s sp_BS_CP_N $l_BS_CP_N nBSn nNin

## CP
m2 CPN1 0 $L_CP_N1 0 nNin nCPNi1
s CPN_sub $CPN_thick $nsilica nCPNi1 nCPNi2
m2 CPN2 0 $L_CP_N2 0 nCPNi2 nCPNi3

## Thermal Lens (at null distance from CP)
s sp_CP_TL_N 0 nCPNi3 nCPNi4
lens CPN_TL $f_CP_N_TL nCPNi4 nCPMN
s sp_TL_NI 0.2 nCPMN nNI1

## NI mirror
m2 NIAR $R_NIAR $L_NIAR $phi_NIAR nNI1 nNI1
s NI_sub $NI_thick $nsilica nNI1 nNI2
m1 NI $T_NI $L_NI $phi_NI nNI2 nNI2

## Nord cavity lenght
s sNARM $l_NARM nNI2 nNE1

## NE mirror
m1 NE $T_NE $L_NE $phi_NE nNE1 nNE1
s NE_sub $NE_thick $nsilica nNE1 nNE2
m2 NEAR $R_NEAR $L_NEAR $phi_NEAR nNE2 nNE2

#####SRC_mirror

## distance to dark port
s sp_BS_SR $l_BS_SR nBSe nB1p

## set NARM and WARM as reference cavities
#cav NORTH_CAVITY NI nNI2 NE nNE1
#cav WEST_CAVITY WI nWi2 WE nWE1

#####Constants
const nsilica 1.44963

```

```

lambda 1.064u

#phases used in the interferometer components

const phi_PRAR 0
const phi_PR 0
const phi_POP2 0
const phi_POP1 0
const phi_BS 0
const phi_BSAR 0
const phi_NIAR 0
const phi_NI 0
const phi_NEAR 0
const phi_NE 0
const phi_WIAR 0
const phi_WI 0
const phi_WEAR 0
const phi_WE 0

#dinstances
const l_PR_POP 0.06
const l_POP_BS 5.9399
const l_BS_CP_N 5.3662
const l_BS_CP_W 5.244
const l_NARM 2999.8
const l_WARM 2999.8
const l_BS_SR 5.943

#THICKNESSES
const PR_thick 0.1003
const POP_thick 0.03549
const BS_thick 0.074459
const CPN_thick 0.035
const CPW_thick 0.035
const NI_thick 0.20026
const NE_thick 0.2
const WI_thick 0.20031
const WE_thick 0.2

## Transmissions
#const T_PR 0.04835
const T_BS 0.5012
const T_NI 0.01377
const T_NE 4.4u
const T_WI 0.01375
const T_WE 4.3u

## Losses
const L_BS 30u
const L_NI 27u
const L_NE 27u
const L_WI 27u
const L_WE 27u

## AR Surfaces

const L_BSAR 329u
const R_BSAR 329u
const alpha_BS -45

```

```

const alpha_BSAR -29.1951
const L_WEAR 155u
const R_WEAR 0 #155u
const L_WIAR 0
const R_WIAR 58u
const L_NEAR 133u
const R_NEAR 0 #133u #?
const L_NIAR 0
const R_NIAR 32u

## POP and CPs
const R_POP2 0
const L_POP2 125u
const alpha_POP2 6
const R_POP1 184u
const L_POP1 0
const alpha_POP1 4.135015

## CPs + thermal lenses (all CPs are mirrors m2 with R = 0)
const L_CPN1 22u
const L_CPN2 44u
const f_CPN_TL 5.086e+04
const L_CPW1 87u
const L_CPW2 114u
const f_CPW_TL 5.054e+04
attr PR Rc -1477
attr WI Rc -1424.5
attr NI Rc -1424.6
attr WE Rc 1696
attr NE Rc 1695
attr PRAR Rc -3.62
attr WIAR Rc -1424.5
attr NIAR Rc -1424.6

tf suspension 1 0 z 0.7 4200 p 0.4 2578 p 0.8 5000

attr WE mass 42 zmech suspension
attr NE mass 42 zmech suspension

phase 2
maxtem 2
phase 7

const f1 6270777
const f2 8361036
const f3 56436993
const f1_mid 0.15 #frequency components
const f2_mid 0.16
const f3_mid 0.25

const f1double 12541554
const f2double 16722072
const f3double 112873986

const f1triple 18812331
const f2triple 25083108
const f3triple 169310979

cav NORTH_CAVITY NI nNI2 NE nNE1
cav WEST_CAVITY WI nWI2 WE nWE1

```

```

const L_PRAR 160u
const R_PRAR 0

const L_PR 0          #decoupled
const T_PR 1

#DC
pd B1pDC nB1p
pd B2DC nPR1
pd B4DC nB4
pd B5DC nB5
pd B7DC nNE2
pd B8DC nWE2

###B1p
pd1 B1p_6MHz_p $f1 0 nB1p
pd1 B1p_6MHz_q $f1 90 nB1p
pd1 B1p_8MHz_p $f2 0 nB1p
pd1 B1p_8MHz_q $f2 90 nB1p
pd1 B1p_56MHz_p $f3 0 nB1p
pd1 B1p_56MHz_q $f3 90 nB1p

###B2
pd1 B2_6MHz_p $f1 0 nPR1
pd1 B2_6MHz_q $f1 90 nPR1
pd1 B2_8MHz_p $f2 0 nPR1
pd1 B2_8MHz_q $f2 90 nPR1
pd1 B2_56MHz_p $f3 0 nPR1
pd1 B2_56MHz_q $f3 90 nPR1

###B5
pd1 B5_6MHz_p $f1 0 nB5
pd1 B5_6MHz_q $f1 90 nB5
pd1 B5_8MHz_p $f2 0 nB5
pd1 B5_8MHz_q $f2 90 nB5
pd1 B5_56MHz_p $f3 0 nB5
pd1 B5_56MHz_q $f3 90 nB5

###B4
pd1 B4_6MHz_p $f1 0 nB4
pd1 B4_6MHz_q $f1 90 nB4
pd1 B4_8MHz_p $f2 0 nB4
pd1 B4_8MHz_q $f2 90 nB4
pd1 B4_56MHz_p $f3 0 nB4
pd1 B4_56MHz_q $f3 90 nB4

###B7 and B7 - arm powers
pd1 B7_6MHz_p $f1 0 nNE2
pd1 B7_6MHz_q $f1 90 nNE2
pd1 B7_8MHz_p $f2 0 nNE2
pd1 B7_8MHz_q $f2 90 nNE2
pd1 B7_56MHz_p $f3 0 nNE2
pd1 B7_56MHz_q $f3 90 nNE2

pd1 B8_6MHz_p $f1 0 nWE2
pd1 B8_6MHz_q $f1 90 nWE2
pd1 B8_8MHz_p $f2 0 nWE2
pd1 B8_8MHz_q $f2 90 nWE2

```

pd1 B8_56MHz_p \$f3 0 nWE2
pd1 B8_56MHz_q \$f3 90 nWE2

#####

pd1 B1p_6MHz_p_x2 \$f1double 0 nB1p
pd1 B1p_6MHz_q_x2 \$f1double 90 nB1p
pd1 B1p_8MHz_p_x2 \$f2double 0 nB1p
pd1 B1p_8MHz_q_x2 \$f2double 90 nB1p
pd1 B1p_56MHz_p_x2 \$f3double 0 nB1p
pd1 B1p_56MHz_q_x2 \$f3double 90 nB1p

pd1 B2_6MHz_p_x2 \$f1double 0 nPR1
pd1 B2_6MHz_q_x2 \$f1double 90 nPR1
pd1 B2_8MHz_p_x2 \$f2double 0 nPR1
pd1 B2_8MHz_q_x2 \$f2double 90 nPR1
pd1 B2_56MHz_p_x2 \$f3double 0 nPR1
pd1 B2_56MHz_q_x2 \$f3double 90 nPR1

pd1 B4_6MHz_p_x2 \$f1double 0 nB4
pd1 B4_6MHz_q_x2 \$f1double 90 nB4
pd1 B4_8MHz_p_x2 \$f2double 0 nB4
pd1 B4_8MHz_q_x2 \$f2double 90 nB4
pd1 B4_56MHz_p_x2 \$f3double 0 nB4
pd1 B4_56MHz_q_x2 \$f3double 90 nB4

pd1 B5_6MHz_p_x2 \$f1double 0 nB5
pd1 B5_6MHz_q_x2 \$f1double 90 nB5
pd1 B5_8MHz_p_x2 \$f2double 0 nB5
pd1 B5_8MHz_q_x2 \$f2double 90 nB5
pd1 B5_56MHz_p_x2 \$f3double 0 nB5
pd1 B5_56MHz_q_x2 \$f3double 90 nB5

pd1 B7_6MHz_p_x2 \$f1double 0 nNE2
pd1 B7_6MHz_q_x2 \$f1double 90 nNE2
pd1 B7_8MHz_p_x2 \$f2double 0 nNE2
pd1 B7_8MHz_q_x2 \$f2double 90 nNE2
pd1 B7_56MHz_p_x2 \$f3double 0 nNE2
pd1 B7_56MHz_q_x2 \$f3double 90 nNE2

pd1 B8_6MHz_p_x2 \$f1double 0 nWE2
pd1 B8_6MHz_q_x2 \$f1double 90 nWE2
pd1 B8_8MHz_p_x2 \$f2double 0 nWE2
pd1 B8_8MHz_q_x2 \$f2double 90 nWE2
pd1 B8_56MHz_p_x2 \$f3double 0 nWE2
pd1 B8_56MHz_q_x2 \$f3double 90 nWE2

#####

pd1 B1p_6MHz_p_x3 \$f1triple 0 nB1p
pd1 B1p_6MHz_q_x3 \$f1triple 90 nB1p
pd1 B1p_8MHz_p_x3 \$f2triple 0 nB1p
pd1 B1p_8MHz_q_x3 \$f2triple 90 nB1p
pd1 B1p_56MHz_p_x3 \$f3triple 0 nB1p
pd1 B1p_56MHz_q_x3 \$f3triple 90 nB1p

pd1 B4_6MHz_p_x3 \$f1triple 0 nB4
pd1 B4_6MHz_q_x3 \$f1triple 90 nB4
pd1 B4_8MHz_p_x3 \$f2triple 0 nB4
pd1 B4_8MHz_q_x3 \$f2triple 90 nB4

pd1 B4_56MHz_p_x3 \$f3triple 0 nB4
pd1 B4_56MHz_q_x3 \$f3triple 90 nB4

pd1 B2_6MHz_p_x3 \$f1triple 0 nPR1
pd1 B2_6MHz_q_x3 \$f1triple 90 nPR1
pd1 B2_8MHz_p_x3 \$f2triple 0 nPR1
pd1 B2_8MHz_q_x3 \$f2triple 90 nPR1
pd1 B2_56MHz_p_x3 \$f3triple 0 nPR1
pd1 B2_56MHz_q_x3 \$f3triple 90 nPR1

pd1 B5_6MHz_p_x3 \$f1triple 0 nB5
pd1 B5_6MHz_q_x3 \$f1triple 90 nB5
pd1 B5_8MHz_p_x3 \$f2triple 0 nB5
pd1 B5_8MHz_q_x3 \$f2triple 90 nB5
pd1 B5_56MHz_p_x3 \$f3triple 0 nB5
pd1 B5_56MHz_q_x3 \$f3triple 90 nB5

""

Appendix C: ETpathfinder-Light noise budget

The constituent parameters which are used in the computation of ETpathfinder-Light noise budget are shown in Table 1. The noise budget is depicted in Figure 1.

Parameter	Value
Temperature [K]	123
Wavelength [nm]	1550
Arm-cavity finesse	2050
Test mass weight [kg]	3.2
Beam waist [m]	1.8×10^{-3}
Beam radius at test mass [m]	2.2×10^{-3}
Substrate Young modulus [Pa]	155.8×10^9
Substrate thermal conductivity [W/(m·K)]	700
Thermal expansion coefficient [1/K]	1×10^{-9}
Substrate specific heat [J/(kg·K)]	333.0
Thermo-optic coefficient	1×10^{-4}
Substrate loss angle	1.25×10^{-9}
Last stage suspension material	Copper Beryllium
Last stage suspension fibres diameter [m]	1.5×10^{-4}
Coating $\phi_{\text{high-n}}$	5.7×10^{-4}
Coating $\phi_{\text{low-n}}$	4.8×10^{-4}

Table 1: Parameters defining the ETpathfinder-Light configuration and used in the calculation of the noise budget from Figure 1.

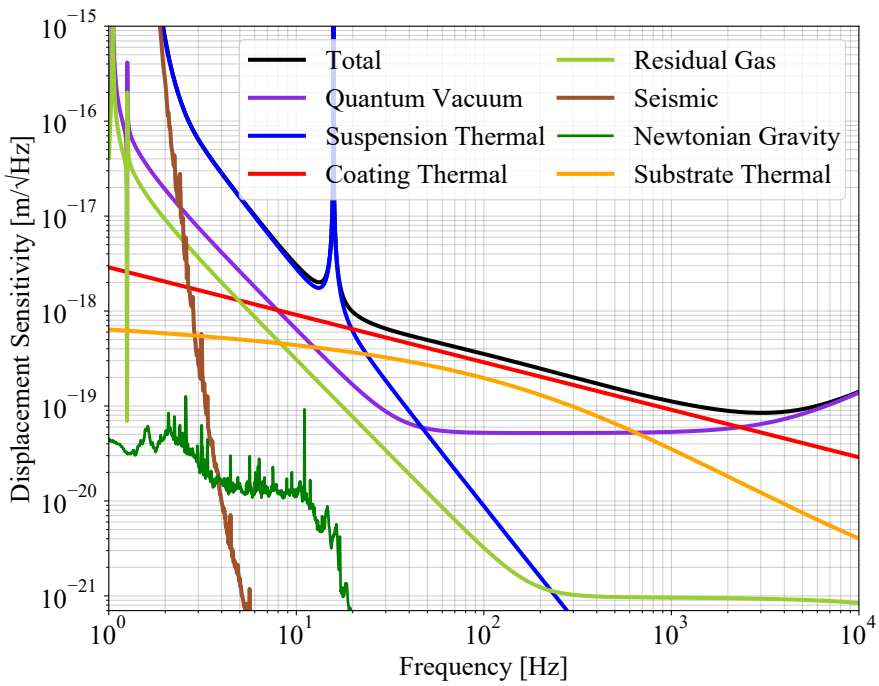


Figure 1: Displacement sensitivity of ETpathfinder-light, the first experimental run of the project at 1550 nm laser light.

Appendix D: PCB393B05 accelerometer technical details

The spectral noise of the accelerometers used in the transfer measurements and for which the noise floor is calculated is shown in Table 2.

Frequency	Spectral noise
1 Hz	$0.50 \mu\text{g}/\sqrt{\text{Hz}}$
10 Hz	$0.10 \mu\text{g}/\sqrt{\text{Hz}}$
100 Hz	$0.07 \mu\text{g}/\sqrt{\text{Hz}}$
1000 Hz	$0.05 \mu\text{g}/\sqrt{\text{Hz}}$

Table 2: PCB393B05 accelerometer electronic spectral noise.

A complete set of technical details is provided into the sensor manual [144].

Appendix E: Calculation of cold-finger acceleration above resonance

The acceleration above resonance is defined as the maximum force F_{max} transferred by the actuator to the suspended cold-finger, divided by the pendulum mass m_{cf} :

$$a = \frac{F_{max}}{m_{cf}}. \quad (7)$$

The maximum force F_{max} is defined as:

$$F_{max} = 4\pi r I_m B_r(r, z), \quad (8)$$

where $I_m = L_m R_m / \mu_0$ is the current associated to the electromotive force produced by the magnet, defined in terms of the magnet remanence R_m , the magnet length L_m and the permeability of free space μ_0 . The term $B_r(r, z)$ represents the magnetic field inside the coil, as a function of radial distance r and longitudinal distance z , as shown in Figure 2. Therefore, one has to estimate the magnetic field distribution inside the coil in order to calculate the maximum electromagnetic force which excites the suspended mass, and this can be performed using the following equation:

$$B_r(r, z) = 2 \frac{\mu_0 I_c z}{2\pi r \sqrt{C}} \left[K(\sqrt{4rR/C}) - \frac{B}{A} E(\sqrt{4rR/C}) \right]. \quad (9)$$

Here, μ_0 is the permeability of free space, R is the radius of the coil and r the radius of the magnet cross-section. I_c is the current through each coil, defined as $I_c = N \times I_w$ for the number of coil windings N and the wire current I_w . The functions K and E are elliptic integrals, while the terms A , B and C are geometric factors defined as:

$$\begin{aligned} A &= (R - r)^2 + z^2 \\ B &= R^2 + r^2 + z^2 \\ C &= (R + r)^2 + z^2. \end{aligned} \quad (10)$$

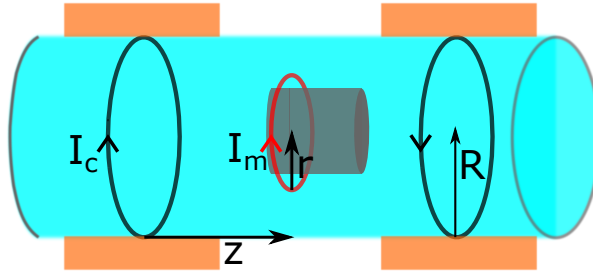


Figure 2: The figure depicts the geometry of the voice-coil actuator used in the heat-link vibration experiments.

Using the coil parameters defined in Table 3, a maximum force of 0.125 N applied on the cold-finger results. For a cold-finger mass of 0.5 Kg, an acceleration of 0.025 g results.

Parameter	Value
Number of windings per coil	112
Coil radius R	7.5 mm
Magnet radius r	4 mm
Actuator resistance R_w	6.8 Ω
Magnet length L_m	5 mm
Distance z	7 mm
Magnet remanence R_m	1.2 T
Wire current I_w	0.37 A

Table 3: Actuator parameters used in the theoretical estimate of the maximum cold-finger acceleration above resonance.

Bibliography

- [1] Kip S. Thorne. *Gravitational Waves*. 1995. DOI: 10.48550/ARXIV.GR-QC/9506086. URL: <https://arxiv.org/abs/gr-qc/9506086>.
- [2] Keith Riles. “Searches for continuous-wave gravitational radiation”. In: *Living Reviews in Relativity* 26.1 (Apr. 2023). ISSN: 1433-8351. DOI: 10.1007/s41114-023-00044-3. URL: <http://dx.doi.org/10.1007/s41114-023-00044-3>.
- [3] S. E. Gossan et al. “Observing gravitational waves from core-collapse supernovae in the advanced detector era”. In: *Phys. Rev. D* 93 (4 Feb. 2016), p. 042002. DOI: 10.1103/PhysRevD.93.042002. URL: <https://link.aps.org/doi/10.1103/PhysRevD.93.042002>.
- [4] L. P. Grishchuk. “Amplification of gravitational waves in an isotropic universe”. In: *Zh. Eksp. Teor. Fiz.* 67 (1974), pp. 825–838.
- [5] Ia B Zeldovich and I D Novikov. “Relativistic astrophysics. Volume 2. The structure and evolution of the universe”. In: *Chicago: University of Chicago Press* (Jan. 1983). URL: <https://ui.adsabs.harvard.edu/abs/1983reas.book.....Z/abstract>.
- [6] Marc Kamionkowski, Arthur Kosowsky, and Michael S. Turner. “Gravitational radiation from first-order phase transitions”. In: *Phys. Rev. D* 49 (6 Mar. 1994), pp. 2837–2851. DOI: 10.1103/PhysRevD.49.2837. URL: <https://link.aps.org/doi/10.1103/PhysRevD.49.2837>.
- [7] Edward Witten. “Cosmic separation of phases”. In: *Phys. Rev. D* 30 (2 July 1984), pp. 272–285. DOI: 10.1103/PhysRevD.30.272. URL: <https://link.aps.org/doi/10.1103/PhysRevD.30.272>.

- [8] C. J. Hogan. “Gravitational radiation from cosmological phase transitions”. In: *Monthly Notices of the Royal Astronomical Society* 218.4 (Feb. 1986), pp. 629–636. ISSN: 0035-8711. DOI: 10.1093/mnras/218.4.629. eprint: <https://academic.oup.com/mnras/article-pdf/218/4/629/3299141/mnras218-0629.pdf>. URL: <https://doi.org/10.1093/mnras/218.4.629>.
- [9] T W B Kibble. “Topology of cosmic domains and strings”. In: *Journal of Physics A: Mathematical and General* 9.8 (Aug. 1976), pp. 1387–1398. DOI: 10.1088/0305-4470/9/8/029. URL: <https://doi.org/10.1088/0305-4470/9/8/029>.
- [10] R. Abbott et al. “Constraints on Cosmic Strings Using Data from the Third Advanced LIGO–Virgo Observing Run”. In: *Phys. Rev. Lett.* 126 (24 June 2021), p. 241102. DOI: 10.1103/PhysRevLett.126.241102. URL: <https://link.aps.org/doi/10.1103/PhysRevLett.126.241102>.
- [11] Sylvia Biscoveanu et al. “Measuring the Primordial Gravitational-Wave Background in the Presence of Astrophysical Foregrounds”. In: *Phys. Rev. Lett.* 125 (24 Dec. 2020), p. 241101. DOI: 10.1103/PhysRevLett.125.241101. URL: <https://link.aps.org/doi/10.1103/PhysRevLett.125.241101>.
- [12] Daniel J. Reardon et al. “Search for an Isotropic Gravitational-wave Background with the Parkes Pulsar Timing Array”. In: *The Astrophysical Journal Letters* 951.1 (June 2023), p. L6. DOI: 10.3847/2041-8213/acdd02. URL: <https://dx.doi.org/10.3847/2041-8213/acdd02>.
- [13] Rainer Weiss. “Gravitation research”. In: (*MIT: Research Laboratory of Electronics*) 105 (1972). URL: http://dspace.mit.edu/bitstream/handle/1721.1/56271/RLE_gQPR_g105_gV.pdf?sequence=1.
- [14] Andreas Freise and Kenneth Strain. “Interferometer Techniques for Gravitational-Wave Detection”. In: *Living Reviews in Relativity* 13.1 (Feb. 2010). DOI: 10.12942/lrr-2010-1. URL: <https://doi.org/10.12942/lrr-2010-1>.
- [15] Brian J. Meers. “Recycling in laser-interferometric gravitational-wave detectors”. In: *Phys. Rev. D* 38 (8 Oct. 1988), pp. 2317–2326. DOI: 10.1103/PhysRevD.38.2317. URL: <https://link.aps.org/doi/10.1103/PhysRevD.38.2317>.
- [16] K. A. Strain and B. J. Meers. “Experimental demonstration of dual recycling for interferometric gravitational-wave detectors”. In: *Phys. Rev. Lett.* 66 (11 Mar. 1991), pp. 1391–1394. DOI: 10.1103/PhysRevLett.66.1391. URL: <https://link.aps.org/doi/10.1103/PhysRevLett.66.1391>.

- [17] J Aasi et al. “Advanced LIGO”. In: *Classical and Quantum Gravity* 32.7 (Mar. 2015), p. 074001. DOI: 10.1088/0264-9381/32/7/074001. URL: <https://dx.doi.org/10.1088/0264-9381/32/7/074001>.
- [18] F. Matichard et al. “Advanced LIGO two-stage twelve-axis vibration isolation and positioning platform. Part 1: Design and production overview”. In: *Precision Engineering* 40 (2015), pp. 273–286. ISSN: 0141-6359. DOI: <https://doi.org/10.1016/j.precisioneng.2014.09.010>. URL: <https://www.sciencedirect.com/science/article/pii/S0141635914001561>.
- [19] F. Matichard et al. “Advanced LIGO two-stage twelve-axis vibration isolation and positioning platform. Part 2: Experimental investigation and tests results”. In: *Precision Engineering* 40 (2015), pp. 287–297. ISSN: 0141-6359. DOI: <https://doi.org/10.1016/j.precisioneng.2014.11.010>. URL: <https://www.sciencedirect.com/science/article/pii/S0141635914002098>.
- [20] N A Robertson et al. “Quadruple suspension design for Advanced LIGO”. In: *Classical and Quantum Gravity* 19.15 (July 2002), pp. 4043–4058. DOI: 10.1088/0264-9381/19/15/311. URL: <https://doi.org/10.1088/0264-9381/19/15/311>.
- [21] Patrick Kwee, Benno Willke, and Karsten Danzmann. “Shot-noise-limited laser power stabilization with a high-power photodiode array”. In: *Opt. Lett.* 34.19 (Oct. 2009), pp. 2912–2914. DOI: 10.1364/OL.34.002912. URL: <https://opg.optica.org/ol/abstract.cfm?URI=ol-34-19-2912>.
- [22] P. Kwee et al. “Stabilized high-power laser system for the gravitational wave detector advanced LIGO”. In: *Opt. Express* 20.10 (May 2012), pp. 10617–10634. DOI: 10.1364/OE.20.010617. URL: <https://opg.optica.org/oe/abstract.cfm?URI=oe-20-10-10617>.
- [23] Tobin T Fricke et al. “DC readout experiment in Enhanced LIGO”. In: *Classical and Quantum Gravity* 29.6 (Feb. 2012), p. 065005. DOI: 10.1088/0264-9381/29/6/065005. URL: <https://doi.org/10.1088/0264-9381/29/6/065005>.
- [24] Adam J. Mullavey et al. “Arm-length stabilisation for interferometric gravitational-wave detectors using frequency-doubled auxiliary lasers”. In: *Opt. Express* 20.1 (Jan. 2012), pp. 81–89. DOI: 10.1364/OE.20.000081. URL: <https://opg.optica.org/oe/abstract.cfm?URI=oe-20-1-81>.
- [25] R X Adhikari et al. “A cryogenic silicon interferometer for gravitational-wave detection”. In: *Classical and Quantum Gravity* 37.16 (July 2020), p. 165003. DOI: 10.1088/1361-6382/ab9143. URL: <https://doi.org/10.1088/1361-6382/ab9143>.

- [26] T Accadia et al. “Virgo: a laser interferometer to detect gravitational waves”. In: *Journal of Instrumentation* 7.03 (Mar. 2012), P03012–P03012. DOI: 10.1088/1748-0221/7/03/p03012. URL: <https://doi.org/10.1088/1748-0221/7/03/p03012>.
- [27] F Acernese et al. “Advanced Virgo: a second-generation interferometric gravitational wave detector”. In: *Classical and Quantum Gravity* 32.2 (Dec. 2014), p. 024001. DOI: 10.1088/0264-9381/32/2/024001. URL: <https://doi.org/10.1088/0264-9381/32/2/024001>.
- [28] The Virgo Collaboration. *Advanced Virgo Technical Design Report*. VIR-0128A-12, 2012.
- [29] B Willke et al. “The GEO 600 gravitational wave detector”. In: *Classical and Quantum Gravity* 19.7 (Mar. 2002), p. 1377. DOI: 10.1088/0264-9381/19/7/321. URL: <https://dx.doi.org/10.1088/0264-9381/19/7/321>.
- [30] H Grote et al. “Dual recycling for GEO 600”. In: *Classical and Quantum Gravity* 21.5 (Feb. 2004), S473. DOI: 10.1088/0264-9381/21/5/013. URL: <https://dx.doi.org/10.1088/0264-9381/21/5/013>.
- [31] A Heptonstall et al. “Invited article: CO₂ laser production of fused silica fibers for use in interferometric gravitational wave detector mirror suspensions”. In: *Review of Scientific Instruments* 82.1 (2011).
- [32] “A gravitational wave observatory operating beyond the quantum shot-noise limit”. In: *Nature Physics* 7.12 (Sept. 2011), pp. 962–965. DOI: 10.1038/nphys2083. URL: <https://doi.org/10.1038/nphys2083>.
- [33] H. Grote et al. “First Long-Term Application of Squeezed States of Light in a Gravitational-Wave Observatory”. In: *Phys. Rev. Lett.* 110 (18 May 2013), p. 181101. DOI: 10.1103/PhysRevLett.110.181101. URL: <https://link.aps.org/doi/10.1103/PhysRevLett.110.181101>.
- [34] T Akutsu et al. “Construction of KAGRA: an underground gravitational-wave observatory”. In: *Progress of Theoretical and Experimental Physics* 2018.1 (Jan. 2018). 013F01. ISSN: 2050-3911. DOI: 10.1093/ptep/ptx180. eprint: <https://academic.oup.com/ptep/article-pdf/2018/1/013F01/23570266/ptx180.pdf>. URL: <https://doi.org/10.1093/ptep/ptx180>.
- [35] T Akutsu et al. “Overview of KAGRA: Detector design and construction history”. In: *Progress of Theoretical and Experimental Physics* 2021.5 (Aug. 2020). 05A101. ISSN: 2050-3911. DOI: 10.1093/ptep/ptaa125. eprint: <https://academic.oup.com/ptep/article-pdf/2021/5/05A101/37974994/ptaa125.pdf>. URL: <https://doi.org/10.1093/ptep/ptaa125>.

- [36] B P Abbott et al. “Exploring the sensitivity of next generation gravitational wave detectors”. In: *Classical and Quantum Gravity* 34.4 (Jan. 2017), p. 044001. DOI: 10.1088/1361-6382/aa51f4. URL: <https://doi.org/10.1088%2F1361-6382%2Faa51f4>.
- [37] David Reitze et al. “The US Program in Ground-Based Gravitational Wave Science: Contribution from the LIGO Laboratory”. In: (2019). DOI: 10.48550/ARXIV.1903.04615. URL: <https://arxiv.org/abs/1903.04615>.
- [38] Matthew Evans et al. *A Horizon Study for Cosmic Explorer: Science, Observatories, and Community*. 2021. DOI: 10.48550/ARXIV.2109.09882. URL: <https://arxiv.org/abs/2109.09882>.
- [39] Evan D Hall and Matthew Evans. “Metrics for next-generation gravitational-wave detectors”. In: *Classical and Quantum Gravity* 36.22 (Oct. 2019), p. 225002. ISSN: 1361-6382. DOI: 10.1088/1361-6382/ab41d6. URL: <http://dx.doi.org/10.1088/1361-6382/ab41d6>.
- [40] M. G. Beker et al. “Improving the sensitivity of future GW observatories in the 1–10 Hz band: Newtonian and seismic noise”. In: *General Relativity and Gravitation* 43 (2011), pp. 623–656.
- [41] F Badaracco and J Harms. “Optimization of seismometer arrays for the cancellation of Newtonian noise from seismic body waves”. In: *Classical and Quantum Gravity* 36.14 (June 2019), p. 145006. DOI: 10.1088/1361-6382/ab28c1. URL: <https://dx.doi.org/10.1088/1361-6382/ab28c1>.
- [42] Soumen Koley et al. “Surface and underground seismic characterization at Terziet in Limburg—the Euregio Meuse–Rhine candidate site for Einstein Telescope”. In: *Classical and Quantum Gravity* 39.2 (Jan. 2022), p. 025008. DOI: 10.1088/1361-6382/ac2b08. URL: <https://dx.doi.org/10.1088/1361-6382/ac2b08>.
- [43] L Naticchioni et al. “Characterization of the Sos Enattos site for the Einstein Telescope”. In: *Journal of Physics: Conference Series* 1468.1 (Feb. 2020), p. 012242. DOI: 10.1088/1742-6596/1468/1/012242. URL: <https://dx.doi.org/10.1088/1742-6596/1468/1/012242>.
- [44] A Freise et al. “Triple Michelson interferometer for a third-generation gravitational wave detector”. In: *Classical and Quantum Gravity* 26.8 (Apr. 2009), p. 085012. DOI: 10.1088/0264-9381/26/8/085012. URL: <https://doi.org/10.1088%2F0264-9381%2F26%2F8%2F085012>.
- [45] S Hild et al. “A xylophone configuration for a third-generation gravitational wave detector”. In: *Classical and Quantum Gravity* 27.1 (Dec. 2009), p. 015003. DOI: 10.1088/0264-9381/27/1/015003. URL: <https://doi.org/10.1088%2F0264-9381%2F27%2F1%2F015003>.

- [46] A Utina et al. “ETpathfinder: a cryogenic testbed for interferometric gravitational-wave detectors”. In: *Classical and Quantum Gravity* 39.21 (Sept. 2022), p. 215008. DOI: 10.1088/1361-6382/ac8fdb. URL: <https://dx.doi.org/10.1088/1361-6382/ac8fdb>.
- [47] Anthony E. Siegman. *Lasers*. University Science Books, 1986.
- [48] Ronald W. P. Drever et al. “Laser phase and frequency stabilization using an optical resonator”. In: *Applied Physics B* 31 (1983), pp. 97–105.
- [49] Eric D. Black. “An introduction to Pound–Drever–Hall laser frequency stabilization”. In: *American Journal of Physics* 69.1 (2001), pp. 79–87. DOI: 10.1119/1.1286663. eprint: <https://doi.org/10.1119/1.1286663>. URL: <https://doi.org/10.1119/1.1286663>.
- [50] Lisa Barsotti. “The control of the Virgo interferometer for gravitational wave detection”. PhD thesis. Pisa University, 2006.
- [51] Julia Casanueva Diaz. “Control of the gravitational wave interferometric detector Advanced Virgo”. PhD thesis. Paris-Saclay University, 2017.
- [52] F Acernese et al. “The variable finesse locking technique”. In: *Classical and Quantum Gravity* 23.8 (Mar. 2006), S85–S89. DOI: 10.1088/0264-9381/23/8/s12. URL: <https://doi.org/10.1088/0264-9381/23/8/s12>.
- [53] Daniel D. Brown et al. “Pykat: Python package for modelling precision optical interferometers”. In: *SoftwareX* 12 (2020), p. 100613. ISSN: 2352-7110. DOI: <https://doi.org/10.1016/j.softx.2020.100613>.
- [54] Peter D. Welch. “The use of fast Fourier transform for the estimation of power spectra: A method based on time averaging over short, modified periodograms”. In: *IEEE Transactions on Audio and Electroacoustics* 15 (1967), pp. 70–73.
- [55] Tania Regimbau et al. “Mock data challenge for the Einstein Gravitational-Wave Telescope”. In: *Physical Review D* 86.12 (Dec. 2012). DOI: 10.1103/physrevd.86.122001. URL: <https://doi.org/10.1103/physrevd.86.122001>.
- [56] Tania Regimbau, Duncan Meacher, and Michael Coughlin. “Second Einstein Telescope mock science challenge: Detection of the gravitational-wave stochastic background from compact binary coalescences”. In: *Physical Review D* 89.8 (Apr. 2014). DOI: 10.1103/physrevd.89.084046. URL: <https://doi.org/10.1103/physrevd.89.084046>.
- [57] Herbert B. Callen and Theodore A. Welton. “Irreversibility and Generalized Noise”. In: *Phys. Rev.* 83 (1 July 1951), pp. 34–40. DOI: 10.1103/PhysRev.83.34. URL: <https://link.aps.org/doi/10.1103/PhysRev.83.34>.

- [58] F. Travasso et al. “Low-frequency internal friction in silica glass”. In: *Europhysics Letters (EPL)* 80.5 (Oct. 2007), p. 50008. DOI: 10.1209/0295-5075/80/50008. URL: <https://doi.org/10.1209/0295-5075/80/50008>.
- [59] Dermot McGuigan et al. “Measurements of the mechanical Q of single-crystal silicon at low temperatures”. In: *Journal of Low Temperature Physics* 30 (1978), pp. 621–629. DOI: 10.1007/BF00116202. URL: <https://doi.org/10.1007/BF00116202>.
- [60] S Hild et al. “Sensitivity studies for third-generation gravitational wave observatories”. In: *Classical and Quantum Gravity* 28.9 (Apr. 2011), p. 094013. DOI: 10.1088/0264-9381/28/9/094013. URL: <https://doi.org/10.1088/0264-9381/28/9/094013>.
- [61] R Schnabel et al. “Building blocks for future detectors: Silicon test masses and 1550 nm laser light”. In: *Journal of Physics: Conference Series* 228 (May 2010), p. 012029. DOI: 10.1088/1742-6596/228/1/012029. URL: <https://doi.org/10.1088/1742-6596/228/1/012029>.
- [62] Jerome Degallaix et al. “Bulk optical absorption of high resistivity silicon at 1550 nm”. In: *Opt. Lett.* 38.12 (June 2013), pp. 2047–2049. DOI: 10.1364/OL.38.002047. URL: <http://opg.optica.org/ol/abstract.cfm?URI=ol-38-12-2047>.
- [63] Moritz Mehmet et al. “Squeezed light at 1550 nm with a quantum noise reduction of 12.3 dB”. In: *Opt. Express* 19.25 (Dec. 2011), pp. 25763–25772. DOI: 10.1364/OE.19.025763. URL: <http://opg.optica.org/oe/abstract.cfm?URI=oe-19-25-25763>.
- [64] J. Steinlechner et al. “Silicon-Based Optical Mirror Coatings for Ultrahigh Precision Metrology and Sensing”. In: *Phys. Rev. Lett.* 120 (26 June 2018), p. 263602. DOI: 10.1103/PhysRevLett.120.263602. URL: <https://link.aps.org/doi/10.1103/PhysRevLett.120.263602>.
- [65] Sibilla Di Pace et al. “Research Facilities for European’s Next Generation Gravitational-Wave Detector Einstein Telescope”. In: *Galaxies* 10.3 (2022). ISSN: 2075-4434. URL: <https://www.mdpi.com/2075-4434/10/3/65>.
- [66] Homare Abe et al. “The Current Status and Future Prospects of KAGRA, the Large-Scale Cryogenic Gravitational Wave Telescope Built in the Kamioka Underground”. In: *Galaxies* 10.3 (2022). ISSN: 2075-4434. URL: <https://www.mdpi.com/2075-4434/10/3/63>.
- [67] T Akutsu et al. *Overview of KAGRA: Detector design and construction history*. 2020. DOI: 10.48550/ARXIV.2005.05574. URL: <https://arxiv.org/abs/2005.05574>.

- [68] Fabian Meylahn, Nicole Knust, and Benno Willke. “Stabilized laser system at 1550 nm wavelength for future gravitational-wave detectors”. In: *Phys. Rev. D* 105 (12 June 2022), p. 122004. DOI: 10.1103/PhysRevD.105.122004. URL: <https://link.aps.org/doi/10.1103/PhysRevD.105.122004>.
- [69] Ken Strain and Russel Jones. *HAM Relay-optics Suspension: pre-conceptual design*. LIGO-T1900036-v5, 2020.
- [70] Bas Swinkels and Paolo Ruggi. *Lock acquisition of the Advanced Virgo arm-cavities with reduced force*. VIR-0019A-12, 2012.
- [71] T. Accadia et al. In: *Journal of Low Frequency Noise, Vibration and Active Control* 30.1 (2011), pp. 63–79. DOI: 10.1260/0263-0923.30.1.63. eprint: <https://doi.org/10.1260/0263-0923.30.1.63>. URL: <https://doi.org/10.1260/0263-0923.30.1.63>.
- [72] The ETpathfinder team. *ETpathfinder design report*. ET-0011A-20, 2020. URL: <https://www.etpathfinder.eu/wp-content/uploads/2020/03/ETpathfinder-Design-Report.pdf>.
- [73] Carlton M. Caves. “Quantum-mechanical noise in an interferometer”. In: *Phys. Rev. D* 23 (8 Apr. 1981), pp. 1693–1708. DOI: 10.1103/PhysRevD.23.1693. URL: <https://link.aps.org/doi/10.1103/PhysRevD.23.1693>.
- [74] Jon Peterson. *Observations and modeling of seismic background noise*. U.S. Geological Survey, 1993. URL: <https://doi.org/10.3133/ofr93322>.
- [75] Calum Iain Eachan Torrie. *Development of suspensions for the GEO 600 gravitational wave detector*. University of Glasgow, 2000.
- [76] Matthew Edward Husman. *Suspension and control for interferometric gravitational wave detectors*. University of Glasgow, 2000.
- [77] Paolo Alberto Ruggi. *L’ATTENUAZIONE DEL RUMORE SISMICO NEL RIVELATORE DI ONDE GRAVITAZIONALI VIRGO*. UNIVERSITÀ DEGLI STUDI DI PISA, 2003. URL: https://www.nikhef.nl/~jo/virgo/gw/theses/Tesi_Ruggi.pdf.
- [78] R.Del Fabbro. *Super Attenuator Dynamics, Part 1*. VIRGO TDS, VIR-NOT-PIS-1380-78, 1994.
- [79] Gregory M Harry et al. “Thermal noise in interferometric gravitational wave detectors due to dielectric optical coatings”. In: *Classical and Quantum Gravity* 19.5 (Feb. 2002), pp. 897–917. DOI: 10.1088/0264-9381/19/5/305. URL: <https://doi.org/10.1088/0264-9381/19/5/305>.
- [80] G. Cagnoli et al. “Advanced optical coatings for the discovery of gravitational waves”. In: *SPIE News* (2017). URL: <https://spie.org/news/6767-advanced-optical-coatings-for-the-discovery-of-gravitational-waves?SSO=1>.

- [81] R Flaminio et al. “A study of coating mechanical and optical losses in view of reducing mirror thermal noise in gravitational wave detectors”. In: *Classical and Quantum Gravity* 27.8 (Apr. 2010), p. 084030. DOI: 10.1088/0264-9381/27/8/084030. URL: <https://doi.org/10.1088/0264-9381/27/8/084030>.
- [82] Massimo Granata et al. “Mechanical loss in state-of-the-art amorphous optical coatings”. In: *Phys. Rev. D* 93 (1 Jan. 2016), p. 012007. DOI: 10.1103/PhysRevD.93.012007. URL: <https://link.aps.org/doi/10.1103/PhysRevD.93.012007>.
- [83] Xiao Liu et al. “Amorphous Solid without Low Energy Excitations”. In: *Phys. Rev. Lett.* 78 (23 June 1997), pp. 4418–4421. DOI: 10.1103/PhysRevLett.78.4418. URL: <https://link.aps.org/doi/10.1103/PhysRevLett.78.4418>.
- [84] R. Birney et al. “Amorphous Silicon with Extremely Low Absorption: Beating Thermal Noise in Gravitational Astronomy”. In: *Phys. Rev. L* 121 (19 Nov. 2018), p. 191101. DOI: 10.1103/PhysRevLett.121.191101. URL: <https://link.aps.org/doi/10.1103/PhysRevLett.121.191101>.
- [85] Jessica Steinlechner et al. “Optical absorption of ion-beam sputtered amorphous silicon coatings”. In: *Phys. Rev. D* 93 (6 Mar. 2016), p. 062005. DOI: 10.1103/PhysRevD.93.062005. URL: <http://link.aps.org/doi/10.1103/PhysRevD.93.062005>.
- [86] H.-W. Pan et al. “Silicon nitride and silica quarter-wave stacks for low-thermal-noise mirror coatings”. In: *Phys. Rev. D* 98 (10 2018), p. 102001. DOI: 10.1103/PhysRevD.98.102001. URL: <https://link.aps.org/doi/10.1103/PhysRevD.98.102001>.
- [87] Xiao Liu et al. “Elastic Properties of Several Silicon Nitride Films”. In: *MRS Proceedings* 989 (2007), 0989–A22–01. DOI: 10.1557/PROC-0989-A22-01.
- [88] Jessica Steinlechner et al. “Optical absorption of silicon nitride membranes at 1064 nm and at 1550 nm”. In: *Phys. Rev. D* 96 (2 July 2017), p. 022007. DOI: 10.1103/PhysRevD.96.022007. URL: <https://link.aps.org/doi/10.1103/PhysRevD.96.022007>.
- [89] Jessica Steinlechner et al. “Thermal noise reduction and absorption optimization via multimaterial coatings”. In: *Phys. Rev. D* 91 (4 Feb. 2015), p. 042001. DOI: 10.1103/PhysRevD.91.042001. URL: <https://link.aps.org/doi/10.1103/PhysRevD.91.042001>.
- [90] William Yam, Slawek Gras, and Matthew Evans. “Multimaterial coatings with reduced thermal noise”. In: *Phys. Rev. D* 91 (4 Feb. 2015), p. 042002. DOI: 10.1103/PhysRevD.91.042002. URL: <https://link.aps.org/doi/10.1103/PhysRevD.91.042002>.

- [91] Simon C. Tait et al. “Demonstration of the Multimaterial Coating Concept to Reduce Thermal Noise in Gravitational-Wave Detectors”. In: *Phys. Rev. Lett.* 125 (1 July 2020), p. 011102. DOI: 10.1103/PhysRevLett.125.011102. URL: <https://link.aps.org/doi/10.1103/PhysRevLett.125.011102>.
- [92] Yuk Tung Liu and Kip S. Thorne. “Thermoelastic noise and homogeneous thermal noise in finite sized gravitational-wave test masses”. In: *Physical Review D* 62.12 (Nov. 2000). DOI: 10.1103/physrevd.62.122002. URL: <https://doi.org/10.1103/physrevd.62.122002>.
- [93] Jameson Graef Rollins et al. *pygwinc: Gravitational Wave Interferometer Noise Calculator*. Astrophysics Source Code Library, record ascl:2007.020, 2020. URL: <https://ascl.net/2007.020>.
- [94] V.B. Braginsky and S.P. Vyatchanin. “Corner reflectors and quantum-non-demolition measurements in gravitational wave antennae”. In: *Physics Letters A* 324.5 (2004), pp. 345–360. ISSN: 0375-9601. DOI: <https://doi.org/10.1016/j.physleta.2004.02.066>. URL: <https://www.sciencedirect.com/science/article/pii/S037596010400310X>.
- [95] V.B. Braginsky, M.L. Gorodetsky, and S.P. Vyatchanin. “Thermodynamical fluctuations and photo-thermal shot noise in gravitational wave antennae”. In: *Physics Letters A* 264.1 (1999), pp. 1–10. ISSN: 0375-9601. DOI: [https://doi.org/10.1016/S0375-9601\(99\)00785-9](https://doi.org/10.1016/S0375-9601(99)00785-9). URL: <https://www.sciencedirect.com/science/article/pii/S0375960199007859>.
- [96] M. Cerdonio et al. “Thermoelastic effects at low temperatures and quantum limits in displacement measurements”. In: *Physical Review D* 63.8 (Mar. 2001). DOI: 10.1103/physrevd.63.082003. URL: <https://doi.org/10.1103/physrevd.63.082003>.
- [97] J. Komma et al. “Thermo-optic coefficient of silicon at 1550 nm and cryogenic temperatures”. In: *Applied Physics Letters* 101 (2012), p. 041905.
- [98] Peter R. Saulson. “Thermal noise in mechanical experiments”. In: *Phys. Rev. D* 42 (8 Oct. 1990), pp. 2437–2445. DOI: 10.1103/PhysRevD.42.2437. URL: <https://link.aps.org/doi/10.1103/PhysRevD.42.2437>.
- [99] Gabriela González. “Suspensions thermal noise in the LIGO gravitational wave detector”. In: *Classical and Quantum Gravity* 17.21 (Oct. 2000), pp. 4409–4435. DOI: 10.1088/0264-9381/17/21/305. URL: <https://doi.org/10.1088/0264-9381/17/21/305>.
- [100] Gabriela I. González and Peter R. Saulson. “Brownian motion of a torsion pendulum with internal friction”. In: *Physics Letters A* 201.1 (1995), pp. 12–18. ISSN: 0375-9601. DOI: [https://doi.org/10.1016/0375-9601\(95\)00194-8](https://doi.org/10.1016/0375-9601(95)00194-8). URL: <https://www.sciencedirect.com/science/article/pii/S0375960195001948>.

- [101] R Birney et al. “Coatings and surface treatments for enhanced performance suspensions for future gravitational wave detectors”. In: *Classical and Quantum Gravity* 34.23 (Nov. 2017), p. 235012. DOI: 10.1088/1361-6382/aa9354. URL: <https://doi.org/10.1088/1361-6382/aa9354>.
- [102] Peter R. Saulson. “Terrestrial gravitational noise on a gravitational wave antenna”. In: *Phys. Rev. D* 30 (4 Aug. 1984), pp. 732–736. DOI: 10.1103/PhysRevD.30.732. URL: <https://link.aps.org/doi/10.1103/PhysRevD.30.732>.
- [103] Jan Harms. “Terrestrial gravity fluctuations”. In: *Living Reviews in Relativity* 22.1 (Oct. 2019). DOI: 10.1007/s41114-019-0022-2. URL: <https://doi.org/10.1007%2Fs41114-019-0022-2>.
- [104] Scott A. Hughes and Kip S. Thorne. “Seismic gravity-gradient noise in interferometric gravitational-wave detectors”. In: *Phys. Rev. D* 58 (12 Nov. 1998), p. 122002. DOI: 10.1103/PhysRevD.58.122002. URL: <https://link.aps.org/doi/10.1103/PhysRevD.58.122002>.
- [105] Matteo Beccaria et al. “Relevance of Newtonian seismic noise for the VIRGO interferometer sensitivity”. In: *Class.Quant.Grav.* 15 (Jan. 1998), pp. 3339–3362. DOI: 10.1088/0264-9381/15/11/004.
- [106] Jan Harms and Brian O’Reilly. “Velocity and Attenuation Characterization of the LIGO Site near Livingston, Louisiana”. In: *Bulletin of the Seismological Society of America* 101.4 (Aug. 2011), pp. 1478–1487. ISSN: 0037-1106. DOI: 10.1785/0120100095. eprint: <https://pubs.geoscienceworld.org/ssa/bssa/article-pdf/101/4/1478/2653804/1478.pdf>. URL: <https://doi.org/10.1785/0120100095>.
- [107] Rainer Weiss. *Scattering by Residual Gas*. 1989. URL: <https://dcc.ligo.org/public/0028/T890025/001/T890025-01.pdf>.
- [108] Michael Edward Zucker and Stanley E. Whitcomb. *Measurement of optical path fluctuations due to residual gas in the LIGO 40-meter interferometer*. LIGO-P940008-x0, 1994. URL: <https://dcc-lln.ligo.org/public/0073/P940008/000/P940008-00.pdf>.
- [109] A. Cavalleri et al. “Gas damping force noise on a macroscopic test body in an infinite gas reservoir”. In: *Physics Letters A* 374.34 (2010), pp. 3365–3369. ISSN: 0375-9601. DOI: <https://doi.org/10.1016/j.physleta.2010.06.041>. URL: <https://www.sciencedirect.com/science/article/pii/S0375960110007279>.
- [110] R. Dolesi and others. “Brownian force noise from molecular collisions and the sensitivity of advanced gravitational wave observatories”. In: *Phys. Rev. D* 84 (6 Sept. 2011), p. 063007. DOI: 10.1103/PhysRevD.84.063007. URL: <https://link.aps.org/doi/10.1103/PhysRevD.84.063007>.

- [111] J.C. Thompson and B.A. Younglove. “Thermal conductivity of silicon at low temperatures”. In: *Journal of Physics and Chemistry of Solids* 20.1 (1961), pp. 146–149. ISSN: 0022-3697. DOI: [https://doi.org/10.1016/0022-3697\(61\)90146-9](https://doi.org/10.1016/0022-3697(61)90146-9). URL: <https://www.sciencedirect.com/science/article/pii/0022369761901469>.
- [112] Takafumi Ushiba et al. “Cryogenic suspension design for a kilometer-scale gravitational-wave detector”. In: *Classical and Quantum Gravity* 38.8 (Mar. 2021), p. 085013. DOI: [10.1088/1361-6382/abe9f3](https://doi.org/10.1088/1361-6382/abe9f3). URL: <https://doi.org/10.1088/1361-6382/abe9f3>.
- [113] Eric Hennes. *Private communication*. in progress, 2021.
- [114] Tomohiro Yamada et al. “High performance thermal link with small spring constant for cryogenic applications”. In: *Cryogenics* 116 (2021), p. 103280. ISSN: 0011-2275. DOI: <https://doi.org/10.1016/j.cryogenics.2021.103280>. URL: <https://www.sciencedirect.com/science/article/pii/S0011227521000382>.
- [115] G. Cagnoli et al. “Damping dilution factor for a pendulum in an interferometric gravitational waves detector”. In: *Physics Letters A* 272.1 (2000), pp. 39–45. ISSN: 0375-9601. DOI: [https://doi.org/10.1016/S0375-9601\(00\)00411-4](https://doi.org/10.1016/S0375-9601(00)00411-4). URL: <https://www.sciencedirect.com/science/article/pii/S0375960100004114>.
- [116] F Matichard et al. “Seismic isolation of Advanced LIGO: Review of strategy, instrumentation and performance”. In: *Classical and Quantum Gravity* 32.18 (Aug. 2015), p. 185003. DOI: [10.1088/0264-9381/32/18/185003](https://doi.org/10.1088/0264-9381/32/18/185003). URL: <https://doi.org/10.1088/0264-9381/32/18/185003>.
- [117] R.B. Randall. *Frequency Analysis*. Brüel & Kjaer, 1987. ISBN: 9788787355070. URL: <https://books.google.nl/books?id=RzFEAQAAIAAJ>.
- [118] Gabriele Vajente. “Readout, Sensing, and Control”. In: *Advanced Interferometers and the Search for Gravitational Waves: Lectures from the First VESF School on Advanced Detectors for Gravitational Waves*. Ed. by Massimo Bassan. Cham: Springer International Publishing, 2014, pp. 153–192. ISBN: 978-3-319-03792-9. DOI: [10.1007/978-3-319-03792-9_6](https://doi.org/10.1007/978-3-319-03792-9_6). URL: https://doi.org/10.1007/978-3-319-03792-9_6.
- [119] H. Kogelnik and T. Li. “Laser Beams and Resonators”. In: *Appl. Opt.* 5.10 (Oct. 1966), pp. 1550–1567. DOI: [10.1364/AO.5.001550](https://doi.org/10.1364/AO.5.001550). URL: <http://opg.optica.org/ao/abstract.cfm?URI=ao-5-10-1550>.
- [120] Nergis Mavalvala. “Alignment Issues in Laser Interferometric Gravitational-Wave Detectors”. PhD thesis. MIT, 1997.

- [121] Euan Morrison et al. “Automatic alignment of optical interferometers”. In: *Appl. Opt.* 33.22 (Aug. 1994), pp. 5041–5049. DOI: 10.1364/AO.33.005041. URL: <http://opg.optica.org/ao/abstract.cfm?URI=ao-33-22-5041>.
- [122] S. Solimeno et al. “Fabry-Pérot resonators with oscillating mirrors”. In: *Phys. Rev. A* 43 (11 June 1991), pp. 6227–6240. DOI: 10.1103/PhysRevA.43.6227. URL: <https://link.aps.org/doi/10.1103/PhysRevA.43.6227>.
- [123] Dana Z. Anderson. “Alignment of resonant optical cavities”. In: *Appl. Opt.* 23.17 (Sept. 1984), pp. 2944–2949. DOI: 10.1364/AO.23.002944. URL: <http://opg.optica.org/ao/abstract.cfm?URI=ao-23-17-2944>.
- [124] L. R. Hofer et al. “Hermite-Gaussian mode detection via convolution neural networks”. In: *J. Opt. Soc. Am. A* 36.6 (June 2019), pp. 936–943. DOI: 10.1364/JOSAA.36.000936. URL: <http://opg.optica.org/josaa/abstract.cfm?URI=josaa-36-6-936>.
- [125] Yi An et al. “Fast modal analysis for Hermite-Gaussian beams via deep learning”. In: *Appl. Opt.* 59.7 (Mar. 2020), pp. 1954–1959. DOI: 10.1364/AO.377189. URL: <http://opg.optica.org/ao/abstract.cfm?URI=ao-59-7-1954>.
- [126] Mitchell G. Schiworski, Daniel D. Brown, and David J. Ottaway. “Modal decomposition of complex optical fields using convolutional neural networks”. In: *J. Opt. Soc. Am. A* 38.11 (Nov. 2021), pp. 1603–1611. DOI: 10.1364/JOSAA.428214. URL: <http://opg.optica.org/josaa/abstract.cfm?URI=josaa-38-11-1603>.
- [127] Allison McCarn Deiana et al. *Applications and Techniques for Fast Machine Learning in Science*. 2021. DOI: 10.48550/ARXIV.2110.13041. URL: <https://arxiv.org/abs/2110.13041>.
- [128] Elena Cuoco et al. “Enhancing gravitational-wave science with machine learning”. In: *Machine Learning: Science and Technology* 2.1 (Dec. 2020), p. 011002. DOI: 10.1088/2632-2153/abb93a. URL: <https://doi.org/10.1088%2F2632-2153%2Fabb93a>.
- [129] Hunter Gabbard et al. “Matching Matched Filtering with Deep Networks for Gravitational-Wave Astronomy”. In: *Physical Review Letters* 120.14 (Apr. 2018). DOI: 10.1103/physrevlett.120.141103. URL: <https://doi.org/10.1103%2Fphysrevlett.120.141103>.
- [130] G. Vajente et al. “Machine-learning nonstationary noise out of gravitational-wave detectors”. In: *Phys. Rev. D* 101 (4 Feb. 2020), p. 042003. DOI: 10.1103/PhysRevD.101.042003. URL: <https://link.aps.org/doi/10.1103/PhysRevD.101.042003>.

- [131] Rich Ormiston et al. “Noise reduction in gravitational-wave data via deep learning”. In: *Phys. Rev. Research* 2 (3 July 2020), p. 033066. DOI: 10.1103/PhysRevResearch.2.033066. URL: <https://link.aps.org/doi/10.1103/PhysRevResearch.2.033066>.
- [132] Frederic B. Fitch. “Warren S. McCulloch and Walter Pitts. A logical calculus of the ideas immanent in nervous activity. Bulletin of mathematical biophysics, vol. 5 (1943), pp. 115–133.” In: *Journal of Symbolic Logic* 9.2 (1944), pp. 49–50. DOI: 10.2307/2268029.
- [133] Rosenblatt F. “The Perceptron — a perceiving and recognizing automaton”. In: *Cornell Aeronautical Laboratory Report* 85–460–1 (1957).
- [134] David E. Rumelhart, Geoffrey E. Hinton, and Ronald J. Williams. “Learning Internal Representations by Error Propagation”. In: *Parallel Distributed Processing: Explorations in the Microstructure of Cognition, Volume 1: Foundations*. Ed. by David E. Rumelhart and James L. McClelland. Cambridge, MA: MIT Press, 1986, pp. 318–362.
- [135] Yann LeCun et al. “Gradient-based learning applied to document recognition”. In: *Proc. IEEE* 86 (1998), pp. 2278–2324.
- [136] Alex Krizhevsky, Ilya Sutskever, and Geoffrey E Hinton. “ImageNet Classification with Deep Convolutional Neural Networks”. In: *Advances in Neural Information Processing Systems*. Ed. by F. Pereira et al. Vol. 25. Curran Associates, Inc., 2012. URL: <https://proceedings.neurips.cc/paper/2012/file/c399862d3b9d6b76c8436e924a68c45b-Paper.pdf>.
- [137] C. Szegedy et al. “Going deeper with convolutions”. In: *2015 IEEE Conference on Computer Vision and Pattern Recognition (CVPR)*. June 2015, pp. 1–9. DOI: 10.1109/CVPR.2015.7298594. URL: <https://ieeexplore.ieee.org/document/7298594>.
- [138] Robert Cornell Walet. “Advanced instrumentation for gravitational-wave research”. PhD thesis. Vrije Universiteit Amsterdam, Nikhef, 2022.
- [139] Stéfan van der Walt et al. “scikit-image: image processing in Python”. In: *PeerJ* 2 (July 2014), e453. ISSN: 2167-8359. DOI: 10.7717/peerj.453. URL: <https://doi.org/10.7717/peerj.453>.
- [140] Pauli Virtanen et al. “SciPy 1.0: Fundamental Algorithms for Scientific Computing in Python”. In: *Nature Methods* 17 (2020), pp. 261–272. DOI: 10.1038/s41592-019-0686-2.
- [141] Alex Clark. *Pillow (PIL Fork) Documentation*. 2015. URL: <https://buildmedia.readthedocs.org/media/pdf/pillow/latest/pillow.pdf>.
- [142] François Chollet et al. *Keras*. <https://keras.io>. 2015.

- [143] Martín Abadi et al. *TensorFlow: Large-Scale Machine Learning on Heterogeneous Systems*. Software available from tensorflow.org. 2015. URL: <https://www.tensorflow.org/>.
- [144] PCB Piezotronics. *Model 393B05, Installation and Operating Manual*. PCB Piezotronics. URL: https://www.pcb.com/contentStore/docs/pcb_corporate/vibration/products/manuals/393b05.pdf.

Acknowledgements

My journey through the PhD was challenging, but at the same time rewarding. I would like to thank everyone who helped me along the way.

I would like to start by expressing my profound gratitude to my supervisors, Stefan and Sebastian. Stefan, this thesis would not have been possible without you. I have learned many lessons from you, both in science and life. Thank you for trusting me to explore unknown territories for my thesis. Sebastian, thank you very much for your prompt help with my research activities. You have always been approachable and supportive with my questions. Special thanks for your guidance with the ET and ETpathfinder noise budgets. Your software mastery was inspiring, and it will continue to benefit me in my future endeavors.

I would like to thank Valera Frolov, who motivated me in the first place to pursue a PhD in gravitational-wave field.

I would like to thank Ken Strain for his always-good advice in my first PhD year at the University of Glasgow.

Thank you, Peter, for being a good friend and helping me with my speedometer adventures in the lab. I need to come to Slovakia soon and learn some of your skiing talents.

I would like to express my special thanks to Marcel for giving me valuable advice with the progression of the PhD thesis. Marcel, those beers might be on me in the end.

Andreas, thank you for your useful help with the ETpathfinder paper and for many lessons on optical simulations. I have always found it very inspiring to learn from your mastery of the field.

Many thanks to the entire Maastricht Group, namely: Jessica, Stefan D, Gideon, Zeb, Ayatri, Viola, Peter, Tim, Jan, and Margot. The first half of the year of COVID was very difficult for me at that time during the PhD. Jessica, thank you for always thinking about the struggles of PhD students and for triggering social events online.

They sure helped. Stefan D., it was inspiring to explore random intellectual ideas with you. Thank you for your help with the ETpathfinder noise budget. Gideon, thanks for the many engaging discussions we had about relativity. We probably had the most interesting start of the pandemic together with Rob being caught in the panicking Malta. I wish you the best of luck breaking the push-up record you set on that rock next to the Mediterranean. Viola and Ayatri, thanks for sharing your thoughts about our PhD journeys. Peter, thanks for your help with ETpathfinder activities. Tim, you helped me greatly. Thank you for that, and many thanks for boosting the social life of PhD students in Maastricht. To Margot and Jan, many thanks for reviewing the ETpathfinder paper and for your useful advice. Zeb, thanks for being a good friend, we should definitely see the next Nolan movie together!

I would like to thank Alessandro Bertolini for his valuable lessons on scientific instrumentation. Many thanks for helping me when I was stuck in the suspensions lab and guiding the modeling of suspension thermal noise.

Bas, thank you for all your help regarding ETpathfinder control strategies and for my VIRGO project. It was always nice to learn from your immense insights into this field.

Eric, thank you for your inspiration and your help with ETpathfinder suspensions. You are a very humble person, and you inspired me with your love for physics.

Rogier, many thanks for your enormous effort with proto-0. You were always very approachable and helpful. We had a lot of fun with our proto-0 trips, and I hope you guys decommissioned it.

I would like to thank Jan-Harms for his valuable suggestions regarding the modeling of Newtonian noise for ETpathfinder. I enjoyed very much our conversation.

Henk-Jan, thank you for your discussions about the cryogenics for ETpathfinder. This helped me with the finalization of the jellyfish project.

Special thanks to Madda and Julia for their guidance and help with the VIRGO control project. We definitely had a lot of fun with this project, and I hope it helped you in some way. Thank you for making the time at the site enjoyable for me.

I would like to thank Elena for our machine learning research together. Elena, a special thanks for your guidance and lessons about data analysis. I always liked to work with you.

Rob, thanks for giving me the chance to work with you on your test setup. I had a lot of fun exploring what is possible with machine learning for cavity control, and it was useful to learn from you.

I would like to thank the ASML folks: Kramer, Jean, Joshua, Deniz, Michiel, and Giuseppina. Thanks for your lessons and making the start at ASML an amazing experience. I think OSLO is the best team out there.

Dan, thanks for helping me with the cover, and being a great friend.

Finally, to my family and Catalina, thank you for everything! Thank you, Catalina, for always being there for me. You have surely made this journey easier for me, and it has been a pleasure to share it with you.

Gravitational waves are ripples in the fabric of spacetime, predicted by Einstein's theory of general relativity. An observable effect generated by a passing gravitational wave is the change in distance between two test masses in geodesic free fall; this observable effect can be measured across a broad frequency spectrum using a laser interferometer by monitoring the differential displacement between two orthogonal test masses positioned at the interferometer's end. Current gravitational-wave interferometers, such as LIGO (Laser Interferometer Gravitational-wave Observatory), VIRGO or KAGRA (Kamioka Gravitational Wave Detector), have been successful in detecting a variety of events, starting with the first detection of a binary black hole by LIGO, GW150914, measured on the 14th of September 2015. Third generation detectors, such as Einstein Telescope (ET) and Cosmic Explorer (CE), employ new interferometric technologies and aim to exceed the capabilities of existing ground-based detectors, enabling them to achieve a measurement sensitivity that is almost ten times higher than current interferometers. This thesis studies some of the advanced technologies for the new generation of gravitational-wave detectors, such as cryogenic interferometry and advanced sensing and control schemes. A more rigorous introduction to the topic is presented in Chapter 1.

Chapter 2 of this thesis presents an analysis of the the Advanced Virgo Interferometer radio-frequency (RF) control sidebands throughout the third scientific run, denoted as O3, particularly during February 2020. This research is motivated by previous challenges encountered in interferometric control due to the saturation of control electronics by the sidebands of sidebands. The chapter commences by providing an overview of Gaussian optics fundamentals and the Pound-Drever-Hall (PDH) technique, which serves as the primary approach for controlling the resonant cavity of the Advanced Virgo detector. The application of the fundamental principles results in the formulation of an analytical representation of the PDH error signal in the presence of a higher-order Hermite-Gaussian mode. The primary focus of the

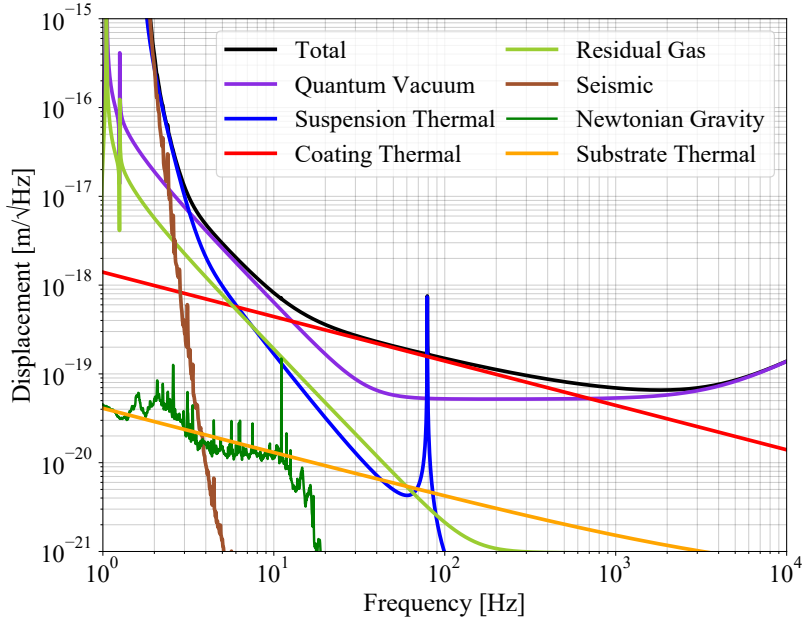
chapter is to validate a Finesse sideband evolution simulation against experimental signals from the operating detector. The comparison between simulation and data is conducted by analyzing the amplitude trends of different sidebands in various detection ports when the interferometer is locked to its operating point. The input of the simulation is the O3 baseline configuration of the Virgo detector. The simulation involves measuring the changes in the electromagnetic field at various detection ports while manipulating the optical cavities in a way that emulates the variable-finesse locking technique of the VIRGO detector. The simulation's output is the evolution of sideband amplitude during the interferometric lock, starting from the half-fringe interference condition. The experimental data consists of amplitude spectral density values collected from longitudinal detection ports during twenty distinct interferometric lock acquisitions for each sideband frequency under investigation. The chapter's findings suggest that the Pearson linear coefficients for the simulation and measurement data show a high degree of significance in 75% of the experiments. Conversely, the remaining coefficients either indicate negligible significance or are linked to noise data, which can be discounted.

In Chapter 3, the ETpathfinder facility is introduced. ETpathfinder is a cryogenic research and development laboratory that plans to evaluate and incorporate the fundamental technologies for the third-generation of gravitational-wave detectors. This will be done using a 10 m arm-length, low-noise interferometer in an environment similar to that of Einstein Telescope. The chapter begins with an overview of the fundamental principles of third-generation detectors, followed by a comprehensive examination of the ETpathfinder facility and the optical configuration of the interferometers. The primary focus of the chapter is to calculate the fundamental noise contributions for two specific configurations of ETpathfinder: 1) ETpathfinder-A, which functions at a temperature of 18 K and a wavelength of 1550 nm; and 2) ETpathfinder-B, which operates at a wavelength of 2090 nm and a temperature of 123 K. The resultant displacement sensitivity is shown in Figure 1. At a temperature of 123 K, the interferometer's amplitude spectral density is constrained by suspension thermal noise at low frequencies, coating thermal noise in the medium frequency range, and shot noise at high frequencies. At this temperature, the significant thermo-optic coefficient of crystalline silicon, along with the use of small beam diameters on optics, results in the middle sensitivity band being predominantly affected by the thermo-refractive noise. In order to address this issue, the arm-cavity finesse has been raised from 800 to a value of 2050. This helps to decrease the noise and enables the middle sensitivity range to be constrained by the coating Brownian noise, a noise source of high interest for current and future interferometers. The incorporation of silicon suspension fibers and decreasing the operating temperature of the interferometer aids in lowering the broadband thermal noises, therefore making the radiation pressure noise to become significant between 4 to 10 Hz. This large increase in sensitivity allows the ETpathfinder interferometer, operating with 1550 nm laser light and below 20 K temperature, to meet the design

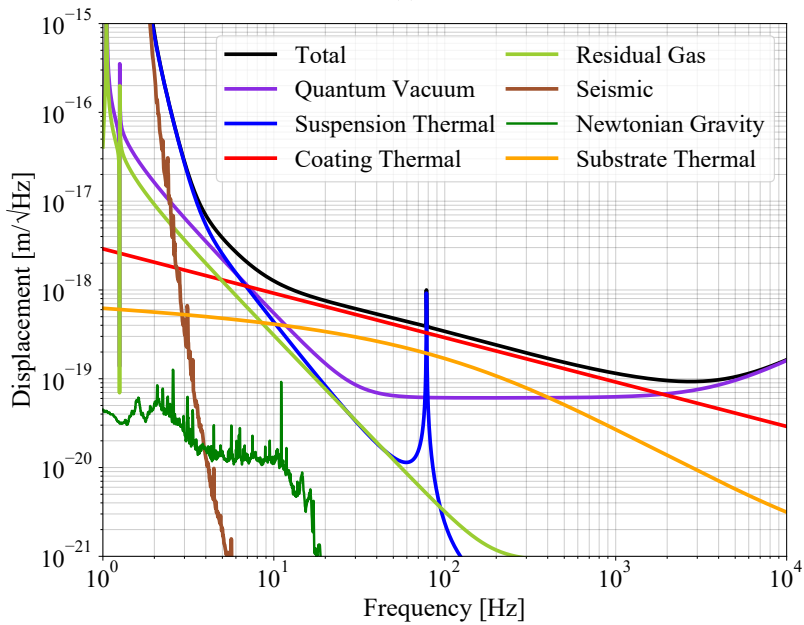
sensitivity of $1 \times 10^{-18} \text{ m}/\sqrt{\text{Hz}}$ at 10 Hz.

The fourth part of this thesis, Chapter 4, examines the influence of acoustic vibrations transmitted through the flexible conductive heat-links in a test setup that is compatible with the ETpathfinder suspension systems. This study begins by introducing the experimental setup: a triple pendulum suspension that is isolated from the ground using three inverted pendula. The suspension system includes a series of rings that facilitate the transmission of vibrations from the external environment to the various stages of the pendulum system. The main body of the chapter describes in detail various experimental measurements of vibrations via conductive heat-links and simulations of these couplings. Theoretical and finite-element calculations are used to simulate the acoustic transmission via the soft links between the excitation ring (referred to as the cold finger) and the coupling ring (referred to as the heat-link ring). In general, it was determined that the simulations closely resemble the measurements. A marginal disparity is identified between the model and the data with regard to the broadband roll-off of the transfer function. This represents a 25% increase in the overall effective heat-link stiffness, for which an adjustment was made in the simulation. In the final part of the chapter, seismic noise is projected onto the ETpathfinder noise budget using a data-driven simulation. This provides a sensitivity analysis of the displacement noise associated with the conductive cooling strength.

Chapter 5, the last chapter of the thesis, delves deeper into the interferometric control techniques that were initially introduced in Chapter 2. Nevertheless, the main focus lies in the angular control of the mirrors, particularly the automated alignment of Fabry-Perot resonant cavities using machine learning techniques. The study presents a novel computer vision-based method for automatically detecting and controlling the angular misalignment of optical cavities. The fundamental concept is to utilize a two-dimensional convolutional neural network to learn the transverse electromagnetic modes generated when a mirror is misaligned and to generate an error signal that is effective for mirror control. A neural network was successfully trained and evaluated using experimental phase images taken in the near-field from an optical test setup constructed at Nikhef, in Amsterdam, serving as a proof of concept. The neural network demonstrated exceptional precision and efficiency in predicting mode numbers from experimental phase images. The comprehensive methodology was successfully integrated into a sequence of control scripts to lock the resonant cavity. Each identified mode number was assigned a gain inside the control and actuation script, which methodically adjusts the mirror to its correct position and triggers the linear PDH error signal control.



(a)



(b)

Figure 1: Projection of displacement sensitivity for the ETpathfinder operating at two targeted configurations: a) with 1550 nm laser light and at 18 K and b) with a wavelength of 2090 nm and radiatively cooled down at 123 K.

Zwaartekrachtsgolven zijn rimpelingen in het weefsel van de ruimtetijd, voorspeld door Einsteins Theorie van Algemene Relativiteit. Een waarneembaar effect dat wordt geproduceerd door een passerende zwaartekrachtsgolf is de verandering in afstand tussen twee testmassa's in geodetische vrije val; dit waarneembare effect kan over een breed frequentiespectrum worden gemeten met een laserinterferometer door de differentiële verplaatsing tussen twee loodrecht op elkaar staande testmassa's aan het einde van de interferometer te monitoren. Huidige zwaartekrachtsgolfinterferometers, zoals LIGO (Laser Interferometer Gravitational-wave Observatory), Virgo of KAGRA (Kamioka Gravitational Wave Detector), zijn succesvol geweest in het detecteren van een verscheidenheid aan gebeurtenissen, te beginnen met de eerste detectie van een binair zwart gat door LIGO, GW150914, gemeten op 14 september 2015. Detectoren van de derde generatie, zoals de Einstein Telescoop (ET) en Cosmic Explorer (CE), maken gebruik van nieuwe interferometrische technologieën en streven ernaar de mogelijkheden van bestaande grondgebonden detectoren te overtreffen, waardoor ze een meetgevoeligheid voor passerende zwaartekrachtsgolven kunnen bereiken die bijna tien keer hoger is dan huidige interferometers. Dit proefschrift bestudeert enkele van de geavanceerde technologieën voor de nieuwe generatie van zwaartekrachtsgolfdetectoren, zoals cryogene interferometrie en geavanceerde detectie- en controleschema's. Een meer diepgaande introductie tot het onderwerp wordt gepresenteerd in Hoofdstuk 1.

Hoofdstuk 2 van deze thesis verdiept zich in een analyse van de evolutie van de radiofrequentie (RF) controlezijbanden van de Advanced Virgo Interferometer gedurende de derde wetenschappelijke run, aangeduid als O3, met name in Februari 2020. Dit onderzoek wordt gemotiveerd door eerdere uitdagingen die zijn ondervonden bij interferometrische controle door de verzadiging van de controle-elektronica door de zijbanden van zijbanden. Het hoofdstuk begint met een overzicht van de basisprincipes van de Gaussische optica en de Pound-Drever-Hall (PDH)-techniek,

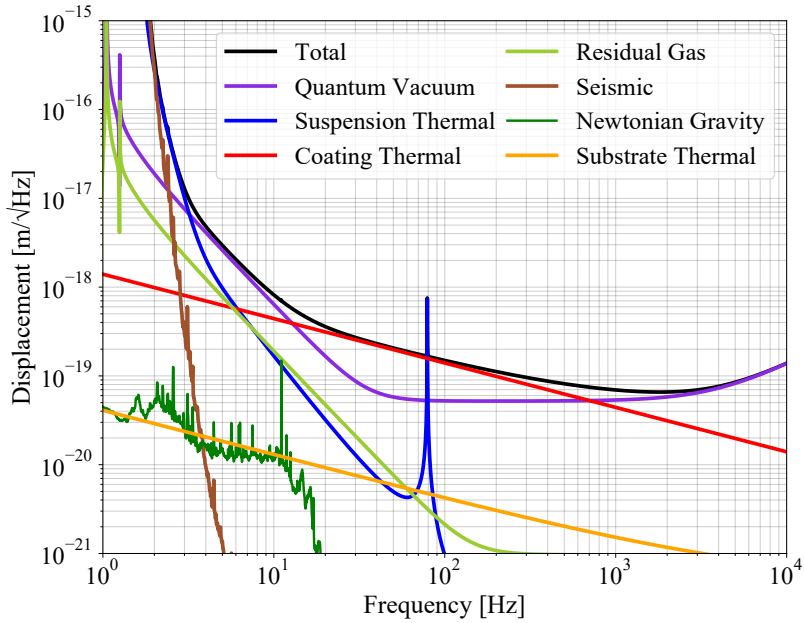
die dient als de primaire benadering voor het controleren van de resonante holte van de Geavanceerde Virgo- detector. De toepassing van de basisprincipes resulteert in de formulering van een analytische representatie van het PDH-foutsingaal in de aanwezigheid van een hogere-orde Hermite-Gaussische mode. De primaire focus van het hoofdstuk is het valideren van een FINESSE zijbandevolutiesimulatie tegen experimentele signalen van de werkende detector. De vergelijking tussen simulatie en gegevens wordt uitgevoerd door de amplitude trends van verschillende zijbanden in verschillende detectiepoorten te analyseren wanneer de interferometer wordt vergrendeld naar zijn werkingpunt. De invoer van de simulatie is de O3-basisconfiguratie van de Virgo-detector. De simulatie omvat het meten van de veranderingen in het elektromagnetische veld bij verschillende detectiepoorten terwijl de optische holtes op een manier worden gemanipuleerd die de variabele-finesse vergrendeltechniek van de VIRGO-detector emuleert. De uitvoer van de simulatie is de evolutie van de zijbandamplitude tijdens de interferometrische vergrendeling, beginnend vanaf de half-fringe interferentieconditie. De experimentele gegevens bestaan uit amplitude spectrale dichtheidswaarden verzameld van longitudinale detectiepoorten tijdens twintig afzonderlijke interferometrische vergrendelacquisities voor elke onderzochte zijbandfrequentie. De bevindingen van het hoofdstuk suggereren dat de Pearson lineaire coëfficiënten voor de simulatie- en meetsets een hoge mate van significantie vertonen in 75% van de experimenten. Omgekeerd geven de resterende coëfficiënten een verwaarloosbare significantie aan of zijn gekoppeld aan ruisgegevens, die genegeerd kunnen worden.

In Hoofdstuk 3 wordt de ETpathfinder-faciliteit geïntroduceerd. ETpathfinder is een cryogeen onderzoeks- en ontwikkelingslaboratorium dat van plan is de fundamentele technologieën voor de derde generatie van zwaartekrachtsgolfdetectoren te evalueren en te integreren. Dit zal worden gedaan met behulp van een 10 meter lange, geluidsarme interferometer in een omgeving vergelijkbaar met die van de Einstein Telescoop. Het hoofdstuk begint met een overzicht van de fundamentele principes van detectoren van de derde generatie, gevolgd door een uitgebreide analyse van de ETpathfinder-faciliteit en de optische configuratie van de interferometers. De primaire focus van het hoofdstuk is het berekenen van de fundamentele ruisbijdragen voor twee specifieke configuraties van ETpathfinder: 1) ETpathfinder-A, die functioneert bij een temperatuur van 18 K en een golflengte van 1550 nm; en 2) ETpathfinder-B, die werkt bij een golflengte van 2090 nm en een temperatuur van 123 K. De resulterende verplaatsingsgevoeligheid wordt getoond in Figuur 1. Bij een temperatuur van 123 K wordt de verplaatsingsgevoeligheid van de interferometer beperkt door suspensie-thermische ruis bij lage frequenties, coating-thermische ruis in het middenfrequentiebereik, en hagelruis bij hoge frequenties. Bij deze temperatuur leidt de aanzienlijke thermo-optische coëfficiënt van kristallijn silicium, samen met het gebruik van kleine bundeldiameters op optica, ertoe dat het middeengevoeligheidsbereik voornamelijk wordt beïnvloed door ITM thermo-refractieve ruis. Om dit probleem aan te pakken, is de finesse van de armholte verhoogd

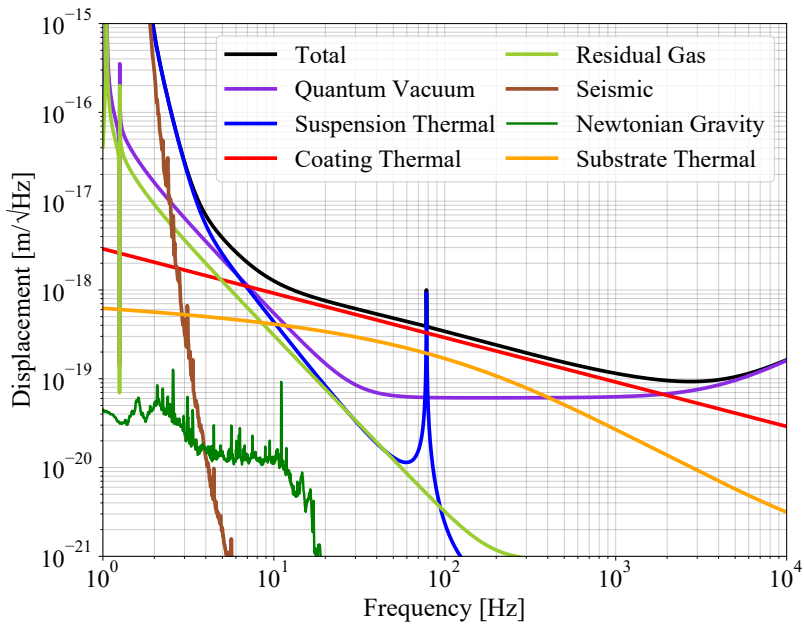
naar een waarde van 2050. Dit helpt om de ruis te verminderen en zorgt ervoor dat het middengevoeligheidsbereik wordt beperkt door de Brownse ruis van de coating, een bron van ruis die van groot belang is voor huidige en toekomstige interferometers. De integratie van silicium ophangingsvezels en het verlagen van de bedrijfstemperatuur van de interferometer helpt om de breedbandige thermische ruis te verlagen, waardoor de stralingsdrukruis significant wordt tussen 4 en 10 Hz. Deze grote toename in gevoeligheid stelt de ETpathfinder, die werkzaam is met een laser van 1550 nm en een temperatuur onder 20 K, in staat om de gewenste gevoeligheid van $1 \times 10^{-18} \text{ m}/\sqrt{\text{Hz}}$ bij 10 Hz te bereiken.

Het derde deel van dit proefschrift, Hoofdstuk 4, onderzoekt de invloed van akoestische trillingen die worden overgedragen via de flexibele geleidende warmteverbindingen in een testopstelling die compatibel is met de ophangsystemen van ETpathfinder. Het hoofdstuk begint met het introduceren van de experimentele opstelling: een drievoudige pendulumophanging die is geïsoleerd van de grond met behulp van omgekeerde pendula. Deze ophanging bevat een reeks ringen die de overdracht van trillingen van de externe omgeving naar de verschillende stadia van het pendulumsysteem vergemakkelijken. Het hoofdonderdeel van het hoofdstuk beschrijft in detail verschillende experimentele metingen van trillingen via geleidende warmteverbindingen en simulaties van deze koppelingen. Theoretische en eindige-elementenberekeningen worden gebruikt om de akoestische overdracht via de zachte verbindingen tussen de excitatie (aangeduid als de koude vinger) en de koppelingsring (aangeduid als de warmteverbindingring) te simuleren. Over het algemeen werd vastgesteld dat de simulaties sterk lijken op de metingen. Een marginale afwijking wordt geïdentificeerd tussen het model en de gegevens met betrekking tot de breedbandige afname van de overdrachtsfunctie. Dit vertegenwoordigt een toename van 25% in de algehele effectieve stijfheid van de warmteverbinding, waarvoor een aanpassing werd gemaakt in de simulatie. In het laatste deel van het hoofdstuk wordt seismische ruis geprojecteerd op het ruisbudget van ETpathfinder met behulp van een datagestuurde simulatie. Dit biedt een gevoeligheidsanalyse van de verplaatsingsruis die samenhangt met de sterkte van de geleidende koeling.

Hoofdstuk 5, het laatste hoofdstuk van het proefschrift, gaat dieper in op de interferometrische controletechnieken die in Hoofdstuk 2 werden geïntroduceerd. De belangrijkste focus ligt echter op de hoekcontrole van de spiegels, met name de geautomatiseerde uitlijning van Fabry-Perot resonantieholtes met behulp van machine learning-technieken. De studie presenteert een nieuwe computervisie-gebaseerde methode voor het automatisch detecteren en regelen van de angulaire misuitlijning van optische holtes. Het fundamentele concept is het gebruik van een tweedimensionaal convolutioneel neurale netwerk om de transversale elektromagnetische modi te leren die gegenereerd worden wanneer een spiegel is misuitgelijnd en om een foutsignaal te genereren dat effectief is voor spiegelcontrole. Een neurale netwerk is succesvol getraind en geëvalueerd met behulp van experimentele fasebeelden genomen in het nabije veld van een optische testopstelling gebouwd bij Nikhef in Amsterdam,



(a)



(b)

Figure 1: Projectie van verplaatsingsgevoeligheid voor de ETpathfinder werkend in twee doelconfiguraties: a) met 1550 nm laserlicht en bij 18 K en b) met een golflengte van 2090 nm en radiatief gekoeld tot 123 K.

als een proof-of-concept. Het neurale netwerk toonde uitzonderlijke precisie en efficiëntie in het voorspellen van modusnummers uit experimentele fasebeelden. De uitgebreide methodologie is met succes geïntegreerd in een reeks van controlescripts om de resonantieholtte te vergrendelen. Elk geïdentificeerd modusnummer kreeg een versterking binnen het controle- en actuatiescript, dat de spiegel methodisch aanpast naar zijn juiste positie en de lineaire Pound-Drever-Hall foutsigitaalcontrolle activeert.

Albert Einstein advanced Newton's description of gravity by formalizing the theory of general relativity, in which he established a profound correlation between the mass of an object and the complex geometry of spacetime. This groundbreaking framework has since become the principle theory for comprehending gravitational phenomena, profoundly influencing the field of theoretical physics. Einstein also predicted the existence of waves in the fabric of spacetime, called gravitational waves. As the fabric of spacetime is very stiff, detecting gravitational waves requires cataclysmic events like black hole collisions or supernovae. As they propagate, these waves stretch and squeeze spacetime, and carefully designing instruments to capture this effect is the key to measuring them. Devices like interferometers measure this effect by monitoring the time difference in light travel along perpendicular arms. LIGO (Laser Interferometer Gravitational-wave Observatory) achieved this on September 14, 2015, detecting the inaugural collision of a binary black hole. The first generation of gravitational-wave detectors, such as LIGO and Virgo, were only built for detection and not for large-scale surveys of the Universe. With the next generation of detectors, such as the Einstein Telescope (ET) or Cosmic Explorer (CE), gravitational-wave science will expand its horizons before the creation of the first stars, almost to the point of the Big Bang.

The second part of this thesis discusses interferometric control strategies for the Advanced Virgo detector's longitudinal degrees of freedom. The longitudinal degrees of freedom are the main distances between the mirrors of the interferometer that must be controlled to allow the interferometer to measure astronomical signals. The mathematical form of a controlling signal is presented in this chapter. As an example, this signal is highly relevant for the Advanced Virgo power-recycling cavity. Additionally, the chapter looks at a match between simulation and experimental data to see how various controlling signals vary as the Advanced Virgo interferometer is brought to its operating point. The match is significant for the majority of the studied

cases. Therefore, these results are highly relevant for the sensing and controlling strategies of the Virgo detector, and the subtle links between the controlling signals and their interaction with different mirror surfaces in the optical cavities of the detector.

The thesis continues with the investigation of the ETpathfinder facility, which is a research laboratory for testing new-generation gravitational-wave detection technologies. The readiness of all subsystems, as well as the development of new technologies, must be performed during the technical design of large-scale next-generation interferometers. This is done in specialized testing facilities such as ETpathfinder. As a result, analyzing and contributing to the construction of such facilities is critical for the gravitational-wave community. The chapter develops noise budgets for two ETpathfinder future configurations. These curves, which result from the interaction of various physical processes with interferometer test masses, illustrate the ETpathfinder detector sensitivity to differential displacements. This study is significant for two reasons: first, it sheds light on how different physical phenomena interact with the ETpathfinder interferometer; second, it provides the ETpathfinder scientific team and the gravitational-wave community with an overview of the test-bed's potential performance for future research.

Einstein Telescope plans to operate at cryogenic temperatures below minus 250 degrees Celsius. Therefore, the test masses of this instrument must be cooled down and stabilized at such low temperatures. This operation must be carried out without introducing parasitic noises to the test mass displacement, such as acoustic noises from the cooling instruments. The fourth part of the thesis addresses this question by developing an experimentally-validated model of how conductive cooling vibrations influence ETpathfinder sensitivity. This work is the first experimental demonstration of acoustic transfer through soft conductive wires employed in the ETpathfinder cooling system. As a result, it is significant in the context of cryogenic cooling system design for ETpathfinder or future gravitational-wave experiments. Furthermore, being able to simulate the impact of cooling vibrations on ETpathfinder sensitivity is critical for comprehending and expanding the scientific case of the test-bed.

The last part of this thesis focuses on the angular control of the interferometer optics using the power of modern computer vision techniques. The suspended optics in gravitational-wave detectors deviate from their aligned positions due to their interaction with the seismic fields present in the instrument's surroundings. Typically, skilled operators use various alignment techniques to sense and correct the angular positions of the mirrors. This process often involves lengthy commissioning times. A novel technique which uses machine learning-based pattern recognition has been demonstrated in a test-setup at Nikhef. This work is highly relevant for commissioning gravitational-wave detectors and offer a starting point in automation via machine learning. Besides the gravitaitional-wave field, the work can be significant in many other areas of automatic and fast feedback control.

Propositions

1. The displacement sensitivity of the targeted ETpathfinder configuration operating at cryogenic temperatures of 18 K with a laser wavelength of 1550 nm meets the design requirement of $1 \times 10^{-18} \text{ m}/\sqrt{\text{Hz}}$ at 10 Hz.
2. Sensing and controlling the angular misalignments of suspended optics in gravitational-wave detectors can be achieved using machine learning-based computer vision to recognize the light field transverse mode patterns.
3. Maintaining test masses at cryogenic temperatures for next-generation gravitational-wave detectors should not decrease the test mass displacement sensitivity. This can be realized with passive and active seismic isolation of the radiative cooling pathways.
4. The control of marginally stable optical cavities in gravitational-wave detectors can be improved by understanding how the control sidebands interact with higher order Hermite-Gaussian modes in the cavities.
5. Research test beds are vital in paving the way for large-scale physical experiments.
6. Commissioning of large-scale detectors, such as Einstein Telescope, will benefit from a fully automatic sequence of global and local instrumental control of multiple co-located interferometers.
7. Future gravitational-wave instruments should operate large scale networks optimized for specific scientific targets.
8. Directly probing the early stages of the Universe prior to the recombination epoch is only possible by detecting gravitational waves.

Curriculum Vitae

Andrei Utina was born on May 25, 1994, in Bucharest, Romania. He studied at the University of Glasgow in the United Kingdom from 2013 to 2018, earning an MSci in Physics with Astrophysics. During his studies, he worked on several summer research projects at the University of Glasgow and the Virgo interferometer near Pisa, Italy.

In 2018, he started his PhD in Physics and Astronomy at the University of Glasgow, under the supervision of Professors Stefan Hild and Ken Strain. In 2019, he was transferred to the University of Maastricht and Nikhef in the Netherlands to continue his PhD. Until October 2022, he was a PhD researcher working on his thesis named “Instrumentation and characterization techniques for advanced gravitational-wave observatories”.

Andrei has been working at ASML since October 2022 as an optical design engineer for the EUV Optical Column of the most advanced ASML nodes.

